THESIS FOR THE DEGREE OF DOCTOR OF PHILOSOPHY

Superinductance and fluctuating two-level systems

Loss and noise in disordered and non-disordered superconducting quantum devices

DAVID NIEPCE

Department of Microtechnology and Nanoscience (MC2)

Quantum Technology Laboratory

CHALMERS UNIVERSITY OF TECHNOLOGY

Göteborg, Sweden 2020

Superinductance and fluctuating two-level systems
Loss and noise in disordered and non-disordered superconducting quantum devices
DAVID NIEPCE
ISBN 978-91-7905-312-3

Doktorsavhandlingar vid Chalmers tekniska högskola
Ny serie nr. 4779
ISSN 0346-718X

Quantum Technology Laboratory
Department of Microtechnology and Nanoscience (MC2)
Chalmers University of Technology
SE-412 96 Göteborg
Sweden
Telephone: +46 (0)31-772 1000

Cover:
Histogram of frequency fluctuations of a nanowire superinductor against circulating power (in units of the average photon occupation number $\langle n \rangle$).

Chalmers Digitaltryck
Göteborg, Sweden 2020

Superinductance and fluctuating two-level systems
Loss and noise in disordered and non-disordered superconducting quantum devices
Thesis for the degree of Doctor of Philosophy
DAVID NIEPCE
Department of Microtechnology and Nanoscience (MC2)
Chalmers University of Technology

Abstract

In this thesis, we first demonstrate that a disordered superconductor with high kinetic inductance can realise a microwave low-loss, non-dissipative circuit element with impedance greater than the quantum resistance ($R_Q = h/4e^2 \simeq 6.5\,\mathrm{k\Omega}$). This element, known as a superinductor, can suppress the fluctuations of charge in a quantum circuit.

For this purpose, we fabricated and characterised 20 nm thick, 40 nm wide niobium-nitride nanowires and determined the impedance to 6.795 kΩ. We demonstrate internal quality factors $Q_i = 2.5 \times 10^4$ in nanowire resonators at single photon excitation, which is significantly higher than values reported in devices with similar materials and geometries. Moreover, we show that the dominant dissipation in our nanowires is not an intrinsic property of the disordered films, but can instead be fully understood within the framework of two-level systems.

To further characterise these losses, we then explore the geometrical scaling, toward nanowire dimensions, of dielectric losses in superconducting microwave resonators fabricated with the same techniques and from the same NbN thin-film as the nanowire superinductors. For this purpose, we perform an experimental and numerical study of dielectric loss at low temperatures. Using 3D finite-element simulation of the Maxwell–London equations, we compute the geometric filling factors of the lossy regions in our resonator structures and fit the experimental data to determine the intrinsic loss tangents of its interfaces and dielectrics.

Finally, we study the effect of two-level systems on the performance of various superconducting quantum circuits. For this purpose, we measure coherence-time fluctuations in qubits and frequency fluctuations in resonators. In all devices, through statistical analysis, we identify the signature of individual Lorentzian fluctuators in the noise. We find that fluctuations in qubit relaxation are local to the qubit and are caused by instabilities of near-resonant two-level-systems. Furthermore, when examining the low-frequency noise of three different types of superconducting resonator—one NbN nanowire, one Al coplanar waveguide, and one Al 3D cavity—we observe a similar power-law dependence of the Lorentzian switching time and amplitude on the circulating power in the resonators, suggesting a common noise mechanism in the three different types of devices.

Keywords: Nanowire, Superinductance, Superinductor, Superconducting circuits, Quantum information, Two-level Systems, TLS, Disordered Superconductors

List of Publications

This thesis is based on the work containted in the following appended papers:

Paper A D. Niepce, J. Burnett and J. Bylander. High Kinetic Inductance NbN Nanowire Superinductors. *Phys. Rev. Appl.* **11**, 044014 (2019)

Paper B D. Niepce, J. Burnett, M. Gutierrez Latorre and J. Bylander. Geometric Scaling of Two-Level-System Loss in Superconducting Resonators. *Supercond. Sci. Technol.* **33**, 025013 (2020)

Paper C D. Niepce, J. Burnett, M. Kudra, J H. Cole and J. Bylander. Drive-power Dependent Fluctuations of Single Two-Level Systems in Superconducting Resonators. *Manuscript in preparation* (2020)

Paper D J. Burnett, A. Bengtsson, D. Niepce and J. Bylander. Noise and Loss of Superconducting Aluminium Resonators at Single Photon Energies. *J. Phys. Conf. Ser.* **969**, 012131 (2018)

Paper E J. Burnett, A. Bengtsson, M. Scigliuzzo, D. Niepce, M. Kudra, P. Delsing and J. Bylander. Decoherence Benchmarking of Superconducting Qubits. *npj Quantum Inf.* **5**, 54 (2019)

Other papers that are outside of the scope of this thesis:

Paper I I. Harrysson Rodrigues, D. Niepce, A. Pourkabirian, G. Moschetti, J. Schleeh, T. Bauch and J. Grahn. On the angular dependence of InP high electron mobility transistors for cryogenic low noise amplifiers in a magnetic field. *AIP Adv.* **9**, 085004 (2019)

Paper II M. Kudra, J. Biznárová, A. Fadavi Roudsari, J. Burnett, D. Niepce, S. Gasparinetti, B. Wickman and P. Delsing. High Quality Aluminium Cavities. *arXiv.org*, 2006.02213 (2020)

Contents

List of Symbols

Constants

h	Planck constant	$h \simeq 6.626 \times 10^{-34}\,\mathrm{J\,s}$
$\hbar$	Reduced Planck constant	$h/2\pi \simeq 1.055 \times 10^{-34}\,\mathrm{J\,s}$
e	Elementary charge	$e \simeq 1.602 \times 10^{-19}\,\mathrm{C}$
m_e	Mass of an electron	$m_e \simeq 9.109 \times 10^{-31}\,\mathrm{kg}$
c	Speed of light in vacuum	$c \simeq 2.998 \times 10^{8}\,\mathrm{m\,s^{-1}}$
k_B	Boltzmann's constant	$k_B \simeq 1.381 \times 10^{-23}\,\mathrm{J\,K^{-1}}$
μ_0	Vacuum permeability	$\mu_0 \simeq 1.257 \times 10^{-6}\,\mathrm{H\,m^{-1}}$
ε_0	Vacuum permittivity	$\varepsilon \simeq 8.854 \times 10^{-12}\,\mathrm{F\,m^{-1}}$
R_K	Von Klitzing constant	$h/e^2 \simeq 25.812\,\mathrm{k\Omega}$
R_Q	Superconducting resistance quantum	$h/4e^2 \simeq 6.453\,\mathrm{k\Omega}$
γ	Euler-Mascheroni constant	$\gamma \simeq 5.772 \times 10^{-1}$
Φ_0	Magnetic flux quantum	$h/2e \simeq 2.068 \times 10^{-15}\,\mathrm{Wb}$

Chapter 1: Introduction

L_{nw}	Inductance per length of the nanowire
C_{nw}	Capacitance per length of the nanowire
Z_{nw}	Characteristic impedance of the nanowire

Chapter 2: Disordered Superconductors

T_c	Critical temperature of a superconductor
τ	Average time between scattering events
σ_n	Normal electrons conductivity (two-fluid model)
σ_s	Superconducting electrons conductivity (two-fluid model)
ω	Angular frequency
n_n	Density of normal electrons
n_s	Density of superconducting electrons
ε_f	Fermi energy
k_F	Fermi wavevector
v_F	Fermi velocity
ρ_n	Normal metal density of states
l	Electron mean free path
$\vec{E}$	Electric field
$\vec{B}$	Magnetic field
$\vec{H}$	Auxiliary magnetic field
$\vec{A}$	Magnetic vector potential
$\vec{j_n}$	Current density of normal electrons
$\vec{j_s}$	Current density of superconducting electrons

λ_L	London penetration depth
ψ	Superconducting order parameter
φ	Superconducting phase
F	Free energy
ξ_{GL}	Ginzburg-Landau coherence length
κ	Ginzburg-Landau parameter
H_c	Critical field
H_{c1}	Lower critical field
H_{c2}	Upper critical field
ρ_s	BCS density of states
Δ	Superconducting gap
Δ_0	Superconducting gap at zero temperature
ω_D	Debye frequency
ξ_0	BCS coherence length
$k_F l$	Ioffe-Regel parameter
λ_{dirty}	London penetration depth (dirty limit)
Λ	Effective penetration depth
L_m	Magnetic inductance (internal)
L_k	Kinetic inductane
E_{mag}	Magnetic energy
E_{kin}	Kinetic energy
Z_S	Surface impedance
δ	Skin depth
σ_1	Real part of Mattis-Bardeen conductivity
σ_2	Imaginary part of the Mattis-Bardeen conductivity
R_N	Normal state resistance
σ_{2D}	Fluctuations paraconductivity
T_{BKT}	Berezinskii-Kosterlitz-Thouless ordering temperature
U_{VAP}	Vortex-Antivortex Pair potential energy
$A(T)$	Vortex polarizability
$\mu_c(T)$	Vortex core energy
$\rho(T)$	Unbound VAP resistivity
D	Quasiparticle diffusivity
$\vec{j_c}$	Critical current density
L_J	Josephson inductance
E_J	Josephson energy
E_C	Charging energy
α_r	Relative anharmonicity
E_m	Eigenenergy of the m^{th} level
ε_m	Charge dispersion
Z_0	Characteristic impedance
$\vec{E_{\lambda/4}}$	Electric field in the cavity
$\vec{H_{\lambda/4}}$	Magnetic field in the cavity
β_{01}	Cavity propagation constant

Chapter 3: Superconducting Microwave Resonators

S	Scattering parameters matrix
S_{11}	Reflection coefficient
S_{21}	Transmission coefficient
γ	Propagation constant
α	Real part of the propagation constant
β	Imaginary part of propagation constant
Z_{in}	Input impedance
v_{ph}	Phase velocity
ω_0	Resonance frequency
$\Delta\omega$	Frequency detuning
Q_i	Internal quality factor
Q_c	Coupling quality factor
Q_l	Loaded quality factor
M	Mutual inductance
$\langle E_{int} \rangle$	Resonator internal energy
$\langle n \rangle$	Average number of photons
P_{in}	Input power

Chapter 4: Losses in Superconducting Circuits

$1/Q_{TLS}$	TLS induced loss
$1/Q_{qp}$	Quasiparticle induced loss
$1/Q_{disorder}$	Disorder induced loss
$1/Q_{rad}$	Radiation loss
F	TLS Filling factor (participation ratio)
$F \tan \delta^i_{TLs}$	Intrinsinc loss tangent
R_{ESR}	Capacitor equivalent series resistor
P_γ	TLS switching rate ratio
γ_{min}	Minimum TLS switching rate
γ_{max}	Maximum TLS switching rate
δ_0	Next dominant loss

Chapter 5: Fluctuation Processes in Superconducting Circuits

$z(t)$	Real-valued time-dependent signal
$\mu(t)$	Mean of $z(t)$
$\sigma^2(t)$	Variance of $z(t)$
$y(t)$	Fractional fluctuations, $y(t) = z(t)/\mu$
$R(t_1, t_2)$	Autocorrelation function
$S_z(\omega)$	Power spectral density of $z(t)$
$S_y(\omega)$	Power spectral density of $y(t)$
$\sigma^2_y(t)$	Allan variance of $y(t)$
$\sigma_y(t)$	Allan deviation of $y(t)$

f_L	Leeson frequency
h_{-2}	Random walk noise amplitude
h_{-1}	Flicker $(1/f)$ noise amplitude
h_0	White nosie amplitude
A	Lorentzian/RTS amplitude
τ_0	Lorentzian/RTS characteristic time constant

Chapter 6: Nanofabrication Techniques

γ	Resist contrast
D_0	Threshold dose
D_1	Clearing dose
λ_e	De Broglie wavelength
D	EBL exposure dose
τ_{dwell}	EBL beam dwell time
I_{beam}	EBL beam current
δ	EBL beam step

Chapter 7: Measurement Techniques

A	Phase modulated signal
β	Phase modulation depth
Ω	Modulation frequency
ε	Error signal
$\hat{\mathcal{H}}_{JC}$	Jaynes-Cumming Hamiltonian
$\hat{\mathcal{H}}_{disp}$	Dispersive readout Hamiltonian

Chapter 8: Simulation Techniques

ε_{SC}	Equivalent permittivity for a superconductor
l_{cpw}	Length of a section of coplanar waveguide (CPW)
w_{cpw}	Width of the CPW central conductor
g_{cpw}	Gap between the central conductor and ground plane of the CPW

Chapter 9: Device Design and Considerations

Γ_S	Phase slip rate
R_H	Hall coefficient

Chapter 10: Results - NbN Thin-film Charactersation and Optimisation

I_r	Retrapping current
σ_K	Kapitza conductance

Chapter 13: Results - Fluctuations in Superconducting Circuits

T_1	Qubit relaxation time
T_2^*	Qubit dephasing time
W	Characteristic switching rate
$\hat{\mathcal{H}}_0$	TLS Hamiltonian
Δ_0	Tunnel coupling
ε	Driving amplitude
ε	Equilibrium position
ε_{rf}	RF driving amplitude
$\hat{\mathcal{H}}_{RF}$	TLS Hamiltonian with RF driving
Γ_1	TLS relaxation rate
Γ_2	TLS dephasing rate

List of Figures

List of Tables

Acknowledgements

At the end of this long journey, I wish to express my sincere appreciation toward everyone that helped make this thesis possible.

First and foremost, I would like to express my gratitude towards my supervisor, Prof. Jonas Bylander. Jonas, throughout this work, you have been an endless source of optimism, support and inspiration. Thank you for giving me the opportunity to pursue this captivating project and thank you for always finding the right words to keep me motivated when things were looking dire. Sadly, we didn't get the chance to do *everything* we wanted to do — I guess making these nanowires was a bit more complicated than the "one week project" we originally had in mind... Let's take a rain check on all these ideas!

I would also like to take the opportunity to thank my co-supervisor and examiner, Prof. Sergey Kubatkin, for his valuable feedback on my work, and Prof. Per Delsing, the head of our division, for always finding the time to answer my random questions about superconductivity, despite his busy schedule.

Thank you to all the present and past members of QTL and QDP for making our research groups an amazing work environment!

I am also grateful toward Marcus Rommel, Niclas Lindvall, Henrik Frederiksen, Johan Andersson, Mats Hagberg, Bengt Nilsson and the rest of the staff of the Nanofabrication Laboratory clean room for training me on so many tools and always being available for input and support.

A big thank you to Lars Jönsson, for his invaluable help in the workshop and always putting up with us, our last minute machining jobs and back of the envelope designs...

Next, I would like to thank Linda Brånnel and Susannah Carlsson for their great administrative support, and Henric Fjellstedt for always being available, helpful and, most importantly, always fighting on the good side of many IT-related battles!

Last but certainly not least, I would like to thank my friends and my family for their unrelenting support throughout the years. Thank you mom, dad, Janka, for all your support and love, for always believing in me and for always being there for me.

David Niepce, Göteborg, August 2020

Chapter 1

Introduction

In this thesis, we present the *nanowire superinductor*—a new mesoscopic, superconducting quantum device made of a thin-film disordered superconducting material. Superinductors can be used as crucial circuit components for applications within, e.g., quantum computer processors or sensors for photon detection.

In particular, new types of improved superconducting qubits are notable applications of superinductors, motivating our work. Qubits are the fundamental building blocks of quantum computers—a currently very hot research topic promising enormously enhanced computing capability compared to even the best supercomputers of tomorrow. Today's quantum processors are small, and there are a few competing technologies, but superconducting qubits seem to represent the best-performing and most scalable approach to building larger quantum computers.

Recent years have witnessed tremendous progress in the preservation of quantum coherent states in superconducting qubits [1]. This evolution has been driven by both device and materials engineering, and it is now common to see a variety of device architectures with coherence times around 100 µs [1–5], allowing us to implement coupled-qubit gates, driven by microwave pulses of duration shorter than 100 ns, with gate fidelity (accuracy) in excess of 99%. However, this is barely good enough to start implementing interesting quantum algorithms on small-scale quantum processors: higher fidelities are desired in order to drastically increase the usefulness of these processors.

To this end, novel superconducting qubits based on superinductors, such as the fluxonium [6–9], have shown promising performance. Superinductors have high reactive impedance at microwave frequency (but low loss), and zero impedance for direct currents (DC), and therefore efficiently suppress charge fluctuations leading to decoherence, i.e. loss of quantum information.

We design, fabricate, and characterise in depth the performance of nanowire superinductors by measuring their dominant loss and noise, which we attribute to temporal fluctuations of the electric susceptibility of dielectric interfaces and surfaces. We interpret these fluctuations as originating from charged two-level systems (TLS) that are spectrally unstable due to TLS–TLS interactions. We observe fluctuations of individual TLS in different types of superconducting microwave resonators, including those comprised of a niobium-nitride nanowire superinductor, a "regular" aluminium coplanar waveguide resonator, and a high-purity aluminium cavity resonator. We find that the fluctuations have identical characteristics in these three different types of resonators, made of different materials, suggesting a common cause. We also characterise the fluctuations of the

coherence time and resonant frequency of state-of-the-art transmon-type qubits made of aluminium (a standard material for qubits), and argue that the quality of superconducting qubits should not be benchmarked by only one number (the relaxation time), as is often done, but rather by a their average performance or even by a complete characterisation of its parameters over time, and its reproducibility. We discuss the limitations on the performance of superconducting qubits due to current levels of TLS fluctuations.

1.1 Superinductance

In quantum circuits, detrimental charge fluctuations can be suppressed by embedding the circuit in a low-loss microwave environment of high impedance—a *superinductance* shunt with a characteristic impedance greater than the quantum resistance, $R_Q = h/4e^2 \simeq 6.5\,\mathrm{k}\Omega$ [10]. This impedance is so high that a purely electromagnetic inductance is bound to be insufficient because of its unavoidable shunt capacitance, which limits the impedance to that of free space, $\sqrt{\mu_0/\varepsilon_0} \simeq 377\,\Omega$.

The limit set by the impedance of free space can be surpassed by exploiting the kinetic inductance of a superconductor. Previously, a one-dimensional array of Josephson junctions was used to realise superinductance [10, 11] and fluxonium qubits [6, 12]. These qubits—a Josephson tunnel junction shunted by a superinductor—have sufficiently reduced charge noise sensitivity to show relaxation times on the order of milliseconds [3, 9].

An attractive alternative to Josephson junction arrays is offered by the high kinetic inductance of strongly disordered superconducting thin films. When patterned into a nanowire, such films can produce inductances orders of magnitude higher than an ordinary geometric inductance, while keeping the capacitance arbitrarily small. Importantly, this approach does not feature the complex dynamics of a Josephson junction array.

Previously, a superconducting nanowire-based approach was overlooked, as a variety of superconducting nanowire circuits were found to exhibit significant internal dissipation [13, 14]. However, it was recently shown that it is possible to fabricate superconducting nanowires embedded within resonators that do not exhibit high dissipation [15]. In addition, 100 nm wide resonators made from low-disorder superconductors have also shown high quality factors at the relatively high temperature of 300 mK [16]. Consequently, we figured that with sufficient materials engineering, a nanowire patterned from a strongly disordered superconducting thin film should be a viable route for realizing a superinductor.

In the first part of this work (Papers A and B), we demonstrate a nanowire-based superinductor with an impedance $Z_{nw} = \sqrt{L_{nw}/C_{nw}} = 6.8\,\mathrm{k}\Omega$, fabricated from disordered niobium nitride (NbN). This was made possible by a thorough characterisation of the properties of disordered NbN thin films and extensive nanofabrication process development. Important components of this work also include device modeling and design, including extensive electromagnetic simulations of the non-standard nanowire geometry made with equally non-standard disordered materials; improvements of the measurement

and cryogenic experimental setups; and sensitive advanced measurement techniques at DC and microwave frequencies. We study both the microwave transmission and DC transport properties of several nanowires to characterise their impedance and microwave losses. We demonstrate a quality factor of 2.5×10^4, measured in a resonator geometry with single-photon occupation, which is comparable to Josephson junction array-based superinductors [10]. Furthermore, we find that parasitic TLS represent the dominant loss mechanism, which is exacerbated by the unfavorable TLS filling factor [17] that arises from the small dimensions required to obtain a high impedance.

Subsequently, other implementations of high-impedance nanowire circuits have also been reported in the literature [7, 18–20].

1.2 Dielectric fluctuations in disordered and non-disordered superconducting quantum devices

Dielectric loss and noise associated with parasitic two-level systems (TLS), residing in surfaces and interfaces, are longstanding problems in superconducting circuits. Specifically, some high-frequency TLS are nearly resonant with the device under study, typically in the few-GHz range, resulting in dissipation that often limits the observed internal quality factor (Q_i) or T_1 energy-relaxation time. These TLS become spectrally unstable due to their interaction with a bath of thermally activated, low-frequency TLS [21, 22], which leads to fluctuations of the observed Q_i value and resonant frequency f_r. Such fluctuations represent an effective capacitance noise affecting all superconducting quantum circuits.

While these fluctuations can be studied by superconducting qubits [23, 24] (as we do in Paper E), that method imposes several constraints on the parameter space that can be explored: firstly, superconducting qubits are routinely made with aluminium, which reduces the temperature range that can be examined to well below 0.1 K, above which quasiparticle excitation contribute significantly to losses. Secondly, the range of materials examined for qubit devices is effectively limited to aluminium or niobium on a substrate of silicon or sapphire. Expanding this parameter space is crucial for developing the microscopic understanding of TLS fluctuations and for further developments in coherence times.

Instead of qubits, resonators can provide a route to study few-TLS effects [25]; however, noise studies of resonators typically reveal capacitance noise due to many weakly coupled TLS rather than few strongly coupled TLS [26–28]. This gap can be filled with high impedance nanowires devices: the narrow geometry and high impedance results in a high concentration of electrical field around the device and hence a strong coupling to the TLS host volume (Papers A–C), which makes these devices an ideal test bed for the study of individual TLS noise and fluctuations.

In a second part of this thesis (Papers C–E), we study fluctuations and noise in several superconducting circuits using a type of statistical analysis common in the field of

frequency metrology. We find the signature of individual Lorentzians in the noise of both superconducting resonators and superconducting qubits, which is the signature of individual TLS. Additionally, we compare the frequency fluctuations in different superconducting resonators. We observe a narrowing of the fluctuations histogram with increasing applied power: this saturation of TLS is reminiscent of motional narrowing, i.e. the averaging of the effect of several fluctuators as a result of modulating them. We also observe a power-law dependence of the switching time and amplitude of the Lorentzian features on the applied microwave drive. This behaviour is shared between three different types of superconducting resonators, suggesting a common mechanism.

1.3 Thesis layout

This work is laid out as follows. In **chapters 2 to 5**, we introduce the relevant theoretical background for the understanding of the experimental results. Most notably, in **chapter 4**, we discuss the various loss mechanisms that limit the performance of superconducting quantum circuits and in **chapter 5**, we introduce a set of statistical tools that are commonly used in the field of frequency metrology. **Chapters 6 to 8** discuss the various experimental techniques that were used for the fabrication (**chapter 6**), measurement (**chapter 7**) and simulation (**chapter 8**) of the devices used throughout this work. Moreover, in **chapter 9**, we present the various practical considerations involved in the design of the devices.

Chapters 10 to 13 represent the core of the thesis, where we present the experimental results of **Papers A to E**. In **chapter 10**, we present an in-depth characterisation of niobium nitride thin films. These thin films are key for the fabrication of nanowire superinductors, and therefore a good understanding and control of the film properties is required.

In **chapter 11**, we present the results of **Paper A**, which reports the first successful implementation of a superinductor made from a disordered superconductor, with a characteristic impedance of $6.8\,\mathrm{k}\Omega$ and an internal quality factor of 2.5×10^4 in the quantum limit (i.e. at single-photon occupation of a resonator comprised of a superinductor). Additionally, we examine the loss rates in the superinductor and we demonstrate that the microwave dissipation in our device can be fully understood within the framework of two-level system loss, which previously was not clear.

In **chapter 12**, we present the results of **Paper B**. In this work, we study the geometric scaling of dielectric loss in superconducting resonators with widths toward nanowire dimensions. Through simulations of the Maxwell–London equations, we calculate the participation ratio of the lossy regions in our devices and fit the experimental data to understand the loss in the interfaces and dielectrics.

Lastly, in **chapter 13**, we present the results of **Papers C to E**. Here, we measure and analyse fluctuations in various types of superconducting devices. We start with the results of **Paper D**, where we study the noise properties of a traditional aluminium supercon-

ducting coplanar waveguide resonator. We perform a statistical analysis of the frequency fluctuations of the resonator and find that the noise is well described by Lorentzian switching noise, consistent with the presence of two-level systems. Furthermore, this work highlights the usefulness of this type of analysis for the identification of noise processes in superconducting devices. Then, we continue with the results of **Paper E** where we now analyse the fluctuations of the relaxation time in state-of-the-art transmon qubits. We once again perform a statistical analysis of the fluctuations and show consistency of the dominant relaxation rate with the presence of spectrally unstable, near-resonant TLS. Finally, we discuss the results of **Paper C**, in which we measure the frequency fluctuations in three types of resonators: a niobium-nitride nanowire superinductor, an aluminium coplanar resonator and an aluminium 3D cavity. We analyse the frequency fluctuations and find a common drive-power dependence of the Lorentzian noise in all the devices, suggesting a common origin.

Chapter 2

Disordered Superconductors

On April 8, 1911, while studying the resistance of solid mercury at cryogenic temperatures using liquid helium as refrigerant, Heike Kamerlingh Onnes observed that the resistance abruptly disappeared below a critical temperature T_c of 4.2 K [29]. This phenomenon, known as *superconductivity*, was soon observed in several other metals such as lead, in 1913 ($T_c = 7\,\mathrm{K}$) or niobium nitride, in 1941 ($T_c = 16\,\mathrm{K}$). In 1933, about twenty years after Onnes' discovery, Meissner and Ochsenfeld discovered that superconductors are ideal diamagnets that expel applied magnetic fields [30], and in 1935, Rjabinin and Shubnikov experimentally discovered the existence of type-II superconductors [31].

In 1934, Gorter and Casimir proposed the classical *two-fluid model* [32] to describe the electrodynamics of a superconductor at a finite temperature. A year later, the Meissner effect was phenomenologically described by the London brothers [33]. In 1950, Ginzburg and Landau proposed a semi-classical theory of the superconducting state [34] based on Landau's previously established theory of second-order phase transitions. This model was later extended by Abrikosov [35] and Gor'kov [36], in 1957 and 1959 respectively. Finally, a full microscopic quantum description of the superconducting state was published in 1957 by Bardeen, Cooper and Schrieffer (BCS) [37, 38] and in 1958, Mattis and Bardeen extended the BCS theory and proposed the *Mattis-Bardeen theory* [39] to describe the electrodynamics of superconductors.

This chapter aims to give the reader a brief overview of the concepts of superconductivity relevant to this work. We start by reviewing the key results of the various theories involved in the description of the superconducting state. Then, we put these results in the context of disordered superconductors: the majority of the devices studied throughout this thesis are fabricated from disordered niobium nitride (NbN) and the design and properties of these devices rely on the results derived in this chapter. Finally, we conclude the chapter with a brief presentation of the superconducting devices studied in this work and any additional related models.

2.1 Electronic Transport in Metals

We start this section by reviewing early models describing the electronic transport in metals. We start with the simple, but surprisingly accurate, Drude model as an introduction for the semi-classical Drude-Sommerfeld model, which is of particular interest for the experimental characterisation of the normal state properties of the disordered NbN thin-films used in this work (see section 10.2).

2.1.1 Drude Conductivity

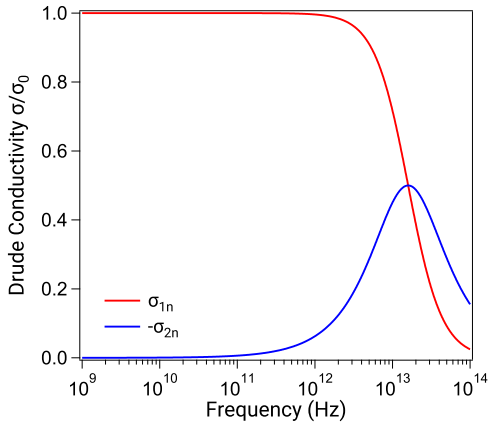

Figure 2.1: Drude conductivity for a typical metal ($\tau = 1 \times 10^{-14}$ s) as a function of frequency. The imaginary part σ_{2n} is negligible for frequencies below 1 THz.

The conductivity of a normal metal can be derived using the Drude model where an electric field is applied to an electron gas [40–42]. The electrons respond to the field by being accelerated and gaining momentum until they scatter off an ion and are given some new random direction and velocity. The scattering process is characterised by an average time τ between scattering events and after many scattering events, the electrons will have some average momentum in the direction of the field. The derivation of the Drude model leads to the following expression for the conductivity at a frequency ω

$$\sigma_n(\omega) = \frac{\sigma_0}{1 + i\omega\tau} = \frac{\sigma_0}{1 + \omega^2\tau^2}(1 - i\omega\tau) = \sigma_{1n} - i\sigma_{2n} \tag{2.1}$$

where $\sigma_0 = n_n e^2\tau/m_e$ with e the elementary charge, m_e the effective electron mass and n_n the electron density. In normal metals, the mean free time is typically $\tau \simeq 1 \times 10^{-14}$ s, therefore, for frequencies < 1 THz, the term $\omega^2\tau^2$ is very small and can be ignored as shown in Fig. 2.1. Despite its simple and classical approach, the Drude model accurately predicts the AC and DC conductivity, Hall effect and magnetoresistance in metals. An additional success of the model at the time was the explanation of the empirical Wiedemann-Franz law [43].

2.1.2 Drude-Sommerfeld Model

The Drude-Sommerfeld model, also known as the *free electron model*, is the simplest quantum mechanical description of the behaviour of charge carriers in a metallic solid. Introduced by Sommerfeld in 1927 [44], this model combines the classical Drude model with the quantum mechanical Fermic-Dirac statistic. It consists of the solutions of the

time-independent Schrödinger equation for a gas of N free electrons, for which the electron-electron and electron-lattice interactions are neglected, confined in a space of volume V. This leads to the well established dispersion relation of the free electron model

$$\varepsilon(\vec{k}) = \frac{\hbar^2 \vec{k}^2}{2m_e} \tag{2.2}$$

where ε is the energy and $\vec{k}$ is the wavevector. The *Fermi energy* ε_F, which corresponds to the energy of the highest populated level, can be derived by counting the number of states in the sphere of radius k_F. Accounting for spin, we get

$$k_F = \left(3\pi^2 n_n\right)^{1/3} \tag{2.3}$$

with $n_n = N/V$, the density of electrons. By using Eq. 2.2 and Eq. 2.3, we can write

$$\varepsilon_F = \frac{\hbar^2}{2m_e}\left(3\pi^2 n_n\right)^{2/3} \tag{2.4}$$

Finally, the density of states, defined as the number of states per unit energy, is given by

$$\rho_n(\varepsilon) = \frac{\mathrm{d}n_n}{\mathrm{d}\varepsilon} = \frac{m_e}{\pi^2\hbar^3}\sqrt{2m_e\varepsilon} = \frac{k_F m_e}{\pi^2\hbar^2} \tag{2.5}$$

If we consider a similar scattering process as in the Drude model, characterised by an average time τ between scattering events, we can introduce the *mean free path* l, defined by the average distance an electron travels between successive scattering events. The mean free path is given by

$$l = v_F\tau = \frac{m_e\sigma_0}{n_n e^2} \tag{2.6}$$

where $v_F = \sqrt{2\varepsilon_F/m_e}$ is the Fermi velocity.

Despite its simplicity (the crystal lattice and resulting band structure are not taken into account), this model is able to describe many important properties of metals.

In the case of the NbN thin-films considered in this work, the free electron model is of particular interest to asses the quality and level of disorder of the fabricated films (see sections 2.3 and 10.2 for more details).

2.2 Low-Temperature Superconductivity

2.2.1 The Two-Fluid Model [32]

The two-fluid model is a classical description of the electrodynamics of a superconductor at a finite temperature: when the superconductor undergoes its transition into the superconducting state ($T < T_c$) the population of electrons is divided in two parts. One population, of density n_n, consists of normal single electrons, known as quasi-particles, subject to scattering and thus exhibiting losses. The other population, of density n_s, consists of superconducting electrons, known in this model as *superelectrons*, immune to scattering and effects hence exhibit no loss.[1]

In the two fluid model, the current in a superconductor follows two paths: one path through the superconducting electrons (n_s) and one through normal electrons (n_n). The total density of charge carriers in the material is given by $n = n_s + n_n$ and the ratio n_s/n is given by

$$\frac{n_s}{n} = 1 - \left(\frac{T}{T_c}\right)^4 \tag{2.7}$$

The conductivity σ_n of the normal electrons is described by equation 2.1. The superconducting electrons do not scatter, therefore by taking $\tau \to \infty$, equation 2.1 leads to the conductivity σ_s of the superconducting electrons:

$$\sigma_s = -i\frac{n_s e^2}{\omega m_e} \tag{2.8}$$

This leads to the general expression of the conductivity for a superconductor in the two-fluid model

$$\sigma = \frac{n_n e^2 \tau}{m_e(1+\omega^2\tau^2)} - i\left(\frac{n_n e^2 \omega \tau^2}{m_e(1+\omega^2\tau^2)} + \frac{n_s e^2}{\omega m_e}\right) \tag{2.9}$$

In the DC regime ($\omega = 0$) at $T = 0\,\mathrm{K}$, the conductivity is purely imaginary and accounts for the zero resistance effect for which superconductors are famous. However, as we move to higher temperatures and non-zero frequencies, an increase of σ_n along with the decrease of σ_s means that a larger fraction of the current is shunted through the resistive path compared to lower temperatures or frequencies: the superconductor will exhibit losses as the temperature or frequency increases. Moreover, the inertia of the superconducting electrons produces a reactance leading to a large impedance at high frequencies: this is the *kinetic inductance*. Figure 2.2 gives a schematic representation of the two current paths.

[1] In the two-fluid model, no other assumption is taken on the nature of the superelectrons. The concept of electrons paired in Cooper pairs is introduced by Cooper in 1956 [45].

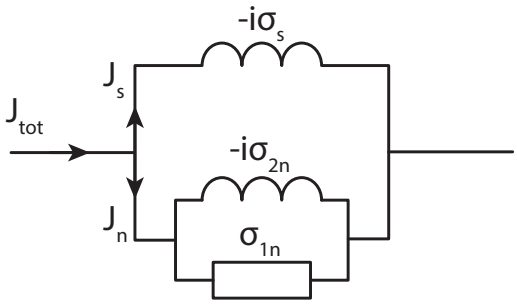

Figure 2.2: Two-fluid model current paths equivalent circuit. The supercurrent (J_s) flows through an inductive current path with zero loss. The normal electrons current (J_n) path takes the form of a resistive path in parallel with an inductive path accounting for both the real (σ_{1n}) and imaginary components (σ_{2n}) of the normal conductivity.

In the microwave regime, where $\omega\tau \ll 1$, equation 2.9 can be simplified into

$$\sigma = \sigma_1 - i\sigma_2 = \frac{n_n e^2 \tau}{m_e} - i\frac{n_s e^2}{\omega m_e} \tag{2.10}$$

where σ_1 accounts for the conductivity of normal electrons and σ_2 for the superconducting electrons. Moreover, since for $T > T_c$ all electrons are in the normal state, we have

$$n_n = n \quad \text{and } \sigma = \sigma_n = \frac{ne^2\tau}{m_e} \tag{2.11}$$

In the same way, at $T = 0\,\mathrm{K}$, all the electrons are in the superconducting state and we have

$$n_s = n \quad \text{and } \sigma = \sigma_s = \frac{ne^2}{\omega m_e} \tag{2.12}$$

Because the two-fluid model relies on the only assumption that two different populations of electrons exist in a superconductor, it is insufficient to explain the properties of superconductivity other than the absence of resistance. However, despite its simplicity, the two-fluid model gives a good qualitative picture of the electrodynamics of superconductors.

The concept of kinetic inductance introduced by the two-fluid model will be further expanded in section 2.3.

2.2.2 The London Theory

Two years after the discovery of the Meissner effect, F. and H. London proposed a phenomenological model describing the ideal diamagnetism of a superconductor. This

model introduces the *London equations*, which complement Maxwell's equations, to describe the behavior of fields and currents in and around a superconductor [33]:

$$\frac{\partial \vec{j_s}}{\partial t} = \frac{n_s e^2}{m_e}\vec{E} \tag{2.13}$$

$$\nabla \times \vec{j_s} = -\frac{n_s e^2}{m_e}\vec{B} \tag{2.14}$$

where $\vec{E}$ and $\vec{B}$ are the electric and magnetic fields respectively and $\vec{J_s}$ is the superconducting current density.

In contrast to Ohm's law, the first London equation (Eq. 2.13) describes a frictionless flow of superconducting current and implies that no electric field exists in the superconductor in the stationary state. The second equation (Eq. 2.14) describes the ideal diamagnetism of superconductors. By applying Ampère's law to the second London equation, we get

$$\nabla \times \vec{B} = \frac{\mu_0 n_s e^2}{m_e}\vec{B} = 1/\lambda_L^2 \vec{B} \quad \text{with } \lambda_L = \sqrt{m_e/\mu_0 n_s e^2} \tag{2.15}$$

The solution of this differential equation is a magnetic field that decays inside the superconductor on a length scale λ_L, known as the *London penetration depth*. In other words, any external magnetic field is exponentially screened inside the superconductor over a characteristic distance λ_L. Because of the temperature dependence of n_s, the London penetration depth also depends on temperature. Using Eq. 2.7, we get

$$\lambda_L(T) = \lambda_L(0)\left[1 - \left(\frac{T}{T_c}\right)^4\right]^{-1/2} \tag{2.16}$$

with $\lambda_L(0) = \sqrt{m_e/\mu_0 n e^2}$, the London penetration depth at 0 K ($n_s = n$ at 0 K).

2.2.3 The Ginzburg-Landau Theory

In 1950, Ginzburg and Landau (GL) applied the results of Landau's mean field theory in the context of superconductivity [34]. The GL theory introduces a pseudo wavefunction $\psi = \sqrt{n_s}e^{i\varphi}$ (the *order parameter*) and postulates that if ψ is small and varies slowly in space, in the vicinity of $T = T_c$, the free energy of the superconductor can be expanded into a series of ψ^2:

$$F = F_n + \alpha\left|\psi\right|^2 + \frac{\beta}{2}\left|\psi\right|^4 + \frac{1}{2m_e}\left|(-i\hbar\nabla - 2e\vec{A})\psi\right|^2 + \frac{|\vec{B}|^2}{2\mu_0} \tag{2.17}$$

where F_n is the free energy of the normal state, $\vec{A}$ is the magnetic vector potential and α and β are parameters. Minimizing the free energy with respect to variations in the order parameter and the vector potential leads to the *Ginzburg-Landau equations* [34]:

$$\alpha\psi + \beta|\psi|^2\psi + \frac{1}{2m_e}\left(-i\hbar\nabla - 2e\vec{A}\right)^2\psi = 0 \tag{2.18}$$

$$\nabla \times \vec{B} = \mu_0\vec{j} \quad \text{with } \vec{j} = \frac{2e}{m_e}\,\mathrm{Re}\left[\psi^*\left(-i\hbar\nabla - 2e\vec{A}\right)\psi\right] \tag{2.19}$$

The solutions to Eq. 2.18 and 2.19 rely on two characteristic length scales: in the superconductor, magnetic fields are exponentially suppressed and decay over a penetration depth λ_L, as introduced by the London theory. The second characteristic length scale is the *coherence length* ξ_{GL}, given by

$$\xi_{GL} = \sqrt{\frac{\hbar^2}{4m_e|\alpha|}} \tag{2.20}$$

The coherence length reflects the quantum mechanical character of the GL theory and represents the minimum spatial length scale over which the order parameter varies. The ratio of these two length scales, $\kappa = \lambda_L/\xi_{GL}$, is known as the Ginzburg-Landau parameter.

Type-I and Type-II Superconductors

The GL theory suggests the existence of two different types of superconductors depending on the energy of the interface between the normal and superconducting states.

When $\kappa < 1/\sqrt{2}$, the free energy at the interface is positive and it is therefore energetically favorable to form either a continuous superconducting or a continuous normal state: when in the superconducting phase, the superconductor completely rejects magnetic fields (Meissner effect), until a critical field H_c is reached and superconductivity is abruptly destroyed via a first order phase transition. These superconductors are known as type-I superconductors.

On the other hand, when $\kappa > 1/\sqrt{2}$, the free energy is negative. In this case, it becomes energetically favorable to form a composite state of the normal and superconducting phases for a wide range of applied magnetic fields. These superconductors, known as type-II, are characterised by the existence of two critical fields: H_{c1} and H_{c2}. Below H_{c1}, no magnetic field penetrates the superconductor (*Meissner phase*). When the applied field becomes larger than H_{c1}, magnetic fields start to penetrate the superconductor, until another critical field, known as the *upper critical field*, H_{c2} is reached and the superconducting phase is completely destroyed. A schematic summary of the phase diagram and magnetization of type-I and type-II superconductors is shown in Fig. 2.3.

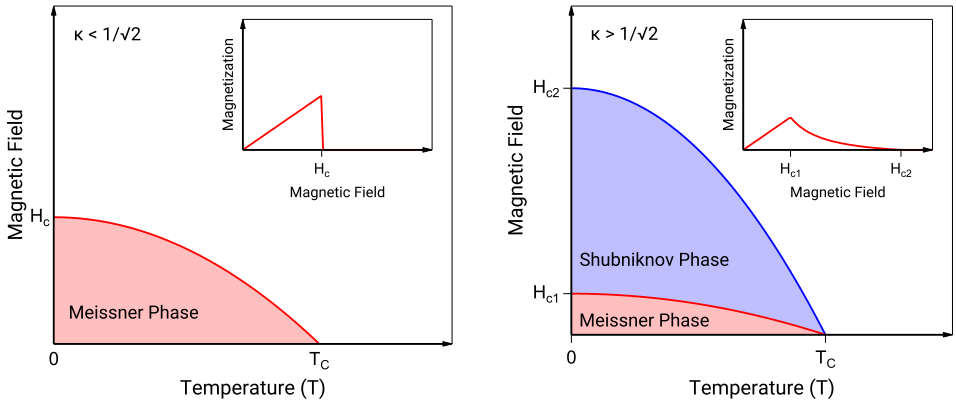

Figure 2.3: Phase diagram of a type-I **(left)** and type-II **(right)** superconductors. The insets show the magnetization as a function of the magnetic field for each case.

Moreover, Abrikosov showed that the magnetic field penetrates type-II superconductors in the shape of quantized flux lines, known as *vortices* [46]. The phase where vortices and the superconducting state coexist is known as the *mixed state* or *Shubnikov phase*. Type-II superconductors are of particular interest in the laboratory as they exhibit very large critical fields ($\sim 16\,\mathrm{T}$ in the case of NbN) which allows for the preservation of superconductivity under a wide range of magnetic fields; however, as will be discussed later, vortices can be a source of unwanted dissipation and special care should be taken to minimise their influence.

2.2.4 The BCS Theory

In 1956, Cooper showed [45] that in a metal, an arbitrarily small attraction between electrons can lead to the formation of a paired state of electrons with an energy lower than the Fermi energy. This bound state, known as a Cooper pair, consists of a pair of two electrons of opposite spin and momentum and is therefore of bosonic nature.

A year later, Bardeen, Cooper and Schrieffer demonstrated [37, 38] that the electron-phonon interaction can lead to the formation of Cooper pairs below a critical temperature T_c. Moreover, they showed that due to their bosonic nature, the Cooper pairs tend to condense into the same coherent quantum state. This quantum-statistical condensation is accompanied by the development of an energy gap Δ around the Fermi energy and in order to break Cooper pairs, one needs to provide an energy 2Δ.

This energy gap is calculated to be, at $0\,\mathrm{K}$:

$$\frac{\Delta_0}{k_B T_c} = \frac{\pi}{e^{\gamma}} \simeq 1.764 \tag{2.21}$$

where k_B is the Boltzmann constant and γ is the Euler-Mascheroni constant. Moreover, the BCS theory predicts the dependence of the energy gap on temperature T with

$$\frac{1}{\rho_n} = \int_0^{\hbar\omega_D} \frac{\tanh\left[(\xi^2+\Delta^2)^{1/2}/2k_BT\right]}{(\xi^2+\Delta^2)^{1/2}} d\xi \tag{2.22}$$

where ω_D is the Debye frequency, which corresponds to the cut-off frequency above which no lattice vibration can occur. Unfortunately, Eq. 2.22 has no analytical solution, but the values of $\Delta(T)$ can be computed numerically [47]. Near T_c, the value of the energy gap can be approximated by

$$\Delta(T) \simeq 3.2 k_B T_c \left(1 - \frac{T}{T_c}\right)^{1/2} \tag{2.23}$$

Additionally, the BCS density of states is given by

$$\frac{\rho_s(\varepsilon)}{\rho_s(\varepsilon_F)} = \begin{cases} \dfrac{\varepsilon}{\sqrt{\varepsilon^2-\Delta^2}} & \varepsilon > \Delta \\ 0 & \varepsilon < \Delta \end{cases} \tag{2.24}$$

Finally, like the London and GL theories, the BCS theory introduces a characteristic length scale analogous to the GL coherence length and known as the BCS coherence length. It is given by

$$\xi_0 = \frac{e^\gamma}{\pi^2}\frac{\hbar v_F}{k_B T_c} = \frac{\hbar v_F}{\pi \Delta_0} \tag{2.25}$$

All these length scales are key for understanding the influence of disorder on the properties of a superconductor, which will be discussed more in detail in section 2.3 below.

Weakly and Strongly Coupled Superconductors

The BCS theory revealed the importance of the electron-phonon interaction for the existence of the superconducting state, however, the results are derived in the so-called *weak electron-phonon coupling* limit, where $\hbar\omega_D \gg k_B T_c$.

Niobium nitride is experimentally found to be a strongly coupled superconductor [48] and therefore does not fall under the case described by the BCS theory. The *strong electron-phonon coupling* limit ($\hbar\omega_D \ll k_B T_c$) has been studied in detail by Thouless [49], and he concluded that the results of the weak-coupling BCS theory also apply for a

strongly coupled superconductor, barring an adjustment of the prefactors in Eq. 2.21 and 2.23. In the case of NbN, we have

$$\begin{cases} \Delta(T) \simeq 3.45 k_B T_c \left(1 - \frac{T}{T_c}\right)^{1/2} & \text{near } T_c \\ \Delta_0 = 2.08 k_B T_c \end{cases} \tag{2.26}$$

Additionally, Thouless showed that the energy gap of a superconductor (in both the weak and strong coupling limits) can be self-consistently calculated from

$$\frac{\Delta(T)}{\Delta_0} = \tanh\left(\frac{T_c}{T}\frac{\Delta(T)}{\Delta_0}\right) \tag{2.27}$$

2.2.5 Critical Magnetic Fields in Superconductors

Thermodynamic Critical Field H_c

The Meissner effect [30] implies that the superconducting state will be destroyed by magnetic fields larger than a critical magnetic field $H_c(T) = B_c(T)/\mu_0$, known as the thermodynamic critical field. This critical field is related to the free-energy difference between the normal and superconducting states at zero applied magnetic field. The ground-state condensation energy density of the Cooper pair condensate can be expressed in terms of the critical field with [50]

$$\frac{1}{4}\rho_s(\varepsilon_F)\Delta_0^2 = \frac{B_c^2(0)}{2\mu_0} \tag{2.28}$$

which leads to

$$H_c(T = 0\,\mathrm{K}) = \sqrt{\frac{\rho_s(\varepsilon_F)\Delta_0^2}{2\mu_0}} \tag{2.29}$$

For temperatures in the vicinity of T_c, the GL theory gives an analytical expression for the critical field [51]

$$H_c^{GL}(T) = \sqrt{\frac{4\pi^2\rho_s(\varepsilon_F)}{7\zeta(3)}}(k_B T_c)\left(1 - \frac{T}{T_c}\right) \tag{2.30}$$

where ζ is the Riemann zeta function. Using Eq. 2.29, Eq. 2.30 becomes

$$H_c^{GL}(T) = \sqrt{\frac{8\pi^2}{7\zeta(3)\mu_0}}\frac{k_B T_c}{\Delta_0} H_c(0)\left(1 - \frac{T}{T_c}\right) \tag{2.31}$$

In the strong-coupling limit relevant for this work, Eq. 2.31 further simplifies to

$$H_c^{GL}(T) = \frac{1}{2.08}\sqrt{\frac{8\pi^2}{7\zeta(3)}}H_c(0)\left(1-\frac{T}{T_c}\right) \simeq 1.473H_c(0)\left(1-\frac{T}{T_c}\right) \tag{2.32}$$

Finally, with the help of the two-fluid model [32] and using Eq 2.32 as the $T = T_c$ limit, we can derive an expression for the full temperature range of the critical field:

$$H_c(T) = \sqrt{\frac{2\pi^2}{7\zeta(3)}}\frac{k_B T_c}{\Delta_0}H_c(0)\left[1-\left(\frac{T}{T_c}\right)^2\right] \tag{2.33}$$

Similarly to Eq. 2.32, in the strong coupling limit, Eq. 2.33 can also be reduced to

$$H_c(T) = \frac{1}{2.08}\sqrt{\frac{2\pi^2}{7\zeta(3)}}H_c(0)\left[1-\left(\frac{T}{T_c}\right)^2\right] \simeq 0.736H_c(0)\left[1-\left(\frac{T}{T_c}\right)^2\right] \tag{2.34}$$

Upper Critical Field H_{c2}

In section 2.2.3, we highlighted the existence of the *upper critical field* for type-II superconductors. In the framework of the GL theory, the upper critical field is given by

$$\mu_0 H_{c2}(T) = B_{c2}(T) = \frac{\Phi_0}{2\pi\xi_{GL}^2(T)} \tag{2.35}$$

where Φ_0 is the magnetic flux quantum.

2.3 Disordered Superconductors

2.3.1 Length Scales and Limits

In the previous sections, we have introduced three characteristic length scales: the electron mean free path l, the London penetration depth λ_L and the BCS coherence length ξ_0. These length scales define a broad parameter space inside which various regimes can be identified. In the context of this work, we will focus on the *local dirty limit*, where $l \ll \xi_0 \ll \lambda_L$. An in-depth review of the different regimes can be found in [52].

As detailed in the experimental results (see chapter 10), with values of l of the order of 100 pm, ξ_0 of the order of 200 nm and λ_L of the order of 1 µm, the NbN thin-films considered in this work fall well inside the local dirty limit.

2.3.2 Ioffe-Regel Criterion

The study of crystalline materials has always played a prominent role in solid state physics. Perfect crystallinity introduces considerable simplifications in the formulation of theories for the physical properties, however, in many practical applications, a certain degree of disorder is present. Defects, vacancies or dislocations, frequently observed in real materials, are defined as *weak disorder* and are usually treated as a perturbation of the perfect crystalline order. On the other hand, *strong disorder* is characterised by an absence of long range translational order and signifies a marked departure from crystalline order.

Ioffe and Regel introduced a criterion that qualitatively quantifies the level of disorder in a system [53], knows as the *Ioffe-Regel parameter* and defined by the product $k_F l$ of the Fermi wavevector and the electron mean free path. Moreover, they predicted that when $k_F l \simeq 1$, a metal-insulator transition should be observed. An increasing amount of disorder translates into a diminishing electron mean free path which leads to a gradual localization of charge carriers [54] until an insulating state is reached (see section 2.4 for more details).

In a superconductor, disorder leads a competition between two interactions: on one hand, superconductivity is a manifestation of long-range phase coherence between electron pair states. On the other hand, localization involves a limitation of the spatial extent of the wavefunctions and should inhibit such pairing. Therefore, we can anticipate that superconductivity should disappear as disorder increases and states become localized. Such a phenomenon is known as the superconductor to insulator transition (SIT) and was reported as early as 1978 by Dynes [55], who observed that lead thin-films with resistances larger than $30\,\mathrm{k}\Omega/\square$ were no longer superconducting (see Fig. 4 in [55]).

A big challenge of this work resides in the fabrication of strongly disordered thin-films close to the SIT (with $k_F l \simeq 1$) in order to maximise the kinetic inductance (see the following sections for more details). In such a regime, the thin-film becomes extremely sensitive to the deposition parameters and careful characterisation and optimisation is necessary.

2.3.3 Dirty Superconductor

Strongly disordered superconductors have extremely small electron mean free paths and therefore fall under the regime of the local dirty limit. In this regime, several quantities defined in the previous sections become dependent on the electron mean free path and need to be adjusted [36, 50]. Most importantly for this work, the magnetic penetration depth at $T = 0\,\mathrm{K}$ (Eq. 2.16) is given by

$$\lambda_{dirty}(0) = \lambda_L(0)\sqrt{\frac{\xi_0}{l}} = \sqrt{\frac{\hbar}{\pi\mu_0\Delta_0\sigma_n}} \tag{2.36}$$

The temperature dependence of the penetration depth is given by

$$\frac{\lambda_{dirty}(T)}{\lambda_{dirty}(0)} = \left[\frac{\Delta(T)}{\Delta_0}\tanh\left(\frac{\Delta(T)}{2k_BT}\right)\right]^{-1/2} \tag{2.37}$$

Additionally, in the limit of a thin-film ($t \ll \lambda_{dirty}$), the penetration depth is replaced by an *effective penetration depth* [50, 56]:

$$\Lambda(T) = \frac{2\lambda^2_{dirty}(T)}{t} \tag{2.38}$$

In the dirty limit, the GL coherence length (Eq. 2.20) is given by

$$\xi_{GL}(T) = \sqrt{\frac{\pi^3 e^{-\gamma}\xi_0 l}{24}}\left(1-\frac{T}{T_c}\right)^{-1/2} = \xi_{GL}(0)\left(1-\frac{T}{T_c}\right)^{-1/2} \tag{2.39}$$

Finally, Helfand and Werthamer showed [57–59] that the upper critical field can be obtained from

$$B_{c2}(0) = -0.69T_c \left.\frac{dB_{c2}}{dT}\right|_{T=T_c} \tag{2.40}$$

2.3.4 Kinetic Inductance

In section 2.2.1, we briefly introduced a concept known as *kinetic inductance*. Formally, kinetic inductance is the manifestation of the inertial mass of mobile charge carriers in alternating electric fields as an equivalent series inductance. In other words, in an alternating field, it takes time for the charge carriers to reach their final velocity and the current "lags" behind the voltage. Kinetic inductance is observed at very high frequencies in high carrier mobility conductors and also, crucially, in superconductors at significantly lower frequencies.

In a superconductor, energy can be stored in two ways: one part is stored in the magnetic field penetrating the superconductor (with a depth λ_L). This energy depends on the geometry of the superconductor and is given by

$$E_{mag} = \int \frac{\mu_0 \vec{H}^2}{2} dA = \frac{1}{2} L_m I^2 \tag{2.41}$$

A second part of the energy is associated with the kinetic energy of the Cooper pairs. We can write the kinetic energy E_{kin} of the Cooper pairs using $\vec{J}_s = n_s e \vec{v}$ with

$$E_{kin} = \int \frac{m_e n_s \vec{v}}{2} dA = \frac{m_e}{2n_s e^2}\int \vec{J_s}^2 dA = \mu_0 \lambda_L^2 \int \vec{J_s}^2 dA = \frac{1}{2} L_k I^2 \tag{2.42}$$

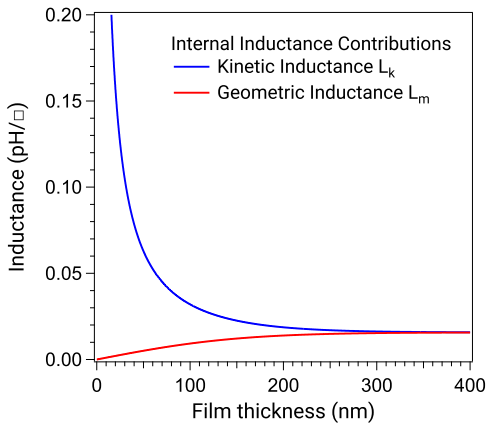

Figure 2.4: Internal inductance contributions calculated for $\lambda_L = 50\,\text{nm}$. The kinetic inductance greatly increases when the film thickness is reduced.

where $\vec{v}$ is the average velocity of the charge carriers and L_k is the *kinetic inductance*. We can see from this last equation that an increase in the density of Cooper pairs n_s leads to a decrease of the kinetic energy, reaching a minimum at $T = 0\,\text{K}$. Additionally, from Eq. 2.10, we see that when the temperature increases and Cooper pairs break up into normal electrons, n_s and σ_2 decrease and n_n and σ_1 increase. For a given energy, a lower Cooper pair density forces the Cooper pairs to increase their velocity in order to provide the same supercurrent J_s, leading to a larger kinetic inductance.

The evaluation of the integrals has been derived by Doyle [60] for a superconducting strip of width w and thickness t and read as

$$L_k = \frac{\mu_0 \lambda_L}{4w}\left[\coth\left(\frac{t}{2\lambda_L}\right) + \left(\frac{t}{2\lambda_L}\right)\text{cosec}^2\left(\frac{t}{2\lambda_L}\right)\right] \tag{2.43}$$

$$L_m = \frac{\mu_0 \lambda_L}{4w}\left[\coth\left(\frac{t}{2\lambda_L}\right) - \left(\frac{t}{2\lambda_L}\right)\text{cosec}^2\left(\frac{t}{2\lambda_L}\right)\right] \tag{2.44}$$

leading to the following expression for the total internal inductance

$$L_{int} = L_m + L_k = \frac{\mu_0 \lambda_L}{4w}\coth\left(\frac{t}{2\lambda_L}\right) \tag{2.45}$$

Fig. 2.4 shows a comparative plot of the magnetic and kinetic contributions to the inductance as a function of the film thickness. As the thickness decreases, the magnetic inductance is gradually suppressed while the kinetic inductance dramatically increases. In the case of a very thin superconducting strip of thickness t and width w, with $t \ll \lambda_L$,

the geometric contribution is negligible, the current density is approximately constant and the kinetic inductance can immediately be calculated to

$$L_k = \frac{\lambda_L^2 \mu_0}{wt} \tag{2.46}$$

2.3.5 Surface Impedance in the Thin-Film Limit

The surface impedance Z_S is defined as the ratio of the transverse components of the electric and magnetic fields at the surface. It is well known that an electromagnetic field penetrates into a normal metal with a finite skin depth δ which can be calculated using Maxwell's equations and the local Ohm's law $\vec{J_n}(\vec{r}) = \sigma_n \vec{E}(\vec{r})$:

$$\delta = \sqrt{\frac{2}{\mu_0 \omega \sigma}} \tag{2.47}$$

This skin depth implies that the in-plane electromagnetic field components will decay exponentially inside the conductor. We can therefore write, for the electric field in the conductor:

$$E_x(z) = E_x(0) e^{-z(1+i)/\delta} \tag{2.48}$$

And by applying the Maxwell-Faraday equation, an expression for the magnetic field immediately follows

$$H_y(z) = \frac{1-i}{\mu_0 \omega \delta} E_x(z) \tag{2.49}$$

This finally leads to

$$Z_S = \frac{E_x(0)}{H_y(0)} = \sqrt{\frac{i\omega\mu_0}{\sigma}} \tag{2.50}$$

It was shown [61] that for a thick film ($t \gg l$) in the local dirty limit, the surface impedance of a superconductor can be simply obtained by replacing σ in Eq. 2.50 with the conductivity from the two fluid model (Eq. 2.9). In the thin-film limit, the surface impedance expression should be modified to [61]:

$$Z_S = \frac{1}{t(\sigma_1 - i\sigma_2)} \tag{2.51}$$

In the previous section, we demonstrated that in the case of a thin film, the kinetic inductance dominates the internal inductance, therefore, if we define $Z_S = R_S + i\omega L_S$, from Eq. 2.51, we immediately get

$$R_S = \frac{\sigma_1}{t(\sigma_1^2 + \sigma_2^2)} \quad \text{and} \quad L_S \equiv L_k = \frac{\sigma_2}{t\omega(\sigma_1^2 + \sigma_2^2)} \tag{2.52}$$

Mattis-Bardeen Theory

The Mattis-Bardeen theory [39] was developed to describe the anomalous skin effect in metals and superconductors. Under the assumption that either $\xi_0 \gg \lambda_L$ or $\xi_0 \gg l$, the Mattis-Bardeen equations for the complex conductivity $\sigma(\omega) = \sigma_1 - i\sigma_2$ relative to the normal state conductivity σ_n read as:

$$\begin{aligned}\frac{\sigma_1}{\sigma_n} =& \frac{2}{\hbar\omega}\int_{\Delta}^{\infty} \frac{[f(\varepsilon) - f(\varepsilon+\hbar\omega)]\,(\varepsilon^2 + \Delta^2 + \hbar\omega\varepsilon)}{\sqrt{\varepsilon^2 - \Delta^2}\sqrt{(\varepsilon+\hbar\omega)^2 - \Delta^2}} d\varepsilon \\ &+ \frac{1}{\hbar\omega}\int_{\Delta-\hbar\omega}^{-\Delta} \frac{[1 - 2f(\varepsilon+\hbar\omega)]\,(\varepsilon^2 + \Delta^2 + \hbar\omega\varepsilon)}{\sqrt{\varepsilon^2 - \Delta^2}\sqrt{(\varepsilon+\hbar\omega)^2 - \Delta^2}} d\varepsilon\end{aligned} \tag{2.53}$$

$$\frac{\sigma_2}{\sigma_n} = \frac{1}{\hbar\omega}\int_{\max(-\Delta,\Delta-\hbar\omega)}^{\Delta} \frac{[1 - 2f(\varepsilon+\hbar\omega)]\,(\varepsilon^2 + \Delta^2 + \hbar\omega\varepsilon)}{\sqrt{\Delta^2 - \varepsilon^2}\sqrt{(\varepsilon+\hbar\omega)^2 - \Delta^2}} d\varepsilon \tag{2.54}$$

where f is the Fermi-Dirac distribution function $f(\varepsilon) = 1/(1 + \exp(\varepsilon/k_B T))$. In Eq. 2.53, the first integral represents the contribution of thermal excitation of quasi-particles. The second integral represents the creation of quasi-particles when an excitation larger than the superconducting gap splits Cooper pairs and therefore vanishes for $\hbar\omega < 2\Delta$. At low enough frequencies[2] ($\hbar\omega \ll 2\Delta$) and low temperatures ($T \ll T_c$), σ_1 will vanish and we can rewrite σ_2 as

$$\frac{\sigma_2}{\sigma_n} \simeq \frac{\pi\Delta_0}{\hbar\omega}\left[1 - \frac{1}{16}\left(\frac{\hbar\omega}{\Delta_0}\right)^2 - \frac{3}{1024}\left(\frac{\hbar\omega}{\Delta_0}\right)^4 + ...\right] \tag{2.55}$$

Since σ_1 vanishes at very low temperatures, by using a sufficiently low temperature one can make the microwave dissipation of a superconductor arbitrarily low: the dissipative response of the electron system becomes very small compared to the reactive response ($\sigma_1 \ll \sigma_2$). In the limit that the film is thin compared to its London penetration depth

[2] In the case of NbN, $\Delta \simeq 1\,\text{meV}$ and therefore the condition $\hbar\omega \ll 2\Delta$ is verified for microwave frequencies.

($t \ll \lambda_L$), we can use these results in equation 2.52 and a first order development (in σ_1/σ_2) leads to

$$L_k(T=0) = \frac{\sigma_2}{t\omega(\sigma_1^2+\sigma_2^2)} = \frac{\sigma_2}{t\omega\sigma_2^2(1+(\sigma_1/\sigma_2)^2)} \simeq \frac{1}{t\omega\sigma_2} = \frac{\hbar}{\pi\Delta_0 t\sigma_n} = \frac{\hbar R_N}{\pi\Delta_0} \quad (2.56)$$

where $R_N = 1/(\sigma_n t)$ represents the normal-state sheet resistance of the thin film.

From Eq. 2.56, we see that the kinetic inductance is directly proportional to the normal state resistance of the film, and inversely proportional to its critical temperature. This implies that the kinetic inductance will scale with disorder in the film.

2.4 Electronic Transport in Disordered Superconductors

2.4.1 Weak Localization and Fluctuations Paraconductivity

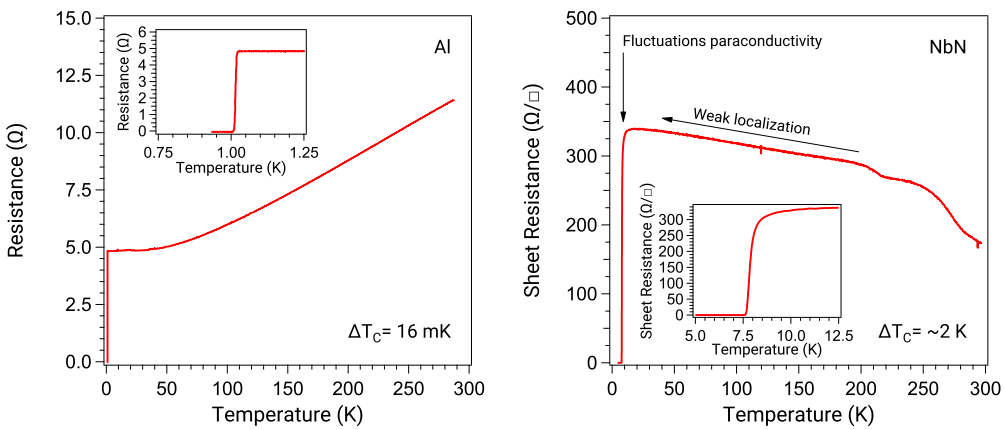

Figure 2.5: Resistance against temperature measurements for a conventional **(left)** and a strongly disordered (NbN) **(right)** superconductor. The insets correspond to a magnification of the R vs. T curve around the superconducting transition.

In a conventional superconductor, such as aluminium (Fig. 2.5 (left)), we observe a decrease of the resistance against decreasing temperature, due to out-freezing of the electron-phonon scattering processes. Finally, as the temperature reaches T_c, the resistance abruptly drops to zero. By contrast, in a strongly disordered superconductor like NbN (Fig. 2.5 (right)), the resistance increases with decreasing temperatures until a plateau is reached. Further decreasing the temperature, the resistance gradually decreases and a broad superconducting transition is observed: in strongly disordered superconductors,

there are several corrections to the conductivity at low temperatures that go beyond the classical Boltzmann transport equation [42].

The increasing resistance can be explained by the so-called *weak localization* scenario [54, 62], which finds its origin in coherent backscattering of electronic charge carriers and gives a positive contribution to the resistivity in the absence of a magnetic field. In a disordered electronic system, the electron motion is diffusive and because of random scattering events, there is a finite probability for self-crossing electron paths. If no inelastic scattering has occurred along the trajectory, quantum interference can happen at the intersection and the electron will localize in a circular motion. Localized electrons do not contribute to the conductivity anymore, therefore this leads to an increase in the net resistivity.

In principle, weak localization can happen in any system, however it is much more likely to find a self-crossing trajectory in system with low dimensionality or in disordered superconductors. As the temperature decreases, more and more electrons are localized and the resistance gradually increases.

The broad superconducting transition in disordered superconductors can be fully described by two different mechanisms:

Above T_c, thermodynamic fluctuations give rise to short-lived Cooper pairs, which increase the conductivity: as the temperature decreases, more and more Cooper pairs come in and out of existence, gradually decreasing the overall resistance of the sample, until the condensation temperature is reached. These conductivity fluctuations have been described by Aslamasov and Larkin [50, 63]. In the two-dimensional case relevant to our devices[3], the fluctuation term is given by

$$\sigma_{2D}(T) = \frac{e^2}{16\hbar t}\left(\frac{T_c}{T - T_c}\right) \tag{2.57}$$

The total conductivity above T_c is now expressed as $\sigma(T) = \sigma_n + \sigma_{2D}(T)$. This result is particularly remarkable by its simplicity and it is worth noting that it contains no adjustable parameters apart from T_c.

The second mechanism, contributing to the broad superconducting transition below T_c, is described in the following section.

2.4.2 Vortex-induced Dissipation

In a thin disordered superconductor, below T_c, the resistance doesn't immediately vanish. This can be explained by a Berezinskii–Kosterlitz–Thouless (BKT) topological phase transition [64, 65] where thermal fluctuations excite pairs of vortices. These vortex-antivortex pairs (VAP) are bound states, formed by vortices with supercurrents circulating

[3]The disordered NbN thin films used in this thesis are typically of a thickness of the order of one to a few coherence lengths but the device lateral dimensions are much larger than the coherence length (see sections 9 and 10), therefore these devices fall under the 2D limit

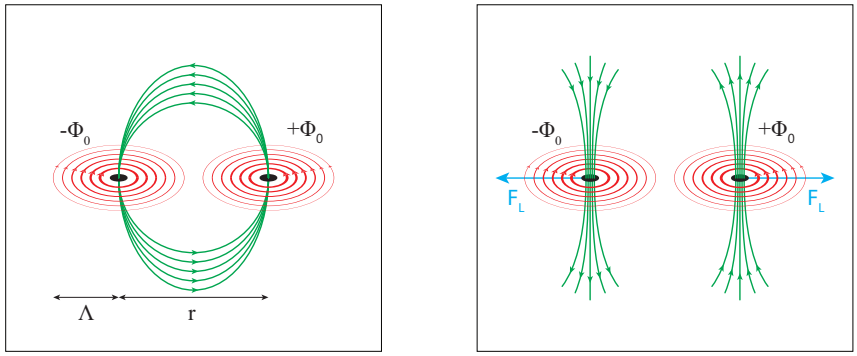

Figure 2.6: **(left)** Vortex-antivortex pair. The supercurrents (red) of the two individual vortices generate a magnetic flux quantum Φ_0 which electromagnetically vortices together and circulates through both vortex cores (black). In a disordered superconductor, the relatively low vortex interaction $A(T)$ allows for the thermal excitation of an ensemble of fluctuating vortex-antivortex pairs (VAPs) with statistically distributed core-to-core elongation r. **(right)** With increasing fluctuation strength k_BT, the averaged elongation increases until the VAP unbinds above T_{BKT}, the unbound vortices are now free to move due to the Lorentz force and cause dissipation. As the temperature increases further, more and more VAPs unbind and the resistive contribution gets bigger.

in opposite directions [66–68]. Above the ordering temperature T_{BKT}, VAPs start to dissociate and their movement cause the observed finite resistance.

The necessary criterion for a BKT phase transition is a logarithmic dependence of the electromagnetic vortex interaction on the distance between the vortex centers. The potential energy of an isolated VAP is given by [69]

$$U_{\mathrm{VAP}}(r,T) = A(T)\ln\left(\frac{r}{\xi_{GL}}\right) + 2\mu_c(T) \tag{2.58}$$

where $\mu_c(T)$ is the vortex core energy and $A(T)$ is the vortex interaction constant. The vortex interaction constant is given by

$$A(T) = \frac{\Phi_0^2}{\pi\mu_0\Lambda(T)} \tag{2.59}$$

Using Eq. 2.37 and 2.38, we can calculate the effective penetration depth for a superconductor in the dirty limit

$$\Lambda(T) = \frac{2\Phi_0^2}{\pi^3\mu_0}\frac{R_N e^2}{\hbar}\left[\Delta(T)\tanh\left(\frac{\Delta(T)}{2k_BT}\right)\right]^{-1} \tag{2.60}$$

Using this, the vortex interaction constant becomes

$$A(T) = \frac{\pi^2}{2}\frac{\hbar}{R_N e^2}\Delta(T)\tanh\left(\frac{\Delta(T)}{2k_B T}\right) \tag{2.61}$$

In Eqs. 2.58 and 2.61, we immediately see that a high normal state resistance leads to a small vortex interaction constant, and in turn translates into a small VAP binding potential. The smaller the binding potential, the easier it becomes for thermal fluctuations to unbind VAPs and therefore the smaller the ordering temperature becomes. Unbound vortices move due to the Lorentz force and cause a finite resistance given by

$$\rho(T) = a\exp\left(-2\sqrt{b\frac{T_c - T}{T - T_{BKT}}}\right) \quad \text{with } T_{BKT} < T < T_c \tag{2.62}$$

where a, b are material dependent parameters.

2.4.3 Quasiparticle Diffusivity

When considering disordered materials, it is convenient to introduce the diffusion constant of electrons in the material, known as the *the quasiparticle diffusivity* D, and given by [70–73]

$$D = \frac{1}{3}v_f l \tag{2.63}$$

Analog to the Ioffe-Regel criterion, the diffusivity quantifies the amount of disorder and, in the dirty limit, by using Eqs. 2.25, 2.35 and 2.39, the quasiparticle diffusivity can be rewritten as [74]

$$D = -\frac{4k_B}{e\pi}\left[\left.\frac{dB_{c2}}{dT}\right|_{T=T_c}\right]^{-1} \tag{2.64}$$

Furthermore, we can directly relate the diffusivity to the density of states at the Fermi level using the Einstein relation [75, 76] $\rho_s(\varepsilon_F) = (e^2\rho_n D)^{-1}$. From Eq. 2.64, we see that the diffusivity and density of states can be readily accessed experimentally by measuring the transport properties of a given superconducting film in a magnetic field. The values derived from these measurements are found to be in excellent agreement with the results of more traditional specific-heat measurements of the density of states [74].

2.4.4 Critical Current in Disordered Nanowires

Due to Ampère's law, the current carried by the superconductor will generate a magnetic field. Therefore, the existence of a critical magnetic field implies the existence of a maximum current the superconductor can carry before the superconducting state collapses. This current is known as the *critical current*.

For temperatures close to T_c, the GL theory states that the critical current density j_c in a superconductor is given by [77]

$$j_c^{GL}(T) = \frac{2\sqrt{2}}{3\sqrt{3}}\sqrt{\frac{4\pi e^{\gamma}}{7\zeta(3)}}\frac{B_c^{GL}(T)}{\mu_0\lambda_L(T)} \tag{2.65}$$

Using Eqs. 2.26, 2.31, 2.36 and 2.64, we can rewrite Eq. 2.65 as the well known GL critical current density expression $j_c^{GL}(T) = j_c^{GL}(0)(1 - T/T_c)^{3/2}$ where [36, 78]

$$j_c^{GL}(0) = \frac{8\sqrt{2}}{21\sqrt{3}}\frac{\pi^2\sqrt{e^{\gamma}}}{\zeta(3)}\sqrt{2.08}\frac{(k_B T_c)^{3/2}}{e\rho_n\sqrt{D\hbar}} \tag{2.66}$$

The full temperature dependence has been the source of several investigations. Most notably, Bardeen derived an analytical expression for the critical current of a thin and narrow superconducting strip, valid for all temperatures [79]

$$j_c^{B}(T) = \frac{1}{2\sqrt{2}}j_c^{GL}(0)\left[1 - \left(\frac{T}{T_c}\right)^2\right]^{3/2} \tag{2.67}$$

Alternatively, Kupriyanov and Lukichev showed that, for a dirty superconductor, the results derived from the GL theory holds for the full temperature range barring an adjustment with a temperature dependent correction factor $KL(T)$ which needs to be self-consistently calculated [80, 81]:

$$j_c^{KL}(T) = j_c^{GL}(0)KL(T)\left(1 - \frac{T}{T_c}\right)^{3/2} \tag{2.68}$$

2.5 Superconducting Devices

In this section, we present the reader with a brief description of the superconducting devices relevant for this work, with the exception of superconducting microwave resonators and superconducting nanowires that will be covered in a later part of this thesis. For each device, we introduce the basic principles and equations necessary for the analysis of the experimental results.

2.5.1 Superconducting Tunnel Junctions

Superconductor-Insulator-Normal Metal Junction

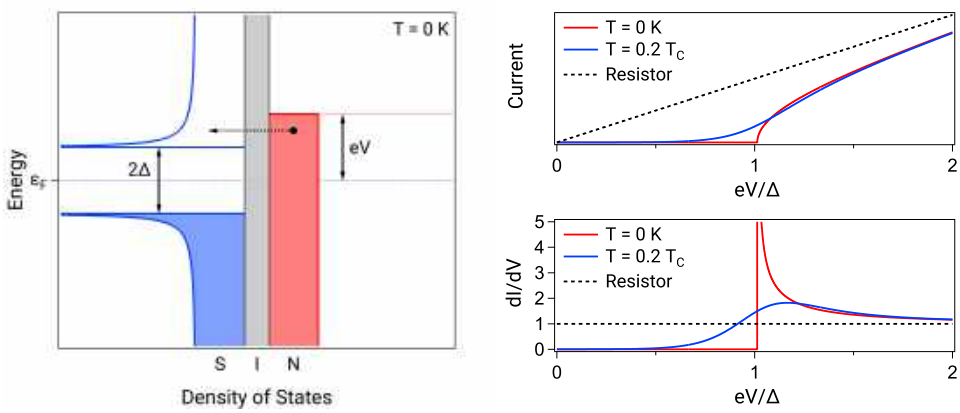

Figure 2.7: **(left)** Semiconductor model of quasiparticle tunneling in an SIN junction. Shading denotes the states occupied by electrons. When the junction bias voltage overcomes the gap of the superconducting state ($eV > \Delta$), electrons can tunnel from the normal metal through the barrier to empty states in the superconductor. **(right)** IV characteristic (top) and differential conductance (bottom) of a typical SIN junction at zero and finite temperature. The dashed lined corresponds to the characteristic of an ohmic junction with the same resistance as the junction normal state resistance R as a reference.

As the name suggests, a superconductor-insulator-normal metal (SIN) junction is a device consisting of a superconductor and a normal metal separated by a very thin layer of insulating material through which quasiparticles can tunnel [82–84]. At $T = 0\,\mathrm{K}$, when a voltage bias V is applied to the junction, the Fermi level of the normal metal rises accordingly and it is only once it crosses the gap of the superconductor ($\Delta = eV$) that current starts flowing through the junction (Fig. 2.7 (left)). The current flowing through the junction is given by [50]:

$$I(V,T) = \frac{1}{eR}\int_{-\infty}^{+\infty} \rho_s(E)\,[f(E,T) - f(E+eV,T)]\,dE \tag{2.69}$$

where R is the junction resistance, $\rho_s(E)$ the superconductor density of states (see Eq.2.5) and $f(E,T) = 1/(1+\exp(E/k_BT))$ is the Fermi-Dirac distribution. The current-voltage (IV) characteristic and the differential conductance dI/dV resulting from Eq. 2.69 are shown in Fig. 2.7 (right). In the limit $T \to 0\,\mathrm{K}$, the differential conductance proves particularly useful as it directly measures the density of states of the superconductor [50]:

$$\frac{dI}{dV} \underset{T\to 0}{=} \frac{1}{R}\rho_s(eV) \tag{2.70}$$

The simplicity of Eqs. 2.69 and 2.70 make SIN junctions a particularly useful tool to investigate the superconducting gap of a given superconductor. Furthermore, the experimental study of superconducting junctions made of disordered superconductors revealed a broadening of the edges of the superconducting gap. This broadening was attributed by Dynes to the existence of energy states below the superconducting gap due to pair-breaking events, and he proposed a phenomenological correction to the density of states as follows [85]:

$$\rho_s(\varepsilon) = \mathrm{Re}\left(\frac{E - i\Gamma}{\sqrt{(E-i\Gamma)^2 - \Delta^2}}\right) \tag{2.71}$$

where Γ, known as the Dynes parameter, quantifies the effect of the pair-breaking processes. By simply substituting the BCS density of state with in Eq. 2.69 with Eq. 2.71, excellent agreement between measurements and Eq. 2.69 can be achieved.

In this work, we have used NbN-AlN-Au SIN junctions to characterise the temperature dependence of the superconducting gap in disordered NbN thin-films. The results of these measurements are detailed in chapter 10.

The Josephson Junction

A Josephson junction (JJ) consists of a two superconductors coupled by a weak link. Traditionally, the weak link consists of a thin insulating layer (SIS junction), but the *Josephson effect* has been observed in various types of superconducting weak links [86, 87], such as a constriction (ScS junction) or superconductor-normal metal-superconductor junctions (SNS junction). As the name suggests, the behaviour of the Josephson effect was originally described by Josephson in 1962 when he predicted that a zero-voltage tunneling current of Cooper pairs can flow through the junction [88, 89]: if the weak link barrier is small enough, the superconducting wavefunction of each electrode overlaps and a current can flow (Fig. 2.8 (top)). The current flowing through the junction as a function of the phase difference across the junction is given by:

$$I = I_c \sin(\varphi) \tag{2.72}$$

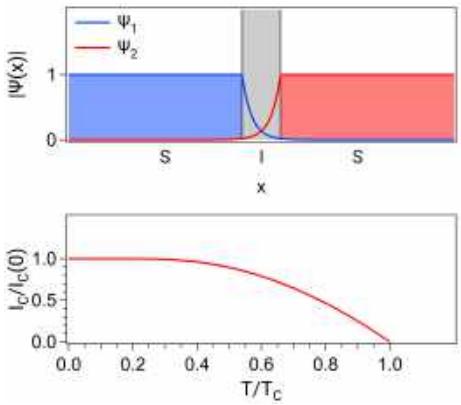

Figure 2.8: **(top)** Superconducting wavefunctions inside a Josephson junction. Outside the superconducting regions, the superconducting wavefunctions exponentially decay but overlap, which allows a supercurrent to flow through the junction. **(bottom)** Critical current I_c as a function of temperature as calculated by Ambegaokar and Baratoff.

where I_c is the critical current of the junction, which corresponds to the maximum current the junction can carry before switching to its resistive state. Eq. 2.72 is known as the *DC Josephson effect*. Additionally, the voltage across the junction is given by the expression known as the *AC Josephson effect*:

$$V = \left(\frac{\hbar}{2e}\right)\frac{d\varphi}{dt} = \left(\frac{\Phi_0}{2\pi}\right)\frac{d\varphi}{dt} \tag{2.73}$$

where Φ_0 is the magnetic flux quantum. Combining Eqs. 2.72 and 2.73 leads to

$$\frac{dI}{dt} = I_c\cos(\varphi)\frac{d\varphi}{dt} \tag{2.74}$$

and

$$V = \frac{\hbar}{2eI_c\cos(\varphi)}\frac{dI}{dt} = L_J\frac{dI}{dt} \tag{2.75}$$

where $L_J = \hbar/2eI_c\cos(\varphi)$ is known as the *Josephson inductance*: the Josephson junction accumulates reactive energy as Cooper pairs tunnel through it. Furthermore, Ambegaokar and Baratoff [90, 91] derived the temperature dependence of the critical current I_c:

$$I_cR_N = \frac{\pi\Delta}{2e}\tanh\left(\frac{\Delta}{2k_BT}\right) \tag{2.76}$$

At $T = 0\,\mathrm{K}$, Eq. 2.76 reduces to

$$I_c R_N = \frac{\pi \Delta_0}{2e} \tag{2.77}$$

Using Eq. 2.77, the expression for the Josephson inductance at zero temperature becomes

$$L_J(T=0) = \frac{\hbar R_N}{\pi \Delta_0} \frac{1}{\cos(\varphi)} \tag{2.78}$$

This relation is reminiscent of the expression for the kinetic inductance of disordered superconductors at zero temperature (Eq. 2.56) and the Josephson inductance is sometimes referred to as the kinetic inductance of the junction. The non-linearity of the Josephson inductance ($\cos(\varphi)$ term) is a particularly attractive property as it allows the design and fabrication of artificial atoms with non-equidistant energy levels.

2.5.2 Transmon Qubit

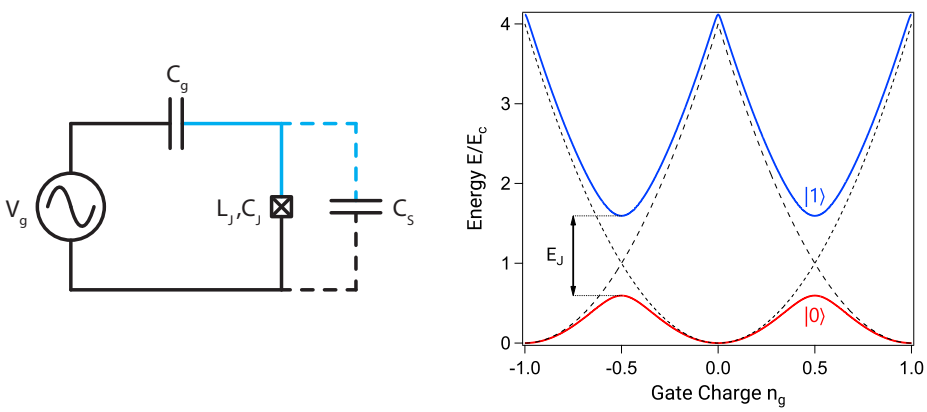

Figure 2.9: **(left)** Circuit diagram of a Cooper-pair box (fixed-frequency transmon qubit). The island in blue is biased via the gate voltage V_g through the gate capacitance C_g and is separated from the reservoir by a Josephson junction (and an extra capacitor C_S in the case of the transmon qubit). **(right)** First two energy levels of the Cooper-pair box calculated at $E_J/E_C = 1$.

Introduced in 2007 [92], the transmon qubit quickly rose in popularity and is today one of the most popular qubit designs and is a refinement of the Cooper-pair box [93–95]. A circuit diagram of a Cooper-pair box and a transmon qubit is shown in Fig. 2.9 (left). In this thesis, we study the fluctuations of coherence in fixed-frequency transmon qubits in chapter 13 and Paper E.

The circuit is characterised by two different energies: the Josephson energy, E_J, which is the potential energy accumulated in the junction as a supercurrent passes through it and the charging energy E_c, corresponding to the kinetic energy needed to transfer one charge onto the island. The Josephson energy is given by

$$E_J = \frac{\Phi_0 I_c}{2\pi} = \frac{\Phi_0}{2\pi}\frac{\pi\Delta_0}{2eR_N} = \frac{\Delta_0}{2}\frac{R_Q}{R_N} \tag{2.79}$$

and the charging energy is defined as

$$E_C = \frac{e^2}{2C_\Sigma} \tag{2.80}$$

where $C_\Sigma = C_g + C_J$ is the total capacitance of the island. Additionally, the system is represented by a reduced gate charge defined $n_g = C_g V_g/2e$. The Hamiltonian of the system is given by

$$\hat{\mathcal{H}} = 4E_C(\hat{n} - n_g)^2 - E_J\cos(\hat{\varphi}) \tag{2.81}$$

The first two solutions of Eq. 2.81 are plotted as a function of the reduced gate charge n_g and $E_J/E_C = 1$ in Fig. 2.9 (left). These energy bands are periodic and the required energy to transition between the ground state and excited state is minimum at $n_g \equiv 1/2 \pmod 1$, known as the *charge degeneracy point*. However, fluctuations of the gate charge due to the environment (charge noise) will lead to a fluctuation of the spacing between the energy levels and has for consequence a short coherence time.

To overcome this sensitivity to charge noise, a capacitor C_S is added in parallel to the junction (see Fig. 2.9 (right)) to form a new circuit known as the transmon qubit. An increased capacitance has for consequence a decreased charging energy[4] which in turn translates into a flattened energy diagram as shown in Fig. 2.10 (left). For sufficiently large values of E_J/E_C, the energy bands are flat and the device is virtually insensitive to charge noise. This, however, comes at the price of a reduced anharmonicity with the risk of driving unwanted transitions and the device no longer acting as an effective two-level system. This is quantified by the relative anharmonicity, which corresponds to the relative difference at the degeneracy point between the $1 \to 2$ (E_{12}) and $0 \to 1$ (E_{01}) transitions, and is given by

$$\alpha_r = \frac{E_{12} - E_{01}}{E_{01}} \tag{2.82}$$

[4]In Eq. 2.80, C_Σ becomes $C_\Sigma = C_g + C_J + C_S$.

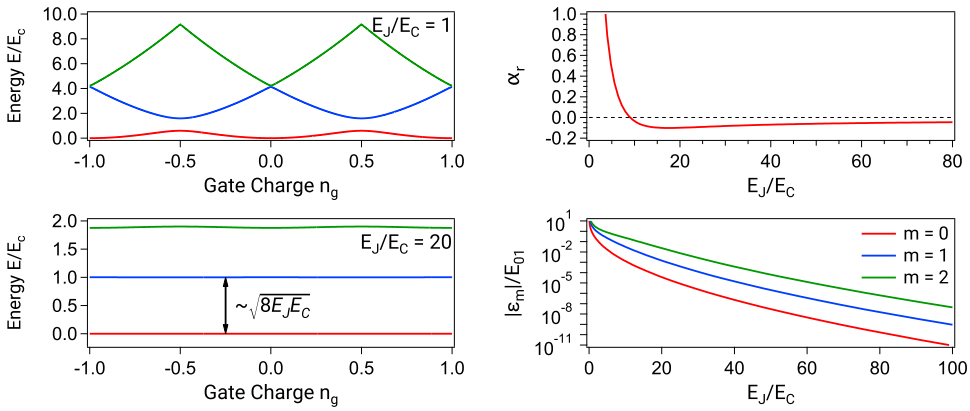

Figure 2.10: **(left)** Energy band diagram of the first three levels of the Cooper-pair box for $E_J/E_C = 1$ (top) and $E_J/E_C = 20$ (bottom). **(right)** Relative anharmonicity (top) and charge dispersion (bottom) as a function of E_J/E_C of a transmon qubit.

At the degeneracy point, the eigenenergy of the m^{th} level is approximately given by [92]

$$E_m \simeq -E_J + \sqrt{8E_JE_C}\left(m + \frac{1}{2}\right) - \frac{E_C}{12}\left(6m^2 + 6m + 3\right) \tag{2.83}$$

From Eq. 2.83, the spacing between two adjacent energy levels follows as

$$E_{m(m+1)} = E_{m+1} - E_m = \sqrt{8E_JE_C} - E_C(m+1) \tag{2.84}$$

Additionally, the sensitivity to charge noise of the qubit is quantified by the charge dispersion, defined as the peak-to-peak value of the m^{th} energy level:

$$\varepsilon_m = E_m(n_g = 1/2) - E_m(n_g = 0) \tag{2.85}$$

The smaller the charge dispersion, the less the qubit frequency will change due to charge fluctuations on the gate. Fig. 2.10 (right) shows both the anharmonicity (top) and charge dispersion for the first three energy levels (bottom). We see that both Eq. 2.82 and Eq. 2.85 depend on E_J/E_C: the charge dispersion decreases exponentially for $E_J/E_C \to +\infty$ and the relative anharmonicity exhibits a shallow local minimum around $E_J/E_C \simeq 17.5$ and asymptotically approaches zero for $E_J/E_C \to +\infty$. Therefore, it is possible to find a regime of E_J/E_C where the system sensitivity to charge noise is small while the relative anharmonicity is large enough. This regime of $E_J/E_C \gtrsim 20$ is known as the *transmon regime*.

For practical applications, it is often preferable and convenient to tune the transition frequency of the qubit. This is achieved with the addition of a second Josephson junction

in parallel with the first one forms a dc-SQUID that enables the tuning of the Josephson energy with magnetic flux.

2.5.3 Superconducting 3D Cavities

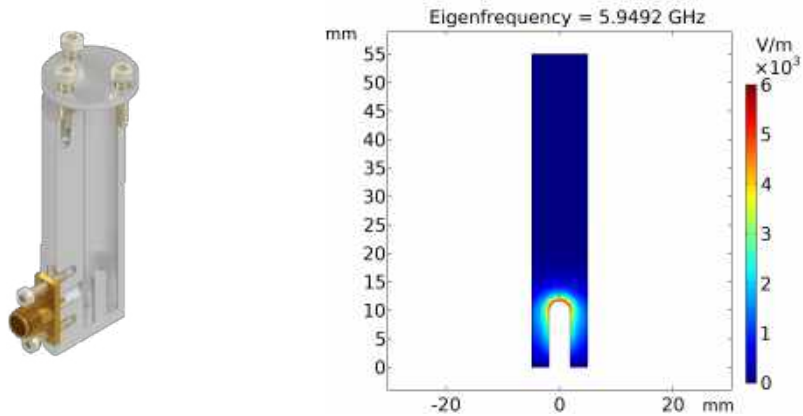

Figure 2.11: **(left)** Cut-out view of the superconducting 3D cavity used in this work. Energy is coupled into the cavity through the SMA connector located near an anti-node of the electric field. **(right)** 3D FEM simulation of the electric field in the cavity at the resonance frequency.

Superconducting 3D microwave cavities are particularly interesting for quantum information processing as they can reach very high quality factors and exhibit extremely high stability, enabling photon storage times on the order of a second [96–98]. The cavity used in this work (chapter 13 and Paper C) consists of a coaxial section of length L forming a $\lambda/4$ resonator (shorted to ground on one end and open-circuited on the other end) and terminated by a circular waveguide section that is then closed with a light-tight cap [99–101]. The cavity is designed in such a way that the cut-off frequency of the circular waveguide section is well above the fundamental resonance frequency of the $\lambda/4$ section and therefore, the resonant mode will be exponentially suppressed in the circular waveguide section. Provided that this section is made long enough, any radiation and environmental losses are mitigated [102].

The coaxial part of the cavity supports a TEM mode propagating along the z direction and for which the electromagnetic field is given by [103]

$$\vec{E} = E_r e^{-\beta z} \vec{e_r} = \frac{V_0 e^{-\beta z}}{r \ln(b/a)} \vec{e_r} \tag{2.86}$$

$$\vec{H} = H_\theta e^{-\beta z} \vec{e_\theta} = \frac{I_0 e^{-\beta z}}{2\pi r} \vec{e_\theta} \tag{2.87}$$

where a and b are the radii of the inner and outer conductors respectively, and $\beta = \omega\sqrt{\mu\varepsilon}$ is the propagation constant in a lossless medium of permittivity ε and permeability μ. Additionally, the wave impedance is given by $Z_w = E_r/H_\theta = \omega\mu/\beta = \eta = 377\,\Omega$ and the characteristic impedance by

$$Z_0 = \frac{V_0}{I_0} = \frac{E_r \ln(b/a)}{H_\theta 2\pi} = \frac{\eta \ln(b/a)}{2\pi} \tag{2.88}$$

For the cavity used in this work, we have $a = 1.85\,\text{mm}$ and $b = 4.90\,\text{mm}$, which corresponds to $Z_0 = 58.4\,\Omega$.

As previously mentioned, the coaxial section of the cavity is short-circuited at one extremity and open-ended at the other extremity. These boundary conditions lead to the existence of a $\lambda/4$ mode with $\beta L = (n - 1/2)\pi$, $n \in \mathbb{N}$. Using Eqs. 2.86, 2.87 and 2.88, we get:

$$\vec{E_{\lambda/4}} = \frac{V_0}{r \ln(b/a)} \sin\left(\frac{\pi z}{2L}\right) e^{i\omega t} \vec{e_r} \tag{2.89}$$

$$\vec{H_{\lambda/4}} = \frac{-V_0}{r\eta \ln(b/a)} \cos\left(\frac{\pi z}{2L}\right) e^{i\omega t} \vec{e_\theta} \tag{2.90}$$

The circular waveguide section of the cavity supports both TE and TM modes and the mode with the lowest cutoff frequency to propagate is a TM_{01} mode [103] with a propagation constant

$$\beta_{01} = \sqrt{k^2 - (p_{01}/b)^2} \tag{2.91}$$

where $p_{01} = 2.405$ is the smallest root of the Bessel function of the first kind $J_0(x)$. The cutoff frequency is given by

$$f_{c_{01}} = \frac{k_c}{2\pi\sqrt{\mu\varepsilon}} = \frac{p_{01}}{2\pi b\sqrt{\mu\varepsilon}} \tag{2.92}$$

Any wave with a frequency lower than $f_{c_{01}}$ will exponentially decay along z in the circular waveguide section. Here, with $b = 4.90\,\text{mm}$, we find $f_{c_{01}} = 23.42\,\text{GHz}$, which is well above the resonant frequency of the cavity, designed to be around 6 GHz.

Using Eq. 2.91, we calculate the propagation constant of the wave in the circular waveguide at $f = 6\,\text{GHz}$ and find $\beta_{01} = i0.475\,\text{mm}^{-1}$: the amplitude of the resonant mode of the cavity falls to 0.1% after $\simeq 14.5\,\text{mm}$. In this work, the total length of the cavity is $L = 35\,\text{mm}$ and the circular waveguide section is $\simeq 23\,\text{mm}$ long.

2.6 Summary

In this chapter, we have introduced the reader to the key concepts of superconductivity that are relevant to this work.

We started with the results of the the Drude-Sommerfeld model (section 2.1). This model is key to understand the normal-state transport properties of the NbN thin-films used throughout this work (see chapters 9 and 10).

Next, the central results of the theories of low-temperature superconductivity (section 2.2) were introduced as a framework to understand of the properties of disordered superconductors (section 2.3). Then, in section 2.4, we discussed the implications of disorder on the transport properties of the superconductor. These results are important for the design and characterisation of disordered thin-films (see chapters 9 and 10)

We conclude this chapter with a discussion of the different type of superconducting devices that were used throughout this thesis (see chapters 9, 10, 11, 12 and 13 and Papers A–E).

Chapter 3

Superconducting Microwave Resonators

A resonator is by definition a device or system that exhibits resonance, that is, it naturally oscillates at some frequencies, called its resonant frequencies. In particular, superconducting microwave resonators are of interest due to their extremely low losses and have found many applications in circuit quantum electrodynamics [104].

This chapter first describes the basic concepts of microwave transmission lines and resonators and continues with a description of the different loss mechanisms that limit the performance of resonators.

In this work, we study superconducting resonators and the self-resonant modes of high-impedance superconducting nanowires. The concepts and models introduced in this chapter will provide the necessary framework to understand the origin of these losses.

3.1 Two-port Network

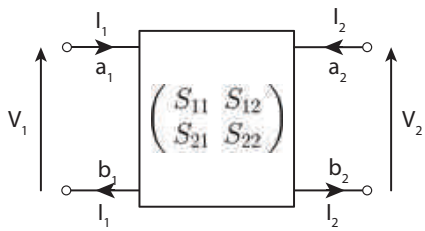

Figure 3.1: Schematic of a two-port network characterised by its scattering matrix. The properties of the two-port network can either be expressed as a function of voltage and current at each port (V_1, I_1, V_2, I_2) or as a function of incident and reflected waves (a_1, b_1, a_2, b_2).

A two-port network (Fig. 3.1) is an electric circuit with two pairs of terminals. By definition, two terminals constitute a *port* if and only if the electric current entering one terminal equals the current emerging from the other terminal. Mathematically, a two-port network is fully described by a 2×2 matrix of complex numbers that establish relations between the voltage and current across the ports [103].

A convenient way of expressing the properties of a two-port network is the *ABCD matrix*,

given by

$$\begin{pmatrix} V_1 \\ I_1 \end{pmatrix} = \begin{pmatrix} A & B \\ C & D \end{pmatrix} \begin{pmatrix} V_2 \\ -I_2 \end{pmatrix} \tag{3.1}$$

For a combination of several two-port networks, the total ABCD matrix is simply the product of the ABCD matrix of each two-port network. Morever, the ABCD matrix description is particularly convenient as series and shunt impedances are simply given by

$$ABCD_{series} = \begin{pmatrix} 1 & Z_{series} \\ 0 & 1 \end{pmatrix} \quad \text{for a series impedance } Z_{series}$$

$$ABCD_{shunt} = \begin{pmatrix} 1 & 0 \\ Z_{shunt}^{-1} & 1 \end{pmatrix} \quad \text{for a shunt impedance } Z_{shunt}$$

A two-port network is said to be *reciprocal* if the voltage appearing at port 2 due to a current applied at port 1 is the same as the voltage appearing at port 1 when the same current is applied to port 2. In the ABCD matrix description, this translates into $\det[ABCD] = AD - BC = 1$.

Finally, a two-port network is said to be *symmetrical* if its input and output impedances are equal, which translates into $A = D$ in the ABCD matrix. Experimentally, the devices measured in this work are symmetric and reciprocal, however, due to the presence of amplifiers in the setup (see section 7.3), the measurements are not reciprocal or symmetric.

3.1.1 Scattering Parameters

At high frequencies (microwave frequencies), it is generally difficult to accurately measure voltages and currents directly and the use of power and energy variables is more appropriate. The scattering matrix describes the relationship between the incident (a_1, a_2) and reflected (b_1, b_2) waves and is given by

$$\begin{pmatrix} b_1 \\ b_2 \end{pmatrix} = \begin{pmatrix} S_{11} & S_{12} \\ S_{21} & S_{22} \end{pmatrix} \begin{pmatrix} a_1 \\ a_2 \end{pmatrix} \tag{3.2}$$

Each scattering parameter (S parameter) consists of a unitless complex number that represents the magnitude and phase response of the device at a given frequency. S_{11} (S_{22}) are known as the reflection coefficients from port 1 (port 2), S_{21} (S_{12}) correspond to the transmission from port 1 to port 2 (port 2 to port 1). For a reciprocal two-port network, we have $S_{12} = S_{21}$ and for a symmetrical network $S_{11} = S_{22}$.

The scattering parameters are of particular importance for real devices as they are directly accessible to the experimentalist through measurement equipment such as a vector network analyzer (VNA).

Additionally, the S-parameters can be expressed in terms of the ABCD matrix elements. For a reciprocal and symmetrical network, and assuming the ports are loaded with loads of characteristic impedance Z_0, the scattering matrix is given by [105]

$$S_{11} = \frac{A + B/Z_0 - CZ_0 - D}{A + B/Z_0 + CZ_0 + D} \tag{3.3}$$

$$S_{21} = \frac{2}{A + B/Z_0 + CZ_0 + D} \tag{3.4}$$

3.2 Transmission Lines

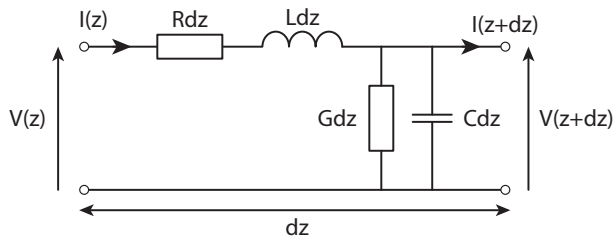

Figure 3.2: Lumped element representation of a segment of length dz of a transmission line with the resistance R, inductance L, capacitance C and shunt conductance G per unit length.

A transmission line is a specialized structure designed to conduct alternating currents with a frequency high enough that their wave nature must be taken into account. The properties of a transmission line can be studied by the telegraph equations [103] where the transmission line is represented by a succession of infinitesimally short segments of length dz as depicted in figure 3.2. The voltage and current can be written as

$$\begin{cases} V(z) = V^+ e^{-\gamma z} + V^- e^{\gamma z} \\ I(z) = I^+ e^{-\gamma z} + I^- e^{\gamma z} \end{cases} \tag{3.5}$$

where $\gamma = \alpha + i\beta = \sqrt{(R + i\omega L)(G + i\omega C)}$ is the complex propagation constant for a travelling wave at the frequency ω. From these, the characteristic impedance of the transmission line follows

$$Z_0 = \frac{V^+}{I^+} = -\frac{V^-}{I^-} = \sqrt{\frac{R + i\omega L}{G + i\omega C}} \tag{3.6}$$

For a superconducting transmission line, we can neglect R and G due to the absence of resistive losses, and therefore rewrite the previous expressions as

$$\gamma = i\beta = i\omega\sqrt{LC} \tag{3.7}$$

$$Z_0 = \sqrt{\frac{L}{C}} \tag{3.8}$$

The transmission lines used in this work are *coplanar waveguides* (CPW). CPWs were originally introduced by Wen [106] and consist of a conducting track of width w together with a pair of return conductors on a substrate (see Fig. 3.2). All three conductors are on the same side of the substrate, and hence are *coplanar*. The return conductors are separated from the central track by a small gap g. The capacitance and inductance per length and the characteristic impedance of a CPW is directly dependent on w and g, and is calculated with a technique known as *conformal mapping*. The detailed calculations can be found in appendix B. As standard microwave equipment have a characteristic impedance of $50\,\Omega$, the CPWs in this work are designed to the same $50\,\Omega$ characteristic impedance in order to avoid unwanted reflections.

3.3 Half-wavelength Resonators

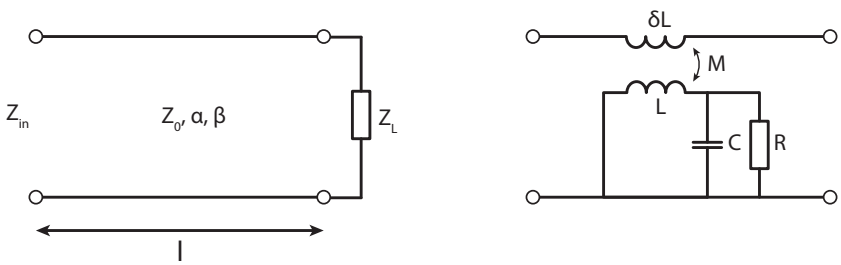

Figure 3.3: **(left)** Portion of transmission line of length l loaded with an impedance Z_L **(right)** Half-wavelength resonator inductively coupled to a transmission line. Energy is exchanged through the mutual inductance between the probing line and the resonator.

Let's consider a length l of transmission line of characteristic impedance Z_0 and loaded by an impedance Z_L (Fig. 3.3 (left)). The input impedance is given by [103]

$$Z_{in} = Z_0 \frac{Z_L + Z_0 \tanh\left[(\alpha + i\beta)l\right]}{Z_0 + Z_L \tanh\left[(\alpha + i\beta)l\right]} \tag{3.9}$$

For an open-ended transmission line, $Z_L \to \infty$ and Eq. 3.9 becomes

$$Z_{in} = Z_0 \coth\left[(\alpha + i\beta)l\right] = Z_0 \frac{1 + i \tan\beta l \tanh\alpha l}{\tanh\alpha l + i \tan\beta l} \tag{3.10}$$

This forms a half-wavelength resonator with a fundamental mode resonance frequency ω_0 verifying $l = \lambda/2 = \pi v_{ph}/\omega_0$, where v_{ph} is the phase velocity in the transmission line. If

we introduce $\Delta\omega = \omega - \omega_0$, a small detuning from the resonance frequency, we can write

$$\beta l = \frac{\omega l}{v_{ph}} = \frac{\omega_0 l}{v_{ph}} + \frac{\Delta\omega l}{v_{ph}} = \pi + \frac{\pi\Delta\omega}{\omega_0} \tag{3.11}$$

For small detunings ($\Delta\omega \ll \omega_0$) and for a superconducting transmission line, for which we can assume $\alpha l \ll 1$, we have:

$$\tanh \alpha l \simeq \alpha l \quad \text{and} \quad \tan \beta l \simeq \frac{\pi\Delta\omega}{\omega_0} \tag{3.12}$$

Using this and introducing the internal quality factor Q_i of the resonator with $Q_i = \beta/2\alpha = \pi/2\alpha l$, Eq. 3.10 becomes

$$Z_{in} = Z_0 \frac{1 + i\frac{\Delta\omega}{\omega_0}\pi\alpha l}{\alpha l + i\frac{\Delta\omega}{\omega_0}\pi} \simeq Z_0 \frac{1}{\frac{\pi}{2Q_i} + i\pi\frac{\Delta\omega}{\omega_0}} = \frac{2Z_0 Q_i/\pi}{1 + 2iQ_i\frac{\Delta\omega}{\omega_0}} \tag{3.13}$$

Eq. 3.13 represents the impedance response of a superconducting half-wavelength resonator for frequencies close to its resonance frequency ω_0. The internal quality factor represents the ratio of the energy stored in the resonator divided by the energy dissipated in the resonator in a single cycle. The study of Q_i gives valuable insight on the nature of dissipation in a device.

Additionally, near the resonance frequency, the resonator can be modeled by a lumped element parallel RLC circuit (Fig. 3.3 (right)) with the following circuit parameters [103]:

$$R = \frac{Z_0}{\alpha l} = \frac{2Q_i Z_0}{\pi}, \quad C = \frac{\pi}{2\omega_0 Z_0} \quad \text{and } L = \frac{1}{\omega_0 C} \tag{3.14}$$

3.3.1 Inductive Coupling

In order to interact with the resonator, the resonator needs to be coupled to the outside world. In this work, the resonators are inductively coupled to a probing transmission line of characteristic impedance Z_0 (see Fig. 3.3 (right)). In an inductive coupling scheme, energy is exchanged between the resonator and the transmission line through a mutual inductance M. A half-wavelength resonator of impedance Z_r, inductively coupled to a portion of transmission line of inductance δL, will have an input impedance [107, 108]:

$$Z_{in} = i\omega\delta L + \frac{\omega^2 M^2}{Z_r} \tag{3.15}$$

Loading the resonator has for effect to change its resonant frequency. Indeed, from Eqs. 3.13 and 3.15, we immediately see that the resonance condition $\mathrm{Im}(Z_{in}) = 0$ will

be verified for different frequencies. However, assuming that the coupling is weak, the frequency shift due to the coupling can be neglected and, at resonance, we have

$$Z_{in} \simeq \frac{\omega_0^2 M^2}{Z_r} \tag{3.16}$$

Using Eq. 3.13, we get

$$Z_{in} = \frac{\pi \omega_0^2 M^2}{2 Z_0 Q_i} \left(1 + 2iQ_i \frac{\Delta\omega}{\omega_0}\right) \tag{3.17}$$

The coupling quality factor Q_c is defined by the ratio of the energy stored in the resonator and the power exchanged between the resonator and the transmission line each cycle. The coupling quality factor Q_c for an inductively coupled resonator is given by [108]

$$Q_c = \frac{\pi \omega_0^2 M^2}{4 Z_0^2} \tag{3.18}$$

Additionally, we define the loaded quality factor Q_l as the total quality factor of the resonator and coupling. The loaded quality factor is given by

$$\frac{1}{Q_l} = \frac{1}{Q_i} + \frac{1}{Q_c} \tag{3.19}$$

Finally, using Eqs. 3.17, 3.18 and 3.19, we can derive the expression for the S_{21} parameter of the resonator coupled to the transmission line, which corresponds to the quantity measured in experiments. S_{21} is given by

$$S_{21} = \frac{1}{1 + Z_0/2Z_{in}} = \frac{1}{1 + Q_i/Q_c(1 + 2iQ_i\Delta\omega/\omega_0)^{-1}} = 1 - \frac{Q_l Q_c^{-1}}{1 + 2iQ_l\Delta\omega/\omega_0} \tag{3.20}$$

3.3.2 Number of Photons

In quantum physics, the electromagnetic field inside the resonator can be quantized and is therefore usually expressed as an average number of photons $\langle n \rangle$ instead of the more traditional (and classical) microwave power.

When probed with an applied power P_{in} at $\omega = \omega_0$, the average energy stored in a resonator of characteristic impedance Z_r is given by [109]

$$\langle E_{int} \rangle = \frac{2}{\pi} \frac{Z_0}{Z_r} \frac{Q_l^2}{Q_c} \frac{P_{in}}{\omega_0} \tag{3.21}$$

This energy corresponds to an average number of microwave photons $\langle n \rangle$ given by

$$\langle n \rangle = \frac{\langle E_{int} \rangle}{\hbar \omega_0} \tag{3.22}$$

3.3.3 Generalised Resonator

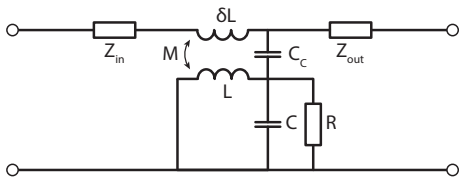

Figure 3.4: Generalised resonator model. The resonator is coupled to the transmission line through both capacitive and inductive coupling. Additionally, the transmission line is not perfectly matched.

The circuit described in the previous section consists of an *ideal* resonator. Unfortunately, non-idealities in the experimental setup, such as impedance mismatch in the probing line, can lead to significant asymmetry in the resonance line shape. Moreover, in practice, the resonator coupling is always a combination of both capacitive and inductive coupling, which significantly complicates calculations.

A generalised model (see Fig. 3.4) that accounts for these imperfections has been proposed by Khalil [110]. In this model, the coupling quality factor Q_c is replaced by a complex quality factor $|Q_c| \exp(-i\varphi)$ that accounts for both inductive and capacitive coupling, and for any impedance mismatch of the probing line. Additional terms are also introduced to compensate for the effects of the environment, such as an imperfect background and propagation delays caused by the length of the cables. Eq. 3.20 becomes

$$S_{21} = a e^{i\alpha} e^{-\omega i \tau} \left[1 - \frac{Q_l |Q_c|^{-1} e^{i\varphi}}{1 + 2iQ_l \Delta\omega/\omega_0} \right] \tag{3.23}$$

where a, α and τ are respectively an amplitude, a phase shift and the electrical delay, and all account for the influence of the environment: a and α account for a non-ideal background signal, while τ accounts for the propagation delay in the cables. Fig. 3.5 shows simulated examples of two resonators with similar parameters ($Q_l = 10000$, $Q_c = 20000$, $\omega_0 = 4\,\mathrm{GHz}$). In Fig. 3.5, the resonator responses are plotted in two different ways: the top panels show the magnitude and phase response of the resonator as a function of the probing frequency and the bottom panels consist of parameterised plots of the imaginary and real parts of the S_{21} forward transmission. The resonator on the left is an ideal resonator in an ideal environment. The magnitude and phase responses are perfectly symmetrical and the real and imaginary components form a perfect circle. The resonator on the right,

on the other hand, was placed in an environment with significant impedance mismatch, attenuation and a large electrical delay and its response is significantly distorted.

In this work, we fit our experimental data to Eq. 3.23 using a traceable fit routine developed by Probst [111]. This method relies on fitting the real and imaginary components of the S_{21} transmission response of the resonator to a circle and accounts for all imperfections.

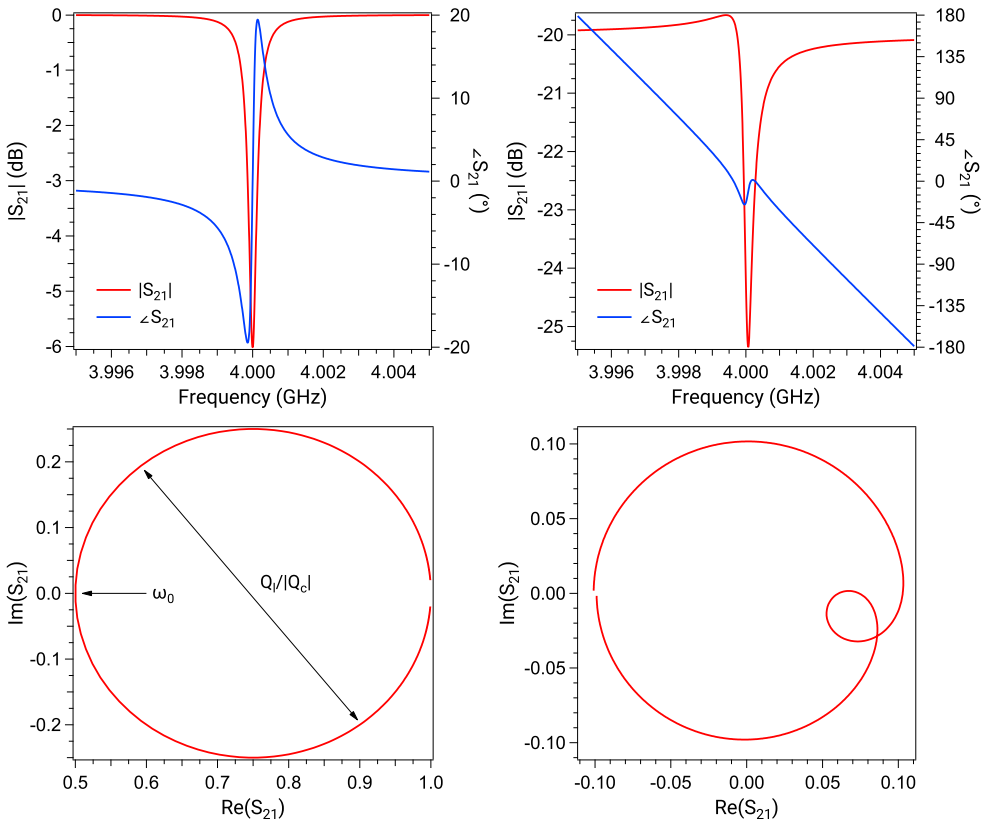

Figure 3.5: **(left)** Magnitude and phase response of an ideal resonator along with its resonance circle. The diameter of the resonance circle corresponds to the ratio of the quality factors and the resonance frequency corresponds to $\mathrm{Im}\, S_{21} = 0$. **(right)** Skewed resonator response due to several imperfections. The resonance line shape is asymmetric due to impedance mismatch in the probing line and the resonance circle is distorted due to significant electrical delay.

Chapter 4

Losses in Superconducting Circuits

4.1 Generalised Loss Model

Several different mechanisms can contribute to the loss of energy in a superconducting resonator. To quantify these losses, we can define a generalised loss model where all the different contributions are accounted for. This generalised expression for the internal quality factor is given by

$$\frac{1}{Q_i} = \frac{1}{Q_{TLS}(T,P)} + \frac{1}{Q_{qp}(T)} + \frac{1}{Q_{disorder}(t)} + \frac{1}{Q_{rad}(w)} + \dots \tag{4.1}$$

From this last equation, we see that the internal quality factor of a resonator will be limited by the largest loss mechanism in the device. To distinguish between the loss mechanisms, we can examine the response of our devices against various parameters, such as temperature, excitation power, device geometry or film thickness. Because each loss mechanism is entirely dependent on a specific set of parameters, by comparing the data with the models described in this section, the dominant loss mechanism can be determined. In the following section, we discuss the main loss mechanisms relevant for this work.

4.2 Resistive Loss: Quasiparticles

At microwave frequencies, current is forced to flow within the skin depth of a conductor (see section 2.3.5). For our thin-films, the skin depth is typically greater than the film thickness. This constraint means that unlike at DC, where conduction can occur by the path of least resistance, at microwave frequencies some current is carried by quasiparticles. The current carried by quasiparticles can then exhibit resistance and therefore limit the quality factor of a superconducting resonator.

The easiest example of this is to examine the temperature dependence of a microwave resonator below T_c. Unlike at DC, where dissipation-less conduction is found for all temperatures below T_c, a microwave resonator will demonstrate a strongly temperature dependent quality factor, which is due to the thermally varying population of quasiparticles.

Temperature is not the only cause of quasiparticles: they can also arise from pair-breaking photons, which are photons with an energy greater than the superconducting gap. This

is the mechanism on which kinetic inductance detector [112] rely as the pair-breaking photons lead to a cloud of quasiparticles. These quasiparticles produce both a change in the kinetic inductance (see section 2.3.4 and 2.3.5) and the dissipation of the resonator. In non-detector applications, the pair-breaking photons are an unwanted effect and cryostats are equipped to attenuate these pair-breaking photons. This attenuation is performed by a combination of lossy in-line filters [113] and absorptive coatings [114] on components below the mixing chamber (see section 7.3 for additional details on the experimental setups used in this work). Despite these efforts, larger than expected residual quasiparticle populations are often found in a variety of quantum circuits [115–119]. While these may arise from non-ideal superconductor behaviour, poor filtering or poor thermalisation, it has also been shown that external sources such as ionizing radiation from the atmosphere can lead to significant pair-breaking effects [120].

4.2.1 Disorder-Induced Loss

A variety of disordered superconducting thin-films are experimentally found to exhibit significant internal dissipation [13, 14, 121]. Additionally, Coumou [122] observed that the internal quality factor of disordered titanium nitride resonators is reduced as the thickness of the film decreases. This decrease in thickness corresponds to a reduction of the Ioffe-Regel parameter, i.e. an increase in disorder.

These results hint toward the existence of a disorder-induced residual quasiparticle density that intrinsically limits the microwave performance of devices made with highly disordered superconductors. The microscopic origin of this loss mechanism is still debated, however recent theoretical work hints at the presence of low-lying sub gap states in the proximity of the SIT [123].

4.3 Resistive Loss: Two-level Systems (TLS)

The lumped-element model of a capacitor includes a lossless ideal capacitor in series with a resistor called the equivalent series resistance (ESR). The ESR is a measure of the non-ideality of the capacitor and accounts for dielectric losses in the capacitor. The impedance of a non-ideal capacitor is therefore rewritten as $Z_c = R_{ESR} + 1/iC\omega$. The presence of the real term means that the impedance points at some angle δ from the imaginary axis. By examining the absolute value of $\tan\delta$, we arrive at $\tan\delta = \omega R_{ESR} C$, which is the inverse of a quality factor. This expression is known as the *loss tangent* and is used to describe the dissipation within a capacitor. The loss tangent is generally frequency dependent due to the dipole relaxation within dielectrics. Additionally the dipole relaxation itself is usually temperature dependent.

Within superconducting resonators, the loss tangent of the effective capacitance per unit length can limit the quality factor. This effect was first quantified by O'Connell [124] where in the low temperature, low microwave power limit, dipoles within the dielectric become desaturated and can absorb microwave photons as a two level system (TLS).

Here, the resonator is directly probing the density of dipoles which are within a narrow energy spectrum that is centered on the resonator frequency. When the microwave power is increased, these dipoles become saturated, leading to a reduction in the amount of power absorbed by the dipoles. Equivalently, Macha [125] demonstrated that within the temperature range of $20-900\,\mathrm{mK}$, the dipoles can become thermally saturated, which also leads to a reduction of the amount of power absorbed by the dipoles. A Kramers-Kronig relation can translate between the real and imaginary parts of the dipole absorption properties [126]. Correspondingly, Gao [17] and Lindström [127] showed that the thermal desaturation of the dipoles leads to a temperature-dependent permittivity. Importantly, this leads to a frequency shift that provides an independent measure of dielectric loss that can be insensitive to other loss mechanisms.

A recent development in understanding dielectric loss is that the dipole energies are not stationary. Qualitatively slow drifts in energy of an individual dipole two-level system was reported by Grabovskij [128]. In further work, Lisenfeld [129] found that these two-level systems interact with one another. This interaction was motivated as the cause of the slow drifts in the TLS energy. In related work, Burnett [26] found that the frequency of superconducting resonators was not stable, with the instability scaling being stronger than $1/T$. This frequency instability was attributed to the interaction between TLS, which produces a time dependence of the permittivity. The time-variation of the TLS energy has an important consequence on the dielectric loss: if the TLS energy shifts to become non-resonant, then it cannot absorb microwave photons from the resonator. In this case, Faoro [22] showed that the microwave-power dependence of the dielectric loss becomes logarithmic. In such a situation, since the logarithmic power dependence of loss is so weak, the temperature dependence of the permittivity is the more reliable measure of dielectric loss.

4.3.1 Logarithmic TLS Model

The logarithmic power dependence of the dielectric loss introduced in the previous paragraph is formally given by [22]

$$\frac{1}{Q_i} = F \tan\delta^i_{TLS} P_\gamma \ln\left(\frac{cn_c}{\langle n\rangle} + \delta'_0\right) \tanh\left(\frac{hf_r}{2k_BT}\right) \tag{4.2}$$

Here, F is the *filling factor* (also known as *participation ratio*), which is the ratio of electric field threading the TLS host volume to the total electric field, and $\tan\delta^i_{TLS}$ is the intrinsic TLS loss tangent (found from an independent measurement of the permittivity), sensitive to the complete TLS spectrum. Additionally, P_γ is the TLS switching rate ratio, defined by $P_\gamma = 1/\ln(\gamma_{max}/\gamma_{min})$ where γ_{max} and γ_{min} are the maximum and minimum rate of TLS switching respectively. c is a large constant, n_c is the number of photons generating the electric field saturating a TLS and δ'_0 is the log-scaled next dominant loss rate. The temperature-dependent hyperbolic tangent scaling highlights the thermal saturation of TLS. A typical curve obtained by this model is shown in Fig. 4.1 (left).

4.3.2 Intrinsic Loss Tangent - Temperature-Dependent Permittivity

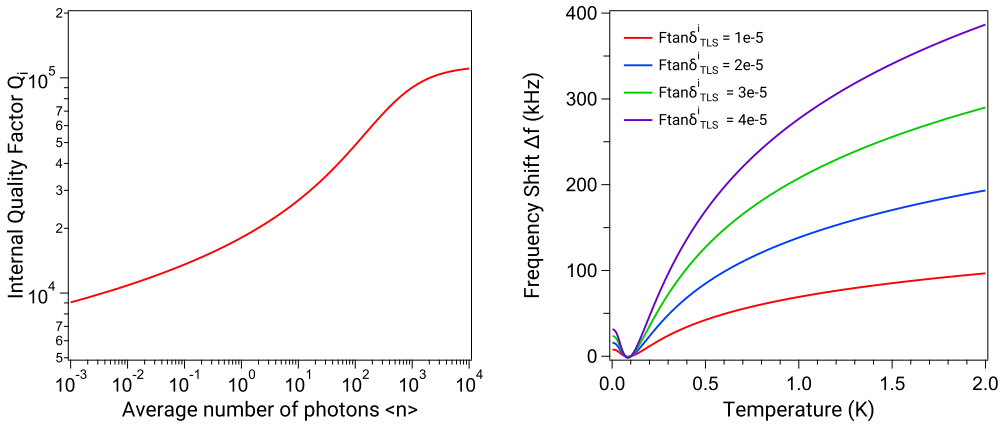

Figure 4.1: **(left)** Eq.4.2 log dependence of TLS related loss calculated at 10 mK and $F \tan \delta^i_{TLS} = 8 \times 10^{-6}$. At high microwave excitation, the TLS are saturated and the loss in the resonator are governed by the next dominant loss rate (δ'_0 in Eq.4.2). As the number of photons in the resonator decreases, TLS start to desaturate and exchange energy with the resonator, leading to the logarithmic loss described by Eq. 4.2. **(right)** Frequency shift as a function of temperature for different values of $F \tan \delta^i_{TLS}$. Larger filling factors correspond to larger losses and hence larger frequency shifts. The minimum corresponds to $T = T_0$ and $T_0 = 100$ mK for this simulation.

The intrinsic loss tangent, sensitive to any thermally varying TLS, can be measured by studying the frequency of a microwave resonator as a function of temperature: as the temperature decreases, TLS desaturate and start exchanging energy with the resonator, leading to a decrease of the resonance frequency. Once all TLS are thermally desaturated, an upturn in frequency is observed as TLS resonantly exchange energy with the resonator. This frequency shift is described by [17]

$$\Delta f = F\delta^i_{TLS}\left(\ln\left(\frac{T}{T_0}\right) - [g(T,f) - g(T_0,f)]\right) \tag{4.3}$$

where $\Delta f = (f_r(T) - f_r(T_0))/f_r(T_0)$, $g(T,f) = \mathrm{Re}\left(\Psi\left(\frac{1}{2} + hf/2\pi i k_B T\right)\right)$, T_0 is a reference temperature and Ψ is the complex digamma function. We see from Eq. 4.3 the frequency shift is directly proportional to $F \tan \delta^i_{TLS}$. For a given $\tan \delta^i_{TLS}$, this means that an increased filling factor F will correspond to an increase in loss.

When the physical dimensions of a resonator are reduced, the concentration of electrical field increases and leads to an increase in the filling factor [17]. Because of this, small dimension resonators have an unfavorable scaling of the filling factor and will lead to additional dissipation due to TLS as highlighted in Fig. 4.1 (right).

4.3.3 Modelling of TLS Loss

Experimentally, devices are often constituted of several regions that may host TLS. These different regions usually consist of different materials or interfaces and can have vastly different loss tangents. The models described by Eqs. 4.2 and 4.3 rely on a total participation ratio and total TLS loss tangent. While this simple approach captures well the overall behaviour of the loss in devices, it does not quantitatively describes the individual contributions of all TLS-containing regions of a device. For this purpose, we split the dielectric loss into a linear combination of loss tangents each associated with a corresponding filling factor [130–134],

$$\frac{1}{Q_{TLS}} = F_{TLS}\delta^i_{TLS} = \sum_k F_k \delta^i_k \tag{4.4}$$

where δ^i_k is the intrinsic loss tangent of region k. Additionally, the filling factor of a given TLS host region k, of volume V_k and relative permittivity ε_k, is given by

$$F_k = \frac{U_k}{U_{total}} = \frac{\int_{V_k} \varepsilon_k \vec{E}^2(\vec{r})d\vec{r}}{\int_V \varepsilon \vec{E}^2(\vec{r})d\vec{r}} \tag{4.5}$$

where U_k and U_{total} are the electric energy stored in region k and the total electric energy, respectively, $\vec{E}$ is the electric field, and ε is the effective permittivity of the entire volume V.

4.4 Radiation Loss

An additional loss mechanism that may hinder performances of superconducting resonators is known as *radiation loss*. A general definition of radiation loss is the energy that is lost by radiating away from the circuit and into the surrounding environment. In other words, radiation loss is the energy radiating into free space rather than being confined in the resonant structure: the circuit acts as an antenna.

Radiation losses are highly dependent on the geometry and are non-trivial to precisely calculate, however, for CPW and microstrip structures, they are usually very small and can be neglected. We estimate the radiation loss in our device to be $\alpha_r = 1/Q_{rad} < 1 \times 10^{-6}$ [112, 135].

Chapter 5

Frequency Noise and Fluctuations

Understanding fluctuations and noise processes is important as they are an undesired and problematic effect. Generally, fluctuations and noise limit the sensitivity and therefore the usefulness of circuits. In fact, the study of noise in electronic circuits has spanned over a century, starting with the introduction of the concept of shot noise by Schottky in 1918 [136, 137], and soon after, the study of flicker noise and thermal noise by Johnson [138, 139] and Nyquist [140].

In superconductors, soon after the Josephson junction was introduced, an effort was made to understand and mitigate the sources of noise in junctions and SQUIDs [141–143]. To this day, the study of fluctuations and their relation to noise processes in superconductors is still a vast field of active research as these fluctuations are sources of decoherence in quantum circuits [4, 23, 26, 27]. In this thesis (chapter 13) and in Papers C-E, we study fluctuations in various types of superconducting circuits and relate these fluctuations to two-level system noise.

5.1 Statistical Analysis of Fluctuations

In general terms, the properties of some quantity are measured as a time series using some instrumentation. By generating some statistics relating the measured quantity at several instances in time, the deviation (the *fluctuations*) that occurred within the time span can be determined quantitatively and analysed. In this section, we introduce the statistical tools used in this thesis for the analysis of frequency fluctuations.

5.1.1 Noisy Signal

An ideal signal consists of a pure sine wave of a given frequency and amplitude. However, any real signal has amplitude and phase modulated noise components. The instantaneous value of a quasi-perfect sinusoidal signal can be expressed as

$$z(t) = Z_0 \left[1 + \alpha(t)\right] \sin(2\pi f_0 t + \varphi(t)) \tag{5.1}$$

where Z_0 and f_0 are the nominal signal amplitude and frequency, and the random variables $\alpha(t)$ and $\varphi(t)$ are the instantaneous amplitude and phase fluctuations respectively. A sketch of such signal is shown in Fig. 5.1. In most cases, it can be assumed that the fluctuations need to be small compared to their nominal values (i.e. $|\alpha(t)| \ll 1$ and

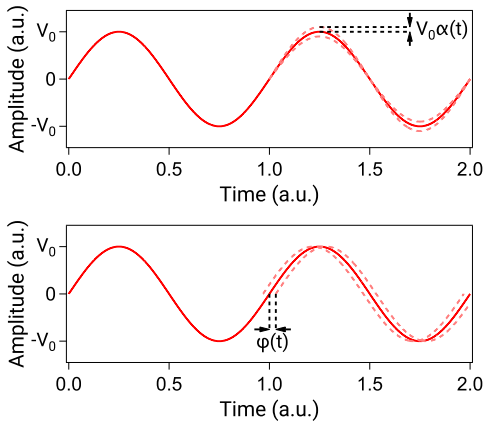

Figure 5.1: Quasi-perfect sinusoidal signal of amplitude V_0. The noise is represented by amplitude ($\alpha(t)$) and phase ($\varphi(t)$) fluctuations.

$|\varphi(t)| \ll 1$), which guarantees that the statistical processes described in the following sections are valid. In the presence of frequency drift, the condition $|\varphi(t)| \ll 1$ is no longer true, however, drift can easily be subtracted from the data prior to the statistical analysis. In this thesis, our measurement setup is not sensitive to amplitude noise (see chapter 7), therefore, in the following, we focus our discussion on phase fluctuations and their implications on the resonant frequency of a device.

The instantaneous frequency of the signal described by Eq. 5.1 is given by

$$f(t) = f_0 + \frac{1}{2\pi}\frac{d\varphi(t)}{dt} \tag{5.2}$$

This equation illustrates that the deviations from the center frequency f_0 are directly related to the fluctuations in the phase of the signal and therefore $d\varphi(t)/dt$ is known as the instantaneous frequency deviation. Additionally, we define the fractional frequency fluctuations, $y(t)$, as

$$y(t) = \frac{f(t) - f_0}{f_0} = \frac{1}{2\pi f_0}\frac{d\varphi(t)}{dt} \tag{5.3}$$

Experimentally, f_0 typically corresponds to the desired frequency of the signal or a reference value close to the signal frequency, however, for a more accurate statistical description, f_0 can be taken as the mean of the frequency fluctuations $\mu = \bar{f}(t)$.

5.1.2 Frequency Domain Analysis: Power Spectral Density

Traditionally, fluctuations are studied in the frequency domain with spectral analysis. According to Fourier analysis, any physical signal can be decomposed into a number of discrete frequencies, or a spectrum of frequencies over a continuous range, and the

calculation of the spectral density sheds light on the frequency content of a given signal. In this section, we describe how the power spectral density (PSD) is calculated and discuss the shortcomings of this technique for the analysis of noise processes.

Starting with a real-valued time-dependent signal $z(t)$ of mean $\mu(t)$ and variance $\sigma^2(t)$, the autocorrelation between times t_1 and t_2 is given by [144]

$$R(t_1, t_2) = \frac{E[(z(t_1) - \mu(t_1))(z(t_2) - \mu(t_2))]}{\sigma(t_1)\sigma(t_1)} \tag{5.4}$$

where E is the expected value operator. We note that this expression is not well-defined for processes with zero variance (constant process) or infinite variance (processes with a distribution lacking well-behaved moments); this is however not the case for the signals considered in this thesis. The autocorrelation function R has values between -1 and 1, known respectively as anti-correlation and perfect correlation. If the signal has a time independent mean μ and variance σ^2, Eq. 5.4 can be simplified as:

$$R(\tau) = \frac{E[(z(t) - \mu)(z(t+\tau) - \mu)]}{\sigma^2} = \langle z(t)z(t+\tau)\rangle \tag{5.5}$$

Finally, according to the Wiener-Khinchin theorem [145, 146], the power spectral density (PSD) is obtained by taking the Fourier transform of the autocorrelation (Eq. 5.5):

$$S_z(\omega) = \int_{-\infty}^{\infty} \langle z(t)z(t+\tau)\rangle \, e^{-i\omega\tau} d\tau = 2\int_{0}^{\infty} \langle z(t)z(t+\tau)\rangle \, e^{-i\omega\tau} d\tau \tag{5.6}$$

In this thesis, we study the fractional frequency fluctuations, $y(t)$, and the associated power spectral density S_y.

Unfortunately, because measurement data is sampled, the calculation of PSDs rely on a discrete Fourier transform (DFT). The finite nature of a sampled measurement leads to aliasing and spectral leakage in the spectrum, which can severely restrict the dynamic range of the PSD. This effect can be alleviated by the use of a window function on the data prior to the DFT. However, because the choice of window function is arbitrary and affects the results of the calculation, it is difficult to quantitatively compare spectra of different measurements or devices.

Furthermore, the variance of the PSD at a given frequency does not decrease as the number of samples used in the DFT computation increases. In other words, the PSD does not provide any averaging effect: more data results in a finer frequency resolution but not lower in noise. This shortcoming can be partially mitigated by using Welch's method [147] where the data is split in multiple overlapping segments. The DFT analysis is done on each section separately and the results are averaged to obtain the final PSD. The trade off in this averaging process is that each section of the data is shorter and therefore yields a coarser frequency resolution.

Finally, we note that the presence of any frequency drifts that may hinder the analysis of the noise processes are not identifiable in a power spectrum density.

5.1.3 Time Domain Analysis: Allan Variance

Because of the limitation of the frequency domain analysis highlighted in the previous section, in this work, we prefer to perform analysis in the time domain. Time domain analysis generally relies on some type of variance. Unfortunately, for many noise processes commonly associated with frequency fluctuations, the standard variance[1] is found to be divergent [148–150]. This problem can be solved by considering the first difference of the fractional frequencies. This is known as the Allan variance [148] (also known as two-sample variance) and is given by

$$\sigma_y^2(\tau = n\tau_s) = \frac{1}{2(M-1)} \sum_{i=1}^{M-1} \left(\bar{y}_{i+1} - \bar{y}_i\right)^2 \tag{5.7}$$

Here, $\bar{y}_i$ is the i-th mean fractional frequency value of a total number M over the measurement interval $n\tau_s$ where τ_s represents the sampling interval. The Allan variance is similar to the standard variance as it is a measure of the fractional frequency fluctuations, however, it presents the advantage of being convergent for most types of noises [148, 150]. The result is often expressed as the Allan deviation σ_y, given by the square root of the Allan variance $\sigma_y = \sqrt{\sigma_y^2}$. The confidence interval of the Allan deviation is given by $\pm\sigma_y(\tau)/\sqrt{M+1}$ [150].

The Allan variance can be further improved by using all possible combinations of the data set. This is known as the overlapping Allan variance, given by [151]:

$$\sigma_y^2(\tau = m\tau_s) = \frac{1}{2m^2(M-2m+1)} \sum_{j=1}^{M-2m+1} \left[\sum_{i=j}^{j+m-1} \left(\bar{y}_{i+1} - \bar{y}_i\right) \right]^2 \tag{5.8}$$

The overlapping Allan variance greatly improves the statistical confidence for long time scales and is therefore particularly useful for the study of low frequency noise processes [150]. The overlapping Allan deviation is once again obtained by the square root of the Allan variance, $\sigma_y = \sqrt{\sigma_y^2}$. The confidence interval of the overlapping Allan deviation is better than of the normal Allan deviation: even though the additional overlapping differences are not all statistically independent, they nevertheless increase the number of degrees of freedom and therefore improve the confidence estimation [149]. Unfortunately, calculating the number of degrees of freedom is directly dependent on the underlying noise type (or noise types) present in the data set. This makes the calculations of the confidence interval, based on Chi-squared statistics, tedious and non-trivial. Therefore, it is generally accepted to simply estimate the confidence interval with $\pm\sigma_y(\tau)/\sqrt{M-2m+1}$ [149, 150].

The Allan deviation can be interpreted as a measure of stability of a given input, depending on the time interval at which it is observed. For example, an Allan deviation of 1.0×10^{-6} Hz at $\tau = 1$ s should be interpreted as there being an instability in frequency

[1] Here, we define the standard variance as the variations around the average value $\bar{y} = \frac{1}{N}\sum_{i=1}^{N} y_i$ and it is given by $\sigma^2 = \frac{1}{N-1}\sum_{i=1}^{N}(y_i - \bar{y})^2$

between two observations a second apart with a relative room mean square value of 1.0×10^{-6} Hz. For a 10 MHz reference clock, this would correspond to a 1.0 Hz movement in frequency.

5.1.4 Phase and Frequency Fluctuations

Noise processes are commonly divided between phase fluctuations and frequency fluctuations [152]. Because the noise spectra of these two categories of fluctuations differ, it is important to distinguish between the spectrum of phase fluctuations and the spectrum of frequency fluctuations for the correct understanding and analysis of the experimental data. In this section, we introduce the necessary concepts to distinguish between these two categories when measuring superconducting resonators and we justify that, in this work, our measurements are only sensitive to frequency fluctuations.

Barkhausen Relation

In Fig. 5.2 (left), we illustrate that the phase response of a resonator can be assumed to be linear with frequency in the vicinity of the resonance. The linear region of the phase response can be described by the Barkhausen relation [152, 153], which relates the frequency and phase response of a resonator. For an ideal critically coupled resonator of resonance frequency f_r and loaded quality factor Q_l (Eq. 3.20 with $Q_i = Q_c$), the Barkhausen relation is given by:

$$\frac{\delta f}{f_r} = \frac{\delta \theta}{2Q_l} \quad \text{for} \quad \frac{\delta f}{f_r} \ll \frac{1}{2Q_l} \tag{5.9}$$

where δf and $\delta \theta$ are an infinitesimal change in frequency and phase respectively. In the general case, Eq. 5.9 becomes [153]:

$$\frac{\delta f}{f_r} = \frac{Q_i}{8Q_l Q_c} \tag{5.10}$$

Within its range of validity, the Barkhausen relation given by Eq. 5.10 provides a useful relation between frequency and phase of the resonator without making any assumption on the nature of the resonator itself. This relation highlights that under the right conditions, the phase and frequency relation is trivial and phase fluctuations can be reconstructed from frequency fluctuations. Furthermore, the algorithms that calculate the power spectral density and Allan variance, introduced in the previous sections, rely on the Barkhausen relation to be satisfied. It is therefore important to ensure that Eq. 5.10 holds for the devices considered in this thesis.

Leeson Equation

Phase fluctuations in superconducting resonators can be described using the Leeson model [153]. This model, originally developed to describe the phase noise spectrum of

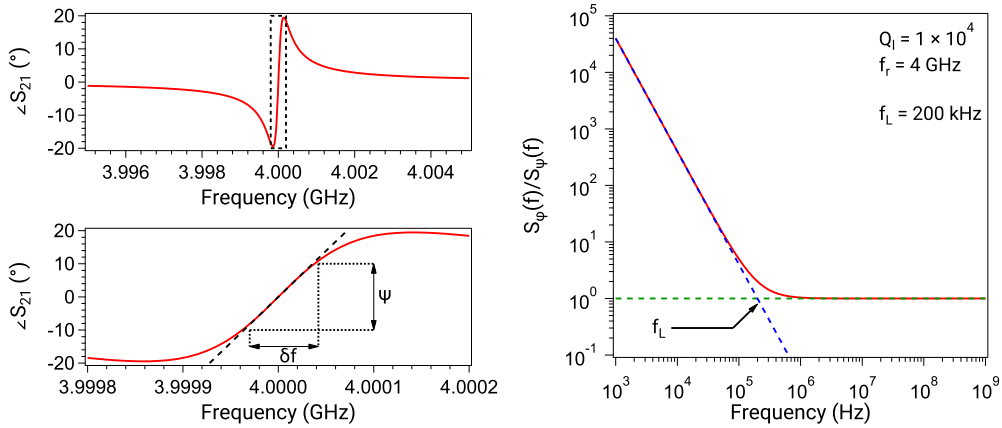

Figure 5.2: **(left)** Typical phase response of a resonator (see chapter 3), calculated for $f_r = 4\,\text{GHz}$, $Q_c = 2 \times 10^4$ and $Q_l = 1 \times 10^4$. The bottom graph is zoomed around the region highlighted in black in the top graph. The phase response can be considered linear in the vicinity of the resonance and we have $\delta f / f_r = \psi / 2Q_l$. **(right)** Leeson phase transfer function of the resonator in the left panel.

feedback oscillators [154], consists of a phase modulator and a resonator in a feedback loop. The phase fluctuations are modeled with the phase modulator that generates a time-varying instantaneous phase $\psi(t)$ and that time-varying phase is then fed through the resonator of loaded quality factor Q_l. Two regimes can be distinguished [152]:

On one hand, for the fluctuations of $\psi(t)$ slower than the inverse of the relaxation time of the resonator $\tau_{ring} = 2Q_l/f_r$, the phase $\psi(t)$ can be considered as a quasi-static perturbation and, therefore, the Barkhausen relation (Eq. 5.9) can be applied. We get:

$$(\Delta f)(t) = \frac{f_r}{2Q_l}\psi(t) \tag{5.11}$$

With this equation, we see that the system responds to slow fluctuations of $\psi(t)$ with frequency fluctuations. These frequency fluctuations are associated with a power spectral density given by

$$S_{\Delta f}(f) = \left(\frac{f_r}{2Q_l}\right)^2 S_\psi(f) \tag{5.12}$$

Using Eq. 5.2, we can calculate the measured phase response at the output of the system with

$$\varphi(t) = 2\pi \int (\Delta f)(t) dt \tag{5.13}$$

From this last equation and Eq. 5.11, we can see this time integration will translate into a multiplication by $1/(jf)$ in the Fourier transform, which, in turn, corresponds to a $1/f^2$

multiplication of the spectrum:

$$S_\varphi(f) = \frac{1}{f^2}\left(\frac{f_r}{2Q_l}\right)^2 S_\psi(f) \tag{5.14}$$

Therefore, in this regime, where the Barkhausen relation applies, the slope of any noise process in the power spectra is changed by -2. This regime is commonly referred to as the *frequency fluctuations* regime.

On the other hand, for the fluctuations of $\psi(t)$ faster than the inverse of the relaxation time of the resonator τ_{ring}, the resonator does not respond to the fast phase fluctuations, no noise regeneration takes place and the instantaneous phase fluctuations are directly mapped to the measured phase fluctuations: we simply directly have $\varphi(t) = \psi(t)$ and $S_\varphi(f) = S_\psi(f)$. This regime is commonly referred to as the *phase fluctuations* regime.

When combining these two regimes into a single expression, we obtain the relationship between the instantaneous phase fluctuations, $\psi(t)$, and the output (measured) phase fluctuations, $\varphi(t)$ for all frequencies. This relationship is known as the Leeson equation and is given by:

$$S_\varphi(f) = \left(1 + \frac{f_L^2}{f^2}\right) S_\psi(f) \tag{5.15}$$

where f_L, the Leeson frequency, corresponds to the inverse of the resonator relaxation time:

$$f_L = \frac{1}{\tau_{ring}} = \frac{f_r}{2Q_l} \tag{5.16}$$

A example plot of Eq. 5.15 is shown in Fig. 5.2 (right). We see that the Leeson frequency corresponds to a cut-off corner frequency below which the Barkhausen relation can be applied and where the measurement is only sensitive to a spectrum of frequency fluctuations.

In this work, we measure devices with resonance frequencies in the range $4 - 8\,\mathrm{GHz}$ and loaded quality factors in the range $1 \times 10^4 - 8 \times 10^5$ (see chapters 11 and 13). Using Eq. 5.16, we calculate that for these devices, $f_L \geq 2.5\,\mathrm{kHz}$. Our experimental data is sampled at 100 Hz, well below f_L, therefore ensuring the validity of Eq. 5.10 and that we always measure the spectrum of frequency fluctuations. Specifically for nanowire superinductor resonators, we have also sampled at 4 kHz, however in these devices $Q_l \simeq 1 \times 10^5$, which corresponds to $f_L \geq 20\,\mathrm{kHz}$ and therefore also well within the validity of the Barkhausen relation.

A rigorous mathematical description and proof of the Leeson model can be found in the chapter 4 of Ref. [152].

5.2 Frequency Fluctuation Processes

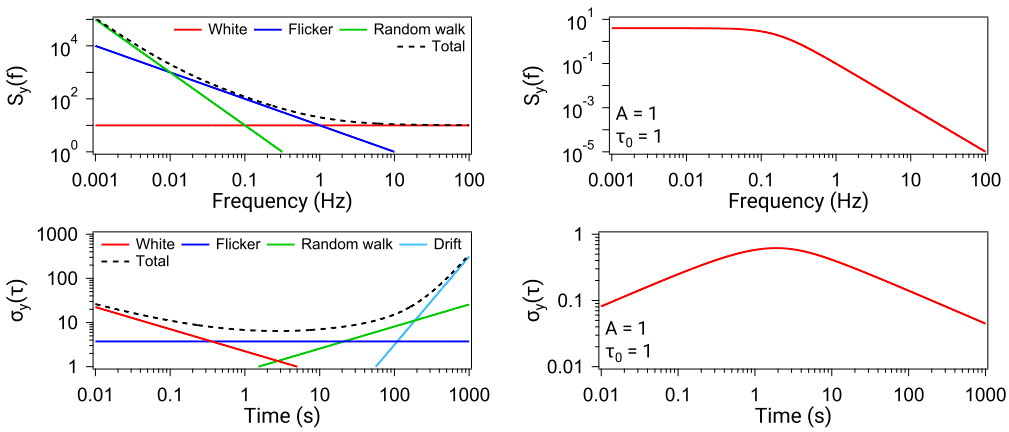

Figure 5.3: Power spectrum S_y (top) and Allan deviation σ_y (bottom) of power law noise processes **(left)** and a Lorentzian noise process **(right)**. We note that only the Allan captures frequency drifts. The power law plots are calculated using $h_0 = 10\,\mathrm{Hz}^{-1}$, $h_{-1} = 10\,\mathrm{Hz}^{-1}$ and $h_{-2} = 0.1\,\mathrm{Hz}^{-1}$.

To understand the frequency stability (or lack thereof) of any given frequency source or resonator, one needs to understand the different mechanisms that lead to the fluctuation of the frequency of the system. Using the statistical tools introduced in the previous section, we can identify various noise process either from a spectral or time domain analysis and quantify their influence on the general frequency fluctuations in the device of interest. In this section, we introduce the common noise processes relevant for this work. A summary of all the noise processes described in the following sections can be found in table 5.1.

5.2.1 Power Law Noise

The analysis of phase and frequency stability of oscillators revealed that the instabilities in most frequency sources can be modeled by a sum of noise processes with a spectral density of the form $S_y(f) \propto f^\alpha$ [148, 150, 152]. These processes are known as power-law noise and can be identified by the slope of the noise spectrum.

In the context of the frequency fluctuations measured in this thesis, the relevant power-law noise processes that can be identified correspond to values of $\alpha \in [-2, 0]$. The shape of the different power law frequency fluctuations noise processes are outlined in Fig. 5.3 (left).

The simplest type of noise, independent of frequency ($\alpha = 0$) and characterised by an amplitude h_0 is commonly known as *white noise* and dominates at high frequencies.

Experimentally, white noise is generally due to shot noise in the measurement electronics. When moving toward lower frequencies, a noise process corresponding to $\alpha = -1$ and of amplitude h_{-1} takes over. This is *flicker noise* (also commonly known as pink or $1/f$ noise). Finally, at even lower frequencies, the noise is dominated by a process with $\alpha = -2$ and an amplitude h_{-2}. This noise process is known as *random walk noise* (and is also known as Brownian or red noise).

The Allan deviation of all these noise processes has been derived by Van Vliet [155] and is summarized in table 5.1.

5.2.2 Lorentzian Noise

For any system that randomly switches between two states 1 and 2 with corresponding discrete values y_1 and y_2, the probability to find the system in a given state i is given by

$$p_i = \frac{\tau_i}{\tau_1 + \tau_2} \tag{5.17}$$

where $i = 1, 2$ and τ_1 and τ_2 are respectively the average time the system spends in state 1 and state 2. The autocorrelation function of this process is given by [156, 157]

$$R(\tau) = H(\tau) p_1 p_2 (y_1 - y_2)^2 e^{-t/\tau_0} \tag{5.18}$$

where $H(\tau)$ is the Heaviside step function and τ_0 is a time constant given by $\tau_0^{-1} = \tau_1^{-1} + \tau_2^{-1}$. Using Eq. 5.5, we can calculate the spectral density of fluctuations and we find

$$S_y(f) = 4 p_1 p_2 (y_1 - y_2)^2 \frac{\tau_0}{1 + (2\pi f \tau_0)^2} \tag{5.19}$$

This spectrum is a Lorentzian function centered at $f = 0$ and of characteristic time constant τ_0 and amplitude $A = \sqrt{p_1 p_2}|y_1 - y_2|$. Similarly to power-law noise processes, the Allan deviation of a Lorentzian noise process has been derived by Van Vliet [155] and is given by

$$\sigma_y(\tau) = \frac{A\tau_0}{\tau} \left(4e^{-\tau/\tau_0} - e^{-2\tau/\tau_0} + 2\frac{\tau}{\tau_0} - 3 \right)^{1/2} \tag{5.20}$$

Experimentally, generation-recombination noise in semiconductor [158, 159] and superconductors [160, 161], and, most importantly for this thesis, parasitic two level system noise [24, 162] are examples of Lorentzian noise processes. Two-level system noise is further discussed in chapter 13 and Papers C and E.

The general shape of a Lorentzian noise process is shown in Fig. 5.3 (right).

Table 5.1: Summary of the expressions for the PSD $S_y(f)$ and Allan deviation $\sigma_y(\tau)$ of the frequency fluctuation noise processes discussed in this chapter.

Frequency noise type	$S_y(f)$	$\sigma_y(\tau)$
White	h_0	$\frac{1}{2}h_0\tau^{-1}$
Flicker	$h_{-1}f^{-1}$	$2\ln(2)h_{-1}$
Random walk	$h_{-2}f^{-2}$	$\frac{(2\pi)^2}{6}h_{-2}\tau$
Linear frequency drift	N/A	$\frac{1}{2}y^2\tau^2$
Lorentzian	$\frac{4A^2\tau_0}{1+(2\pi f\tau_0)^2}$	$\frac{A\tau_0}{\tau}\left(4e^{-\tau/\tau_0}-e^{-2\tau/\tau_0}+2\frac{\tau}{\tau_0}-3\right)^{1/2}$

Chapter 6

Nanofabrication Techniques

In this work, our devices were fabricated using a conventional top-down approach relying on the patterning of thin films via planar lithography and dry or wet etching. In this chapter, we start by discussing the challenges faced with the design and fabrication of the various devices used in the work. Then, in a second part, we present an in-depth description of the various micro- and nanofabrication techniques relevant to this work. Finally, we conclude the chapter with details on the fabrication of our devices and a discussion on the lithographic quality of the fabricated nanowires.

6.1 Fabrication Challenges

6.1.1 Nanowire Superinductors

As described previously, the main devices used in this work are long and narrow nanowires made of a highly disordered superconductor. Due to their dimensions, nanowires are inherently difficult devices to fabricate. Fabricating uniform high-aspect-ratio nanowires, with a length of the order of a millimeter, but a thickness and width of a few nanometers, poses a specific set of constraints on the techniques available. Additionally, because of their microscopic nature, disordered superconductors are not well-behaved materials and present many challenges from a fabrication point of view. Most importantly, disordered superconductors are compound materials and their properties are extremely dependent on the growth conditions, which limits the available deposition techniques and requires a very careful process optimisation.

Combining the constraints of nanowire fabrication with the requirements of disordered superconductors leads to a unique challenge for the researcher and requires an in-depth understanding of nanofabrication in order to find the appropriate process flow at the intersection of both parameter spaces.

Traditionally, nanowires are fabricated by a *lift-off* process (see section 6.2) where a trench at the dimensions of the nanowire is opened in a resist mask before the desired material is deposited (i.e. the resist mask is the negative of final pattern). This approach ensures mechanical stability of the resist mask by only having large areas of resist on the sample. Unfortunately, none of the deposition techniques suitable for disordered superconductors are compatible with such process (see section 6.3).

The alternative approach is therefore to use an *etching* process, where a highly optimised disordered thin film is first deposited on the substrate and then patterned into nanowires using a novel method (see section 6.5). This approach, however, requires the resist mask to be the positive image of the final pattern (i.e. a free-standing, high-aspect-ratio nanowire-shaped resist mask), which is significantly more challenging to fabricate.

After a careful process development, by using a combination of ultra-high resolution negative-tone lithography and a tailored etching process (see section 6.6), we can reliably and reproducibly fabricate high quality disordered superconducting nanowires (see section 6.7).

6.1.2 Superconducting Resonators and Qubits

While comparatively easier to fabricate than nanowires, superconducting coplanar resonators and qubits present their own set of fabrication challenges: quantum circuits are particularly sensitive to noise, as discussed in chapters 4 and 5. These losses originate from defects present at the interface of materials and in the bulk of dielectrics. Furthermore, plasma-based etching processes can lead to damages in the crystalline structure of materials, which will present an additional source of loss.

Therefore, it is particularly important to design the fabrication processes of these devices in such a way as to mitigate the use of materials and techniques that cause loss and decoherence. For example, the use of wet etching is preferred over ion milling or reactive ion etching when possible. Additionally, special care is taken for the cleaning of the substrate and resist residues after each lithography step. Finally, as they are a primary source of loss, the use of any dielectric material should be as limited as possible.

6.2 Lithography Techniques

Any top-down micro- or nanofabrication relies on transferring geometric patterns into the bulk substrate or thin-layers of various materials in a process called *lithography*. For that purpose, a thin-layer of a photon- or electron-sensitive *resist* is spin-coated on the substrate and the casting solvent is evaporated by heating the resist layer in a so-called *baking* step. A pattern is then exposed in the resist with one of the lithography techniques described in this section, and subsequently developed by a dedicated chemical (the *developer*). After a certain amount of energy per unit area is reached (the *exposure dose*), parts of the resist become soluble in the developer and after the development, the resist is only covering parts of the substrate, enabling the transfer of the pattern into the underlying material.

6.2.1 Additive and Subtractive Patterning

Lithography processes can be divided into two different families: subtractive patterning (*etching*) and additive patterning (*lift-off*). In an etching process, a previously deposited layer is spin-coated with resist. After exposure and development, the material in the areas not covered anymore by the resist is etched away (see section 6.5 and Fig. 6.1 (right)). In a final step, the remaining resist is removed. The resulting pattern is therefore the direct image of the areas opened in the resist mask.

In a lift-off process (see Fig. 6.1 (left)), on the other hand, the resist is first spin-coated, exposed and developed. Afterwards, a thin-layer of material is deposited atop. The sample is then immersed in a bath of remover that washes away the resist and the material on top: the thin-layer remains only in the areas where the resist mask was opened, forming this time the negative image of the exposed pattern. It is worth noting that lift-off generally involves two different resists: a so-called *lift-off resist* coated directly on the substrate and a regular resist on top. As shown in figure 6.2, the role of the lift-off resist is to form an undercut under the top resist once developed. Once a new layer is deposited, the presence of the undercut allows remover to enter and dissolve the resist. While an undercut also naturally occurs in most resists, the layer is usually too thin for the undercut to be relevant.

6.2.2 Resists

Resists come in two different flavours: *positive* and *negative*. In the positive case, the solubility in the developer of the exposed resist is greatly increased. In the negative case, the resist is cross-linked in the exposed regions, greatly reducing its solubility.

An important metric of a resist is its *contrast* and is measured by exposing large structures with varying doses. After development for a fixed time (and at a fixed temperature), the remaining resist thickness is measured. The normalised resist thickness against the exposure dose (see Fig. 6.3) is called the contrast curve. The contrast γ of the resist is defined as the slope of the contrast curve by

$$\gamma = \left[\log\left(\frac{D_1}{D_0}\right)\right]^{-1} \tag{6.1}$$

where D_0 is the threshold dose at which the exposure first begins to have an effect. For a positive resist, D_1 is the clearing dose: the minimum exposure dose required to completely remove the resist. In the case of a negative resist, D_1 represents the dose at which the resist has a useful working thickness. It is important to note that γ is not a constant for a particular resist, but rather depends on the process parameters, such as the development chemistry, bake times and temperatures before and after (if applicable) exposure, etc...

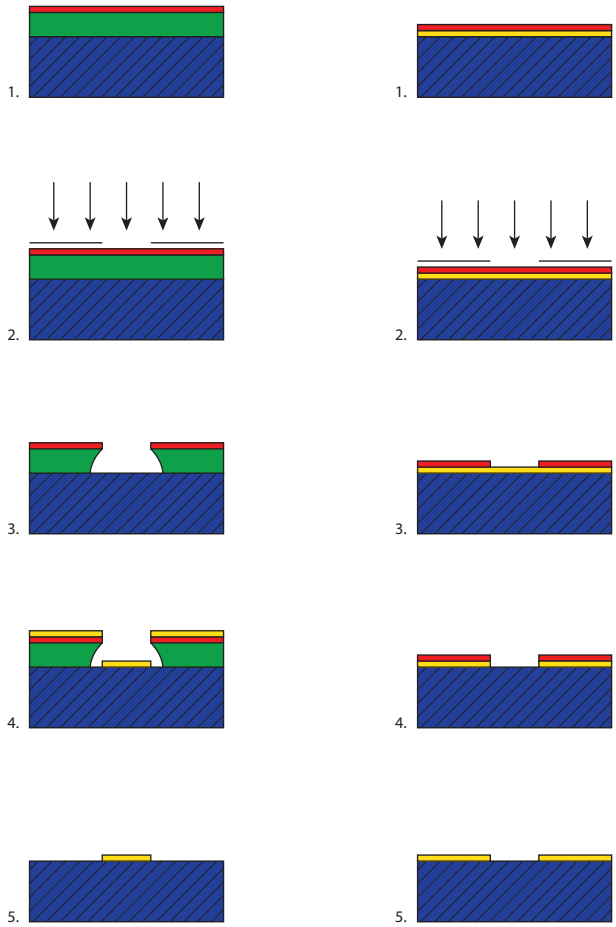

Figure 6.1: **(left)** Lift-off process: Lift-off resist (green) and a positive photoresist (red) are spin-coated on a substrate (blue) (1). The resist is then exposed through a mask (2) and developed (3). A metal layer (yellow) is then deposited on top (4). After the substrate is placed in remover, metal remains only where the resist was originally exposed (5). **(right)** Etching process: A positive photoresist is spin-coated on a substrate covered with a thin film (1), the resist is then exposed through a mask (2). After development, only the unexposed resist remains (3). The uncovered metal is then removed in an etching process (4). Finally, the remaining resist is removed and metal remains in the unexposed area (5).

Contrast curves find their origin over one hundred years ago when Hurter and Driffield (H-D) measured the optical density of photographic negatives as a function of log-exposure [163]. Micro- and nanolithography processes evolved from photographic science and borrowed many of its concepts, including H-D contrast curves. Fig. 6.3 shows typical H-D contrast curves for both positive and negative resists. These curves are calculated with the simple - yet accurate - theoretical model proposed by Ziger and Mack [164, 165]. For positive resists, the colored region illustrates a phenomenon known as *dark erosion*

Figure 6.2: **(left)** With the presence of the undercut, the metal layer (yellow) is not continuous and allows the remover to access the resist. **(right)** Without the undercut and lift-off layer, the metal forms a continuous layer on top and remover can't access the resist.

where the dose is too small to properly define features in the resist but enough for it to start being dissolved by the developer. For a negative resist, the colored zone corresponds to the *bright erosion* region, where the resist is entirely cross-linked by the exposure, yet still dissolved by the developer. Because dark erosion (bright erosion) translates into a loss of thickness of the resist (and reduced contrast), it is generally an unwanted effect. It can however be mitigated by carefully optimizing the resist baking procedure and developer composition.

Understanding the contrast curve, contrast and exposure doses of a resist for given process parameters is of paramount importance to ensure a high quality reproducible lithography.

Organic resins

The most common positive photoresists are based on a mixture of DNQ (Diazonaphthoquinone) and Novolac resin (Phenol formaldehyde resin). The DNQ inhibits the dissolution of the Novolac resin, however, upon exposure to ultra-violet (UV) light, the DNQ undergoes a Wolff rearrangement and forms a ketene [166]. The ketene, in turn, reacts with ambient water to form an indene carboxylic acid, soluble in aqueous base. In these regions, the dissolution of the Novolac is no longer prevented and is therefore also washed away by an aqueous base. Novolac resins can also be used as negative-tone resists, where the exposure directly cross-links the resin, sometimes with the aid of a cross-linking agent to enhance the sensitivity of the resist.

Novolac-based resists are developed by dissolution in a basic solution. Most commonly, metal ion free TMAH (tetramethylammonium hydroxide) aqueous solutions or metal ion bearing KOH and NaOH concentrate aqueous alkaline solutions are used.

Alternatively, organic resins are used in conjunction with a so-called photoacid generator. When exposed to short wavelength particles, the photoacid generator decomposes into an acid. When the resist is subjected to a post-exposure bake, the acid diffuses in the resist and reacts with blocking groups in the polymer resin, causing it to become soluble in a basic solution. Because of this intermediate reaction step compared to DNQ-Novolac resists, these resists are called *chemically amplified resists* (CAR). CAR resists are commonly used for positive deep-UV (DUV) and low resolution electron beam lithography.

For high-resolution lithography, PMMA (poly(methyl methacrylate)) is by far the most

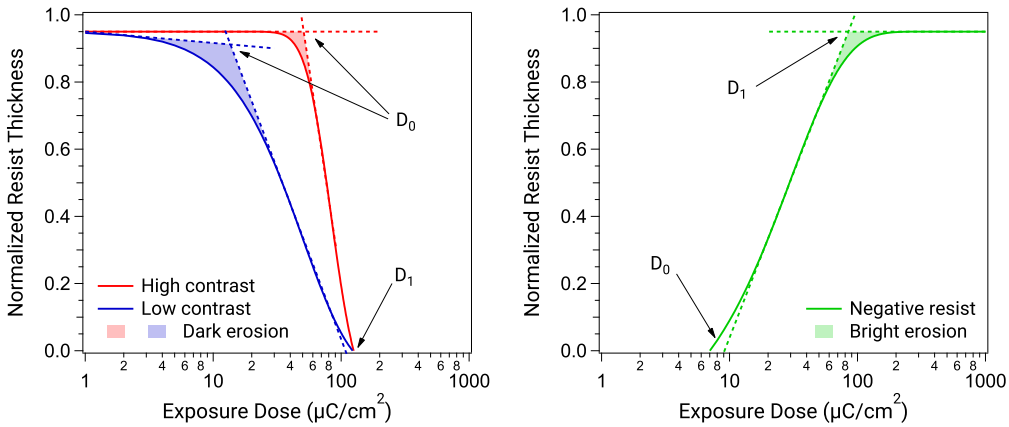

Figure 6.3: **(left)** Contrast curves for a typical high contrast (red) and low contrast (blue) positive resist. **(right)** Contrast curve for a negative resist. In both pictures, the contrast defined by Eq. 6.1 is given by the slope of the contrast curve between D_0 and D_1.

popular positive-tone electron beam lithography resist. Exposure of PMMA causes scission of the polymer chains, increasing their solubility in the developer - typically a mixture of MIBK (methyl isobutyl ketone) and Isopropanol. PMMA is often used in conjunction with copolymer MMA. The vastly different development speeds allow the formation of controlled undercuts for lift-off processes (see section 6.2.1 below) or, for example, the formation of T-shaped gates for HEMT applications. Fig. 6.4 (left) shows a typical contrast curve for PMMA.

Hydrogen Silsesquioxane (HSQ)

Hydrogen silsesquioxane (HSQ) is a well-investigated negative tone inorganic resist [167, 168] known for its high contrast, ultra high-resolution ($< 10\,\text{nm}$) electron beam lithography (EBL) capabilities [169] and its stability against dry etching [170]. Like many high-resolution resists, HSQ requires an exposure dose of the order of $8\,\text{mC/cm}^2$. This dose is one to two orders of magnitude larger than typical exposure doses and makes the use of HSQ unrealistic for large features. However, thanks to its very high contrast and chemical composition, HSQ will not be subject to over development, therefore, prior to any etching step, one can spin another resist and do a subsequent lower resolution/lower dose lithography step.

The HSQ molecules consist of a cage-like structure with a silicon atom at each corner with a hydrogen atom covalently bonded to them. The edges of the cage are formed by oxygen atoms resulting in the stoichiometric formula $\left(\text{HSiO}_{3/2}\right)_8$ for a unit cell as depicted in Fig. 6.4 (right). The high resolution capabilities of HSQ result from its small molecule size and exposing HSQ with accelerated electrons leads to cross-linking of the unit cells via breaking Si-H and Si-O bonds and forming new Si-O-Si bridges [171].

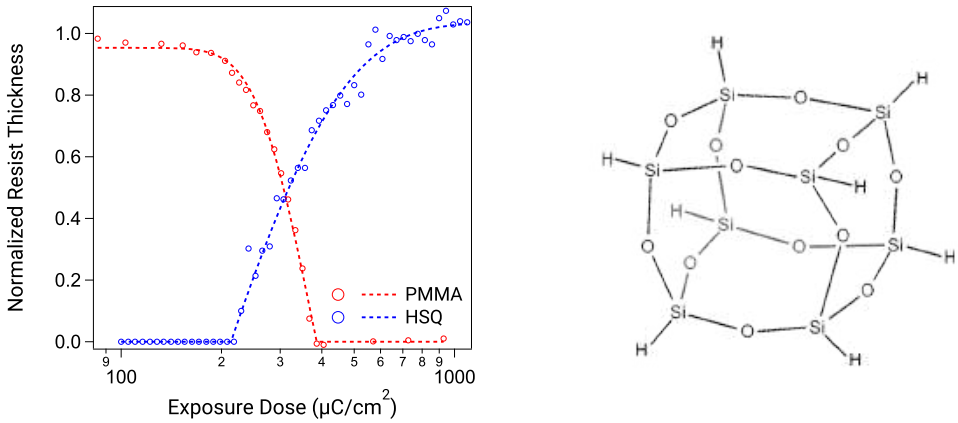

Figure 6.4: **(left)** Experimentally measured contrast curve, with fits, of PMMA (red) and HSQ (blue) used in this work. The corresponding spinning, baking and development parameters can be found in appendix A. **(right)** Schematic picture of the cage-like HSQ molecule.

Three different processes are commonly used to develop HSQ. The first two consist of TMAH aqueous solutions, either a low concentration (less than 3%) or high concentration (more than 25%), respectively known as low- and high-contrast developers. Lastly, HSQ can also be developed by the so-called salty developer, consisting of aqueous solution of sodium hydroxide (NaOH 1%) and sodium chloride (NaCl 4%). Fig. 6.4 (left) shows a typical contrast curve for HSQ.

Because of the extremely high exposure dose required to form the hardened cross-linked HSQ mask and the proximity effect (see section 6.2.5 for more details), a common problem with HSQ is the formation of small agglomerates of partially exposed resist that are not completely dissolved during development. These small particles tend to accumulate on the edges of developed structures and act as micro-masks when the pattern is etched. Due to the inorganic nature of HSQ, these agglomerates cannot be removed by descumming in an oxygen plasma (see next section), but their formation can be mitigated by a careful optimisation of the resist development [172].

Resist Descumming (Ashing)

When using organic resists, it is not uncommon to find resist residues in the developed areas or on resist edges. Such residues can greatly affect the quality of the etching by acting as small "micro-masks": the residues locally protect the surface to be etched, leading to a large surface roughness of the etched layer. Fig. 6.5 (left) shows a typical example of the effect of micro-masking on an etched layer. In a lift-off process, these residues will get trapped under the subsequently deposited layer. If the device is heated again, the residues will reflow and greatly affect the uniformity of the layers deposited atop as depicted in Fig. 6.5 (right).

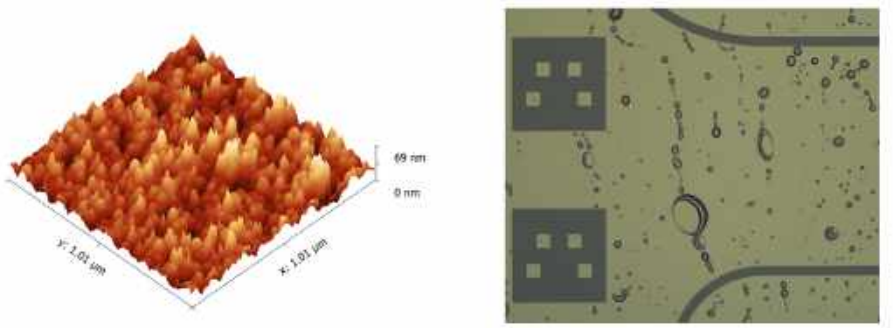

Figure 6.5: **(left)** Atomic force microscope micrograph highlighting the high surface roughness of a Si substrate after micro-masking. **(right)** Optical microscope picture of bubbles of reflowed resist underneath a gold layer after an improper substrate cleaning.

To prevent these unwanted situations, right after development, the wafer is placed in a mild oxygen plasma (10 W to 50 W) for a few seconds. The oxygen ions strongly react with any organic material, effectively removing the residues. However, this process affects the entire resist layer: it is therefore important to consider the resist etching rate and carefully choose the duration of the ashing step for an optimal result. Alternatively, for extremely thin layers of resist or sensitive materials, resist can be ashed in an ozone chamber instead.

In the specific case of HSQ and other spin-on glass resists, an oxygen plasma step can be done to strengthen the resist mask against reactive ion etching: the oxygen ions in the plasma increase the density of the silicon oxide mask.

Resist Removal

A strong oxygen plasma (> 100 W) can be used to strip organic resists very efficiently, however this is not always suitable if other parts of the device are sensitive to oxygen or oxidation (for example in the case of graphene based devices). Alternatively, most exposed and unexposed organic resists can be washed away using certain solvents.

NMP (N-methyl-2-pyrrolidone) based removers offer the greatest effectiveness for removal of most organic resists, however, NMP is highly toxic and is listed as a Substance of Very High Concern (SVHC) by the European Union [173]. Therefore, several safer alternatives have been developed, however with greatly reduced effectiveness for the removal of strongly cross-linked resists. For sensitive devices, a more gentle (but less efficient) resist removal can be done using acetone.

In the specific case of HSQ and other spin-on glass resists, the silicon oxide mask can be

removed either by dry etching in fluorine chemistry or by wet etching using hydrofluoric acid (HF).

6.2.3 Contact Photolithography

Contact lithography is performed in a tool called *mask aligner*. Such a system consists of an intensive UV light source, an optical microscope, a mask holder and a precision stage on which the substrate to be exposed is located. The microscope and the stage can be used to align the mask to preexisting features on the sample. Masks are typically made of a thin chromium layer patterned with the desired circuit layout on top of a soda lime or quartz glass substrate. During the exposure, the UV light shines on the mask and exposes the resist in the areas opened in the chromium mask.

The theoretical minimum feature size d_{min} is given by [174]

$$d_{min} = \frac{3}{2}\sqrt{\lambda\left(g + \frac{1}{2}h\right)} \tag{6.2}$$

where λ is the wavelength of the UV light source, g is the gap between the mask and the photoresist and h is the thickness of the resist.

At a resist thickness of 500 nm and assuming a perfect contact between the mask and the resist ($g = 0$), for $\lambda = 365\,\text{nm}$ (i-line), we obtain $d_{min} \simeq 450\,\text{nm}$. Realistically, accounting for imperfections in the resist thickness and mask contact, resolutions of the order of 700 nm to a micrometer are achievable in contract lithography. In a similar way, for DUV lithography, at $\lambda = 240\,\text{nm}$, $d_{min} \simeq 350\,\text{nm}$. Once again, taking into account imperfections in the aligner and the process, a practical resolution is of the order of 500 nm.

These resolutions are suitable for most microfabrication processes, however, while contact lithography excels in speed (an exposure is done in a matter of seconds), it severely lacks in flexibility: masks are costly to produce and only last for a limited number of exposures. Moreover, in a research environment where designs often change, it is unrealistic to make a new mask every time.

6.2.4 Maskless Photolithography

A popular alternative to mask aligners for optical lithograhy are the so-called *direct write* system where a high resolution laser is used to expose photoresist. Laser writers are typically used for photomasks and stepper reticles production, but can also be used for maskless direct patterning of substrates. Because they eliminate the need for a mask, laser writers offer tremendous flexibility and are of great interest in a research environment.

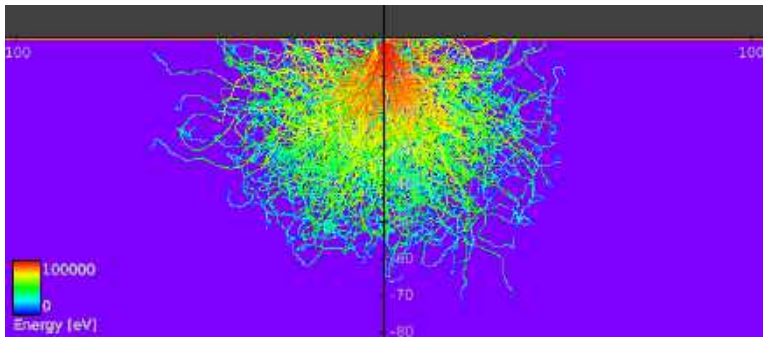

Figure 6.6: Simulated trajectories of electrons penetrating a 400 nm thick PMMA 950k A6 layer on top of a Silicon substrate. The simulation is carried out for an acceleration voltage of 100 kV. The color scale represents the electrons energies.

The minimum achievable feature size is comparable to standard UV contact lithography ($\sim 1\,\mu m$) and writing speeds are typically around $100\,mm^2/min$.

6.2.5 Electron Beam Lithography

While photolithography is a fast and cost-effective process, it is however limited in resolution as detailed in the previous sections. To overcome this resolution limit, an e-beam lithography (EBL) system can be used. An EBL system consists of an electron gun, a collimator, magnetic lenses, beam blanker and deflecting coils [175]. In the electron gun, electrons extracted from a filament are accelerated by an electric field. This stream of electrons is then focused by the collimator and magnetic lenses. The position of the focused electron beam can then be controlled using the deflecting coils. By raster or vector scanning the beam over the surface of a substrate covered with a resist sensitive to electrons, a pattern can be directly written without the need of any mask.

The wavelength of the electrons is given by the de Broglie's relation [176]

$$\lambda_e = h/p_e = \frac{h}{\sqrt{2m_e\varepsilon_{kin}}} \tag{6.3}$$

where $p_e = \sqrt{2m_e\varepsilon_{kin}}$ is the momentum of the electrons, m_e the mass of the electron and ε_{kin} the kinetic energy of an electron. At an acceleration voltage of 100 kV (ie. a kinetic energy $\varepsilon_{kin} = 100\,keV$), the wavelength of the electrons is on the order of $\lambda_e = 4\,pm$. This makes electrons the ideal candidate for ultra-high resolution applications. In fact, in practice, resolution in an EBL system is not limited by the wavelength of the electrons but by technical limitations of the collimator and coils to focus the beam spot size below a few nanometers.

When the beam electrons (primary electrons) reach the sample, they scatter inelastically with the resist or substrate atoms and generate secondary electrons that cause a beam

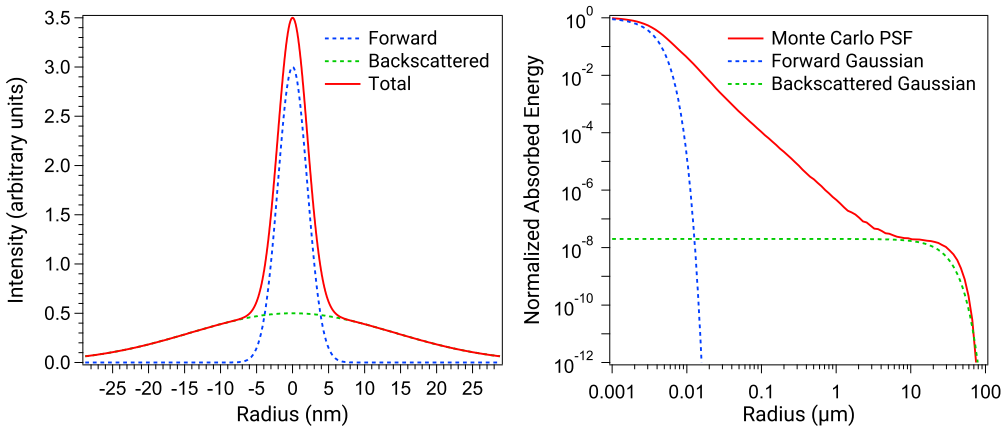

Figure 6.7: **(left)** Example of a double Gaussian distribution approximation of both forward traveling and backscattered electrons. **(right)** Monte Carlo simulation at 100 kV of the point spread function normalised to the absorbed energy at $r = 0$ for a stack of 400 nm PMMA / 20 nm NbN / 250 µm Si. The dashed lines represent the corresponding double Gaussian approximation.

broadening (forward scattering). Electron trajectories in the resist and substrate can be simulated using Monte Carlo simulations as shown in Fig. 6.6. The low energy ($\sim 50\,\text{eV}$) secondary electrons are responsible for the exposure of the resist.

Higher acceleration voltages reduce the forward scattering angles and therefore increase the resolution, however at high kinetic energies, the primary electrons are likely to elastically scatter on the substrate atoms at large angles. Because of their high energies, these backscattered electrons can in turn scatter into secondary electrons and expose the resist outside of the intended region. This unwanted exposure is known as the *proximity effect*.

In an EBL system, the deflecting coils are used to direct the beam off-axis, but the maximum deflection distance is limited since any motion too far from the center causes aberrations that deteriorates the spot geometry and affects resolution. The maximum area within which the system can write without any appreciable decline in resolution is called a *write field*. The deflection system is generally controlled by the pattern generator, usually at a resolution of 16 bits or higher, and each possible position within the write field is placed on a grid on which the beam can jump. The *beam step* δ is an integer multiple of the grid size and corresponds to the distance between each beam movement during a given exposure. The exposure dose received by the resist, defined as the total charge deposited in the resist per unit area, can therefore be calculated by

$$D = \frac{I_{beam}\tau_{dwell}}{\delta^2} \tag{6.4}$$

where I_{beam} is the beam current and τ_{dwell} is the exposure time of a single pixel. By controlling the dwell time τ_{dwell}, the exposure dose received by the resist can be changed.

If one is able to accurately predict the effective dose received by a given area of resist, the proximity effect due to the beam broadening and backscattering can be compensated by adjusting the exposure dose on the fly. Simulations of the electron trajectories as depicted in Fig. 6.6 allows the calculation of the *point spread function* which describes the deposited energy induced by forward and backward scattered electrons. Because Monte Carlo simulations are computationally intensive, the point spread function has traditionally been approximated by the sum of two Gaussian functions, however this model is limited and does not describe well the behaviour of modern systems with high acceleration voltages. Fig. 6.7 (left) shows an example of the effective contributions of both traveling and backscattered electrons in the two-Gaussian approximation. Fig. 6.7 (right) gives a comparison between the point spread function calculated using a Monte Carlo simulation and the two Gaussian model: while good agreement is obtained for small and large radii, the middle region is not correctly captured by the model.

The simulated point spread function can be taken into account during the pattern preparation in a step called *proximity effect correction* where the dose at every beam step is modulated accordingly. Fig 6.8 shows examples of a pattern exposed with proximity correction. Each colored region corresponds to a different modulated exposure dose.

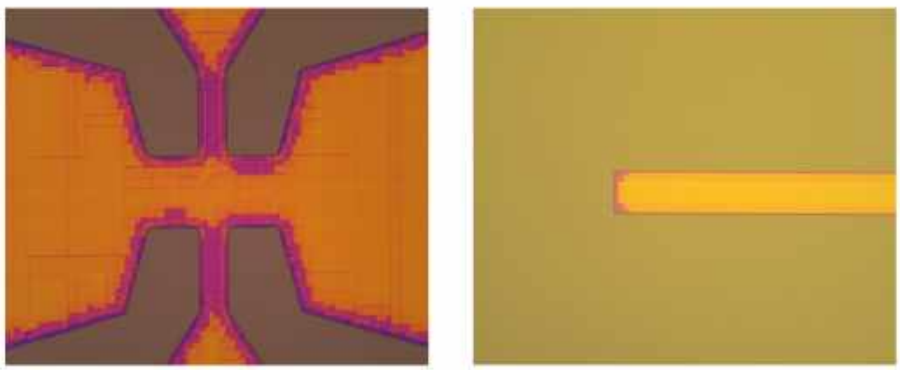

Figure 6.8: Optical micrograph examples of electron beam lithography resist exposed with proximity effect correction. Each colored region corresponds to a different exposure dose in the resist.

6.3 Thin-film Deposition: Sputtering

Sputtering is a common thin-film deposition technique suitable for a broad selection of materials, ranging from metals to dielectics. As with any thin-film deposition technique, sputtering offers both advantages and drawbacks. For example, sputtering allows for the uniform deposition of ultra-thin films - down to a thickness of a few nanometers - but the substrate significantly heats up during the process, making it virtually impossible to

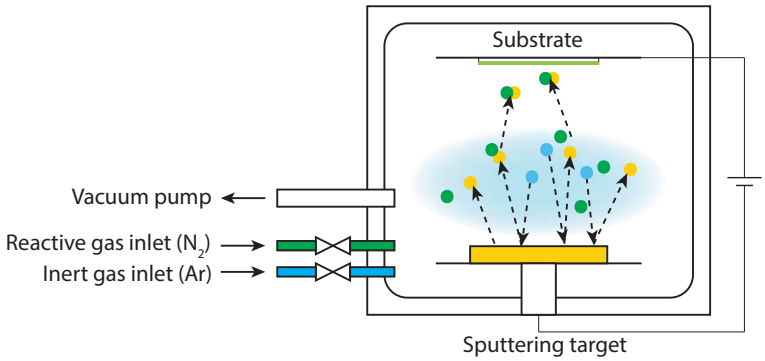

Figure 6.9: Schematic diagram of a typical DC magnetron sputtering system. The argon ions (blue dots) collide with the sputtering target and eject niobium atoms (yellow dots). The niobium atoms react with the nitrogen ions (green dots) and form niobium nitride that then deposit on the substrate.

deposit a film on resist mask for a lift-off process. Sputtering offers a unique range of parameters that can be tuned to affect the properties of the resulting thin film: thickness, stoichiometry, epitaxial to disordered layers, compound materials...

The substrate is loaded in a vacuum chamber and placed directly in front of the source of the material to be deposited (the *sputter target*). A controlled flow of a high-Z neutral gas (typically argon) is let in the chamber and a DC voltage bias is applied, creating a plasma above the target. In the plasma, the argon ions are bombarded in all directions at high velocities. When an ion collides with the sputter target, it transfers its momentum to the surface and one or more atoms of the target are ejected. If the substrate is in the path of the ejected atoms, they will nucleate on the surface and form a thin film. In addition to the sputtering gas, a reactive gas can be introduced in the chamber. The reactive gas is ionized as well and the ions reacts with the ejected atoms, forming compounds, before they reach the substrate. This process is called *reactive sputtering* and the stoichiometry of the deposited film can be controlled by manipulating the partial pressure of the reactive gas in the chamber.

A metallic lid (the *shutter*) is used to obstruct the path between the target and the substrate to prevent deposition. The shutter is used at the start of the process, until the conditions in the chamber are stable, and once the target thickness is achieved. Fig. 6.9 shows a schematic view of a typical DC-magnetron sputtering chamber with a reactive gas inlet.

6.4 Thin-film Deposition: Electron Beam Evaporation

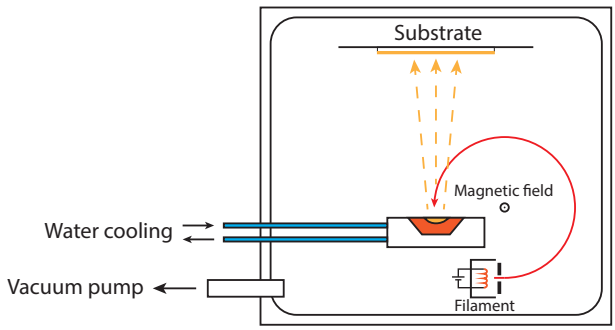

Figure 6.10: Schematic diagram of a typical e-beam evaporation system. The electrons emitted from the filament are directed toward a water cooled crucible with a magnetic field. The material in the crucible heats up in contact with the electrons and evaporates.

Evaporation is another well-established technique routinely used for thin-film deposition. In an evaporator, the substrate is loaded in a vacuum chamber, in front of a crucible loaded with an ingot of the material to be deposited. Inside the chamber, a tungsten filament biased with a high voltage (typically $\simeq 10\,\mathrm{kV}$) emits electrons that are focused on the material inside the crucible using a magnetic field. The material heats up and once a sufficiently high temperature is reached, melts and evaporates. The vapor condenses on the substrate and forms a thin-film. The evaporation rate is directly dependent on the temperature of the material, which can be controlled by varying the current in the filament and water cooling of the crucible. A quartz crystal is used to monitor the deposition rate of the material [1] and a feedback loop ensures stable deposition conditions by controlling the beam current accordingly.

In a similar way to a sputtering system, evaporators are equipped with a shutter between the crucible and the substrate to prevent unwanted deposition. After ramping up the source to stable deposition conditions, the shutter is opened to let the material reach the substrate. Once the desired thickness is reached, the shutter is closed and the source is slowly ramped down. Finally, in some evaporators, the substrate holder can be tilted and rotated which allows advanced deposition techniques such as *double angle evaporations* described in the following section. Fig. 6.10 shows a schematic view of a typical evaporator.

[1] When some material is deposited on the quartz crystal, the material adds weight to the crystal and changes its resonance frequency. By measuring the frequency shift with a frequency counter, the deposition rate can be calculated.

6.4.1 Double Angle Evaporation

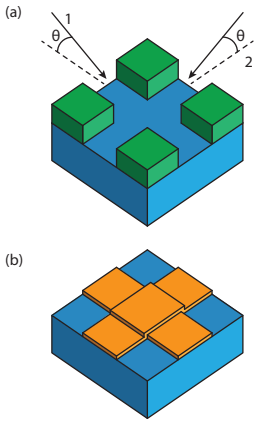

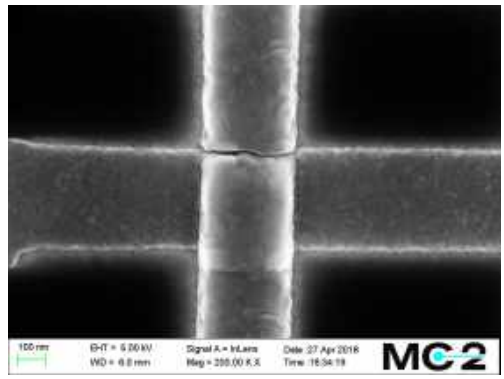

Figure 6.11: **(left)** Schematic diagram of the Manhattan double angle evaporation process. A cross shape is opened in the resist (green) and metal is evaporated at a steep angle in two opposite directions (a). After lift-off, the metal (orange) forming the junction remains (b). **(right)** SEM micrograph of a Josephson junction fabricated with the Manhattan technique. (Image courtesy of A. Fadavi Roudsari)

Josephson junctions rely on the presence of a thin dielectric barrier between two superconductors (see chapter 2.5). A common method to fabricate such a junction is to first evaporate a thin aluminium film, let it oxidise and then deposit another layer of aluminium on top. In order to achieve good control and reproducibility of the junction properties, the oxidation step is realised in-situ in the system by allowing a controlled amount of oxygen into the evaporation chamber.

In this work, the Josephson junctions are fabricated using the bridge-less "Manhattan" technique [177–179] which is an alternative to the more traditional Dolan bridge technique [180, 181]. In this process, the junctions are fabricated using a combination of high aspect ratio resist and evaporating metal at two distinct large angles: if the angle is large enough ($\tan(\theta)$ smaller than the resist thickness), no metal can reach the bottom of the trench. First, a resist mask consisting of a cross pattern is exposed and developed, after which a first metal layer is evaporated, at a large angle, in the direction of an arm of the resist cross. After the first evaporation, the metal layer is oxidised, the substrate is then rotated by 90°and another evaporation takes place to form the top contact and the junction. A lift-off is then used to remove the unwanted metal. A summary of the fabrication steps of a Josephson junction using the Manhattan technique and a SEM picture of fabricated device are shown in Fig. 6.11.

This technique offers several advantages over the Dolan bridge technique. Most notably, the junction size only relies on the accuracy of the lithography of the cross pattern and not on the thickness of the resist and the thermal and mechanical stability of the resist bridge. Using state of the art electron beam lithography and high resolution resists, highly

reproducible junctions can be fabricated [182, 183].

6.5 Etching Techniques

After lithography, material is chemically and/or physically attacked and eroded in areas not covered by a resist mask in an *etching* process. Etching processes can be divided in three families: *ion milling*, *reactive ion etching* and *wet etching*. In the following section, a brief description of the etching techniques relevant to this work can be found.

6.5.1 Ion Milling

Ion milling is a physical etching technique in which ions of an inert gas (typically Ar) are used to remove material from a substrate to some desired depth. When leaving the source, the ions are collimated into a wide beam by the *screen grid* and accelerated toward the surface of a substrate by the *acceleration grid*. When reaching the surface, the atoms from the material to be etched are sputtered away. In a naive picture, ion milling can be compared to sandblasting with ions. Fig. 6.12 shows a schematic of a typical ion milling system.

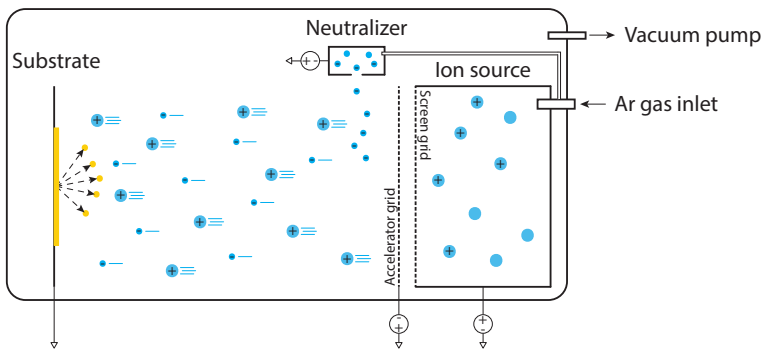

Figure 6.12: Schematic diagram of a typical ion beam etching system. The argon atoms are ionized in the source and accelerated toward the substrate. The neutralizer emits electrons to balance the charge in the beam. When the argon atoms reach the substrate, the surface atoms are sputtered away.

Because of the directionality of the beam, ion milling is a highly anisotropic etching technique. Moreover, due to the mechanical nature of the process, ion milling does not suffer from potential unwanted chemical reactions and is a suitable etching method for any material, however at the cost of a low selectivity to the mask. Additionally, the main drawback of ion milling is the redeposition of the sputtered atoms on the sidewalls of the resist mask, leading to the formation of "fences" after the resist is removed (see Fig. 6.13). This can be mitigated by rotation the substrate and etching at an angle, but at the cost of sloped etch profile.

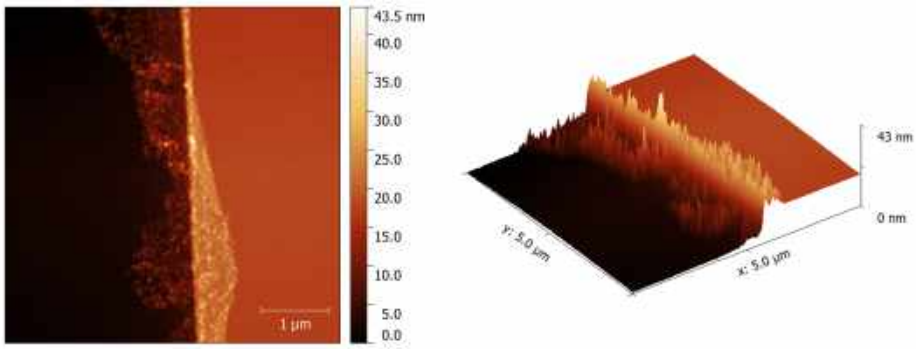

Figure 6.13: AFM micrographs of redeposition after ion milling of NbN. The large surface roughness observable near the side wall are redeposition fences that collapsed when the resist was removed.

6.5.2 Reactive Ion Etching

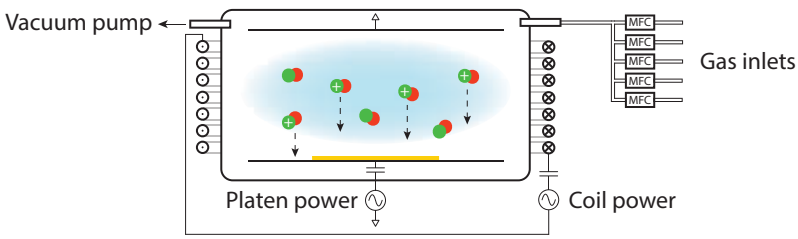

Figure 6.14: Schematic diagram of a typical reactive ion etching chamber. The reactive gas flows are controlled by several mass flow controllers (MFC) and the vacuum pump regulates the pressure in the chamber. The platen and ICP sources provide the necessary RF power to create a plasma. Due to the negative charge build up on the substrate platen, the ions drift toward the substrate and react with the surface, etching it away.

Reactive ion etching (RIE) is a popular type of dry etching that uses chemically reactive plasma to remove material on substrates. A RIE system consists of a vacuum chamber equipped with parallel electrodes AC coupled to a voltage source through a matching network. The substrate to be etched is loaded on the bottom electrode (the *platen*). A small inlet lets a controlled flow of one or more process gas into the chamber. During a process, the pressure in the chamber is a few mTorr and is controlled by a throttle valve placed in front of the vacuum pump. A plasma is initiated in the chamber by applying a strong radio frequency (RF) electromagnetic field to the platen.

The oscillating electric field ionizes the process gas molecules by stripping them of electrons. In each cycle of the field, the electrons are electrically accelerated up and down in the

chamber and at the same time, the much more massive ions move relatively little in response to the RF electric field. When electrons are deposited on the substrate platen, this causes the electrode to build up a charge due to its DC isolation. This charge build up translates to a large negative voltage on the platen, typically around a few hundred volts, while the plasma itself develops a slightly positive charge due to the higher concentration of positive ions compared to free electrons.

Because of the large voltage difference, the positive ions tend to drift toward the wafer platen, where they collide with the samples to be etched and react chemically with the materials on the surface of the samples. Heavy ions can also sputter some material by transferring some of their kinetic energy. Due to the mostly vertical delivery of reactive ions, reactive ion etching can produce highly anisotropic etch profiles.

Additionally, a coil can be wound around the chamber and the plasma can be generated by an RF powered magnetic field inductively coupled into the chamber. Inductively coupled plasma (ICP) can be much denser than platen generated plasma, however, due to the lack of negative charge build up, the etch profiles produced will be isotropic. ICP and platen plasma can be combined to benefit from the high density of the ICP and the directionality due to the bias.

Etch conditions and profiles in an RIE system depend strongly on the many available process parameters, such as pressure, gas flows, and RF power. Fig. 6.14 shows a schematic view of a typical RIE system.

6.5.3 Wet Etching

Wet etching is a form of chemical etching where the material to be etched is immersed in a solution containing a liquid etchant that chemically attacks the material to be etched. The rates of wet chemical reactions are decided by the reactivity of the surface: if the surface reaction is slow, it determines the rate. On the other hand, if the surface reaction is fast, it is the availability of the etchant that will limit the rate. Wet etching processes are typically characterised by a high selectivity but poor anisotropy, however, certain surface reaction-limited processes, such as the etching of Silicon in KOH, can exhibit large anisotropy. The main two wet etching processes used in this work are described below.

HF Cleaning of Silicon Surface

Silicon oxide naturally grows on any silicon surface over time and therefore, any silicon substrate stored in an atmosphere containing oxygen will eventually be passivated with a thin silicon oxide layer. This silicon oxide layer is generally unwanted (see chapter 4) and needs to be removed prior to any further processing. This can be achieved using a solution of diluted hydrofluoric acid (generally 1% or 2%). HF cleaning removes the SiO_2 and leaves the surface oxide-free, hydrogen-terminated and hydrophobic.

In a low oxygen atmosphere (≤ 0.1 ppm), the hydrogen-terminated surface can last for several weeks without the formation of any native oxide layer. In normal cleanroom atmosphere, however, the native oxide will rapidly regrow and a 0.5 nm layer of native oxide will cover the surface within a few hours [184].

Wet Etching of Aluminium

Plasma etching of aluminium can be done using chlorine-based chemistries, however, this process suffers from several drawbacks. First of all, the etching of alumium in Cl_2 is isotropic. The anisotropy can be increased by replacing Cl_2 with $CHCl_3$, $CFCl_3$ or CCl_4 to form so-called sidewall inhibitors consisting of carbon-based polymer chains that cover the sidewalls and prevent the etchant to reach and attack the material. Unfortunately, these polymer chains are usually hard to remove after the etch and leave unwanted residues. Moreover, Cl-based plasma etch leads to the formation of many volatile byproducts that can lead to the corrosion of the etched Al when exposed to ambient atmosphere: any residual Cl can react with the water moisture present in the air and form HCl, which in turn will etch aluminium.

The preferred alternative is to use a 80:4:16 solution of phosphoric acid, nitric acid and water (or alternatively acetic acid to buffer the solution) to wet etch aluminium. This solution is commercially known as Transene aluminium etchant type A. The phosphoric acid reacts with the passivating oxide (Al_2O_3) present at the surface and exposes bare aluminium. In turn, the nitric acid reacts with the oxide-free surface to reform a new layer of Al_2O_3 that is then etched away by the phosphoric acid. This process repeats until depletion of all the aluminium or until the process is stopped in a rinsing bath. The process is summarised by the following balanced equation:

$$7\,Al + 5\,HNO_3 + 21\,H_3PO_4 \longrightarrow 7\,Al(H_2PO_4) + 13\,H_2O + 2\,N_2 + NO_2 \tag{6.5}$$

6.5.4 Etching of disordered NbN

Disordered materials such as niobium nitride are challenging to etch. Traditionally, nitrides are dry etched in RIE using fluorine chemistry gas such as SF_6, NF_3 or CHF_3. However, the etching rates of Nb and NbN with these chemistries greatly differ (by almost a factor of 10). In the case of disordered NbN, grains may have slight variations in stoichiometry, resulting in small to large variations in the etching speed. In a similar way to improperly cleaned resist, this manifests itself by a micro-masking effect and leads to a large surface roughness. Ion milling is not suitable either due to redeposition and the need for sharp etch profiles

To overcome these issues, we developed a "best of both worlds" etch process of disordered NbN using an in-situ combination of a highly anisotropic physical Ar etch with a mild RIE at a low concentration of Cl_2. Low gas pressures allow for good anisotropy due to a high DC bias in the RIE chamber. Additionally, with careful tuning of the reactive

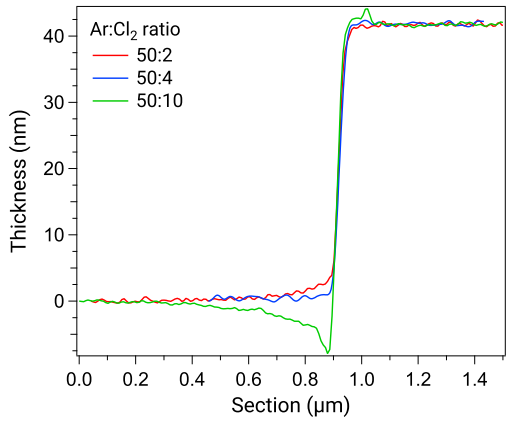

Figure 6.15: Cross section of AFM scans of the etched profile of NbN on top of a Si substrate for various Ar : Cl_2 ratios. At too low/high Cl_2 partial pressures (red/green), bunching/trenching of material is observed at the base of the etch profile.

gas partial pressure, the redeposition due to the Ar physical etch can be mitigated and a good control of the etch profile can be achieved as depicted in Fig. 6.15.

6.6 Device Fabrication

This section describes the fabrication process flows for the devices used in this work. Details of the fabrication recipes can be found in appendix A.

6.6.1 Nanowire Superinductors

The nanowire superinductor samples are fabricated from a NbN thin-film sputtered on a high-resistivity ($\rho \geq 10\,\mathrm{k\Omega\,cm}$) (100) intrinsic silicon substrate. The nanowire and the microwave circuitry are patterned in a two-step electron beam lithograph and dry-etched at the same time using the process introduced in section 6.5.4.

Before processing, the substrate is dipped in hydrofluoric acid (HF) for 30 s to remove any surface oxide. Within 5 min, the wafer is loaded into a DCA MTD 450 near-UHV sputtering system where a 20 nm thick NbN thin film is deposited by reactive DC magnetron sputtering from a 99.99 % pure Nb target in a 6:1 Ar:N_2 atmosphere at 12.7 µbar.

A 500 nm-thick layer of PMMA A6 resist is spin-coated and then exposed with either a JEOL JBX-9300FS 100kV or a Raith EBPG5200 100kV electron beam lithography system to define the microwave transmission lines and alignment marks. After development, the

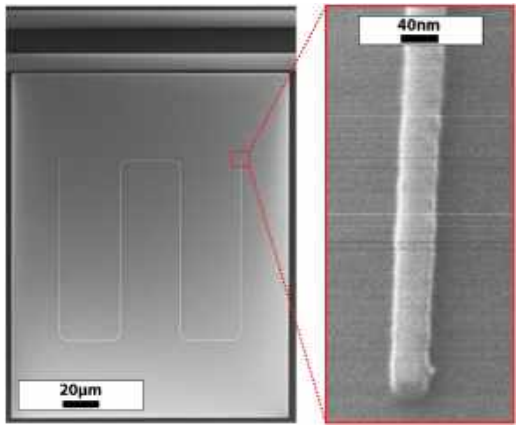

Figure 6.16: **(left)** Scanning electron microscope (SEM) micrograph of a nanowire resonator coupled to its feed line; the NbN feed line and ground plane are shown in black, the Si substrate is in gray, and the 40 nm × 680 µm nanowire is light gray. **(right)** A helium focused ion beam (FIB) image of the nanowire.

pattern is transferred to the film by reactive ion etching in an Oxford Plasmalab 100 RIE system with a 50:4 Ar:Cl_2 plasma at 50 W and 10 mTorr.

The nanowires are then patterned in a subsequent EBL exposure using a 50 nm layer of hydrogen silsesquioxane. After development, and since HSQ is a negative resist, only the area of the to-be-etched nanowires is covered by the resist mask. Therefore, in order to protect the patterns defined in the previous exposure, before any further etching, a 500 nm-thick layer of S1805 photoresist is spin-coated and exposed in an Heidelberg DWL2000 laser writer. The photoresist is only open in a 150 µm × 200 µm area around each nanowire. Finally, the resulting pattern is transferred to the film by the same 50:4 Ar:Cl_2 reactive ion etching previously described. Fig. 6.16 shows micrographs of a typical device.

6.6.2 Coplanar Resonators

NbN Resonators

The NbN resonator samples are fabricated on a high-resistivity ($\rho \leq 10\,\mathrm{k\Omega\,cm}$) (100) intrinsic silicon substrate. The substrate is dipped for 30 s in a 2 % hydrofluoric acid (HF) bath to remove the silicon surface oxide. Within 5 min, the wafer is loaded into a UHV sputtering chamber, where a NbN thin-film of thickness 15 nm is deposited by reactive DC magnetron sputtering from a 99.99 % pure Nb target in a 6:1 Ar:N_2 atmosphere at 12.7 µbar.

Next, a 500 nm-thick layer of PMMA A6 resist is spin-coated and then exposed by electron-beam lithography (EBL) to define the microwave circuitry and resonators. The

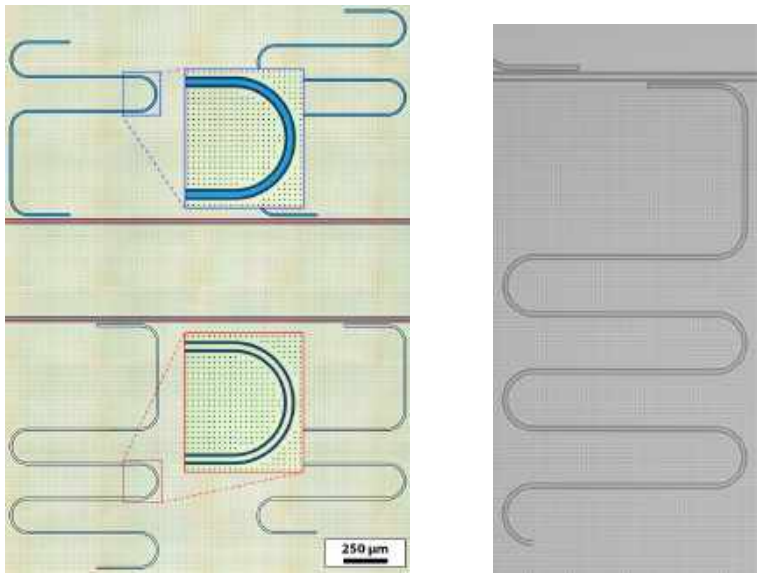

Figure 6.17: **(left)** False-colored optical micrograph of the NbN resonators used in this work. The resonators are coupled to microwave feed lines (red overlay); the exposed Si substrate, where the NbN has been etched away, is in black. Additionally, HSQ covers the central conductor of the top resonators (cyan overlay). **(right)** An optical photograph of an Al $\lambda/4$ resonator, capacitively coupled to a microwave transmission line. The Si substrate is shown by the darker gray tone, while the Al superconductor is shown by the lighter gray tone. The ground plane contains holes for flux trapping.

pattern is developed for 60 s in MIBK:IPA (1:1) and transferred to the film by reactive ion etching (RIE) in a 50:4 Ar:Cl_2 plasma at 50 W and 10 mTorr.

In a subsequent EBL step, a 30 nm layer of HSQ is first spun and then exposed on the center conductor of half of the microwave resonators such that, after development in a 2.45 % TMAH solution, each sample has two copies of each design: one covered with HSQ and one without HSQ. This design enables us to study the influence of HSQ on microwave loss in superconducting resonators (see chapter 12) by comparing two otherwise identical resonators. Fig. 6.17 (left) shows a micrograph of a typical device.

Al Resonators

The fabrication of Al resonators begins with a solvent clean of a high-resistivity ($\rho \leq 10\,\mathrm{k\Omega\,cm}$) (100) intrinsic silicon substrate. Following this, the substrate is dipped for 30 s in a 2 % hydrofluoric acid (HF) bath to remove the native surface oxide and passivate the surface with hydrogen. Within 3 minutes, the substrate is placed under vacuum inside the load lock of a Plassys MEB deposition system. The wafer is then heated to 300 °C while the vacuum chamber pumps. Once the wafer has cooled to room temperature and a base pressure of $\sim 1.1 \times 10^{-7}$ mbar is reached, 150 nm of Al is deposited at a rate of $0.5\,\mathrm{nm\,s^{-1}}$.

Next, the vacuum chamber is filled to 10 mbar of 99.99% pure molecular oxygen for 10 minutes, after this the chamber vented to atmosphere.

A 1.2 µm thick layer of AZ1512HS photoresist is then patterned by direct-write laser lithography to realise the microwave circuitry. The photoresist is developed in AZ developer diluted with H_2O 1:1, which minimises the parasitic etching of aluminium. This pattern is transferred into the Al film by a wet etch in a mixture of phosphoric, nitric, and acetic acids.

Then, a reactive ion etch using an inductively coupled NF_3 plasma was used to isotropically etch the Si substrate, forming a 1 µm deep trench with a 400 nm undercut below the Al features. Fig. 6.17 (right) shows a micrograph of a typical device.

6.6.3 NbN/AlN/Au SIN Junctions

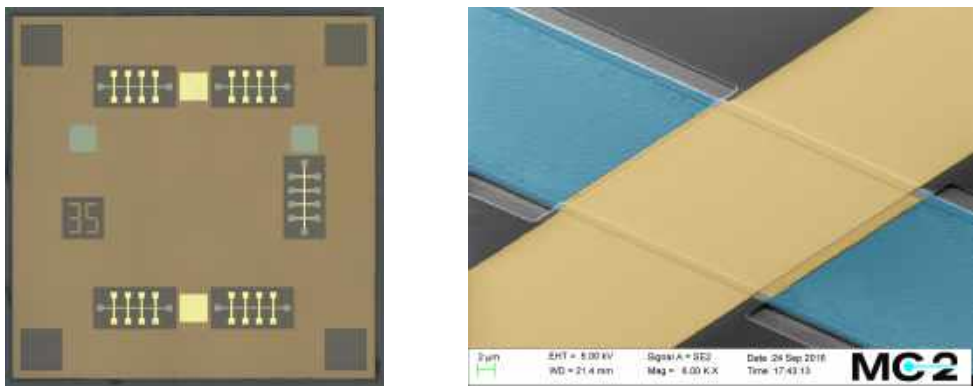

Figure 6.18: **(left)** Optical micrograph of a device containing SIN junctions (top and bottom). The gold contacts are in bright yellow, the exposed NbN is in light grey and the exposed silicon substrate is dark grey. Additionally, on the right side of the chip, a Hall bar test structure is present for transport characterisation. **(right)** False-color SEM micrograph of an SIN junction. The gold top contact and thin-film are shown in yellow, the exposed NbN is in light blue, the silicon substrate in light grey and the silicon dioxide in dark grey.

The SIN samples are fabricated on a high-resistivity ($\rho \leq 10\,\mathrm{k\Omega\,cm}$) (100) intrinsic silicon substrate. The substrate is dipped for 30 s in a 2 % hydrofluoric acid (HF) bath to remove the silicon surface oxide. Within 5 min, the wafer is loaded into a UHV sputtering chamber, where a stack of 40 nm NbN, $\sim$ 2 nm AlN and 60 nm Au thin-films is deposited. An additional layer of 10 nm of titanium is deposited on top of the NbN/AlN/Au trilayer using e-beam evaporation.

Next, in a first direct-write lithography step, the outline of the structure is patterned using a 500 nm layer of S1805 photoresist and etched by reactive ion etching (RIE) in a 50:4 Ar:Cl_2 plasma at 50 W and 10 mTorr. To prevent the top contacts from short-circuiting the junction, the entire structure is then conformally coated with a 120 nm-thick layer of

silicon dioxide. In a second direct-write lithography step, using once again a 500 nm layer of S1805 photoresist, the SiO_2 mask is opened with a NF_3 plasma reactive ion etch at the intended location for contacting to the top of the NbN/AlN/Au trilayer. To form a well-defined junction area and to expose the NbN thin-film for contacting to it, the SiO_2, Au and AlN layers are removed in a third direct-write lithography step, with a 500 nm layer of S1805 photoresist, and a combination of a NF_3 and Ar:Cl_2 plasma reactive ion etches. Finally, in a fourth direct-write lithography, using a stack of LOR3B and S1805 resists, the top of the trilayer is contacted using with lift-off of 10 nm Ti and 100 nm Au. Optical and SEM micrographs of an SIN device are shown in Fig. 6.18.

6.7 Nanowire Fabrication Quality

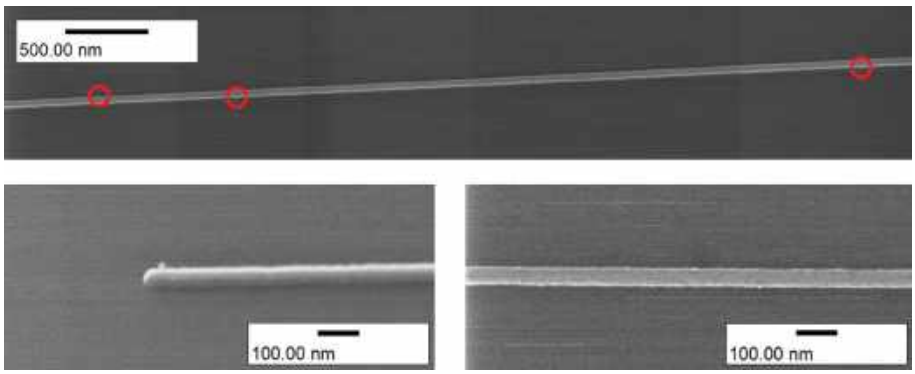

Figure 6.19: Helium FIB micrographs of a nanowire superinductor. **(top)** Shows a low magnification image of a long section (5.5 µm) of the nanowire. Lithographic defects are circled in red. **(left)** Shows a high magnification image of the end of the nanowire. Here we can see the defect is approximately 10 nm wide. **(right)** Shows a high magnification image of a section of nanowire without defects. Here we see the edge roughness is approximately ±1 nm.

In order to assess the quality of the fabrication, our devices have been imaged with a helium focused ion beam (FIB) microscope at the London Centre for Nanotechnology, University College London, courtesy of O. W. Kennedy. He FIB imaging offers unmatched resolution and gives extremely valuable insight on the device geometry at the nanometer scale.

The micrographs (Fig. 6.19) reveal very sharp nanowires on a smooth substrate surface. The line edge roughness of the nanowires is of the order of a nanometer or less. Moreover, we estimate a lithographic defect rate of less than 3 defects per 10 µm.

The defects are 10 nm wide or less. Because they are transferred into the superconducting film during etching, the defects contribute to the effective surface area of the nanowire. For a typical 680 µm long and 40 nm nanowire, this translates to an uncertainty in the surface area of 1% or less.

Chapter 7

Measurement Techniques

In this chapter, we introduce the reader to the various measurement techniques and setup used in this work. We start by a description of the fundamentals of the Pound frequency locked loop and the dispersive readout of superconducting qubits. Then, we discuss the details of the different measurement setups used to perform the experimental measurements presented in chapters 10–13.

7.1 Pound Frequency Locking

7.1.1 Homodyne and Heterodyne Detection Techniques

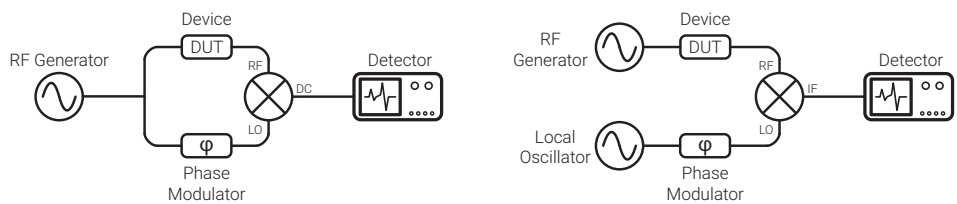

Figure 7.1: Schematic of a simple homodyne **(left)** and heterodyne **(right)** detection setup.

The two most common techniques used for measuring the amplitude and phase of a high frequency signal are called *homodyne* and *heterodyne* detection. In a homodyne detection scheme (Fig. 7.1 (left)), a source signal is split into two paths, one path goes through the device under test (DUT), and the other is used as a reference signal. The two signals are mixed, which allows for the recovery of the phase response of the DUT by measuring the phase difference $\delta\varphi$ between the two paths. The output signal after the mixer is a DC signal proportional to the mean of the amplitudes of the reference signal and the response of the DUT, modulated by the cosine of the phase difference. Homodyne detection is the simplest method to implement experimentally, however it is particularly sensitive to low frequency noise as the readout is done at DC.

This limitation can be overcome in an heterodyne detection scheme (Fig. 7.1 (right)), in which the reference signal of known amplitude is generated by a second source (the local oscillator - LO) at a frequency f_2 different from the frequency f_1 of the tone sent through the DUT, and the two tones are combined with a mixer. The resulting signal is at a frequency $f_1 - f_2$ and can be set well above the cut-off frequency for low frequency noise

by adjusting the frequency of the local oscillator. Because the LO is of known amplitude and frequency, the response of the DUT is encoded in the amplitude of the signal at the output of the mixer and can be reconstructed.

Both these techniques, however, are limited by non-correlated fluctuations in the signal and reference lines.

7.1.2 Pound Locking Theory

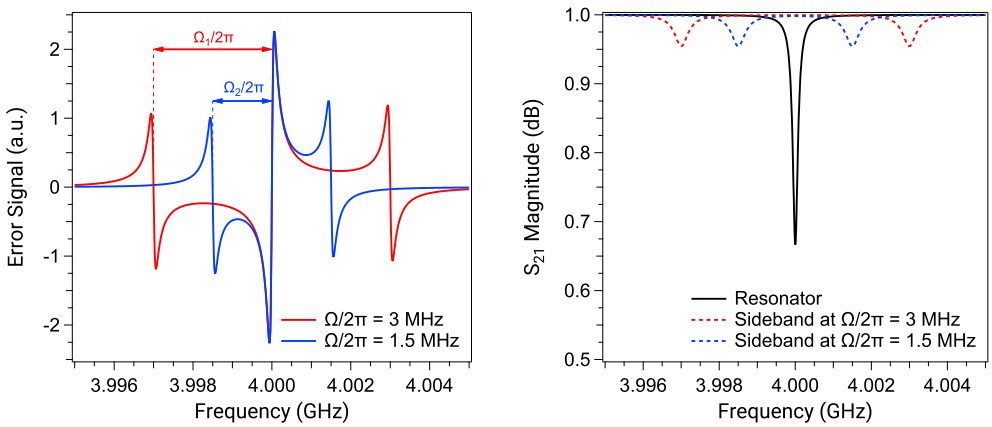

Figure 7.2: **(left)** Error signal for two different side band frequencies. **(right)** S_{21} magnitude response of the corresponding resonator. The dashed lines indicate the location of the side bands.

In this work, for the intrinsic loss tangent measurements (see chapters 3, 11 and 12), we have used a technique called Pound frequency locking that enabled us to track the frequency changes of our resonators against temperature or time with unmatched accuracy. Originally developed to stabilize microwave oscillators [185], this technique is commonly used in optics for frequency stabilization of lasers [186, 187] and has been recently used for noise [127, 188] and ESR [189, 190] measurements with superconducting microwave resonators. The major advantage of this technique is that it can be used to very accurately measure in real time the frequency of any device with a nonlinear phase response. In practice, the bandwidth is only limited by the bandwidth of the control electronics, typically working up to 100 kHz or more.

The Pound frequency locking technique can be thought of a type of heterodyne detection where a phase-modulated signal is used instead of a separate local oscillator. A self-mixing power-law detection results in an interference between the phase-modulated side bands and the main signal. The resulting interference signal is fed through a lock-in amplifier and a PID controller that seek to obtain complete destructive interference. A major advantage of this technique (in particular in a cryogenic environment) is that any phase noise is correlated and will therefore affect the carrier and side bands in a similar way and cancel out.

In the following, we give a brief description of the governing equations of a Pound frequency-locked loop (P-FLL). A schematic of a typical P-FLL measurement setup can be found in section 7.3.3.

We start by considering a phase-modulated signal, which can be expressed as

$$A = A_0 e^{i\omega t + \beta i \sin(\Omega t)} \tag{7.1}$$

where $\Omega/2\pi$ is the phase modulation frequency and β is the modulation depth. Using the Jacobi-Anger expansion, we can rewrite Eq. 7.1 as

$$A = A_0 e^{i\omega t} \sum_{n=-\infty}^{\infty} J_n(\beta) e^{in\Omega t} \tag{7.2}$$

where $J_n(\beta)$ is the n-th Bessel function of the first kind. If β is small, higher-order terms can be neglected since $\lim_{n\to\infty} |J_n| = 0$. A first-order development of Eq. 7.2 leads to

$$\begin{aligned} A &\simeq A_0 \left[J_0(\beta) e^{i\omega t} + J_1(\beta) e^{i(\omega+\Omega)t} - J_1(\beta) e^{i(\omega-\Omega)t} \right] \\ &= A_0 e^{i\omega t} \left[J_0(\beta) + 2i J_1(\beta) \sin(\Omega t) \right] \end{aligned} \tag{7.3}$$

Sending this phase modulated signal through a DUT characterised by a transmission $S(\omega)$ will give the following output signal:

$$A_{out} = A_0 \left[S(\omega) J_0(\beta) e^{i\omega t} + S(\omega+\Omega) J_1(\beta) e^{i(\omega+\Omega)t} - S(\omega-\Omega) J_1(\beta) e^{i(\omega-\Omega)t} \right] \tag{7.4}$$

Feeding this signal to a self-mixing power law detector diode gives (neglecting the 2Ω terms):

$$\begin{aligned} P_{out} = |A_{out}|^2 = {} & P_0 J_0^2(\beta) S^2(\omega) + P_0 J_1^2(\beta) \left[S^2(\omega+\Omega) + S^2(\omega-\Omega) \right] \\ & + 2P_0 J_0(\beta) J_1(\beta) \Big[\mathrm{Re}\left[S(\omega) S^*(\omega+\Omega) - S^*(\omega) S(\omega-\Omega) \right] \cos(\Omega t) \\ & + \mathrm{Im}\left[S(\omega) S^*(\omega+\Omega) - S^*(\omega) S(\omega-\Omega) \right] \sin(\Omega t) \Big] \end{aligned} \tag{7.5}$$

If the DUT is a resonator and if we assume that the side bands do not enter the resonator[1], we have $S(\omega \pm \Omega) \simeq 1$, which leads to

$$S(\omega) S^*(\omega+\Omega) - S^*(\omega) S(\omega-\Omega) \simeq S(\omega) - S^*(\omega) = 2i\,\mathrm{Im}\left[S(\omega) \right] \tag{7.6}$$

[1] The sidebands are generally set $\sim 1 - 2\,\mathrm{MHz}$ away from the center tone; therefore, this statement holds well for resonators with high quality factors where the linewidth is usually of the order of a few kHz.

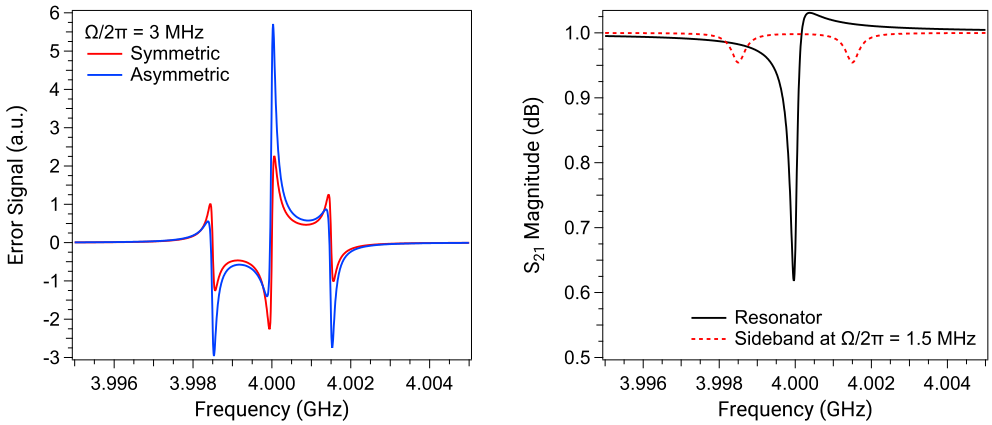

Figure 7.3: **(left)** Comparison between the error signal for a symmetric (red) and an asymmetric (blue) resonator with the same side band frequency. **(right)** S_{21} magnitude response of the asymmetric resonator. The dashed lines indicate the location of the side bands.

This is a purely imaginary quantity, which means that the $\cos(\Omega t)$ term in Eq. 7.5 is negligible. After measuring the remaining $\sin(\Omega t)$ signal using a lock-in amplifier, we get the following *error signal*:

$$\varepsilon = 2P_0 G J_0(\beta) J_1(\beta)\,\mathrm{Im}\left[S(\omega)S^*(\omega+\Omega) - S^*(\omega)S(\omega-\Omega)\right]\cos(\Delta\varphi) \tag{7.7}$$

where G is the gain of the loop and $\Delta\varphi$ represents the phase difference between the measured signal and the reference signal in the lock-in amplifier. The zero-crossing of the error signal happens for $\mathrm{Im}\,S(\omega) = 0$, which corresponds to the resonance frequency of the resonator. Fig. 7.2 shows a plot of the error signal given by a typical resonator. Using a PID controller locked to the zero crossing of the error signal, we can track the center frequency of the resonator by sending the output signal of the PID to the frequency generator to adjust the carrier frequency, thus closing the Pound feedback loop.

In practice, the choice of modulation frequency is not particularly important as long as the side bands are sufficiently outside of the resonance dip of the resonator as shown in Fig. 7.2 (right). If the side bands are too close to the carrier, they will inject power in the resonator and lead to a reduced phase shift and gain.

If the resonator response is asymmetric (see chapter 3), this leads to an asymmetric error signal as shown in Fig. 7.3. In an asymmetric resonator, the minimum of the real response does not occur at the same frequency as the phase zero-crossing. This situation results in an offset between the zero locking frequency and the resonator actual resonance frequency. The offset can however be compensated by using a non-zero set point on the PID controller, at the price of a becoming gain dependent, which complicates power sweeps.

7.2 Dispersive Readout of Qubits

One of the main challenges for any implementation of quantum computing is achieving a high-fidelity measurement of the qubit computational states, which requires a non-demolition quantum measurement [191]. A non-demolition quantum measurement does not disturb the state and allows the integration of the signal to achieve the signal-to-noise ratio required for high-fidelity measurements.

A non-demolition quantum measurement scheme can be implemented using the so-called *dispersive readout* technique [104]. In this method, the two-level artifial atom (qubit) with transition frequency $\omega_a = E_{01}/\hbar$ is coupled to a microwave resonator or cavity of resonance frequency ω_r. If the number of photons in the resonator is kept small and if the detuning $\delta = |\omega_r - \omega_a|$ between the qubit and the cavity is large, the state of the qubit remains undisturbed while the frequency of the resonator becomes dependent on the qubit state.

The interaction between the quantized field inside the resonator and the qubit can be described with the Jaynes-Cummings model [192, 193]. In this model, the resonator is described by the Hamiltonian of a harmonic oscillator in terms of the creation ($\hat{a}^\dagger$) and annihilation ($\hat{a}$) operators. If the anharmonicity of the qubit is large enough (see section 2.5), it can be treated as a system with only two states and we can use the Pauli z-matrix notation for a spin-1/2 system: $\hat{\sigma}_z = \hat{\sigma}_{00} - \hat{\sigma}_{11} = |0\rangle\langle 0| - |1\rangle\langle 1|$. The Hamiltonian of the coupled system is given by

$$\hat{\mathcal{H}} = \hbar\omega_r \left(\hat{a}^\dagger \hat{a} + \frac{1}{2}\right) + \frac{\hbar\omega_a}{2}\hat{\sigma}_z + \hbar g(\hat{\sigma}_+ + \hat{\sigma}_-)(\hat{a} + \hat{a}^\dagger) \tag{7.8}$$

where g is the coupling rate between the qubit and the resonator, and $\hat{\sigma}_- = \hat{\sigma}_{10} = |1\rangle\langle 0|$ ($\hat{\sigma}_+ = \hat{\sigma}_{01} = |0\rangle\langle 1|$) describe excitation (de-excitation) of the qubit. If the coupling rate is small enough ($g \ll \omega_a, \omega_r$), the Hamiltonian can be further simplified, in an operation known as the rotating wave approximation, to the classic form of the Jaynes-Cumming Hamiltonian:

$$\hat{\mathcal{H}}_{JC} = \hbar\omega_r \left(\hat{a}^\dagger \hat{a} + \frac{1}{2}\right) + \frac{\hbar\omega_a}{2}\hat{\sigma}_z + \hbar g(\hat{\sigma}_+ \hat{a} + \hat{\sigma}_- \hat{a}^\dagger) \tag{7.9}$$

From Eq. 7.9, two important distinct regimes can be identified and will be discussed next.

Vacuum Rabi Oscillations

If the resonator and qubit resonant frequencies are close ($\omega_r \simeq \omega_a$), the photon number state of the resonator, $\hat{n} = \hat{a}^\dagger \hat{a}$, and the $|0\rangle$ and $|1\rangle$ states of the qubit are no longer eingenstates of Eq. 7.9. The Hamiltonian eigenstates are instead entangled states between the resonator and qubit states, given by

$$|n, \pm\rangle = \frac{1}{\sqrt{2}}|0\rangle|n+1\rangle \pm |1\rangle|n\rangle \tag{7.10}$$

The energy splitting between the symmetric (+) and antisymmetric (-) state is given by $2\sqrt{n+1}\hbar g$. When the resonator and the qubit are exactly on resonance, energy is coherently exchanged between the two systems at a rate $\Omega_R = \sqrt{n+1}g/\pi$, known as the vacuum Rabi frequency. In the case of qubits with a tunable transition frequency, the coupling rate g can be experimentally obtained by sweeping the qubit frequency and measuring the avoided level crossing.

Dispersive Regime

When the qubit and the resonator are far detuned from each other ($\delta = |\omega_r - \omega_a| \ll g$), no atomic transition can exchange photons between the two systems. This is the dispersive regime, where only a dispersive coupling remains between the qubit and the resonator. In this regime, Eq. 7.9 can no longer be solved analytically. However, by using a second order time dependent perturbation theory, the Hamiltonian can be approximated to

$$\hat{\mathcal{H}}_{disp} = \hbar\left(\omega_r + \frac{g^2}{\delta}\hat{\sigma}_z\right)\left(\hat{a}^\dagger\hat{a} + \frac{1}{2}\right) + \frac{\hbar\omega_a}{2}\hat{\sigma}_z \tag{7.11}$$

In Eq. 7.11, we see that the resonance frequency of the resonator has picked up a term dependent on the state of the qubit: $\omega_r' = \omega_r \pm g^2/\delta$. In other words, the bare resonance frequency of the resonator is shifted up or down by g^2/δ when the qubit is in the $|0\rangle$ or $|1\rangle$ state. By measuring the resonance frequency of the resonator, the state of the qubit can be inferred without causing decoherence. This method is known as the *dispersive readout* of the qubit state.

7.3 Measurement Setups

7.3.1 DC Transport

The DC measurements in this work have been carried out either in a Quantum Design Physical Property Measurement System (PPMS) or in a ^{3}He cryostat. In both case, the samples are wire bonded to a custom sample holder equipped with 150 kHz low pass LC filters and all measurements are done using the standard 4-point method.

Furthermore, the ^{3}He cryostat is equipped with additional filters on each measurement line and at different temperature stages in order to suppress room-temperature Nyquist noise and spurious high frequency radiation. The setup is as follows: at room temperature, Mini-Circuits BLP-1.9+ low pass LC filters, with a cut-off frequency of 1.9 MHz. At the 4 K temperature stage, custom-designed second order RC low pass filters, with a cut-off frequency of 3 kHz. At the ^{3}He-pot stage, a set of Cu-powder filters [194] to block any noise at frequencies ≥ 500 MHz that can leak through discrete filters. Finally, the measurement lines in the cryostat come in sets of twisted pairs which provides additional distributed low-pass filtering due to their capacitance.

$R(T)$ Measurements

The $R(T)$-characteristic measurements are performed on the cold stage of the ^{3}He cryostat. The temperature is controlled by gradually lowering the cryostat insert inside a liquid helium bath. This method, while rather basic, allows for a very precise control of the temperature and cooling speed. In this setup, the sample is current biased using a Yokogawa 7651 DC source and the voltage across the sample is measured using a Keithley 2000 multimeter, with the eventual help of a Stanford Research SR560 voltage amplifier.

Hall Effect Measurements

Hall effect measurements are carried out in PPMS at $15 - 20\,\mathrm{K}$, with magnetic fields up to 6 T and using PPMS standard built-in resistance bridges.

IV Measurements

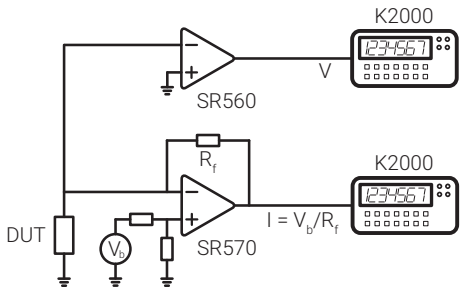

Figure 7.4: Low current DC setup for IV-characteristic measurements. The device is current biased through a modified transimpedance amplifier (SRS SR570) using a Yokogawa 7651 DC source. The current going to the DUT is monitored by measuring the output of the SR570 using a Keithley 2000 multimeter. Additionally, the voltage across the DUT is measured through a SRS SR560 voltage amplifier by a second Keithley 2000 multimeter.

The IV-characteristic measurements are also performed on the cold stage of the ^{3}He cryostat. Two distinct measurements setups were used: for relatively high current measurements ($I \geq 1\,\mu\mathrm{A}$, such as for measuring the critical current density in NbN nanowires (see section 10.2.4), the sample is current biased using a Yokogawa 7651 DC programmable source and the voltage across the sample is measured using a National Instruments PXI-6259 multifunction DAQ. Because of the DAQ multiple isolated differential inputs, this setup allows for the characterisation of up to 10 samples in parallel. This setup provides excellent common-mode noise rejection ($\sim 80\,\mathrm{dB}$) but is not suitable for the measurement of voltages smaller than $\simeq 10\,\mu\mathrm{V}$ as the DAQ accuracy is limited by its voltage preamplifier (minimum $\pm 100\,\mathrm{mV}$ full range).

On the other hand, for low current measurements ($I \leq 1\,\mu A$) and low voltage measurements ($V \leq 10\,\mu V$), such as the IV-characteristic of superconducting tunnel junctions (see section 10.2.5), special care has to be taken to diminish any parasitic noise further. For these measurements, the setup depicted in Fig. 7.4 is used. In this setup, the device is current biased via a transimpedance amplifier (modified SRS SR570 low-noise current preamplifier) through a 1/100 voltage divider. The high division ratio ensures that a relatively high voltage and therefore low noise bias is used even for small currents, which minimizes current noise. The exact applied current is monitored by measuring the voltage at the output of the amplifier. The voltage across the sample is amplified using a SRS SR560 low-noise voltage preamplifier. Both amplifiers are equipped with several integrated filtering stages and offset compensation. This setup has been successfully used for currents down to $\simeq 10\,fA$.

7.3.2 Microwave Measurements

The samples are wire-bonded in a connectorized copper sample-box that is mounted onto the mixing chamber stage of a Bluefors LD250 dilution refrigerator (Fig. 7.5). The inbound microwave signal is attenuated at each temperature stage by a total of 60 dB before reaching the device under test. Accounting for cable losses and sample-box insertion loss, the total attenuation of the signal reaching the sample is 70 dB. To avoid any parasitic reflections and noise leakage from amplifiers, the transmitted signal is fed through two microwave circulators (Raditek RADI-4.0-8.0-Cryo-4-77K-1WR) and a 4-8 GHz band pass filter. Finally, the signal is amplified by a LNF LNC4_8A HEMT cryogenic amplifier (45 dB gain) installed on the 2.8 K stage. Additional amplification is done at room temperature (Pasternack PE-1522 gain block amplifiers).

This microwave setup is connected to a vector network analyzer (Keysight PNA-X N5249A or R&S ZNB20) for initial characterisation and quality factor measurements of the device at various excitation powers (see chapter 3).

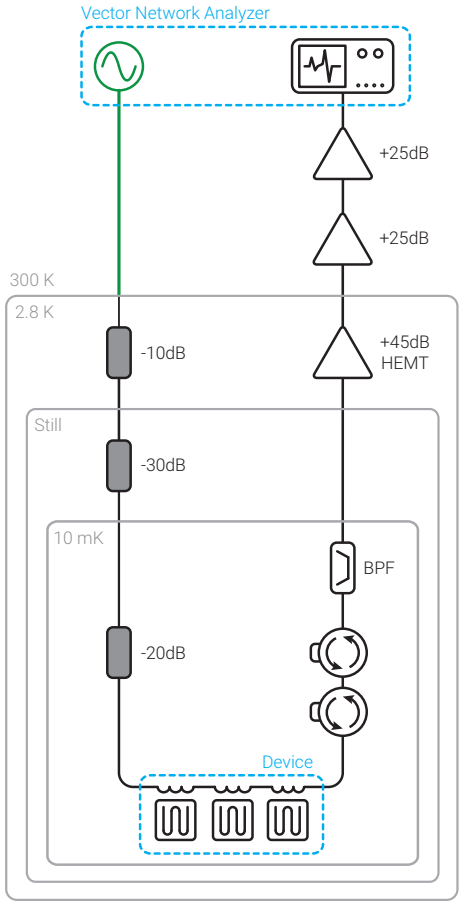

Figure 7.5: Standard cryogenic microwave measurement setup used in this work.

7.3.3 Pound Frequency Locked Loop (P–FLL)

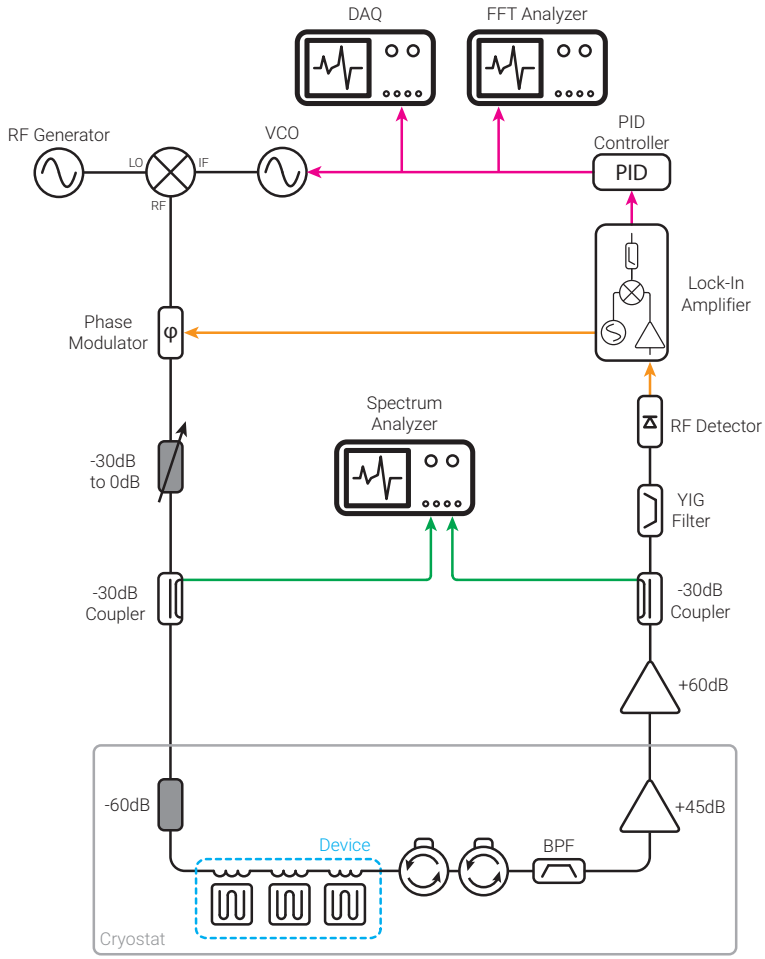

Figure 7.6: Pound frequency locked loop measurement setup.

To measure frequency fluctuations in superconducting resonators, the microwave setup described in the previous section is included in a P–FLL. The carrier signal is generated by mixing the output of a microwave source (Keysight E8257D) and a voltage controlled oscillator (VCO - Keysight 33622A). This carrier is phase-modulated (Analog Devices HMC538) before being passed through the resonator under test. The phase modulation frequency is set so that the side bands are not interacting with the resonator. After amplification, the signal is filtered (MicroLambda MLBFP-64008) to remove the unwanted mixer image and rectified using an RF detector diode (Pasternack PE8016). The diode output is demodulated with a lock-in amplifier (Zurich Instruments HF2LI).

The feedback loop consist of an analog PID controller (SRS SIM960) locked on the

zero-crossing of the error signal which gives an output directly proportional to any shift in resonance frequency of the resonator. This output signal is then used to drive the frequency modulation of the VCO, varying its frequency accordingly and enabling the loop to be locked on the resonator.

In this work, we use the P–FLL to perform two different types of measurements. To study the changes in the resonance frequency of resonators against temperature (Papers A and B and chapters 11 and 12), we only sample the PID output slowly ($\leq 100\,\mathrm{Hz}$) to track frequency changes with a Keithley 2000 or a NI PXI-6259 DAQ as the temperature of the cryostat is swept. However, in Papers C-E, we study the noise in resonators at sampling rates up to 4 kHz using a Keysight 53230A frequency counter.

Chapter 8

Simulation Techniques

In this chapter, we present a brief discussion of the different methods available for the simulation of superconducting devices. First, we discuss the advantages and drawbacks of the simulation packages used in this work. Then, we introduce a method to accurately simulate the electromagnetic field in superconducting devices with dimensions comparable to the magnetic penetration depth.

8.1 Simulating Superconducting Circuits

Computational electromagnetics (CEM) is a vast field that focuses on the process of modeling the interaction of electromagnetic fields with physical objects. It involves using computationally efficient approximations of Maxwell's equations and is widely used in both research and industry for simulating the behaviour of devices and circuits. In these applications, Maxwell's equations often do not have analytically calculable solutions due to complicated geometries, and therefore computational numerical techniques are necessary to overcome the inability to derive closed form solutions.

The typical approach for numerical electromagnetic simulations is to discretize the space in terms of grids (both orthogonal and non-orthogonal) and to solve Maxwell's equations at each point in the grid. However, discretization consumes large amounts of memory and solving the equations takes significant time. Therefore, large-scale CEM problems can face memory and CPU limitations and care has to be taken to properly design the simulation. Discretization can be achieved in several ways [195], with the most popular approaches being the finite element method (FEM), method of moments (MoM) and finite-difference time-domain method (FDTD). Several CEM commercial packages are available, each offering their own sets of advantages and drawbacks, and based on different simulation techniques.

In this work, we used Sonnet *em* [196] and Comsol Multiphysics [197] for the simulations of our devices. Sonnet uses the MoM [198] applied to Maxwell's Equations to solve 3D-planar (also known as 2.5D) problems. In these type of problems, the device consists of a multilayered planar structure where metals are simulated as infinitesimally thin layers. This approach offers comparatively fast calculations and is generally well suited for simulation of planar superconducting circuits. Furthermore, and of particular interest for this work, Sonnet implements a generalised metal model where the properties of the layer can be defined as a surface impedance $Z_S = R_S + i\omega L_S$ (see section 2.3.5) which makes it

trivial to simulate devices dominated by kinetic inductance. However, because of the 3D-planar approach, Sonnet is not suitable for simulating inhomogeneous materials or domains. This makes Sonnet the tool of choice for the simulation of complex on-chip architectures and to predict the resonant frequency of disordered superconducting resonators. Examples of such simulations can be found in chapters 9, 11 and Paper A.

On the other hand, Comsol uses the FEM approach, applied to either 2D or 3D structures where any geometry is possible. Comsol is particularly well suited for the simulation of complex materials and makes it the simulator of choice for studying device with complicated geometries and several different material types. Additionally, Comsol is not limited to electromagnetic simulations and offers a wide range of simulation modules that can be coupled together for the study of multiple interacting physical processes: for example, calculating the heating resulting from the dissipation of a microwave signal in thin-films [199] or the propagation of surface and bulk acoustic waves in superconducting resonators on piezoelectric substrates [200]. In the context of this work, a major drawback of the FEM approach lies in the simulation of high aspect ratio structures, particularly in 3D, as they can lead to extremely high memory usage and an improper meshing can cause incorrect or inaccurate results. For these reasons, it is crucial to take special care in the design of the model and simulation parameters, therefore, in the next sections, we focus the discussion on the FEM simulations used in this work.

8.2 FEM Simulations

The simulation of superconducting devices is challenging as there are various length scales involved and these length scales often differ by several orders of magnitude: devices and wavelengths are generally millimeter sized, features are a few micrometer in size, thin-films are a handful of nanometers in thickness and finally, characteristic length scales in superconductors can vary from sub-nanometer to micrometers (see chapters 2, 9 and 10).

This can lead to extremely high memory usage and incorrect or inaccurate results. Traditionally, this is solved by assuming that any physical phenomenon is uniform across small thicknesses and by approximating these volumes as infinitesimally thin layers. This greatly simplifies the meshing as only a single layer is being considered and simulated and the volumetric data is then recovered by simply multiplying the planar result by the thickness of the layer. This type approximation holds well for boundary conditions and interfaces, however it is not suitable for capturing the physics in thin-films with characteristic length scales of the order of the layer size. Specifically, for superconductors, this approach is not suitable if the magnetic penetration depth is comparable with the layer thickness or width.

For electromagnetic simulations of superconducting devices and for the devices used in this thesis in particular, this means that three different cases need to be considered and singled out: if the dimensions of the superconducting region to be simulated are much larger than the magnetic penetration depth, we can neglect the penetrating magnetic field and treat

currents as surface currents, and the traditional approach is sufficient. In the same way, if the dimensions of the superconducting region are small enough, we can assume that the superconductor is entirely and uniformly penetrated by the magnetic field and we can treat the superconductor as an infinitely thin layer with uniform properties. However, for all the intermediate cases, these approximations do not hold and a static solution of Maxwell's equations is insufficient. Instead, we need to solve the Maxwell–London equations, at the relevant frequency of the alternating current, in order to accurately simulate the densities of the current and electromagnetic fields.

In the following section, we first briefly discuss electrostatic simulations where the currents in the superconductor are treated as surface currents. We then derive a solution of the Maxwell–London equations suitable for the simulation of superconductors in a 3D FEM simulation package and present the results of supporting simulations.

8.2.1 Electrostatic Simulations

If the current density in the superconductor is uniform (i.e. when the device dimensions are much smaller than the magnetic penetration depth, $\lambda_{dirty} \gg w$) or if the current is only carried in a thin layer at the surface of the superconductor ($\lambda_{dirty} \ll w$), the current density in the superconductor can be mapped to a surface current density.

In this case, the current carrying layer can be approximated as an infinitesimally thin perfect electric conductor, and a traditional [130, 134, 201, 202] electrostatic simulation can be performed to accurately model the electromagnetic field distribution in the device, which greatly simplifies calculations as the simulation can be limited to a 2D cross section of the device.

In this work, we have used this approach for the simulation of the electric field distributions in nanowire resonators (see chapters 9 and 11, and Paper A). Additionally, we refer the reader to chapter 12 and Paper B for a comparison, over a wide range of device dimensions, between electrostatic simulations and the Maxwell-London calculations discussed in the next section.

8.2.2 Maxwell–London Equations

In this section, we derive an expression for the permittivity in the superconductor using the Maxwell and London equations.

We start from the Maxwell-Ampère equation:

$$\nabla \times \vec{H} = \vec{j} + \varepsilon \frac{\partial \vec{E}}{\partial t} \tag{8.1}$$

where, in a superconductor, the current density is split between the supercurrent and the quasiparticle current densities such that $\vec{j} = \vec{j_s} + \vec{j_n}$. The supercurrent density $\vec{j_s}$ is given

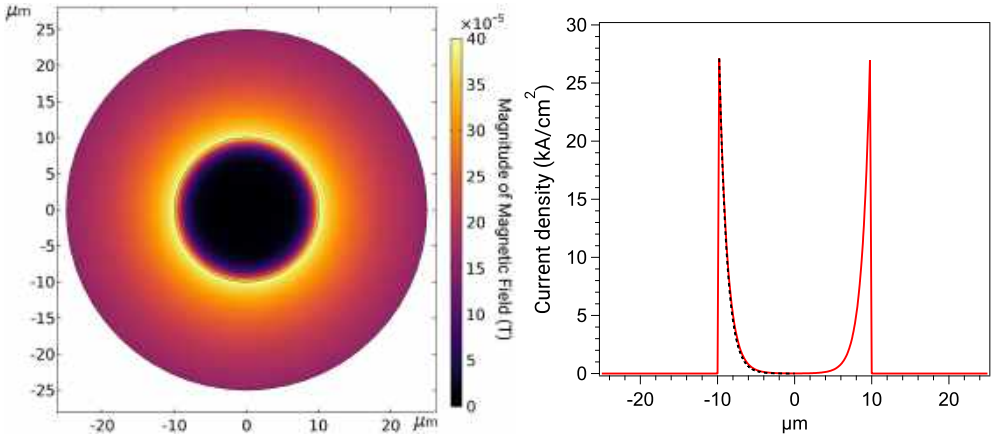

Figure 8.1: **(left)** Magnitude of the magnetic field reponse in a cross section of a superconducting coaxial transmission line, simulated at $f = 1\,\mathrm{GHz}$. The interface of the superconducting region is shown as a black circle. **(right)** Current density along a line cut in the cross section of the coaxial transmission line. The dashed line represent an exponential decay with a characteristic length of 1 µm for comparison.

by the London equations (Eqs. 2.13 and 2.14) and the quasiparticle current density is given by the local Ohm's law, $\vec{j_n} = \sigma_n \vec{E}$.

Assuming sinusoidal waveforms of a single frequency in separable form, we can write $\vec{E} = \vec{E_0} e^{j\omega t}$ and $\vec{j_s} = \vec{j_{s0}} e^{j\omega t}$, and therefore we have:

$$\frac{\partial \vec{E}}{\partial t} = j\omega \vec{E} \quad \text{and} \quad \frac{\partial \vec{j_s}}{\partial t} = j\omega \vec{j_s} \tag{8.2}$$

Using these results, we can rewrite Eq. 2.13 as

$$\vec{j_s} = \frac{1}{\mu_0 \lambda_L^2} \frac{1}{j\omega} \vec{E} \tag{8.3}$$

and Eq. 8.1 becomes

$$\nabla \times \vec{H} = \vec{E} \left(j\omega\varepsilon + \sigma_n + \frac{1}{\mu_0 \lambda_L^2} \frac{1}{j\omega} \right) \tag{8.4}$$

We recall that for any vector $\vec{A}$, $\nabla \cdot (\nabla \times \vec{A}) = 0$, therefore by taking the divergence of Eq. 8.4, we get

$$\nabla \cdot \vec{E} \left(j\omega\varepsilon + \sigma_n + \frac{1}{\mu_0 \lambda_L^2} \frac{1}{j\omega} \right) = 0 \tag{8.5}$$

which, since $\nabla \cdot \vec{E} = \rho/\varepsilon \neq 0$, solves to

$$\varepsilon = j \frac{\sigma_n}{\omega} + \frac{1}{\mu_0 \omega^2 \lambda_L^2} \tag{8.6}$$

Finally, in the dirty limit relevant to the NbN thin-films used in this work, Eq. 8.6 becomes

$$\varepsilon_{SC}(\omega, T) = \varepsilon_0 - \frac{1}{\omega^2 \mu_0 \lambda_{dirty}(T)^2} - j\frac{\sigma_1(\omega, T)}{\omega} \tag{8.7}$$

where $\sigma_1(\omega, T)$ is the real part of the Mattis–Bardeen conductivity (Eq. 2.53) and λ_{dirty} is the magnetic penetration depth in the dirty limit, given by Eqs. 2.36 and 2.37.

To test the validity of this result, we have simulated a section of coaxial transmission line in Comsol Multiphysics, using the *Electromagnetic Waves, Frequency Domain* physics interface. We chose to simulate this structure as the rotational symmetry greatly simplifies the meshing and decreases simulation complexity. Furthermore, the simulation results can be compared against the well-known analytical solutions to the Maxwell-London equations of this type of structure. The coaxial transmission line is designed as follows: the outer conductor is an infinitesimally thin layer of perfect electrical conductor with a radius of 25 µm; this outer conducting layer is separated from a central conductor by vacuum; and the central conductor has a radius of 10 µm and is made of a superconducting material with $\lambda_L = 1\,\mu\text{m}$ and $\sigma_n = 1 \times 10^{-3}\,\Omega^{-1}\,\text{m}^{-1}$. We excite the transmission line with a 1 V excitation using coaxial lumped ports placed at each extremity of the line.

The results of the simulation are presented in Fig. 8.1. In the left panel of Fig. 8.1, we can see that the magnetic field penetrates the outer part of the central superconducting domain. Furthermore, we see in Fig. 8.1 (right) that the current density presents, as it should, an exponentially decaying profile with a characteristic length 1 µm.

8.2.3 Simulations of Superconducting Resonators

In Paper B and chapter 12, we simulate coplanar waveguide resonators of various dimensions in order to calculate the participation ratio of the electric field with various regions and interfaces that are believed to be the source of dissipation. We refer the reader to chapters 9 and 12 for the details of the device design, device characterisation and results, however, we highlight that the most important device parameters for this section are the dimensions of the coplanar waveguide resonators: in these devices, the lateral dimension of the central conductor is comparable with the magnetic penetration depth λ_{dirty} of NbN, the superconducting thin-film used for the fabrication of these devices. Therefore, these resonators fall in the category described in the section 8.2.2 and we use Eq. 8.7 to simulate the superconducting regions of our devices in Comsol Multiphysics.

The meshing of the simulated structure has to be carefully optimised due the vast difference of length scales within the resonator structure (widths, thicknesses, and wavelength). The simulation mesh is manually defined using Comsol's swept mesh functionality and consists of rectangular elements. The edge length of each element is varied from 3 nm to 100 nm, with smaller elements close to the regions of interest (superconducting thin-film and dielectric layers). Due to memory constraints, however, the edge length alongside the wave propagation direction is kept constant to 100 nm and only a short section of co-planar waveguide is simulated ($l_{cpw} = 4\,\mu\text{m}$). A relative tolerance of 1×10^{-5} was

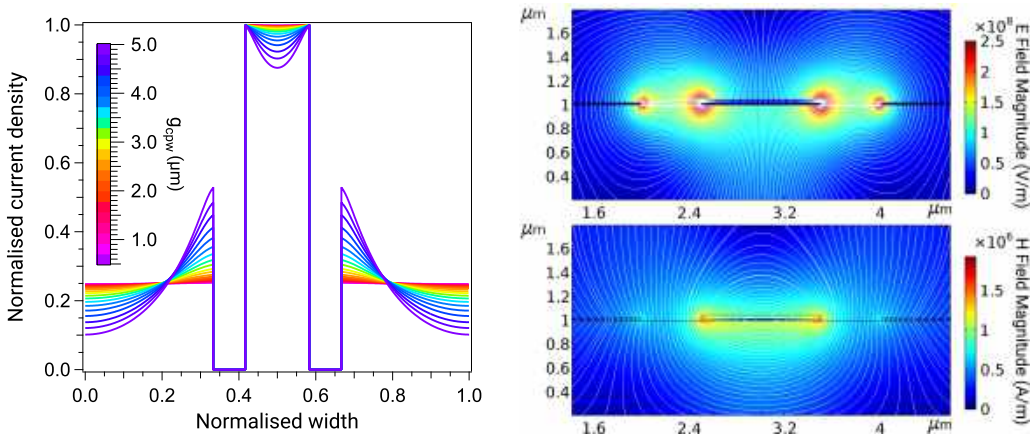

Figure 8.2: **(left)** Simulated normalised current density inside the superconductor, extracted along a line half-way inside it (half the thickness), for all simulated values g_{cpw} in the 500 nm to 5 µm range. **(right)** Magnitude and field lines of the simulated electric (top) and magnetic fields (bottom) for a cross section of the resonators with HSQ covering the central conductor. The permittivity in Eq. (8.7), with $f = 5\,\text{GHz}$, is given as an input to Comsol Multiphysics.

found as a good compromise between the accuracy of the converged solution and the duration of the simulation.

The simulations results for the electromagnetic field and current densities are presented in Fig. 8.2: in figure 8.2 (left), we show the current densities across the superconductor for every simulation. The data is normalised in width and amplitude to increase readability because samples are of different dimensions (but with constant $w_{cpw}/g_{cpw} = 2$). For device dimensions where $g_{cpw} \simeq \lambda_{dirty}$, we see that the current distribution is uniform and therefore an electrostatic simulation would be sufficient to accurately model the electromagnetic field in the device. On the other hand, when $g_{cpw} \geq \lambda_{dirty}$, the current density is not uniform anymore and an electrostatic simulation will not correctly capture the field distribution in the device. Finally, the electric and magnetic fields for a cross section of a resonator with $g_{cpw} = 500\,\text{nm}$ are shown in Fig. 8.2 (left).

Chapter 9

Device Design and Considerations

This chapter, in which we introduce the different design considerations for the devices used in this thesis, serves as a preamble for the results presented in chapters 10–13 and in Papers A-C. First, we discuss the constraints of superinductors and their practical implications on the design of our samples. We discuss the choice of material, geometrical considerations for a superinductor (nanowire geometry, TLS filling factor, parasitic capacitance, phase slips, ...) and practical considerations for the device fabrication. After this, we present the design choices for superconducting resonators and superconducting tunnel junctions.

9.1 Nanowire Superinductors

As defined in the previous chapters, a superinductor is a low loss circuit element with an impedance larger than the superconducting resistance quantum R_Q. These prerequisites pose several constraints on the successful design of a superinductor: in the context of disordered superconductors, this implies that the thin film should have a high kinetic inductance while the fabricated structure should have a capacitance as low as possible.

In this section, we will detail the implications of these constraints on several aspects of the design of a nanowire superinductor.

9.1.1 Material Considerations

In chapter 2, we derived the kinetic inductance contribution for a superconductor in the local dirty limit (Eq. 2.56). This formula reveals that in order to achieve a highly inductive film, we need a superconductor that exhibits a high normal-state resistance R_N and a small superconducting gap (i.e. a small critical temperature T_c).

However, there are several caveats in this simple interpretation. First of all, while a small gap is favourable for a high inductance, a working temperature too close to T_c leads to the presence of quasiparticles. In turn, these quasiparticles lead to significant losses, as highlighted in sections 2.2.1, 2.3.5 and 4. These losses would breach the low loss criterion for a superinductor. Therefore this imposes a practical limit on the critical temperature of the superconductor to realise such device: for a practically obtainable temperature of 10 mK, the minimum practical critical temperature is around 1.5 K.

Additionally, while it is tempting to arbitrarily increase R_N (i.e. the level of disorder) to achieve a high kinetic inductance, films exhibit loss as they get close to the SIT [122] (see section 4), which is once again incompatible with the low loss criterion for a superinductor and imposes another practical limit on the superconductor: we need to fabricate a sufficiently disordered superconductor to obtain high inductance, but not so disordered as to induce dissipation.

In this work, our choice of superconductor is niobium nitride. NbN has a high bulk critical temperature (16 K), however, the critical temperature is suppressed as the thickness of the film is reduced [203], which leads to a favourable scaling of the superconducting gap in Eq. 2.56.

After a careful optimisation of the NbN thin film fabrication (see chapter 10 for more details), a target thickness of 20 nm, corresponding to a critical temperature $T_c = 7.20\,\mathrm{K}$ and a normal-state resistance $R_N = 503\,\Omega/\square$, is found as a good compromise between disorder and kinetic inductance, with a corresponding sheet kinetic inductance $L_k = 82\,\mathrm{pH}/\square$.

9.1.2 Geometrical Considerations

Nanowire Geometry

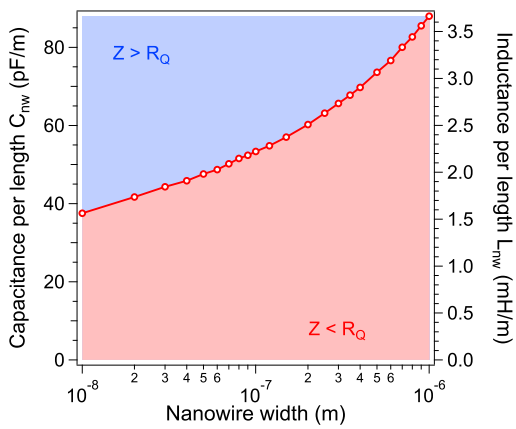

Figure 9.1: Simulated capacitance per length for nanowire widths ranging from 1 µm down to 10 nm. The right axis corresponds to the minimum required inductance per length to verify $Z_{nw} > R_Q$.

In the previous section, we established that we cannot arbitrarily increase the inductance to maximise the impedance. Therefore, to realise a superinductor, it becomes crucial to minimise the stray capacitance, which can be achieved with a nanowire geometry. We have simulated the capacitance per length for several nanowires with widths varying from 1 µm

down to 10 nm. The results are shown in Fig. 9.1. This figure also shows the corresponding minimum inductance per length required for a superinductance: $L_{nw} = R_Q^2 C_{nw}$.

Additionally, in chapter 2, we calculated the geometric contribution to the internal inductance and find it to be entirely negligible for a thin film (see Eq. 2.45 and Fig. 2.4). Any given geometry will also have an external geometric contribution to its magnetic inductance which can be calculated, for similar nanowires, using an empirical formula [204]. It is found to be less than $1\,\mu\mathrm{Hm}^{-1}$ in every case. This number is several orders of magnitude smaller than the minimum inductance per length required for a superinductor (Fig. 9.1). We can therefore conclude that the nanowire inductance arises entirely from the kinetic inductance and that $L_{nw} \equiv L_k$.

For a thin film with a kinetic inductance $L_k = 82\,\mathrm{pH}/\square$, we find an inductance per length $L_{nw} = 2.05\,\mathrm{mH\,m}^{-1}$ for a 40 nm-wide nanowire. With a corresponding capacitance per length $C_{nw} = 44.4\,\mathrm{pF\,m}^{-1}$, we find $Z_{nw} = \sqrt{L_{nw}/C_{nw}} = 6.80\,\mathrm{k}\Omega > R_Q$, indicating that such nanowires are superinductors.

TLS Filling Factor

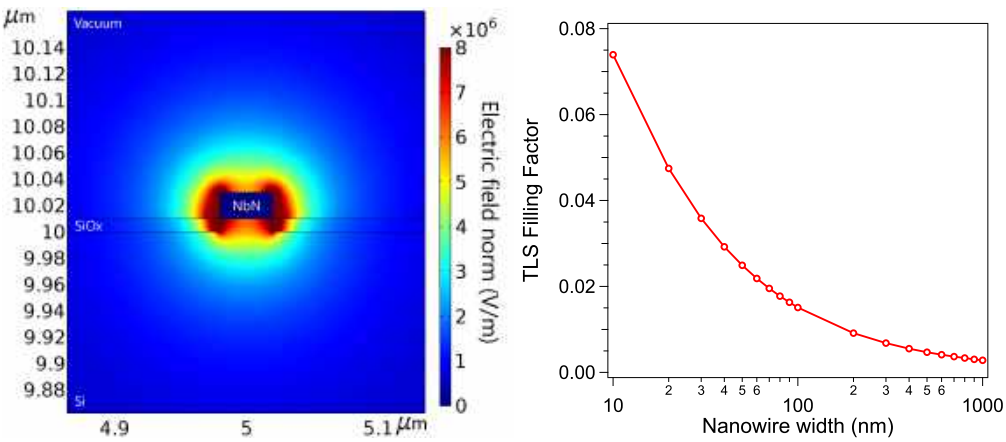

Figure 9.2: **(left)** Magnitude of the electric field for a 40 nm wide nanowire. **(right)** TLS filling factor for nanowire widths ranging from 1 µm down to 10 nm.

In chapter 3, we highlighted the role of the TLS filling factor in the losses and mentioned that reducing the physical dimensions of a resonator leads to an unfavorable scaling. We have simulated the TLS filling factor using an electrostatic simulation in Comsol for nanowires of various widths (see chapter 8). For simplicity, in our model, we assume a TLS host volume V_{TLS} consisting of a 10 nm thick layer of silicon oxide. The filling factor is obtained by calculating the ratio of the electric energy stored in the TLS host volume

to the total electric energy [61]:

$$F = \frac{\int_{V_{TLS}} \varepsilon_{TLS} \vec{E}^2 d\vec{r}}{\int_V \varepsilon \vec{E}^2 d\vec{r}} \tag{9.1}$$

The results of the simulation are shown in Fig. 9.2. We note the significant increase of the filling factor as the width is reduced.

Meandering Parasitic Capacitance

In this section, we analyse the influence of meandering the nanowire to qualitatively study the role of any geometry dependent parasitic capacitance. For that purpose, we simulate the frequency response and current density of various nanowire resonators using Sonnet *em* microwave simulator. In order to reduce meshing and simulation times, we simulate 100 nm-wide nanowires in a simple step-impedance resonator geometry. We start by simulating a straight nanowire as a reference and then proceed to simulate nanowires in a meandered geometry with a fixed meander length $b = 20\,\mu\text{m}$ while gradually decreasing distance between meanders from $a = 30\,\mu\text{m}$ and down to 100 nm (see Fig. 9.3).

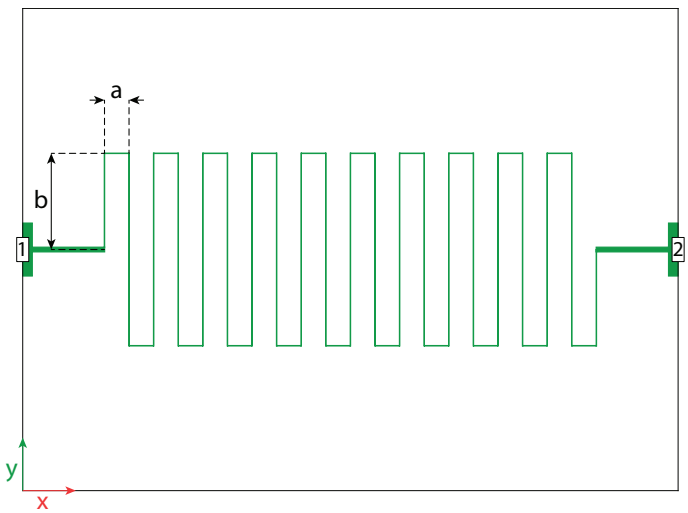

Figure 9.3: Schematic representation of a typical meandered nanowire resonator structure simulated in this section. a and b denote the distance between meanders and the meander length respectively. 1 and 2 are the excitation and measurement ports and the black outline represents the grounded edge of the simulation box.

Figs. 9.4 and 9.5 show the normalised current density along the nanowires at the fundamental resonance frequency of the simulated structure. To be clear, for meandered geometries, the current density is not measured as a line cut along the x-axis, but instead the geometry is unwound and the current density is extracted at every point along the

nanowire. We observe that for the straight wire and for $a > 5\,\mu\text{m}$, the current density is consistent with the expected $\lambda/2$ mode structure of such a resonator and the characteristic impedance of the nanowire resonator is well-defined to $Z_{nw} = \sqrt{L_{nw}/C_{nw}}$.

Below $a = 5\,\mu\text{m}$, we observe that, as the distance reduces between the meanders, the resonance frequency significantly diverges from the straight nanowire reference value and the current density is severely distorted. This is explained by the increasing influence of parasitic capacitance between each meander. This parasitic capacitance is equivalent to shunting the nanowire with an extra capacitance and lowering its impedance. Moreover, the structure cannot be treated as a $\lambda/2$ resonator anymore and has therefore no well-defined wave impedance, which can lead to misinterpretation of experimental data [205].

Based on these results, for the final devices, depending on the desired total length for the nanowire, we retain designs with 3, 5 or 7 meanders[1] and with an inter-meander distance of respectively 15 µm, 25 µm and 35 µm for which any parasitic capacitance is entirely negligible.

Phase Slip Rate

Phase slips in superinductors are unwanted as they can lead to dissipation [10]. We estimate the phase slip rate $\Gamma_S = E_S/h = E_0/h \exp(-\kappa\bar{w})$ for our device within the phenomenological model for strongly disordered superconductors. Our analysis is similar to that of Peltonen *et al.* [14]. In this model, E_S is the phase slip energy and we have $E_0 = \rho\sqrt{l/\bar{w}}$, where l and $\bar{w}$ are the nanowire length and average width respectively, $\rho = (\hbar/2e)^2/L_k$ represents the superfluid stiffness, $\kappa = \eta\sqrt{\nu_p\rho}$, $\eta \simeq 1$ and $\nu_p = 1/(2e^2 R_N D)$ is the Cooper pair density of states with $D \simeq 52.6\,\text{nm}^2\,\text{ps}^{-1}$ (see chapter 10).

For our device parameters ($R_N = 503\,\Omega/\square$, $L_k = 82\,\text{pH}/\square$, $\bar{w} = 40\,\text{nm}$ and $l = 680\,\mu\text{m}$), we find $\Gamma_S \simeq 2 \times 10^{-3}\,\text{Hz}$. This corresponds to an average of one phase slip event every 9 minutes, which is entirely negligible.

9.1.3 Practical Considerations and Device Design

Building on the conclusions of the previous section, we fabricate 40 nm wide nanowire superinductors etched in a 20 nm thick NbN film using the fabrication process described in section 6.6.1.

In order to eliminate potential cross talk between microwave feed lines, the final samples contain one single feed line on which up to 23 nanowire superinductors (with an identical coupling but different resonance frequencies) are multiplexed. Arrays of 2 µm × 2 µm flux-trapping holes are added to the ground planes to limit loss due to magnetic vortices [206].

The sample also contains separate DC transport test structures: Hall bar type structures are included to enable transport measurements on both a conventional "slab" of the

[1] We define a meander by a 180° turn in the nanowire geometry.

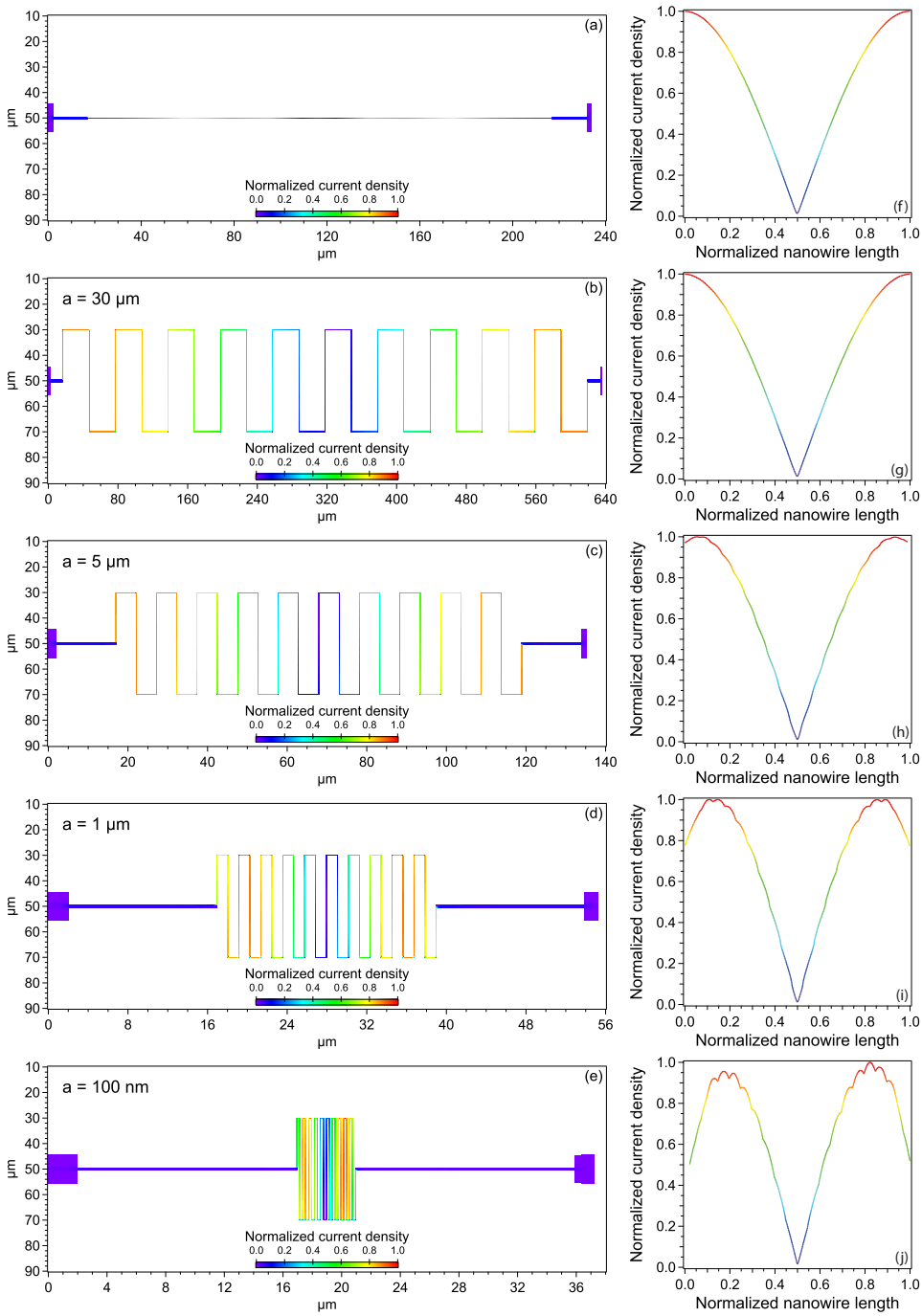

Figure 9.4: **(a-e)** Current density distribution in nanowires at several inter-meander distances. **(f-j)** Corresponding normalised current density along the nanowire.

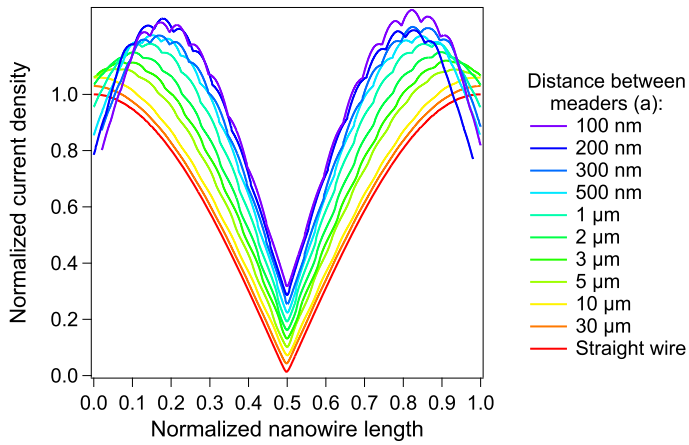

Figure 9.5: Normalised current densities at the fundamental resonance frequencies for all the simulated structures. For clarity, the curves have been offset by 0.03.

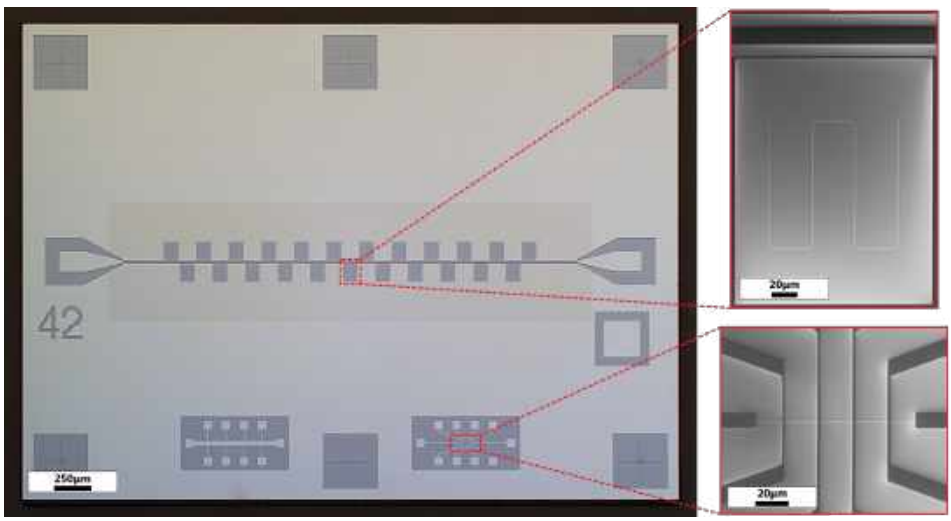

Figure 9.6: **(left)** Optical micrograph of a nanowire superinductor device used in this work. The dark grey regions correspond to the Si substrate. NbN is shown in light gray. The beige region around the feed line corresponds to the arrays of flux trapping holes opened in the NbN ground plane. **(right)** SEM micrograph of a nanowire superinductor resonator (top) and nanowire Hall bar (bottom). In both cases, the NbN feed line, ground plane and contacts are shown in black, the Si substrate is in gray, and the nanowire is light gray.

superconductor and a nanowire of the same 40 nm width as the main device. Pictures of the device are shown in Fig. 9.6 and an extensive experimental characterisation is presented in Paper A and chapter 11.

9.2 Superconducting Resonators

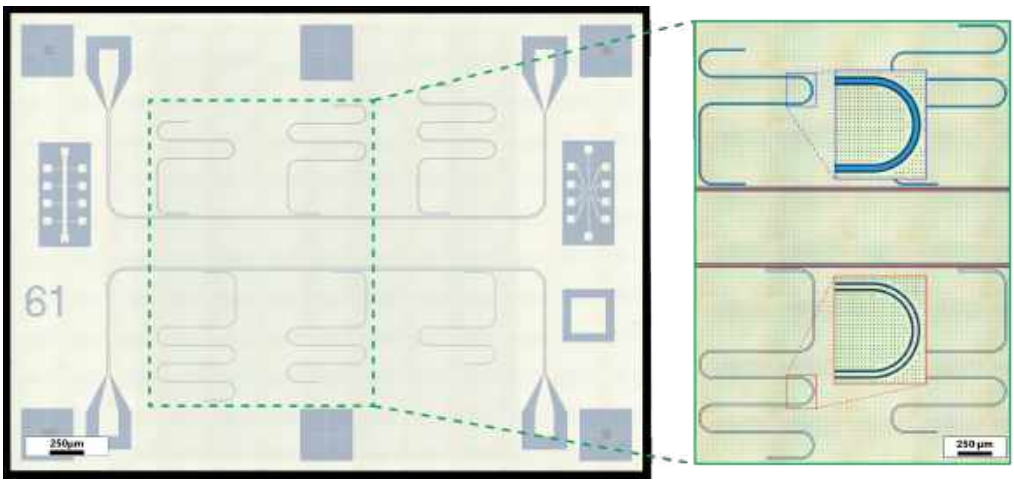

Figure 9.7: **(left)** Optical micrograph of a NbN resonator device used in this work. The dark grey regions correspond to the Si substrate exposed after NbN has been etched away. NbN is shown in light grey. **(right)** False-colored close-ups of four of the NbN resonators. The resonators are coupled to microwave feed lines (red overlay); the exposed Si substrate, where the NbN has been etched away, is in black. Additionally, HSQ covers the central conductor of the top resonators (cyan overlay). Flux trapping holes opened in the ground plane can be seen as black dots.

In Paper B and chapter 12, we study the geometric scaling of two-level system loss in superconducting resonators. Additionally, we study the participation ratio and loss tangent of spin-on-glass resists such as HSQ used for the fabrication of our nanowire superinductors (see sections 6.6.1, 9.1, chapter 11 and Paper A).

We design the samples in the following way: the geometric scaling is studied in a series of coplanar waveguide resonators where we gradually change the widths of the center conductor and of the gap between center conductor and ground planes. The gap width ranges from $g_{cpw} = 500\,\text{nm}$ to $5\,\mu\text{m}$, with the ratio of the gap to the centre conductor kept fixed. To study the influence of HSQ, each resonator has two copies of each resonator design, one of which has its central conductor covered with HSQ and the other one is left without HSQ.

Because the design of resonators with and without HSQ is the same and their resonant frequency is expected to be almost identical, we couple each group of resonators to different microwave feed line. Therefore, each sample consists of two microwave feed lines: one with 3 resonators without any HSQ of a g_{cpw} and different lengths, and one feed line with 3 similar resonators, but with their center conductors covered with HSQ. In total, we have studied 24 resonators distributed across four separate samples.

Finally, similarly to the nanowire superinductor samples, arrays of $2\,\mu\text{m} \times 2\,\mu\text{m}$ flux-

trapping holes are added to the ground planes to limit loss due to magnetic vortices [206] and the device contains separate DC transport test structures: a conventional "slab" of the superconductor and a nanowire of the same 40 nm width as the main device. Optical micrographs of a sample are presented in Fig. 9.7.

9.3 SIN Junctions

We have fabricated NbN/AlN/Au SIN junctions to study the properties of the superconducting gap in NbN thin-films (see section 10.2.5). In this section, we motivate the choice of aluminium nitride for the tunnel barrier and we discuss its implications on the design and fabrication of the junctions.

9.3.1 Choice of tunnel barrier

To fabricate good quality junctions, a thin and pinhole-free tunnel barrier is desired. Aluminium oxide is traditionally used for the fabrication of Josephson junctions, however the process relies on the in-situ oxidation of a layer of aluminium. Such a process is not suitable for our needs as it would require the deposition of an extremely thin layer of aluminium which will not form a uniform barrier bur rather grow in islands and lead to the formation of many pinholes. Furthermore, aluminium oxide is found to be a poor choice of tunnel barrier for NbN junctions [207].

A solution to this problem is to grow a thicker layer of aluminium on top of NbN, then oxidise this layer and rely on the proximity effect to induce superconductivity in the aluminium layer sandwiched between the NbN and aluminum oxide for temperatures $T > T_{c,Al}$. However, this leads to complicated physics as the tunneling current becomes mostly sensitive to the density of states in the proximitised Al layer [208] and makes the study of the energy gap in NbN significantly more complicated. For this reason, we have excluded this approach.

One could also rely on the natural oxide that grows on NbN, however the growth of this oxide barrier takes several days in atmospheric conditions [209]. The growth can be stimulated by heating the NbN film in an oxygen atmosphere, however this also leads to the migration of nitrogen defects in NbN toward the surface and significantly affects the film properties [210].

An alternative barrier material is aluminium nitride (AlN): a good lattice matching between AlN and NbN ensures a better growth of the film in contrast to aluminium [211]. Additionally, AlN being a dielectric, the deposition rate in a DC sputtering system is extremely slow (of the order of $1.3\,\text{Å}\,\text{s}^{-1}$) which guarantees a very good control of the film thickness. Furthermore, AlN can be reactively sputtered in the same vacuum chamber where our NbN thin-films are deposited, which has the significant advantage of allowing the deposition of the barrier in-situ. This ensures that the NbN surface is not contaminated nor oxidised and that the thickness of the tunnel barrier is well controlled.

For these reasons, we have decided to use AlN as the barrier material of choice for the SIN junctions used in this work.

9.3.2 Device design

The in-situ deposition of AlN atop NbN ensures a contamination-free interface between both films. For the same reason, it is preferable to also deposit the top layer of the junction in-situ; therefore, for the fabrication of our SIN junctions, we have decided to use the classic trilayer-type approach popular for the fabrication of Josephson junctions for RSFQ[2] applications [212, 213].

On the other hand, the major disadvantage of a trilayer process in contrast to shadow evaporation techniques is that the bottom metal is covered by the subsequent layers and several lithography steps are required to contact the junction (see section 6.6.3 for an in-depth description of the fabrication steps of the SIN junctions measured in this work). However, shadow evaporation necessitates the use of a resist mask and a lift-off process which are unreliable when combined with sputtering (see section 6.3).

For the top normal-metal contact, we need a material that is not superconducting at the temperatures at which the junctions will be measured ($T \geq 250\,\mathrm{mK}$). Additionally, this material needs to be a good conductor to avoid any Joule heating of the junction as current passes through the contact. This material also needs to be compatible with the processing steps necessary for the fabrication of the device. Finally, this choice of material for the normal-metal top contact is limited by what is available in our sputtering system. For all these reasons, our choice for the top contact material goes to gold.

One potential issue with using gold relates to the adhesion of gold on materials: due to its limited surface reactivity, gold generally has a low adhesion strength on most materials. This can be mitigated with the well-known use of a thin titanium layer as an adhesion promoter [214–218]. However, while poor, the adhesion of gold on AlN proved sufficient for our needs in this project.

[2] A rapid single flux quantum (RSFQ) device is a digital electronic device that uses Josephson junctions to process digital signals. In RSFQ logic, information is stored in the form of magnetic flux quanta and transferred in the form of single flux quantum (SFQ) voltage pulses.

Chapter 10

Results - NbN Thin-film Characterisation and Optimisation

In the previous chapter, we established the need for a highly disordered superconductor to fabricate our devices. This requires a careful optimisation of the NbN thin film fabrication process with a high level of control of the deposition parameters. In this work, NbN thin films are reactively sputtered (see sections 6.3 and A) and several "tuning knobs" are available to adjust the level of disorder in the film: film thickness, nitrogen content and choice of substrate. In this chapter, we first discuss the effect of these deposition parameters on the properties of the thin-film. Then, we present the techniques used of the in-depth characterisation of the NbN thin-films used in this work.

10.1 NbN Thin-film Deposition Parameters

In NbN, the level of disorder can be tuned by adjusting the thickness of the thin film [219, 220]. The increase in disorder in films of decreasing thicknesses manifest itself in an increased normal state resistance R_N and a reduced critical temperature T_c. The microscopic mechanism explaining this reduction of T_c is still debated in the literature to this day but is believed to stem either from weak localisation [221, 222], proximity effect [73, 223, 224] or electron wave leakage [225–227]. The thickness dependent disorder is shown in Fig. 10.1, where the critical temperature T_c, normal state resistance R_N and kinetic inductance L_k (calculated using Eq. 2.56) are presented for NbN thin-films of various thicknesses, deposited on silicon substrates at a nitrogen molar fraction of 10.7 %.

Furthermore, for a given thickness, the disorder in the film can be further tuned by adjusting the stoichiometry of the film [219]. This is done by adjusting the partial pressure of nitrogen in the chamber during deposition. This increase in nitrogen content can be regarded as doping: as more and more nitrogen is added to the film, more and more scattering sites are introduced and increase the amount of disorder in the film. This effect needs to be studied in a chamber-by-chamber basis as the geometry of the chamber (volume, substrate distance from the target, gas inlets, pump location...) will affect the results. In Fig. 10.2, we present the results of such a study in the DCA MTD 450 near-UHV sputter system where all the NbN films used in this thesis were deposited.

Additionally, the choice of substrate is also relevant. Alumina (sapphire) and magnesium oxide have a very small lattice mismatch with NbN and are therefore the substrates of

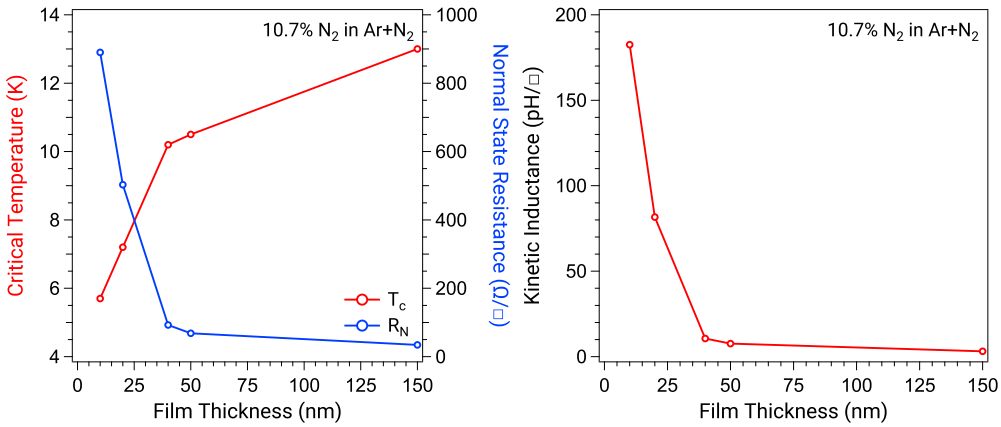

Figure 10.1: Critical temperature T_c and normal-state resistance R_N **(left)**, and kinetic inductance L_k **(right)** as a function of thickness for films deposited on silicon substrates at room temperature and at a fixed nitrogen mole fraction of 10.7 %.

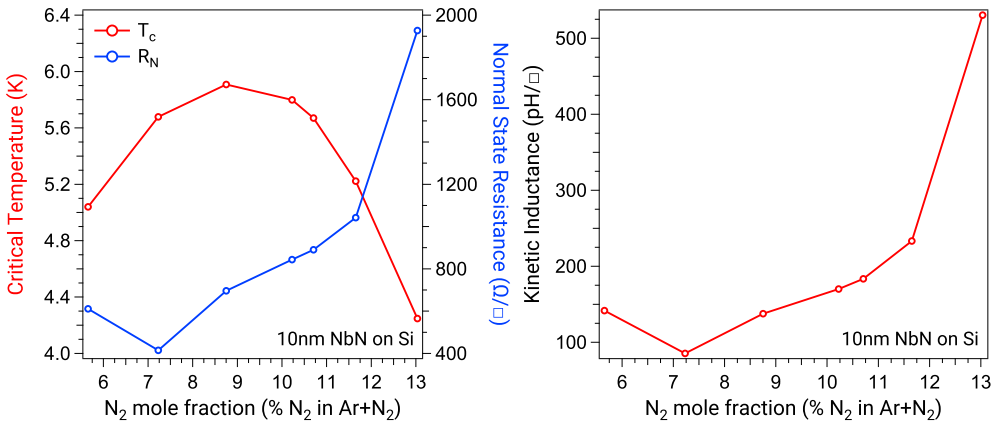

Figure 10.2: Critical temperature T_c and normal-state resistance R_N **(left)**, and kinetic inductance L_k **(right)** as a function of nitrogen content for films of a a fixed thickness of 10 nm deposited at room temperature on silicon substrates.

choice for epitaxial NbN depositions. For disordered films, however, it is preferable to use a less favourable substrate such as silicon. Finally, the substrate temperature during deposition plays a role on the level of disorder. Epitaxial films are usually sputtered at a substrate temperature ranging from 600 °C to 800 °C while films deposited at ambient temperature are inherently more disordered [228]. In Fig. 10.3, we show the results of a comparative study between 10 nm-thick NbN films deposited at room temperature on silicon and sapphire substrates for a wide range of nitrogen partial pressures. We can see that films deposited on silicon are consistently more disordered (lower T_c and higher R_N) than on sapphire, regardless of the nitrogen content.

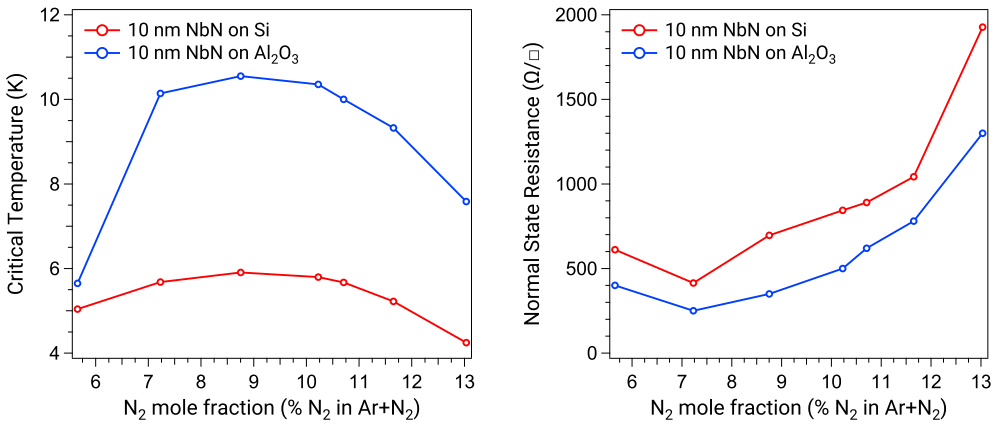

Figure 10.3: Critical temperature **(left)** and normal state resistance R_N **(right)** as a function of nitrogen content for NbN thin-films deposited at room temperature and at a fixed thickness of 10 nm on a silicon or sapphire substrate.

10.2 Transport Characterisation

In chapter 9, we established that the successful implementation of a nanowire superinductor relies on a sufficiently disordered superconductor to obtain high inductance, but not so disordered as to induce dissipation. Additionally, in the previous section, we highlighted that the level of disorder in the film is dependent on the deposition parameters and a slight change of these parameters could potentially greatly affect the film properties (for example, the deposition rate can change over time as the target gets consumed). In order to quantify the level of disorder, produce thin-films meeting all the necessary criteria and to ensure the reproducibility of the process, we systematically study the transport properties of our NbN thin films and nanowires using the DC test structures on each device (see chapter 9 for details on device design). Furthermore, we have fabricated devices that allowed us to experimentally verify the assumptions made on the film properties and confirm that our NbN thin-films are indeed strongly coupled dirty superconductors.

In this section, we present the different transport measurements that we have performed on our devices and using the measurement results of a select group of NbN thin-films, we illustrate how a set of simple experiments can reveal a wide range of key material parameters.

10.2.1 Critical Temperature Measurements

All the devices in this work have several DC test structures and resistance against temperature characteristics are systematically measured prior to any other experiment. The $R(T)$ characteristic is measured by applying a small current (on the order of 10 nA to 100 nA) and recording the voltage drop across the sample while the cryostats cools

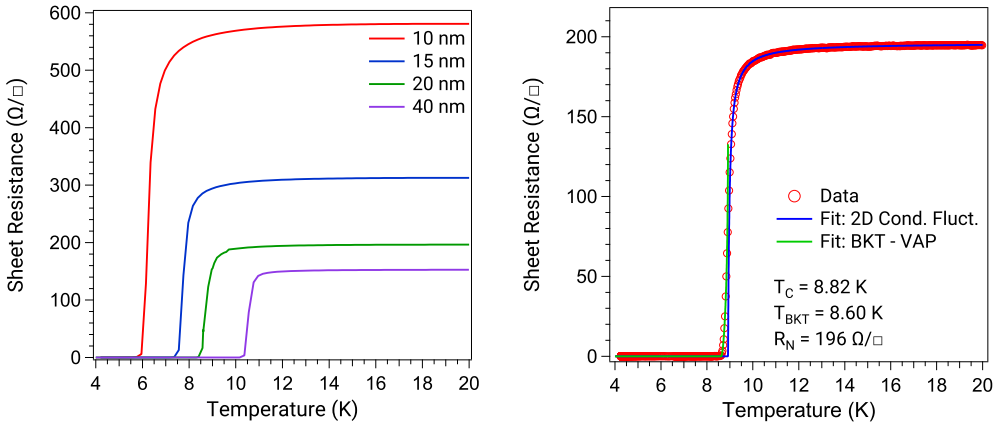

Figure 10.4: **(left)** $R(T)$ characteristic of all four NbN thin-films. We note that T_c is suppressed and R_N increases as the thickness of the film decreases. **(right)** $R(T)$ characteristic of the 20 nm film, with fits using Eq. 2.57 (for $T > T_c$) and 2.62 (for $T < T_c$).

down. If the cryostat is cooled slowly enough (adiabatically), the device thermalises well and any temperature gradient between the device and the temperature sensor on the cryostat cold stage will be minimal and can be neglected. The details of the experimental setup for $R(T)$ measurements can be found in section 7.3.1.

When the temperature reaches the critical temperature T_c, the resistance vanishes as the film enters the superconducting state. Furthermore, if performed on a structure of known dimensions, the $R(T)$ characteristic can be used to accurately determine the normal state sheet resistance R_N of the film. For NbN thin-films, R_N is generally found at temperatures between 15 K and 20 K due to the competition between weak localisation and fluctuations paraconductivity (see section 2.4).

These two parameters – R_N qnd T_c – are of particular interest for the study of disordered superconductors and can be used to derive several other quantities. Most notably for our applications, the superconducting gap at zero temperature Δ_0, the London penetration depth λ_{dirty} and the kinetic inductance L_k of the film can be calculated from R_N and T_c using Eqs. 2.26, 2.36 and 2.56 respectively. In Fig. 10.4 (left), we present the $R(T)$ characteristic of NbN thin-films of thicknesses varying from 10 nm to 40 nm, deposited at room temperature on silicon substrates and at a nitrogen mole fraction of 9.75 %. As the thickness decreases, we observe that the critical temperature is suppressed and the normal state resistance increases. This is consistent with the expected increase of disorder in thinner films as discussed in the previous sections and in chapter 2. We fit the $R(T)$ characteristics using Eqs. 2.57 and 2.62 (Fig. 10.4 (right)) to determine T_c and R_N. The fitted values and the corresponding calculated values of Δ_0, λ_{dirty} and L_k for all the films can be found in Table 10.1.

10.2.2 Hall Measurements

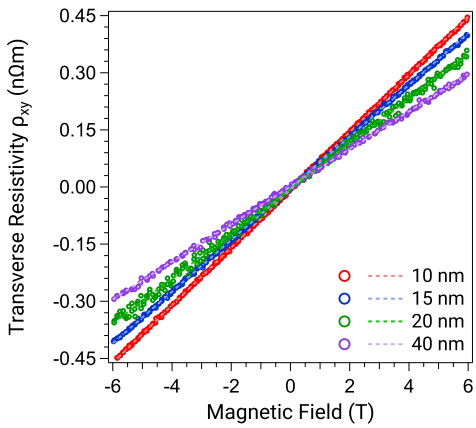

Figure 10.5: Hall transverse resistivity ρ_{xy} as a function of the applied magnetic field for all four NbN thin-films, measured at $T = 20\,\mathrm{K}$. The dashed lines are line fits to the experimental data and R_H, the Hall coefficient, is defined as the slope of the line fit.

In a Hall effect type measurement [229], the sample is placed under a perpendicular magnetic field and biased with a fixed current (see section 7.3.1 for a detailed description of the experimental setup). As the strength of the magnetic field is increased, more and more charges are deflected toward one edge of the sample due to the Lorentz force. This results in an asymmetric distribution of charge density across the sample and the rise of a transverse electric field that establishes a steady electric potential across the sample edges. This difference of potential, known as the Hall voltage, is the quantity that is measured by the experimentalist and can be interpreted as the voltage drop due to the transverse resistivity ρ_{xy} caused by the magnetic field. The transverse resistivity is linearly dependent on the applied magnetic field and its slope is known as the Hall coefficient R_H, given by:

$$R_H = 1/n_n e \tag{10.1}$$

where n_n is the charge carrier density in the normal state.

Experimentally, the Hall effect is measured where the resistance of the sample is maximum (i.e. for $R(T) = R_N$). The Hall coefficient is obtained by fitting the slope of the $\rho_{xy}(H)$ trace and the charge carrier density n_n is obtained from the Hall coefficient using Eq. 10.1. Using the free electron relations (see chapter 2), we can calculate additional key parameters of our film: k_F, ε_F, v_F, $\rho_s(\varepsilon_F)$, l, $k_F l$, ξ_0, D and $j_c^{GL}(0)$. In Fig. 10.5, we present the Hall effect measurements of the same NbN thin-films introduced in section 10.2.1. The fitted values of R_H and the aforementioned calculated parameters for all the films can be found in Table 10.1.

10.2.3 Critical Field Measurements

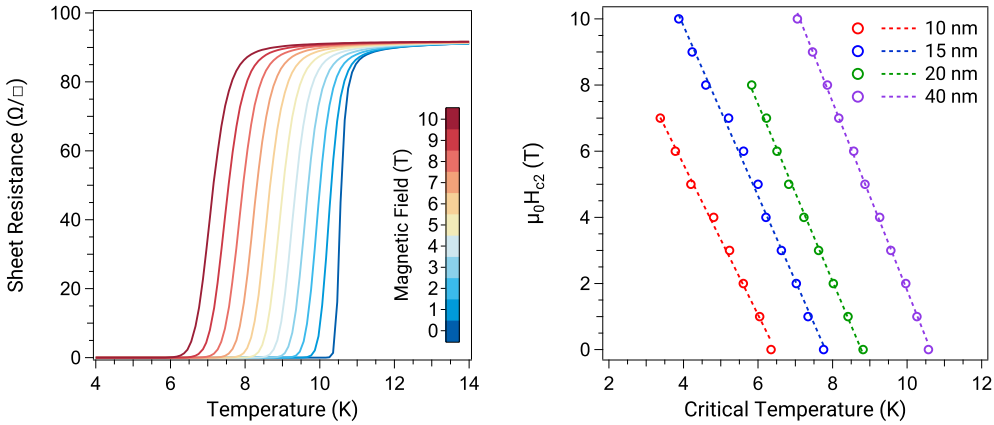

Figure 10.6: **(left)** $R(T)$ characteristic of the 40 nm film at all the applied magnetic fields. As the strength of the applied magnetic field increases, the superconductivity is gradually suppressed and the critical temperature is lowered. **(right)** Critical temperature as a function of the applied magnetic field. The upper critical field H_{c2} is calculated from the slope of the curve using Eq. 2.35.

In sections 2.2.5 and 2.3, we established that the upper critical field H_{c2} of a disordered superconductor can be obtained by studying the magnetic field dependence of the critical temperature. Experimentally, this can easily be done by measuring the $R(T)$ characteristic of the device at various applied magnetic fields.

We have performed such a measurement on all the NbN thin-films introduced in section 10.2.1. For each sample, we fit the $R(T)$ characteristic to determine the critical temperature T_c at every applied magnetic field (Fig. 10.6 (left)). Then, we fit the slope of the $T_c(H)$ trace and we calculate H_{c2} using Eq. 2.40. Finally, using Eq. 2.35, we calculate the GL-coherence length ξ_{GL} for each film. The calculated values of H_{c2} and ξ_{GL} for all the films are summarised in Table 10.1. We note that all films are indeed in the local dirty limit ($l \ll \xi_0 \ll \lambda_{dirty}$).

10.2.4 Critical Current Measurements in NbN Nanowires

To avoid any dissipation due to non-equilibrium quasiparticles, our nanowire superinductors need to operate at currents well below the critical current. To ensure that this is indeed the case in our devices, and to assess their current-carrying capabilities for future DC-transport experiments, we have characterised the critical current density of a wide range of disordered NbN nanowires: using the 10 nm-, 15 nm- and 20 nm-thick disordered NbN thin-films described in the previous section, we have fabricated nanowires of widths ranging from 50 nm to 500 nm and lengths ranging from 5 µm to 25 µm.

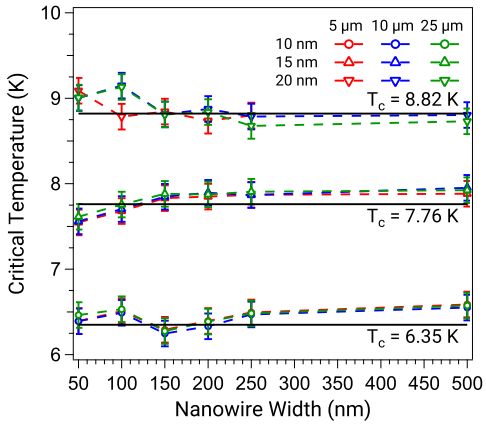

Figure 10.7: Critical temperature T_c of all the nanowires using Eq. 2.57 and Eq. 2.62. The solid lines represent the critical temperatures measured with DC test structures on the same film (see section 10.2.1) as reference. The dashed lines are guides to the eye.

For each nanowire, we first measure the $R(T)$ characteristic while cooling down the cryostat. The $R(T)$ characteristics are measured at an applied current of 100 nA, well below the expected critical current of the devices, but high enough as to mitigate any readout noise. We fit the nanowires $R(T)$ characteristics to Eqs. 2.57 and 2.62. The results are shown in Fig. 10.7. We find that the critical temperature of every nanowire is comparable with the critical temperature previously obtained with the measurement of the DC test structure of the same film (see section 10.2.1). This result is not surprising, as a suppression of T_c is only expected when a change in dimensionality occurs [230, 231], which is not the case in our devices. Nevertheless, it is important to measure the critical temperature of each nanowire as any significant deviation in T_c would affect the calculation of the GL critical current density $j_c^{GL}(0)$ (Eq. 2.66) later used in this section and negatively impact the accuracy of the critical current study.

We measure the I-V characteristic of the nanowire at various temperatures (Fig. 10.8 (left)) using the measurement setup described in chapter 7.3.1, starting from the base temperature of the cryostat ($\sim$ 250 mK) and up to a temperature close to the critical temperature of the nanowire. Additionally, the temperature of the sample holder is recorded throughout the measurement of the I-V characteristic.

We observe a highly hysteretic behaviour of the I-V characteristic, with greatly disparate critical and retrapping currents, as shown in Fig. 10.8 (right). Here, the retrapping current is defined as the current at which the nanowire switches from the resistive state back to the superconducting state. This behaviour is consistent with the expected Joule self-heating that occurs when the nanowire is in the normal state [232–234]. Further evidence of this self-heating can be seen at low temperatures: in the resistive state, the temperature of the sample holder steadily increases as the cooling power of the cryostat is not sufficient to keep the temperature of the stage constant. In the superconducting state, however, the temperature quickly recovers.

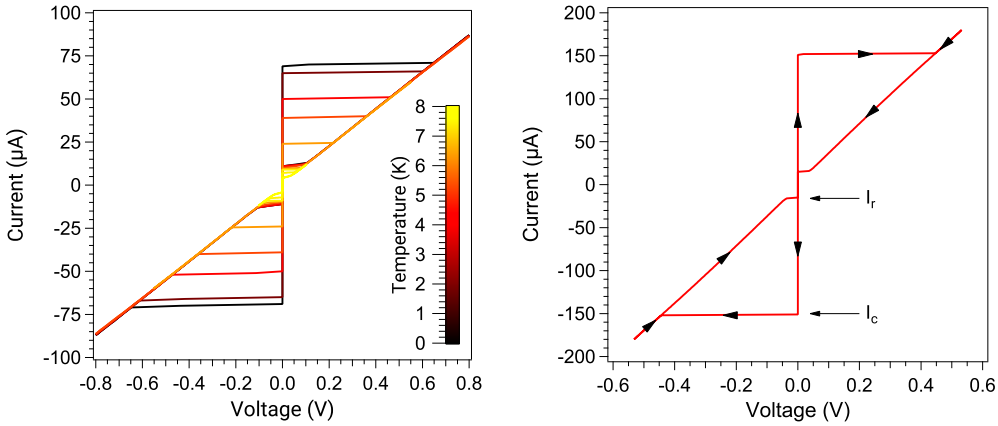

Figure 10.8: **(left)** I-V characteristics of 250 nm × 10 µm nanowire on a 15 nm thin-film and for all measured temperatures. **(right)** Typical I-V characteristic of a nanowire. The black arrows markers represent the direction in which the measurement is swept. We observe a large hysteresis between the current at which the nanowire switches from the superconducting state to the resistive state (I_c) and vice-versa (I_r).

For each nanowire, the critical (Fig. 10.9 (left)) and retrapping (Fig. 10.11) currents are extracted from the data at each measured temperature by examining the differential conductance dI/dV. The temperature dependence of the critical current is fitted to both the Bardeen model (Eq. 2.67) and the Kupriyanov-Lukichev (KL) model (Eq. 2.68). An example of such temperature dependence of the critical current of a 250 nm × 10 µm nanowire on a 15 nm thin-film can be seen in Fig. 10.9 (left).

Here, we emphasize that, while both models reliably fits the experimental data, we can see from Eqs. 2.67 and 2.68 that they predict a different scaling of critical current at zero temperature: $I_c^B(0) = 1/2\sqrt{2}I_c^{GL}(0)$ and $I_c^{KL}(0) = KL(0)I_c^{GL}(0)$. We plot the results of both models and for all measured devices is shown in Fig. 10.9 (right).

To determine which model more accurately describes our data, we use the London equations (Eqs. 2.13 and 2.14) to calculate the current distribution in a cross section of the nanowire as a function of $j_c^{GL}(0)$:

$$I_c^{London}(0)(w,t) = j_c^{GL}(0)\lambda_{dirty}^2 \left[1 - \exp\left(\frac{-t}{\lambda_{dirty}}\right)\right]\left[1 - \exp\left(\frac{-w}{\lambda_{dirty}}\right)\right] \tag{10.2}$$

where w and t are respectively the width of the nanowire and the thickness of the NbN thin-film. The values of λ_{dirty} and $j_c^{GL}(0)$ are calculated using Eq. 2.36 and Eq. 2.66 and using the results of the transport characterisation of the thin-films discussed in the previous sections (see Table 10.1). The results of this independent calculation are compared against the fitted values of $I_c(0)$ and are shown in Fig. 10.10 (left). We find that the Bardeen model matches the experimental data best for the 20 nm-thick film, whereas the KL model describes best the 15 nm- and 10 nm-thick films. Additionally, we note that the Bardeen model describes the 500 nm nanowires best regardless of the film

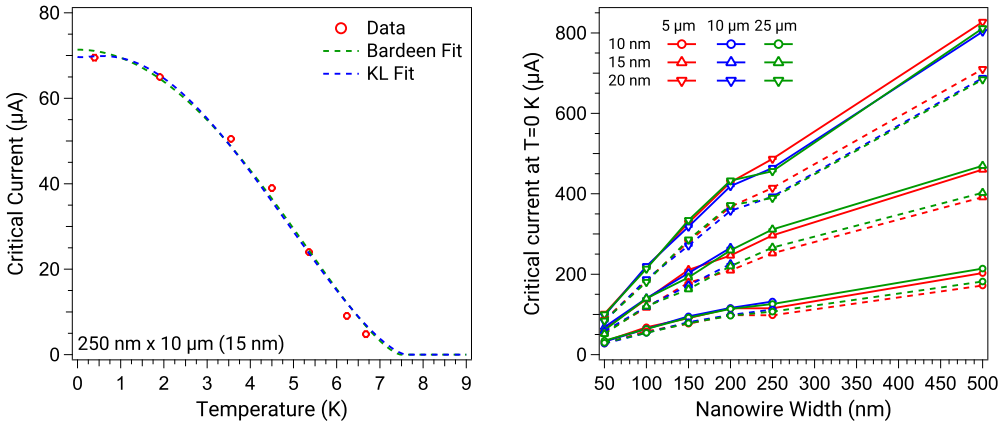

Figure 10.9: **(left)** Temperature dependence of the critical current in a 250 nm × 10 µm nanowire on a 15 nm thin-film, with fits (Bardeen and KL models). **(right)** Critical current at $T = 0\,\mathrm{K}$ for all devices, fitted using both Bardeen (plain lines) and KL-model (dashed lines). In both cases, the lines are guides to the eye.

thickness. The critical current densities of all measured devices is shown in Fig. 10.10 (right).

Finally, we complete the analysis by studying the retrapping current (Fig. 10.11). The temperature dependence of the retrapping current is consistent with the Joule heating of the nanowire in the normal state, as previously mentioned. We find that our experimental data is best described by a Kapitza interfacial thermal conductance σ_K [234, 235] for which the retrapping current temperature dependence is given by:

$$I_r(T) = \sqrt{\frac{\sigma_K w^2}{R_N}(T_c^4 - T^4)} \tag{10.3}$$

where σ_K is the Kapitza conductance, R_N and T_c are the normal state resistance and critical temperature of the nanowire respectively. We use Eq. 10.3 to fit the experimental data and, for all nanowires, we find $\sigma_K \simeq 200\,\mathrm{Wm^{-2}K^{-4}}$, which is consistent with values reported in the literature [236, 237].

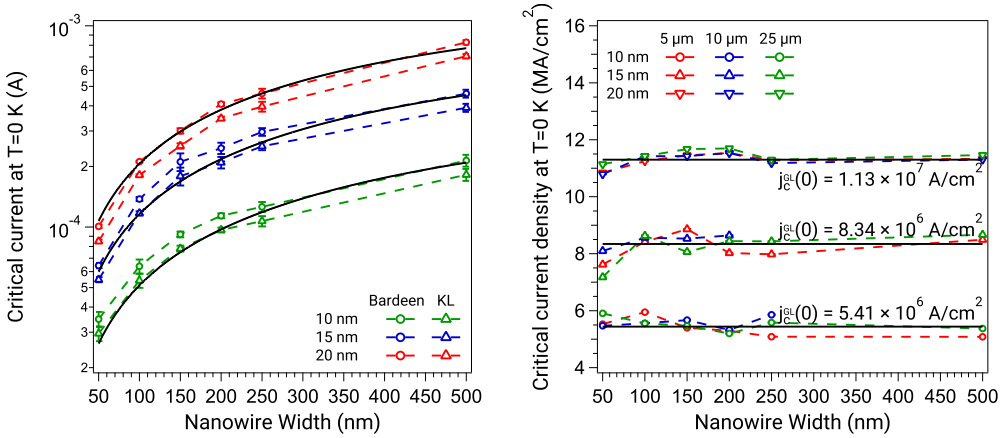

Figure 10.10: **(left)** Fitted values of $I_c(0)$, using both the Bardeen and KL models, compared against Eq. 10.2 (solid lines) **(right)** Critical current densities $j_c^{GL}(0)$ for all measured devices, calculated from the fitted values of $I_c(0)$. The solid lines represent the values of $j_c^{GL}(0)$ obtained using Eq. 2.66 and an independent transport measurement (see sections 10.2.1 and 10.2.2). In both figures, the dashed lines are guides to the eye.

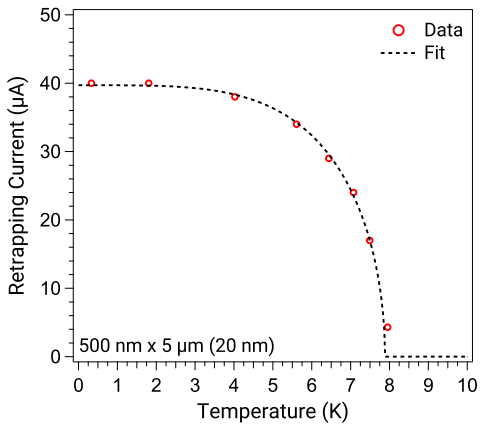

Figure 10.11: Temperature dependence of the retrapping current in a 500 nm × 5 µm nanowire on a 20 nm thin-film, with fit (Kapitza model).

10.2.5 Superconducting Gap Measurements

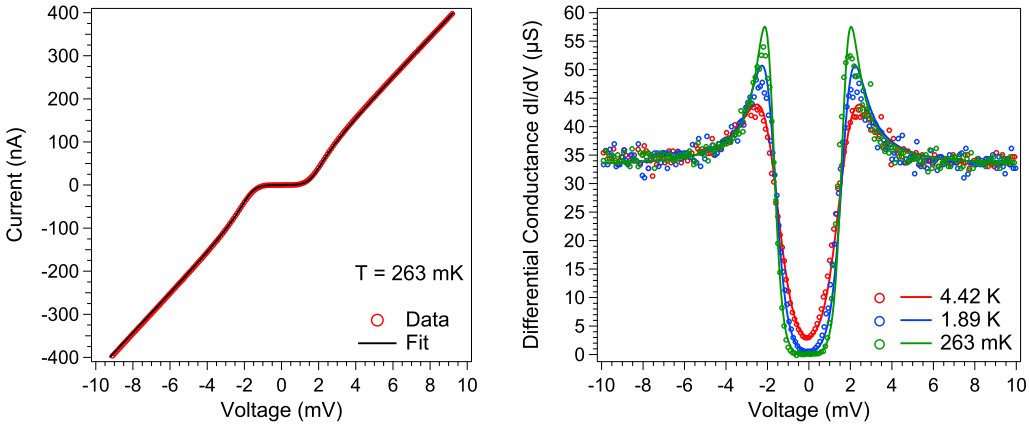

Figure 10.12: **(left)** Current-voltage (I-V) characteristic of an NbN/AlN/Au SIN junction measured at $T = 263\,\text{mK}$, with fit. **(right)** Differential conductance calculated from the IV data at various temperatures, with fits.

As mentioned in chapter 2, NbN is experimentally found to be a strongly coupled superconductor [48]. To verify that this results hold for our devices, we have measured the superconducting gap of our NbN thin-films. For this purpose, we have fabricated NbN/AlN/Au superconductor-insulator-normal metal (SIN) junctions using the fabrication process described in section 6.6.3. The junction current-voltage (IV) characteristic is measured at different temperatures (see section 7.3.1 for details on the measurement setup). From this, the differential conductance dI/dV is calculated and fitted to Eq. 2.70 to extract the superconducting gap. Fig. 10.12 shows a typical IV characteristic (left) and differential conductance at several different temperatures (right) of the SIN junctions measured in this work. We find good agreement between the measured values of the superconducting energy gap of our NbN thin-films when compared against the predictions of the BCS theory in the strong coupling limit, $\Delta_0 = 2.08 k_B T_c$, as shown in Fig. 10.13.

10.3 Discussion

In section 10.1, we have shown that the properties of disordered NbN-thin films greatly depend on the deposition parameters. In order to develop an optimised and reliable deposition process that enables the fabrication of films that meet the requirements for a superinductor (see chapter 9), we have designed a series of simple transport experiments in which a wide range of material parameters can be measured.

From the $R(T)$ characteristic, the critical temperature, normal state resistance, superconducting gap and kinetic inductance can be obtained (section 10.2.1). Additionally, the charge carrier density can be measured in an Hall effect measurement, and using the free

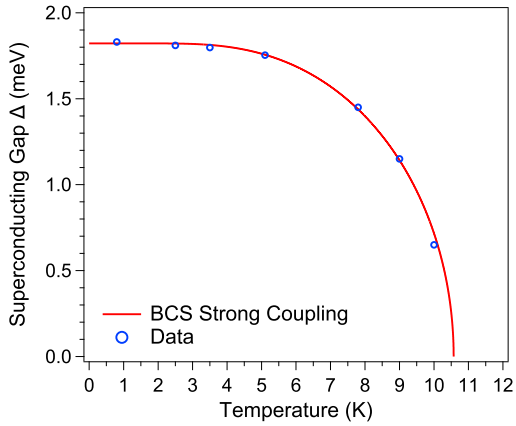

Figure 10.13: Measured energy gap as a function of temperature for a 40 nm NbN thin-film of $T_c = 10.6$ K. The data is obtained by fitting the differential conductance of an NbN/AlN/Au SIN junction measured at different temperatures. The line represents the energy gap temperature dependence predicted by the BCS theory in the strong coupling limit (Eq. 2.26).

electron relations, we can calculate the quantities necessary to assess the level of disorder in the film with the Ioffe-Regel parameters $k_F l$ along with several other key material parameters (section 10.2.2). Finally, by measuring $R(T)$ characteristics under a magnetic field, the upper critical field and related parameters can be measured (section 10.2.3). This method allows for the fast characterisation of NbN films and can be applied to quantify the effect of various depositions parameters on the film quality (section 10.1).

We show the results of a study of four NbN thin-films of different thicknesses (summarised in table 10.1), and we find that the results of these measurements are in excellent agreement with values found in the literature [48, 74, 238, 239].

Furthermore, we compare some of these results with independent measurements: by studying the temperature dependence of the critical current in nanowires (section 10.2.4), we have shown consistency between the critical current density fitted from the experimental data and the critical current density calculated from the free electron relations with Eq. 2.66. Additionally, using NbN/AlN/Au SIN junctions, we have studied the temperature dependence of the superconducting gap in a 40 nm-thin NbN film and confirmed that our NbN thin films indeed fall under the strong coupling limit (section 10.2.5).

Table 10.1: Material parameters for the NbN thin-films discussed in section 10.2. The table first lists the parameters directly measured in the transport experiments, then lists every material parameter derived from the measurements, along with a reference to the relevant equation.

Parameter name	Symbol	Unit	Value			
Film			10 nm	15 nm	20 nm	40 nm
Critical temperature	T_c	K	6.35	7.76	8.82	10.6
Normal-state resistance	R_N	$\Omega/\square$	583	313	196	91.6
Hall coefficient	R_H	$\mathrm{m^3\,C^{-1}}$	7.56×10^{-11}	6.78×10^{-11}	5.90×10^{-11}	4.93×10^{-11}
Upper critical field	$\mu_0 H_{c2}$	T	9.96	13.8	16.3	20.8
Superconducting gap (Eq. 2.26)	Δ_0	meV	1.14	1.39	1.58	1.89
Kinetic inductance (Eq. 2.56)	L_k	$\mathrm{pH}/\square$	107	47.1	26.0	10.1
Carrier density (Eq. 10.1)	n_n	$\mathrm{m^{-3}}$	8.25×10^{28}	9.21×10^{28}	1.06×10^{29}	1.27×10^{29}
Fermi wavevector (Eq. 2.3)	k_F	$\mathrm{m^{-1}}$	1.35×10^{10}	1.40×10^{10}	1.46×10^{10}	1.55×10^{10}
Fermi energy (Eq. 2.4)	ε_F	eV	6.91	7.44	8.16	9.19
Fermi velocity (Eq. 2.6)	v_F	$\mathrm{m\,s^{-1}}$	1.56×10^6	1.62×10^6	1.69×10^6	1.80×10^6
Density of states (Eq. 2.5)	$\rho_s(\varepsilon_F)$	$\mathrm{eV^{-1}\,m^{-3}}$	1.79×10^{28}	1.86×10^{28}	1.95×10^{28}	2.07×10^{28}
Electron mean free path (Eq. 2.6)	l	pm	115	133	145	138
Ioffe-Regel parameter	$k_F l$	-	1.55	1.86	2.12	2.14
London penetration depth (Eq. 2.36)	λ_{dirty}	nm	924	750	644	568
GL coherence length (Eq. 2.35)	ξ_{GL}	nm	5.75	4.89	4.49	3.98
BCS coherence length (Eq. 2.25)	ξ_0	nm	287	244	225	199
Electron diffusivity (Eq. 2.63)	D	$\mathrm{nm^2\,ps^{-1}}$	59.8	71.6	81.6	82.5
Critical current density (Eq. 2.66)	$j_c^{GL}(0)$	$\mathrm{A\,cm^{-2}}$	5.44×10^6	8.34×10^6	1.13×10^7	1.58×10^7

Chapter 11

Results - Nanowire Superinductors

This chapter introduces the results presented in Paper A. In this work, we report the fist successful implementation of a superinductor made from a disordered superconductor, with a characteristic impedance of $6.8\,\mathrm{k}\Omega$ and an internal quality factor of 2.5×10^4 at single microwave photon excitation. Furthermore, by examining the loss rates, we demonstrate that the microwave dissipation in our device can be fully understood in the framework of two-level system loss. A description of the device design can be found in chapter 9 and device fabrication is detailed in section 6.6.1.

11.1 Transport Characterisation

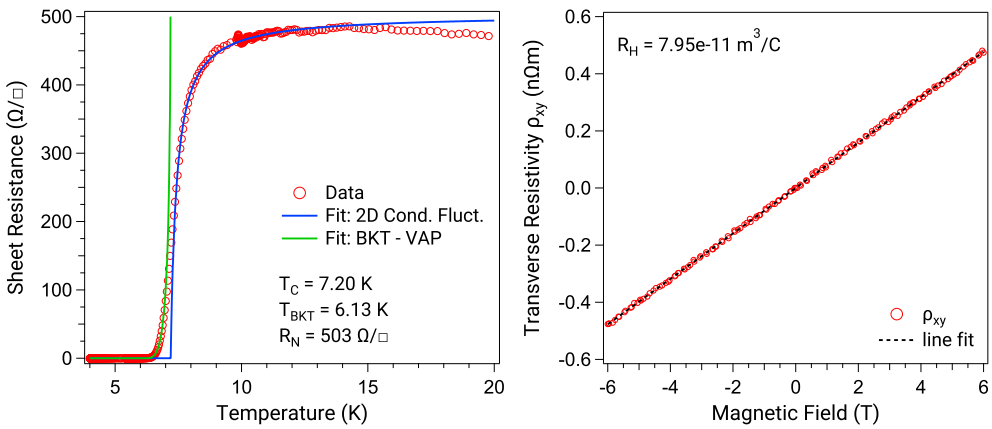

Figure 11.1: **(right)** $R(T)$ characteristic of a NbN nanowire superinductor. The blue and green lines are fits to Eqs. 2.57 and 2.62 respectively. **(left)** Hall transverse resistivity as a function of magnetic field of our NbN thin film, measured at $T = 15\,\mathrm{K}$.

Building on the methods and results presented in chapter 10, we have carefully optimised the fabrication of NbN thin-films. For nanowire superinductors, we found that a film with target thickness of 20 nm and deposited at a nitrogen mole fraction of 10.7 %, corresponding to a critical temperature $T_c = 7.20\,\mathrm{K}$ and a normal-state resistance $R_N = 503\,\Omega/\square$, is a good compromise between disorder and kinetic inductance, with a corresponding sheet kinetic inductance $L_k = 82\,\mathrm{pH}/\square$. In Fig. 11.1 (left), we show the $R(T)$ characteristic,

with fits to Eqs. 2.57 and 2.62, of a 40 nm-wide nanowire fabricated from this film. The Hall measurement of the film is shown in Fig. 11.1. The material parameters derived from these measurements are summarised in table 11.1.

11.2 Microwave Characterisation

11.2.1 Microwave Response

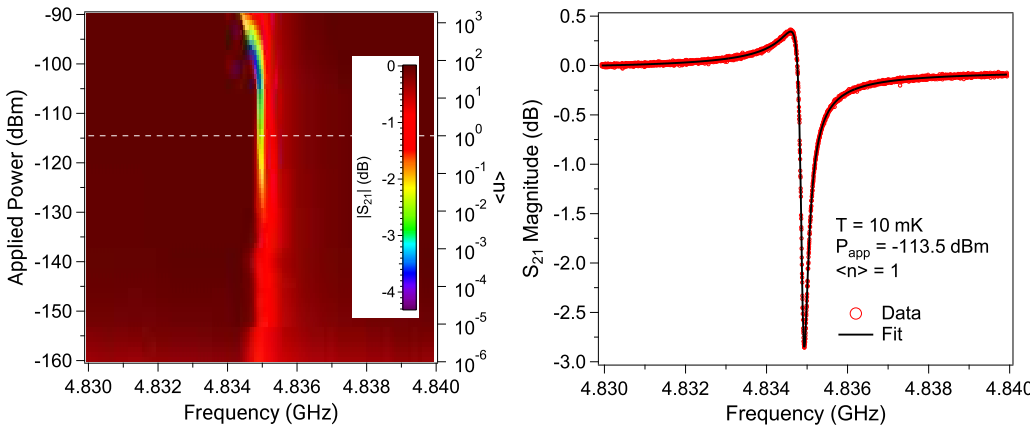

Figure 11.2: **(left)** S_{21} magnitude response across the full range of applied microwave drive for a typical nanowire superinductor. The dashed line corresponds to the single microwave photon regime. **(right)** S_{21} magnitude response of the same device in the single photon regime. The black line is a fit to Eq. 3.23 to determine the resonance parameters.

We study the microwave properties of our superinductors at 10 mK by measuring the forward transmission S_{21} response at a wide range of excitation powers (see section 7.3.2 for details of the measurement setup). We fit the data with the model described in section 3.3.3 to determine the resonator parameters. Due to the large impedance of our resonator, we are able to measure in the low photon regime with a high applied power. Consequently, this enables us to measure, with good signal-to-noise ratio, photon populations two to three orders of magnitude lower than in conventional resonators.

Fig. 11.2 shows the microwave response of a typical nanowire superinductor. For this device, which consists of a 692 µm long nanowire, at an average photon population $\langle n \rangle = 1$, we find a resonance frequency $f_r = 4.835$ GHz and an internal quality factor $Q_i = 2.5 \times 10^4$. We emphasize that the measured resonance frequency is within 1% of the resonance frequency estimated from the simulated capacitance and kinetic inductance obtained from transport measurements. Starting at the dashed line in Fig. 11.2 (left), as we increase power, the resonance frequency does not change until $\langle n \rangle \simeq 10$. From $\langle n \rangle \simeq 10$, as power increases, the frequency decreases until the resonator bifurcates. This

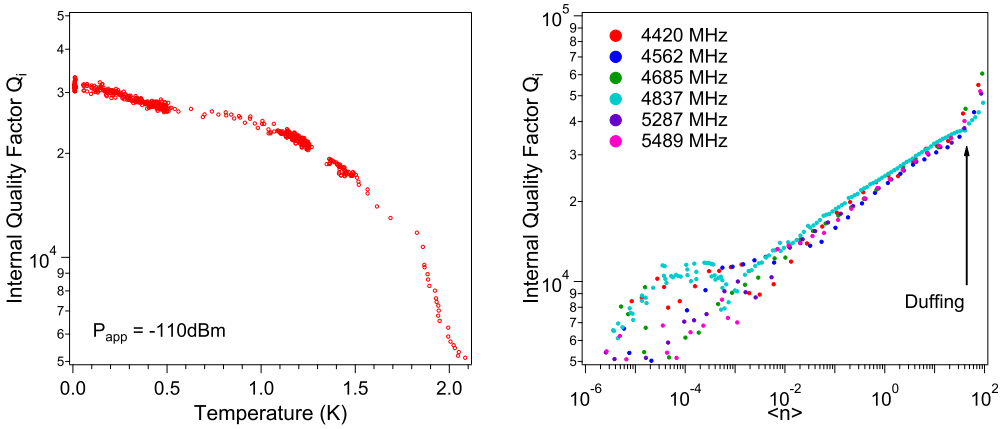

Figure 11.3: **(left)** Plot of the internal quality factor Q_i of a nanowire superinductor resonator as a function of temperature. **(right)** Internal quality factor as a function of average number of photons in the resonator, $\langle n \rangle$, of various nanowire superinductors.

is explained by the power dependence of the kinetic inductance, which behaves as a Duffing-like non-linearity [240] (see appendix D for additional details). We note that this non-linearity occurs at similar microwave drives as junctions-embedded resonators [241, 242].

Starting again at $\langle n \rangle = 1$, as we decrease power, we see the frequency remain approximately constant. Additionally, we see a change in contrast which corresponds to a reduction in the magnitude of the resonance dip and is examined in more detail in the next section. We also find that below $\langle n \rangle = 10^{-3}$, the resonator exhibits frequency jitter (see Fig. 11.4 (left)), consistent with TLS-induced permittivity changes [26]. This frequency noise results in spectral broadening of the resonance curve. A detailed study of these fluctuations is presented in Paper C and chapter 13.

Additionally, we determine the range of temperatures at which we can operate our device. Fig. 11.3 (left) shows a measurement of the internal quality factor Q_i against temperature. We see that from 10 mK to 1.4 K, the quality factor only marginally decreases from 3×10^4 to 2×10^4. We note that this offers a far greater range of operation that aluminium JJA-based superinductors which show significant dissipation above 100 mK [10].

Similar measurements and data analysis were carried out on several nanowire superinductors. We find good reproducibility between resonators and similar internal quality factors as highlighted in Fig. 11.3 (right).

11.2.2 Loss Study

In this section, we characterise the losses in our nanowire superinductors. We start by examining the internal quality factor as a function of the applied microwave power (see

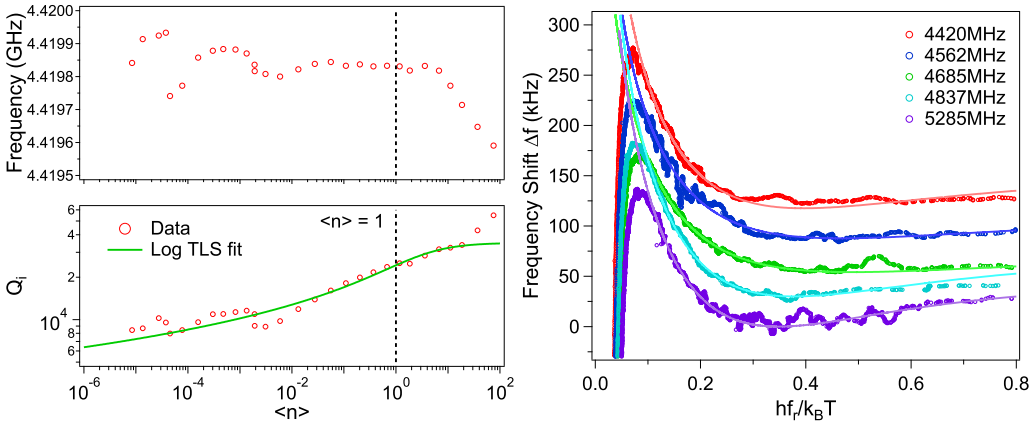

Figure 11.4: **(left)** Resonant frequency (top) and internal quality factor (bottom) of a typical nanowire resonator as a function of microwave drive. The solid line is a fit to Eq. (4.2). The vertical dashed lines highlight the single microwave photon regime. **(right)** Frequency shift as a function of the normalised frequency of all the nanowire superinductor resonators. The solid lines show fits to the theory described by Eq. (4.3), which is then used as an input to the fitting of Q_i in the left panel. For clarity, the curves have been offset by 30 kHz.

Fig. 11.4 (left)). Between the range of $\langle n \rangle \simeq 10^{-5}$ and $\langle n \rangle \simeq 10^{-3}$, we find that Q_i is approximately constant, with changes in Q_i that are caused by frequency jitter-induced spectral broadening. From $\langle n \rangle \simeq 10^{-3}$, as we increase power, Q_i increases, which is consistent with depolarisation of TLS. This effect is magnified in these resonators due to the large impedance which increases the sensitivity to fluctuations of the electric field.

In order to fit the data, we first need to independently determine the intrinsic loss tangent $F \tan \delta^i_{TLS}$. For that purpose, we track the frequency changes of the nanowire resonator against temperature using a Pound frequency-locked loop (P-FLL - see section 7.1). Fig. 11.4 (right) shows the changes in resonance frequency against the natural energy scale of the TLS (hf_r/k_BT). We fit the data with Eq. 4.3, which yields $F \tan \delta^i_{TLS}$. Importantly, this expression fits only the TLS contribution but does not fit the temperature-dependent kinetic inductance contribution which occurs below $hf_r/k_BT = 0.1$. Then, we use this fitted value of $F \tan \delta^i_{TLS}$ to fit the data in Fig. 11.4 (left) to the logarithmic TLS model described in section 4.3.1. The values obtained from both fits are summarised in table 11.2. Most notably, we find values of P_γ between 0.153 and 0.218. As described in section 4.3.1, P_γ is the TLS switching rate ratio, defined by $P_\gamma = 1/\ln(\gamma_{max}/\gamma_{min})$ where γ_{max} and γ_{min} are the maximum and minimum rate of TLS switching respectively. These rates have been measured in the TLS-related charge-noise spectrum of single-electron transistors and were found to extend from $\gamma_{min} \simeq 100$ Hz to $\gamma_{max} \simeq 25$ kHz [243], which corresponds to $P_\gamma = 0.18$. Our fitted values are in good agreement with this estimate and other experimental results [27, 28, 244].

11.2.3 Discussion

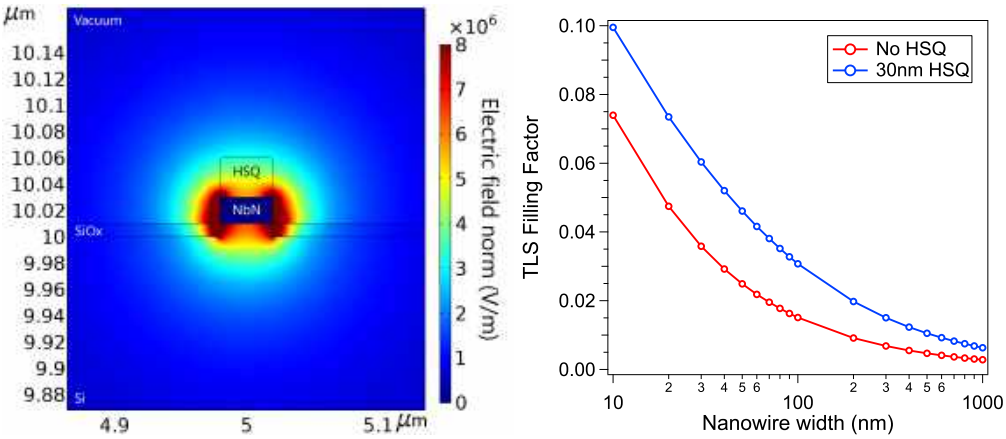

Figure 11.5: **(left)** Magnitude of the electric field for a 40 nm wide nanowire with unetched HSQ on top. **(right)** TLS filling factor for nanowire with (red) and without HSQ (blue) and for widths ranging from 1 µm to 10 nm.

The results shown in the previous sections demonstrate that dissipation in our nanowires is not an intrinsic property of disorder within the film [122, 123] but is instead caused by TLS. This is not surprising as TLS are the predominant source of dissipation and decoherence in a wide variety of quantum devices. We have also shown the role and scaling of the TLS filling factor in our devices, which leads to an unfavorable filling factor for the 40 nm width used here to produce a superinductor. This therefore leads to a much lower Q_i than is found for wider superconducting resonator geometries.

Additionally, as described in section 6.6.1, the nanowire lithography relies on the use of a spin-on glass resist (HSQ) which resembles amorphous silicon oxide. Because some HSQ remains unetched atop our nanowires, we suspect this is the dominant source of TLS in our devices. Cross-linked HSQ has a complex structure [245, 246], however, working under the assumption that it can reasonably be modeled by a conventional silicon oxide layer, we have reproduced the simulations of section 9.1.2 to get a qualitative feel for the influence of the HSQ on the filling factor. We model the unetched HSQ as a 30 nm thick silicon oxide layer on top of the nanowire and the filling factor is once again calculated using Eq. 9.1. The results of the simulation are shown in Fig. 11.5. We see that the filling factor is increased by almost a factor of two for the nanowire with HSQ, which qualitatively shows that the non-trivial removal of the HSQ mask should result in a significant improvement in device performance. In Paper B and in chapter 12, we study the microwave losses due to HSQ in conventional coplanar NbN resonators and quantitatively show that HSQ indeed has a dominant contribution the the loss.

Table 11.1: Parameters of the 20 nm NbN thin-film used for the fabrication of nanowire superinductors, calculated from Hall effect and $R(T)$ measurements.

Parameter name	Symbol	Value
Critical temperature	T_c	$7.20\,\mathrm{K}$
Normal-state resistance	R_N	$503\,\Omega/\square$
Hall coefficient	R_H	$7.95 \times 10^{11}\,\mathrm{m^3\,C^{-1}}$
Upper critical field	$\mu_0 H_{c2}$	$13.2\,\mathrm{T}$
Superconducting gap	Δ_0	$1.29\,\mathrm{meV}$
Kinetic inductance	L_k	$82\,\mathrm{pH}/\square$
Carrier density	n_n	$7.85 \times 10^{28}\,\mathrm{m^{-3}}$
Fermi wavevector	k_F	$1.32 \times 10^{10}\,\mathrm{m^{-1}}$
Fermi energy	ε_F	$1.07 \times 10^{-18}\,\mathrm{J}$
Fermi velocity	v_F	$1.53 \times 10^{6}\,\mathrm{m\,s^{-1}}$
Density of states	$\rho_s(\varepsilon_F)$	$1.76 \times 10^{28}\,\mathrm{eV^{-1}\,m^{-3}}$
Electron mean free path	l	$103\,\mathrm{pm}$
Ioffe-Regel parameter	$k_F l$	1.36
London penetration depth	λ_{dirty}	$905\,\mathrm{nm}$
GL coherence length	ξ_0	$4.99\,\mathrm{nm}$
BCS coherence length	ξ_0	$236\,\mathrm{nm}$
Electron diffusivity	D	$52.6\,\mathrm{nm^2\,ps^{-1}}$
Critical current density	$j_c^{GL}(0)$	$4.06 \times 10^{6}\,\mathrm{A\,cm^{-2}}$

Table 11.2: Nanowire superinductance resonator parameters. $F\delta^i_{TLS}$ is obtained from fits to Eq. (4.3) and P_γ from fits to Eq. (4.2).

NW f_r (MHz)	$F\delta^i_{TLS}$ ($\times 10^{-5}$)	P_γ
4420	4.37	0.195
4562	3.84	0.183
4685	3.53	0.218
4837	4.40	0.153
5285	4.12	0.213

Chapter 12

Results - Geometric Scaling of Loss in Superconducting Resonators

In this chapter, we present the results of Paper B where we study the geometric scaling toward nanowire dimensions of two-level system loss in superconducting resonators. Our devices are made of disordered NbN, which, due to magnetic-field penetration, necessitates 3D finite-element simulation of the Maxwell–London equations at microwave frequencies to accurately model the current density and electric field distribution. From the field distribution, we compute the geometric filling factors of the lossy regions in our resonator structures and fit the experimental data to determine the intrinsic loss tangents of its interfaces and dielectrics. Additionally, we put an emphasis on the loss caused by spin-on-glass resists such as HSQ, which is used for the fabrication of nanowire superinductors (see sections 6.2.2, 6.6.1 and chapter 11). We find that, when used, HSQ is the dominant source of loss, with a loss tangent of $\delta^i_{HSQ} = 8 \times 10^{-3}$. The design of the samples used in this study is discussed in section 9.2 and the details of the sample fabrication can be found in section 6.6.2.

12.1 Microwave characterisation

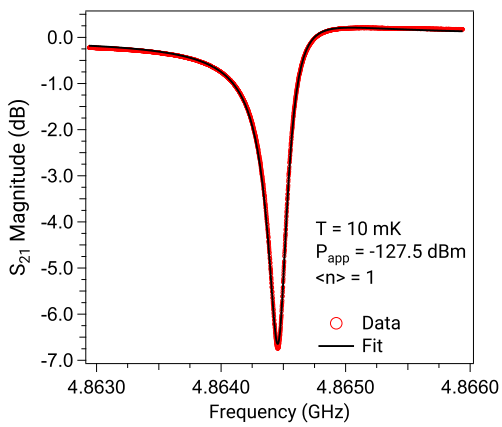

Figure 12.1: S_{21} magnitude response of a typical resonator in the single-photon regime (red points). The black line is a fit to Eq. 3.23 to determine the resonance parameters.

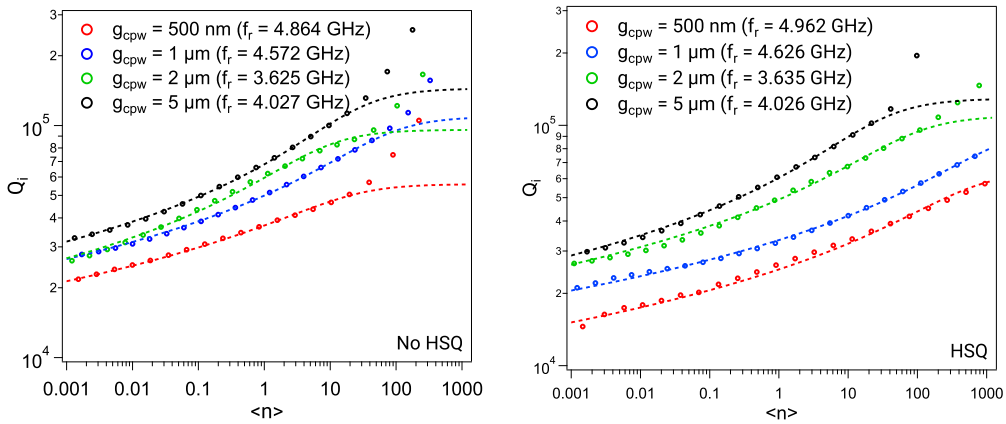

Figure 12.2: Internal quality factor (Q_i) as a function of the microwave drive power (in units of the resonator photon population $\langle n \rangle$) of all measured resonators without HSQ **(left)** and with HSQ covering the central conductor **(right)**. At high powers ($\langle n \rangle \geq 50$), Q_i is overestimated by the fitting routine as the resonator bifurcates due to the non-linear kinetic inductance [240]. The dashed lines are fits to Eq. 4.3.1.

In order to study the geometric scaling of dielectric losses, we fabricated NbN coplanar waveguide resonators, with and without HSQ dielectric on top of the center conductor. These devices span a range of widths of the center conductor and of the gap between center conductor and ground planes. The gap width ranges from $g_{cpw} = 500\,\text{nm}$ to $5\,\mu\text{m}$, with the ratio of the gap to the centre conductor kept fixed.

We start by studying the microwave properties of each of these resonators by measuring the forward transmission (S_{21}) response at a wide range of applied microwave drive, using the measurement setup detailed in section 7.3.2. Figure 12.1 shows a typical S_{21} magnitude response measured at 10 mK and an average photon population $\langle n \rangle = 1$. The resonator parameters are extracted by fitting the data with Eq. 3.23 and the results are shown in Fig. 12.2. We note that, for a given g_{cpw}, the resonators with the central conductor covered by HSQ (Fig. 12.2 (right)) systematically exhibit more loss than the bare resonators (Fig. 12.2 (left)), or, in other words, $Q_i(\text{HSQ}) < Q_i(\text{no HSQ})$. However, from Eq. 4.2 and for a given temperature and applied power, we see that since Q_i is dependent on the product $P_\gamma F \delta^i$, it is impossible to quantify whether this increase in loss is due solely to an increase in the participation ratio (the HSQ layer atop the central conductor adds a new lossy region - see Fig. 12.4) or if the total loss tangent also increases.

Therefore, in an effort to reliably determine the contribution of TLS, we measure the resonant frequency of each resonator against temperature between 10 mK and 1 K [17, 127] using a Pound frequency-locked loop (P–FLL). The data is shown in Fig. 12.3 and details of the measurement technique and setup can be found in section 7.1. This method probes only TLS effects and has the benefit of being sensitive to a wide frequency distribution of TLS and allows us to independently determine the intrinsic loss tangent (times the filling factor) $F_{TLS}\delta^i_{TLS}$. The fitted values are presented in table 12.1.

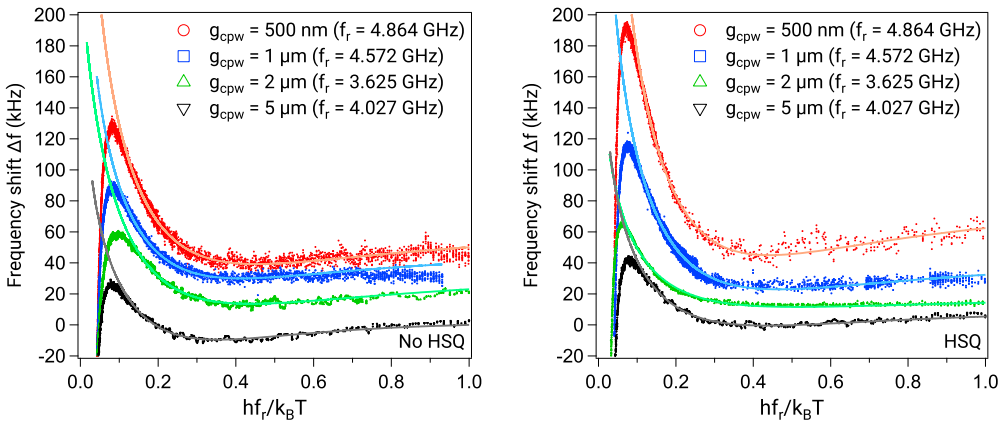

Figure 12.3: Frequency shift Δf as a function of the normalised frequency f_r of the measured resonators without HSQ **(left)** and with HSQ covering the central conductor **(right)**. The data is obtained by applying $P_{app} = -110\,\mathrm{dBm}$ and tracking the changes in resonant frequency against temperature between 10 mK and 1 K using the P–FLL. It is plotted against the natural energy scale of the TLS (hf_r/k_BT). The downturn in frequency occurring below $hf_r/k_BT = 0.1$ corresponds to the temperature-dependent kinetic inductance contribution and is not TLS-related. For clarity, the curves have been offset by 15 kHz. The solid lines are fits to Eq. 4.3.

12.2 Simulation results

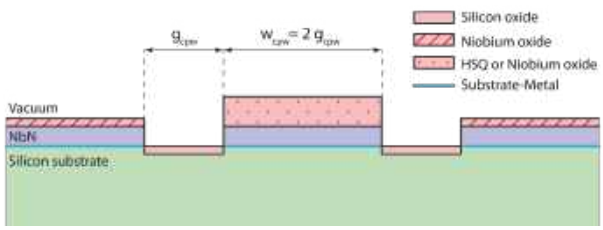

Figure 12.4: Schematic of the cross-section of the resonators. The TLS host volumes are shown in pink and the substrate-metal interface region is highlighted in blue.

In Figs. 12.2 and 12.3, we see that our devices are dominated by TLS loss. In order to analyse dielectric and interfacial losses in our devices, and in particular to identify those from the HSQ top dielectric, we perform electromagnetic simulations (with and without the HSQ layer) in Comsol Multiphysics for a wide range of resonator geometries. A sketch of the cross-section of the simulated structures is shown in Fig. 12.4.

The simulation parameters for the constituent materials are as follows: the substrate-air (SA) interface is modelled as a 5 nm thick layer of SiO_2 [247] with relative permittivity $\varepsilon_r(SiO_2) = 4.2$. The metal-air (MA) interface consists of a 5 nm thick layer of Nb_2O_5 [209] with relative permittivity $\varepsilon_r(Nb_2O_5) = 33$ [248, 249]. The substrate-metal (SM) interface

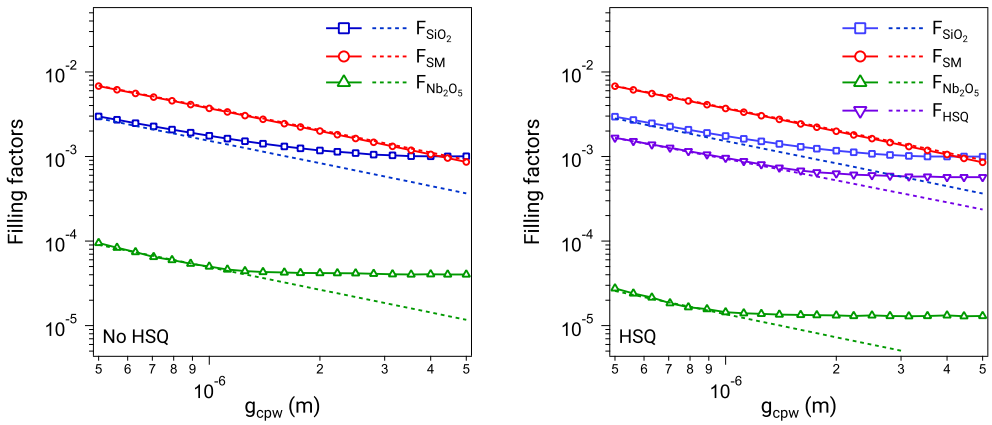

Figure 12.5: Simulated filling factors F as a function of the co-planar waveguide gap g_{cpw} for resonators without HSQ **(left)** and with HSQ covering the central conductor **(right)**. The dashed lines represent the incorrect F obtained with electrostatic simulations.

is modelled by a 2 nm thick layer inside the substrate ($\varepsilon_r(\text{SM}) = \varepsilon_r(\text{Si}) = 11.7$) [134]. Finally, the HSQ region has a thickness of 30 nm and relative permittivity $\varepsilon_r(\text{HSQ}) = 3$ [250]. Because Nb_2O_5 requires several days to achieve any meaningful thickness [209], it is assumed that no Nb_2O_5 is present underneath the HSQ. Therefore, on the samples without HSQ, Nb_2O_5 resides on both the central conductor and ground planes, whereas on the samples with HSQ, Nb_2O_5 is present only on the ground planes.

The superconductor part of the structure requires extra care to simulate accurately: disordered superconductors such as NbN have an extremely small electron mean free path l (see [238], section 10 and Table 10.2). From Eq. 2.36, we see that this small electron mean free path has for consequence an enhanced magnetic penetration depth. Consequently, it is not sufficient to approximate the current density in our NbN devices as a surface density, since magnetic fields significantly penetrate the superconductor. This is in contrast to resonators made of a conventional superconductor such as aluminium ($\lambda_L(0) \simeq 30$ nm [251, 252]) or niobium (100 nm [253]). In a similar way, it is insufficient to assume a uniform current distribution in the superconductor when the resonator dimensions are smaller than $\lambda_L(T)$. Therefore, a static solution of Maxwell's equations is insufficient here and would yield incorrect results, in particular for the wider geometries. We refer the reader to chapter 8 for details on the simulation techniques used to address these challenges.

From the simulated electric fields, we calculate the filling factor of each region using Eq. (4.5) and present the result in Fig. 12.5. Additionally, Fig. 12.5 shows filling factors calculated by means of electrostatic simulation to highlight the significant deviation from the Maxwell–London simulation results for $w_{cpw} > \lambda_L$. Using these simulated filling factors, we can fit Eq. (4.4) to the experimental results in Table 12.1 (see Fig. 12.6) and in this way determine the intrinsic loss tangent of each lossy region. These results are summarised in Table 4.4.

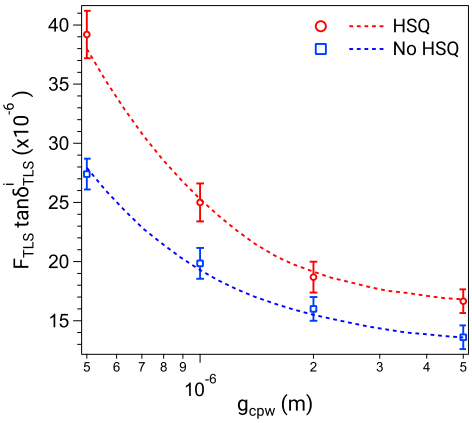

Figure 12.6: Total TLS loss $F_{TLS}\delta^i_{TLS}$ vs. gap width g_{cpw} of the co-planar waveguide for all four measured resonators. The $F_{TLS}\delta^i_{TLS}$ values are determined from fits of the $\Delta f(T)$ data in Fig. 12.3 — see Table 12.1. The error bars represent two standard deviations of uncertainty (95% confidence interval). The dashed lines are fits to Eq. (4.4) using the simulated filling factors F_{TLS} shown in Fig. 12.5.

12.3 Discussion

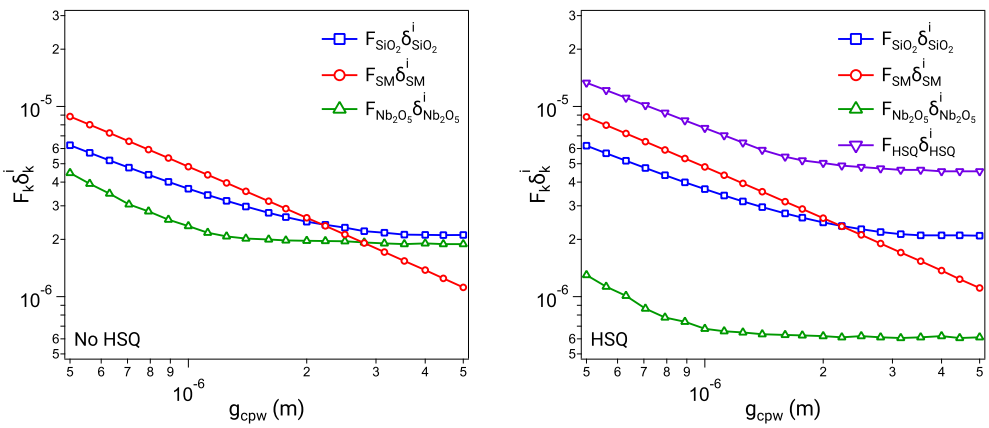

Figure 12.7: Contribution of each individual lossy region for resonators without HSQ **(left)** and with HSQ **(right)** covering the central conductor.

We find that our results are consistent with values found by other groups in similar types of devices [124, 131, 134, 248]. However, we emphasise that the fabrication of our devices was not focused on minimising the influence of TLS and therefore the internal quality factor of the resonators are comparatively small to the state of the art.

Additionally, this analysis allowed us to study the influence of HSQ on the dielectric loss. We find the intrinsic loss tangent for HSQ to be $\delta^i_{HSQ} = 8.0 \times 10^{-3}$. Paired with the relatively large filling factor of the HSQ region, this makes HSQ the dominant contribution to the loss for all dimensions, as highlighted in Fig. 12.7; and for a given dimension, $F_{TLS}\delta^i_{TLS}$ is systematically higher for the sample covered with HSQ, as shown in Fig. 12.6.

These results confirm that the porous amorphous silicon oxide structure of developed HSQ [171, 250] is a major source of dielectric loss. However, it is important to highlight that this situation is the worst case scenario: the use of HSQ is generally followed by an etching step where some of the HSQ mask will be eroded and therefore the participation ratio of the HSQ will be reduced. Furthermore, we note that due to its nature, HSQ can easily be removed with fluorine-based dry and wet etchants. However, such a process is not compatible with a wide range of materials (including NbN and other nitride-based compounds) that are also etched in fluorine chemistry. Therefore, a new process that allows for the removal of the HSQ mask would lead to significant improvements in device performance.

Table 12.1: Resonator parameters. $F_{TLS}\delta^i_{TLS}$ is obtained from fits of the data in Fig. 12.3.

g_{cpw} (µm)	Z_c (Ω)	f_r (MHz)		$F_{TLS}\delta^i_{TLS}$ ($\times 10^{-5}$)	
		no HSQ	HSQ	no HSQ	HSQ
5	207	4027	4026	1.36	1.66
2	312	3625	3635	1.60	1.87
1	441	4572	4626	1.98	2.50
0.5	632	4864	4962	2.74	3.92

Table 12.2: Fitted loss tangents of the different lossy regions. The values are obtained from fits to Eq. (4.4) using the simulated filling factors.

Region	Symbol	Value
HSQ	δ^i_{HSQ}	8.0×10^{-3}
Substrate-Metal interface	δ^i_{SM}	1.3×10^{-3}
Niobium oxide	$\delta^i_{\mathrm{Nb_2O_5}}$	4.7×10^{-2}
Silicon oxide	$\delta^i_{\mathrm{SiO_2}}$	2.1×10^{-3}

Chapter 13

Results - Fluctuations in Superconducting Circuits

In this chapter, we present the results of Papers C–E in which we study loss and noise in various type of superconducting quantum devices: transmon qubits and three different types of resonators: aluminium coplanar resonators, nanowire superinductors and an aluminium 3D cavity. We find that in all devices, the dissipation is dominated by two-level system dielectric loss. Additionally, by studying the parameter fluctuations in these devices and analysing the measurements with the statistical tools introduced in chapter 5, we show that the noise is dominated by a Lorentzian noise process consistent with spectrally unstable TLS. Furthermore, by studying the slow fluctuations of the resonant frequency as a function of drive power, we find that the Lorentzian noise amplitude and time constant of single fluctuators are power-dependent with similar power-law scaling for all resonators, suggesting a common mechanism.

We start our study by characterizing the losses and noise in a superconducting resonator (Paper D and section 13.1). This work was initially motivated as a benchmarking tool for the optimisation of the fabrication process of resonators and qubits. However, here, we present these results in the context of the understanding of TLS noise in superconducting devices, and we show that the measurement and analysis techniques are able to reveal TLS-based Lorentzian noise.

Then, we apply the same type of analysis on the fluctuations to the decoherence properties of superconducting transmon qubits (Paper E and section 13.2). We find that the fluctuations in qubit relaxation are caused by near-resonant TLS and we observe the coherent coupling between individual TLS and the qubit.

Finally, we investigate the noise properties of nanowire superinductors (Paper C and section 13.3), where we expect the loss to be dominated by strongly coupled TLS due to the large impedance of the device. In the noise, we find the signature of individual TLS, and we discover evidence of a power-dependent scaling of the Lorentzian noise amplitude and time constant. Then, we confirm this power dependence in the other two types of resonators, which suggests the universality of this phenomenon.

13.1 Noise in a Superconducting Resonator

In Paper D, we study the loss and noise of a superconducting aluminium resonator. The device consists of a quarter-wavelength ($\lambda/4$) coplanar waveguide resonator made of aluminium on a high resistivity silicon substrate. The details of the device fabrication can be found in section 6.6.2 and appendix A.

In the following, we first present the microwave characterisation of the resonator and show that its losses are consistent with depolarisation of TLS. Then, we study the noise properties of the resonator at single microwave photon energies.

13.1.1 Microwave Characterisation

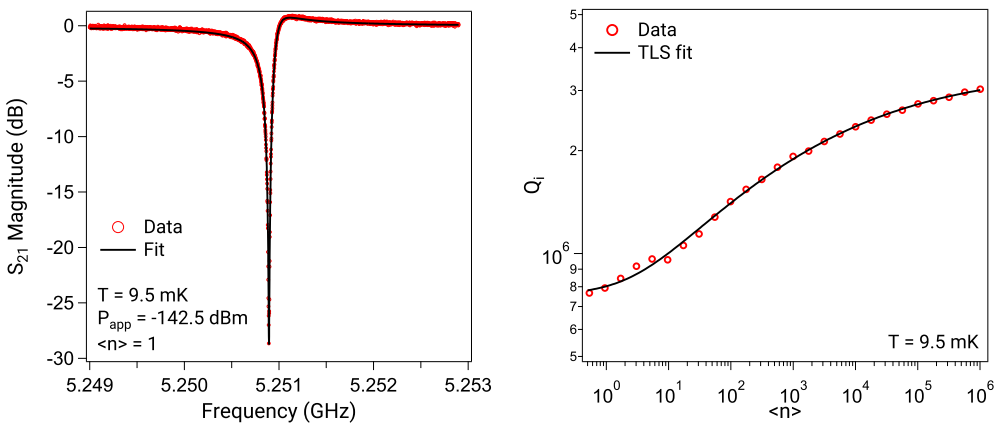

Figure 13.1: **(left)** S_{21} magnitude response of the superconducting resonator, measured at 9.5 mK and applied microwave drive $P_{app} = -142.5$ dBm, which corresponds to $\langle n \rangle = 1$. The black line is a fit to Eq. 3.23 to extract the resonator parameters. **(right)** Q_i as a function of $\langle n \rangle$ for the resonator at 9.5 mK. The black line is a fit to TLS losses described by Eq. 4.2.

The S_{21} transmission response of the superconducting resonator is measured at 9.5 mK while the microwave power is varied. The data is fitted to Eq. 3.23 to extract the resonant frequency (f_r), internal quality factor (Q_i) and coupling quality factor (Q_c). Figure 13.1 (left) shows the fitted S_{21} magnitude response of the resonator at 9.5 mK for an applied microwave power (P_{app}) of -142.5 dBm, which corresponds to an average photon population in the resonator of $\langle n \rangle = 1$ (Eq. 3.22). For this resonator, we find, at $\langle n \rangle = 1$, $f_{\sim}5.250\,93$ GHz, $Q_c \simeq 3.3 \times 10^4$ and $Q_i \simeq 7.9 \times 10^5$.

Fig. 13.1 (right) shows a measurement of Q_i as a function of $\langle n \rangle$. The decrease in Q_i as P_{app} ($\langle n \rangle$) is varied is consistent with depolarisation of TLS [26, 27, 254–258]. To quantify this effect, we fit the data with Eq. 4.2. Most notably, we find $F\delta^i_{TLS} = 1.0 \times 10^{-6}$ (for $P_\gamma \simeq 0.2$) and the next dominant loss is found to be $\delta_0 \simeq 2.9 \times 10^{-7}$. We note that

these loss rates are comparable with those of state of the art resonators reported in the literature [255].

13.1.2 Noise Measurements

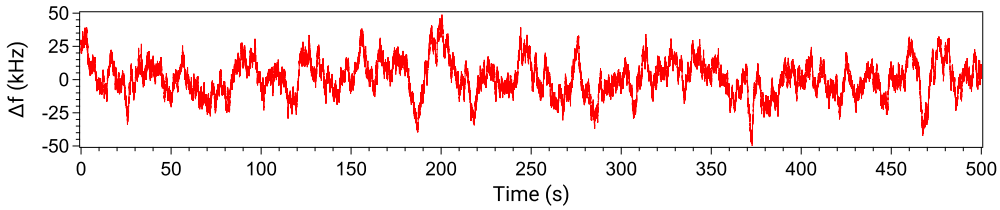

Figure 13.2: Raw frequency jitter of the resonator measured at $\langle n \rangle = 1$ and a temperature of 9.5 mK.

The loss induced by the TLS corresponds to the resonant absorption of microwave photons. Recent experiments have also examined the role of these resonant TLS in contributing noise to the resonator [26, 259]. The dependence of TLS-induced noise has been measured as a function of P_{app} and temperature. Within these studies, the temperature dependence has been thoroughly examined in the range of $50 - 700$ mK; however, the span of P_{app} that was examined corresponds to $\langle n \rangle \simeq 7 - 1 \times 10^4$ and, consequently, the TLS noise in the limit of single-photon excitation has not been examined. Not only is this limit most relevant to dephasing in superconducting qubits, but it is also relevant to revealing properties of TLS in general.

We use the Pound frequency-locked lopp (P-FLL) to continuously monitor the resonant frequency f_r as a function of time. Details of the technique and measurement setup can be found in chapter 7. We operate the P-FLL at a bandwidth of 300 Hz and the data is sampled at 100 Hz, and, therefore, we note that our measurement is only sensitive to slow fluctuations of the resonant frequency. Figure 13.2 shows a 500 s window of a measurement of the frequency jitter of the resonator, measured at $\langle n \rangle = 1$ and at 9.5 mK. This frequency jitter can be better understood by examining the the overlapping Allan deviation σ_y and spectrum S_y of frequency fluctuations. The power spectral density is obtained using the Welch spectral density estimate with a 50% overlap and a Hamming window (see chapter 5). The resulting plots of σ_y and S_y are shown in Fig. 13.3. In Fig. 13.3 (right), we note the peak at $\tau \simeq 10$ s and subsequent decay, which is an unambiguous sign of a Lorentzian noise process (see chapter 5). Therefore, we model the noise in Fig. 13.3 as a combination of a Lorentzian and a white noise floor and we apply the noise to both the spectrum and the Allan deviation such that the noise parameters are the same for both plots. We find a white noise level of $h_0 = 1.1 \times 10^{-15}\,\mathrm{Hz}^{-1}$, and the Lorentzian noise is characterised by a switching characteristic time $\tau_0 = 3.7$ s and an amplitude $A = 13.7$ kHz. We refer the reader to chapter 5 for the expressions of the representation of Lorentzian and white noise in both PSD and Allan deviation.

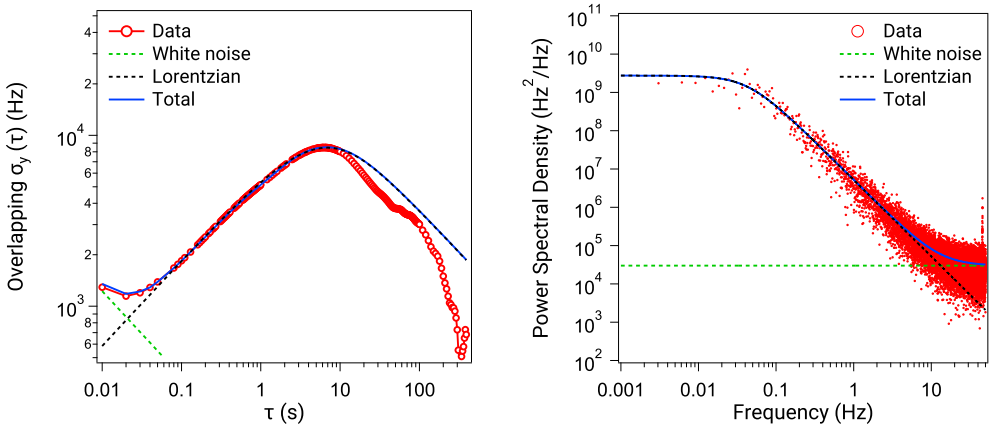

Figure 13.3: Overlapping Allan deviation **(left)** and power spectral density **(right)** for the measured frequency fluctuations of the resonator. The total noise model is shown as a solid blue line, which is formed of white noise (dashed green) and a Lorentzian (dashed black).

13.1.3 Discussion and Conclusion

We measured frequency noise of a high-Q superconducting resonator at single photon energies. This is an important step towards studies of interacting TLS (see chapter 4), which are currently limiting the performance of many superconducting circuits. In showing that noise can be measured at single photon energies with the P-FLL, we extend this technique to characterising noise in circuit-QED architectures, where a superconducting qubit is dispersively coupled to the resonator. Because of the dispersive frequency shift, any noise of the qubit would get mapped to a frequency noise in the resonator.

Furthermore, with the statistical analysis of the frequency fluctuations in the resonator, we find that the noise in the resonator can be explained by a single Lorentzian feature. This implies that the noise is dominated by the switching of one or a few sparse two-level systems [260, 261]. This result is not unexpected as a high Q is an indication that the TLS density is low. On the other hand, for lower quality factor devices, as the density of TLS is higher, a larger number of Lorentzians with different amplitudes and switching rates contribute to the noise and eventually form a continuum, corresponding to $1/f$ noise [260, 261].

13.2 T_1 Fluctuations in a Transmon Qubit

In Paper E, we repeatedly characterise the decoherence of superconducting transmon qubits to examine the temporal stability of energy relaxation, dephasing, and qubit transition frequency. By collecting statistics during measurements spanning multiple days, we find the mean parameters $\overline{T_1} = 49\,\mu s$ and $\overline{T_2^*} = 95\,\mu s$; however, both of these quantities fluctuate by up to 20%, explaining the need for frequent re-calibration in qubit setups. Our main finding is that fluctuations in qubit relaxation are local to the qubit and are caused by instabilities of near-resonant two-level-systems (TLS). Through statistical analysis, we determine sub-millihertz switching rates of these TLS and observe the coherent coupling between an individual TLS and a transmon qubit. Finally, we find evidence that the qubit's frequency stability produces a 0.8 ms limit on the pure dephasing which we also observe.

In this section, we focus on the fluctuations of T_1 and their relation to TLS. We start by a description of the devices and present the results of synchronous measurements of T_1 in two devices, highlighting that fluctuations are local to each qubit. Then, from the T_1 decay profiles across a wide span of measurements, we find evidence of coherent coupling between a TLS and the qubit and we extract the qubit-to-TLS coupling. Finally, we perform a statistical analysis and find that these fluctuations in T_1 can be described by Lorentzian noise with switching rates in the range from 75 µHz to 1 mHz.

13.2.1 Device Description

The devices consist of a single-junction Xmon-type transmon qubit [262] capacitively coupled to a microwave readout resonator and are fabricated with aluminium on a high-resistivity intrinsic silicon substrate. The shunt capacitor and the absence of magnetic-flux tunability (absence of a SQUID) effectively decouple the qubit frequency from electrical charge and magnetic flux, reducing the sensitivity to these typical $1/f$ noise sources [263, 264]. Furthermore, the circuit is intentionally kept simple so that the decoherence is dominated by intrinsic mechanisms and not external ones in the experimental setup. Therefore, there are no individual qubit drive lines, nor any qubit-to-qubit couplings. Additionally, both the spectral linewidth of the resonator and the resonator-qubit coupling are kept small, such that photon emission into the resonator (Purcell effect) and dephasing induced by residual thermal population of the resonator are minimised [265].

The results of Paper E involve two qubits on separate chips which we name A and B. The main differences between qubit A and qubit B are their Josephson and charging energies and that the capacitor of qubit B was trenched to reduce the participation of dielectric loss [266]. The device parameters are summarised in table 13.1.

13.2.2 Synchronous T_1 Measurement of Separate Qubits

We start by assessing the stability of the energy-relaxation time T_1 by consecutive measurements. The transmon is driven from its ground to first-excited state by a calibrated π pulse. The qubit state is then read out with a variable delay. The population of the excited state, as a function of the readout delay, is fit to a single-exponential decay to determine T_1. Fig. 13.4 (a) shows a 65-hour measurement of two separate qubits (in separate sample enclosures) that are measured simultaneously and in Fig. 13.4 (b), we histogram the T_1 data: this demonstrates that T_1 can vary by more than a factor 2 for both qubits, similarly to previous studies[23, 162].

We calculate the magnitude-squared coherence of the two data sets to determine whether the observed fluctuations in T_1 are local to each qubit or not. The magnitude-squared coherence examines how much the T_1 of qubit A corresponds to the T_1 of qubit B and is normalised between 0 and 1, where 1 means completely correlated. We show the magnitude-squared coherence in Fig. 13.4 (c) along threshold levels for 99%, 98% and 95% confidence calculated from statistical bootstrapping (repeatedly examining the magnitude-squared coherence of randomly re-sampled sets of one of the data set vs. the other original data set). The data in Fig. 13.4 (c) is clearly far below these thresholds; therefore, we conclude that the periods of low-T_1 values are not synchronised between the two qubits, indicating that the dominant mechanism for T_1 fluctuations is local to each qubit.

To make a fair comparison of the mean T_1 for two qubits with different frequencies, we can instead compare quality factors with $Q = 2\pi f_{01} T_1$: we find that qubit A has a quality factor $Q = 1.29 \times 10^6$ and qubit B has $Q = 1.67 \times 10^6$. We see that qubit B has a higher quality factor, however, it has a lower ratio of Josephson to charging energy (see table 13.1), resulting in a larger sensitivity to charge noise and parity effects [267]. Consequently, qubit B exhibits switching between two different transition frequencies, which was not suitable for later dephasing and frequency instability studies. Therefore, the following sections focus on qubit A.

13.2.3 T_1 Decay Profiles

We continue our study by measuring T_1 consecutively for approximately 128 hours. We plot the data Fig. 13.4 (right) as a colour map, which makes some features of the data simpler to visualise. The first observation we make is that the fluctuations are comprised of a switching between different T_1 values, where the switching is instantaneous, but the dwell time at a particular value is typically between 2 and 12.5 hours. This behaviour, also visible in Fig. 13.4 (a), is reminiscent of telegraphic noise with switching rates ranging from 20 µHz to 140 µHz.

In Fig. 13.4 (right), the white dashed box and the top inset show this switching behaviour occurring within a single iteration. The decay, found in approximately 3% of the iterations, can be fit to two different values of T_1, one before the switch and one afterwards.

The black dashed box and bottom inset highlight a decay-profile that is no longer purely

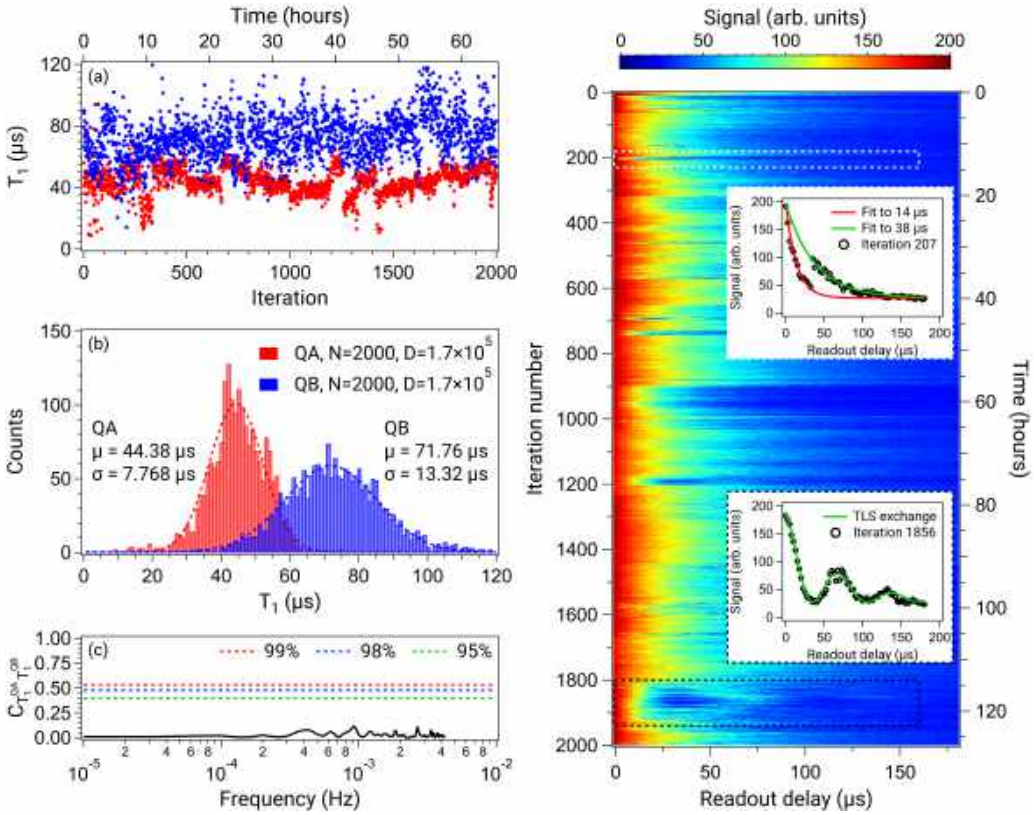

Figure 13.4: **(left)** Multiple T_1 measurements (a) performed simultaneously on qubits A (red) and B (blue) with corresponding histograms (b) and magnitude-squared coherence (c). The data consists of $N = 2000$ consecutive T_1 measurements that lasted a total duration of $D = 2.36 \times 10^5$ s (approximately 65 hours). The histograms have been fit (dashed lines) to Gaussian distributions with the parameters shown. The dashed lines in (c) represent the significance levels obtained from statistical bootstrapping. **(right)** Raw data of T_1 decay-profile. Consecutive T_1 measurements, spanning 4.6×10^5 s (approximately 128 h), of qubit A. The top inset shows a data set with a change in T_1 within a single iteration. These jumps are found to occur in approximately 3% of all measurements. The bottom inset shows a data set with a decaying sinusoidal (rather than a purely exponential) decay profile. The appearance of revivals are due to resonant exchange with a TLS. These profiles are found to occur in approximately 5% of all iterations.

exponential, but instead exhibits revivals. Similar revivals have been observed in both phase [268] and flux [269] qubits, and were attributed to coherently coupled TLS residing in one of the qubit junctions. Approximately 5% of decay profiles show a clear revival structure, with a further 3% showing hints of it. Of these, some revival shapes (such as the one shown in the black box) remained stable and persisted for approximately 10 hours, whereas others lasted for only 2–3 traces (around 10 minutes). Since the qubit here is fixed in frequency, these appearances/disappearances of the coherent TLS arise

due to the TLS shifting in frequency [22, 23, 26, 162] relative to the static qubit. The observation of coherent oscillations in the decay, and in particular that oscillation periods remained stable for hours (for the same duration as the T_1 fluctuations), constitutes clear evidence for TLS being the origin of the T_1 fluctuations, in agreement with both the results of Müller [162] and Klimov [23].

The coherent coupling between the qubit and a single TLS can be extracted by fitting the energy relaxation of the qubit to [270]:

$$\langle\sigma_z(t)\rangle = \langle\sigma_z\rangle_\infty + a_{\downarrow,1}e^{-\Gamma_{\downarrow,1}t} + a_{\downarrow,2}e^{-\Gamma_{\downarrow,2}t} + a_{osc}\cos(2\pi f_{osc}t)e^{-\Gamma_{osc}t} \tag{13.1}$$

where $\langle\sigma_z\rangle$ is the expectation value of the Pauli matrix for the qubit, $\langle\sigma_z\rangle_\infty$ is the zero-temperature equilibrium value, $a_{\downarrow,k}$ and $\Gamma_{\downarrow,k}$ are the amplitude and decay rate from the two excited states k ($k = 1, 2$) to the ground state, and a_{osc}, f_{osc}, and Γ_{osc} describe the amplitude, frequency, and decay rate of an oscillation in $\langle\sigma_z\rangle$. These parameters can be rewritten in terms of coupling, g_{TLS}, and detuning, $\delta f = f_{01} - f_{\mathrm{TLS}}$:

$$f_{osc} = \sqrt{g_{\mathrm{TLS}}^2 + \delta f^2} \tag{13.2}$$

$$a_{osc} = \frac{g_{\mathrm{TLS}}^2}{g_{\mathrm{TLS}}^2 + \delta f^2} \tag{13.3}$$

We fit the oscillations to this model and find a coupling rate $g_{TLS} = 4.8\,\mathrm{kHz}$.

13.2.4 Statistical Analysis and Discussion

To gain further insight into these fluctuations, we perform a statistical analysis using the tools described in chapter 5: we examine both the overlapping Allan deviation (Fig. 13.5 (left)) and the spectral properties (Fig. 13.5 (right)) of the T_1 fluctuations.

In the Allan deviation, we immediately recognise the signature of Lorentzian noise from the peak and subsequent decay around $\tau \simeq 1 \times 10^{-4}\,\mathrm{s}$ (see section 13.1), which is consistent with the switching noise observed in Fig. 13.4. We find that the noise is best described with two Lorentzians and a white noise floor, and apply the modelled noise to both the spectrum and the Allan deviation. Similarly to section 13.1, the noise is fitted in the spectrum and Allan deviation using a common set of parameters. With the data in Fig. 13.5, we obtain Lorentzian switching rates of 80.6 µHz and 158.7 µHz.

The reproducibility of these results across several thermal cycles is discussed in Fig. 4 and supplementary Fig. 2 of Paper E. Interestingly, while the TLS configuration, and therefore the detuning and coupling of the observed near-resonant TLS, is expected to completely change between each cooldown, at least one spectrally-unstable near-resonant TLS that follows similar switching statistics is always found to exist.

Collectively, we find switching rates ranging from 71.4 µHz to 1.9 mHz. While these rates are slower than those obtained by measurements of charge noise [243], they are similar to bulk-TLS dynamics [271, 272] and in agreement with rates determined from

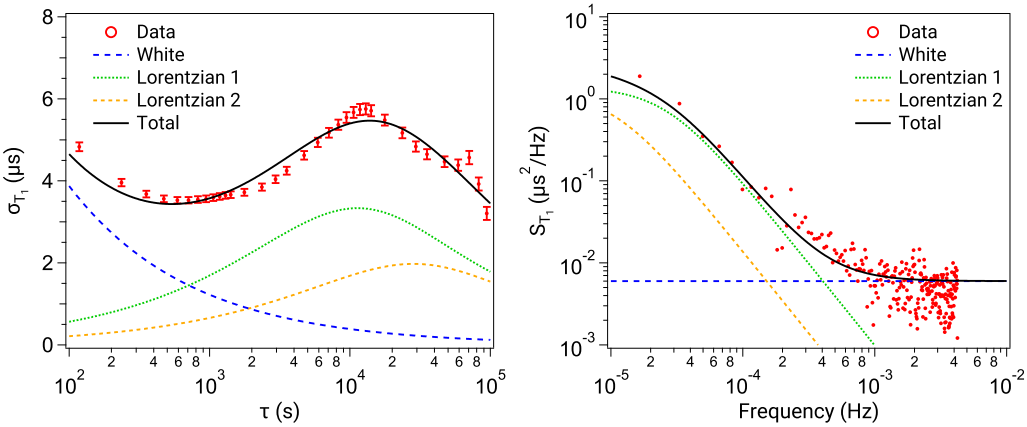

Figure 13.5: Statistical analysis of 2001 sequential T_1 measurements of qubit A spanning a total measurement duration of 2.36×10^5 s. **(left)** Overlapping Allan deviation of T_1 fluctuations. **(right)** Welch power spectral density of T_1 fluctuations. In both plots there are fits to the total noise (black line) which is formed of white noise (blue lines) and two different Lorentzians (green and yellow lines). The amplitudes and time constants of all noise processes are the same for both types of analysis.

measurements tracking the time evolution of individual TLS [23]. In contrast, when comparing to quasiparticle relaxation, we find that quasiparticle-related mechanisms differ by over six orders of magnitude compared to those found in our experiment: in aluminium, the quasiparticle recombination rate is found to be 1 kHz [273] and the timescale of quasiparticle number fluctuations leads to rates in the range $0.1 - 10$ kHz. Finally, quasiparticle tunnelling (parity switching events) in transmons have rates in the range $0.1 - 30$ kHz [267].

Additionally, the observed coherent qubit–TLS coupling (bottom inset in Fig. 13.4 (left)) is a clear sign of the existence of a near-resonant TLS and its fluctuation, following similar time constants as the T_1 fluctuations, constitutes clear evidence of spectral instability, as expected from the interacting-TLS model [22, 26].

Therefore, we attribute the origin of the T_1 decay to near-resonant TLS, and the Lorentzian fluctuations in the qubit T_1 arise due to spectral instabilities of the TLS as described by Müller et al. [162]. The extracted switching rates then represent the rate at which the near-resonant TLS is changing frequency.

These measurements demonstrate not only that superconducting qubits are useful probes of TLS, but unambiguously demonstrate the role of a TLS-based Lorentzian noise profile as a limiting factor to the temporal stability of qubit coherence.

Table 13.1: Summary of device parameters. f_r and f_{01} are the frequency of the readout resonator and the qubit $0 \to 1$ transition, respectively. $f_{12} - f_{01}$ is the frequency difference between the qubit $1 \to 2$ and $0 \to 1$ transitions (anharmonicity). E_J is the Josephson energy, E_C the charging energy, h is Planck's constant, and ε_0 the qubit charge dispersion. We refer the reader to section 2.5 for a detailed description of these parameters.

Parameters	Qubit A	Qubit B
f_r	6.035 GHz	5.540 GHz
f_{01}	4.437 GHz	3.759 GHz
$f_{12} - f_{01}$	−0.226 GHz	−0.278 GHz
E_J/h	13.42 GHz	8.57 GHz
E_C/h	0.201 GHz	0.235 GHz
E_J/E_C	66.67	36.54
ε_0/h	−524 Hz	−109 kHz

13.3 Drive-power Dependent Fluctuations

In Paper C, we examine the frequency fluctuations of types of superconducting resonators – one NbN nanowire superinductor, one Al coplanar waveguide, and one Al 3D cavity – with the Pound frequency-locked loop (P-FLL) to explore whether there is a common noise process between the different devices. By analyzing the power spectra and the overlapping Allan deviation computed from the time-domain fluctuations, we identify individual Lorentzian fluctuators in the noise with mHz timescales in all the resonators. Furthermore, when studying the evolution of this noise as a function of microwave drive power, we observe a similar power-law dependence of the Lorentzian switching time on the circulating power in the resonator for all the devices, which suggests a common noise mechanism.

In this section, we first present the devices that were measured in this study and examine their frequency fluctuations. Then, we perform a statistical analysis of the measured frequency fluctuations and discuss a noise model to interpret the data. Finally, we apply this technique to data sets measured across all devices and a wide range of applied microwave power and show that the noise follows the same dynamic in all three devices, albeit at widely different amplitudes.

13.3.1 Device Description

The devices studied in Paper C consists of three superconducting resonators of different types. The first resonator is a niobium nitride superinductor nanowire coupled to a microwave feed line. The high impedance and narrow geometry of this device results in a high concentration of the electric field around the nanowire, and therefore a strong coupling to the TLS host volume. The second resonator is a "regular" aluminum coplanar waveguide resonator and the third is an aluminum three-dimensional cavity resonator. In the following, we refer to the NbN nanowire superinductor resonator as the "nanowire", the Al coplanar-waveguide resonator as the "coplanar resonator" and the aluminum three-dimensional cavity resonator as the "cavity".

Details of the device design and fabrication can be found in Paper A and sections 6.6.1, 9.1 and A for the nanowire , in Paper D and sections 6.6.2 and 9.2 for the coplanar resonator, and finally in Ref. [101] and section 2.5 for the cavity.

The device characteristics of the three resonators are summarised in table 13.2. The reported internal quality factor Q_i has been measured at single photon energies ($\langle n \rangle = 1$) for both the nanowire and the coplanar resonator, however, for the cavity, it was determined at $\langle n \rangle = 132$, the lowest number measured. Nevertheless, in all cases, this corresponds to a regime where the photon occupation corresponds to when Q_i has saturated to a low-level, consistent with the depolarisation of two-level defects. Additionally, for each device, Z_c represents the characteristic impedance of the resonator and Q_c denotes the quality factor due to the coupling to the microwave excitation port.

13.3.2 Temporal Frequency Fluctuations

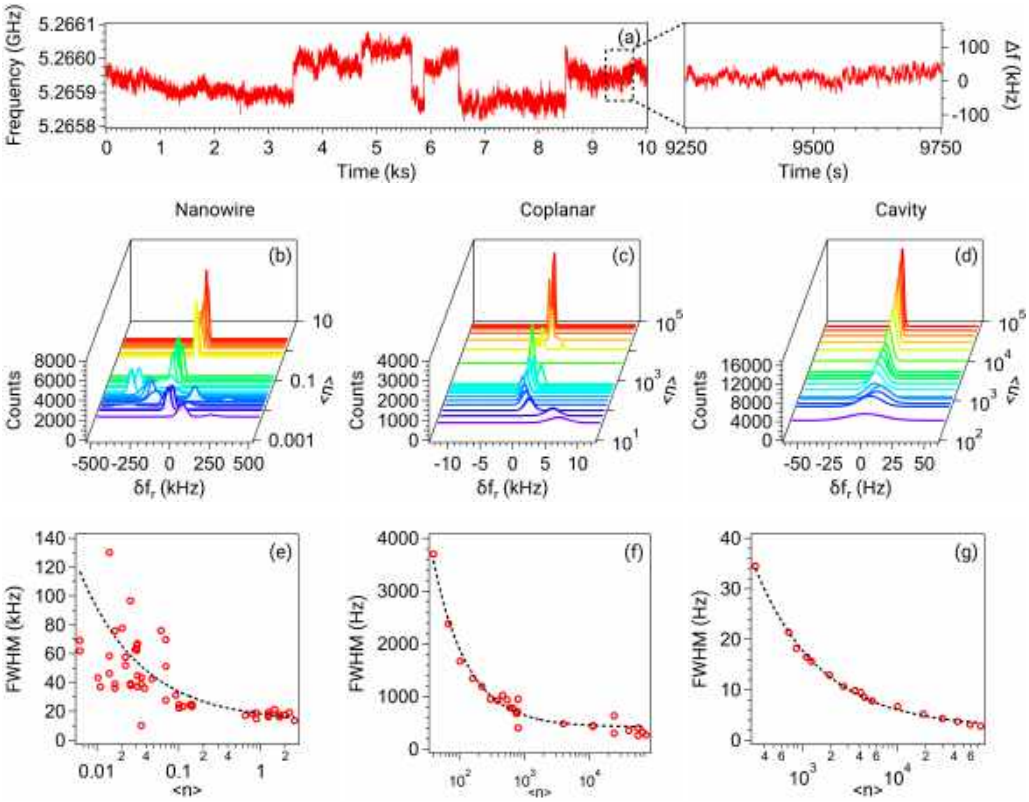

Figure 13.6: Frequency fluctuations of superconducting resonators. **(a)** Raw frequency jitter of the nanowire resonator sampled at 100 Hz, at an applied power corresponding to $\langle n \rangle \simeq 3 \times 10^{-2}$ photons in the resonator and at $T = 10\,\mathrm{mK}$. **(b–d)** Histograms of the frequency fluctuations for the three resonators vs. applied power. The data is normalised to the mean frequency $\bar{f}_r$ of the highest applied power. **(e–g)** Peak widths (FWHM) of the data in (b–d). (Note that FWHM refers to the width of one peak in the histogram and not to the distance between resolvable peaks that correspond to quasi-stable configurations.

The devices are measured using the P-FLL (see section 7.1 for details). We record the resonant frequency fluctuations of the device by sampling the frequency of the P-FLL voltage-controlled oscillator using a frequency counter (Keysight 53230A) at a sampling rate of either 100 Hz or 4 kHz. Each noise trace consists of 1×10^6 samples. In addition, once per noise trace, the absolute frequency and microwave power of the signal going into the cryostat are measured with a spectrum analyser (Agilent E4440A). During a measurement, the cryostat temperature is held constant and noise traces are recorded at various inbound microwave powers. We highlight that the measurements spanned across several weeks and across several different cooldowns and measurement sessions.

An example of frequency jitter measured at a sampling rate of 100 Hz for 2 h 45 min is shown in Fig. 13.6 (a). We observe that the frequency fluctuates between discrete points, as is characteristic of a random telegraph signal (RTS). In fact, these fluctuations occur at all timescales as can be seen in the inset over a much shorter time period.

To qualitatively compare between the different devices, we calculate the histogram of frequency fluctuations measured on each of the resonators against circulating power in units of the average photon occupation number $\langle n \rangle$ (Fig. 13.6 (b–d)) and extract the histogram full width at half maximum (FWHM) (Fig. 13.6 (e–g)).

These figures demonstrate that the fluctuation amplitude (histogram width) is highest for the nanowire resonator (Fig. 13.6 (b) and (e)). We attribute this to the nanowire high sensitivity to electric fields, due to its very high impedance, and to the high filling factor [274, 275] (see chapters 9, 11 and 12, and Papers A-B) of its surrounding dielectrics within the volume permeated by electric field, owing to its narrow geometry. Fluctuations of the real part of the dielectric susceptibility therefore act as an effective capacitance noise on the resonator, leading to frequency fluctuations. When the power applied to the resonator is low, we also observe that the histogram splits into more than one peak, indicating switching between a small number of quasi-stable frequency positions.

The histograms of fluctuations in the coplanar waveguide resonator (Fig. 13.6 (c) and (f)) are narrower, although, at low applied power, single-peak asymmetric distributions occur, due to the coalescence of separately resolvable frequency states, as well as occasional split peaks. These fluctuations originate from the same capacitance noise as those in the nanowire, but the electric field is not as strongly coupled to the coplanar resonator.

Finally, the histograms of fluctuations in the cavity resonator (Fig. 13.6 (d) and (g)) exhibit only one narrow and symmetric peak in all of our measured data sets, although with broadening at low power. We note that while the losses of superconducting cavities have been studied at sub-kelvin temperatures [101, 249, 276, 277], we have found no reports of frequency noise of superconducting cavities at these temperatures.

Qualitatively, Fig. 13.6 (b–d) demonstrate all the hallmarks of motional narrowing due to one or more RTS fluctuators [278–282]. At low power, we see multiple frequency positions, which can be attributed to several slowly varying RTS signals. As the power is increased these peaks coalesce into one distribution whose width narrows as the power increases.

To obtain an estimate for the power dependence of this narrowing, we fit the FWHM, shown in Fig. 13.6 (e–g), to the functional form $F_0 + F_1 / \langle n \rangle^{\beta}$ and we find a β value of 0.58, 0.82, and 0.63 for the nanowire, resonator, and cavity, respectively (see Table 13.4).

This functional form is reminiscent of the form that is typically found to fit the dependence the Q factor of a superconducting resonator on applied power: traditionally, the influence of decoherence mechanisms in superconducting devices is studied by mapping the power dependence of their response (see chapters 4, 11, 12 and Papers A, B and D). The standard tunnelling model predicts that the Q factor of a resonator scales as $\sqrt{1 + \langle n \rangle / n_c}$ for some critical photon number n_c, however variations from this scaling are often seen in experiments. Therefore, several authors have fitted the power dependence of Q to

$\sqrt{1+(\langle n\rangle/n_c)^{\beta}}$ where $\beta = 1$ corresponds to the STM prediction but typically $\beta < 1$ is observed [15, 26, 101, 125, 249, 283, 284]. Deviations from the STM predicted scaling have been interpreted as evidence for TLS-TLS interactions [21, 22, 26, 244, 285], in which case such variations between devices would be considered unsurprising. However, in this experiment it is the frequency jitter that is measured, not the Q factor, and so it is unclear if one would expect a similar response. However, the 1/f noise has been found to scale with the loss tangent (i.e. noise scaling with $1/\sqrt{1+\langle n\rangle/n_c}$) [22, 26], therefore it is reasonable to assume that the power dependence of the FWHM will follow a similar trend.

13.3.3 Spectral and Variance Analysis of Fluctuations

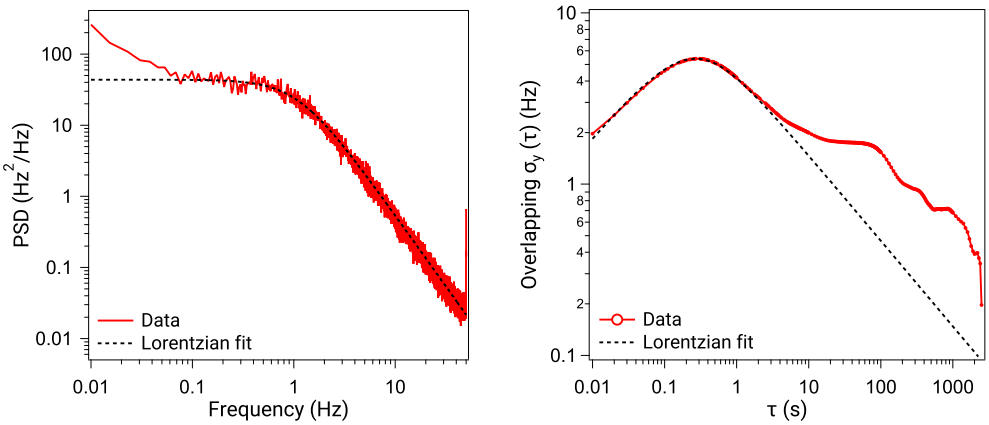

Figure 13.7: Fitting of the noise to a Lorentzian model. The plots show an example of a Welch power spectral density **(left)** and overlapping Allan deviation **(right)** for the measured frequency-fluctuation data from the cavity resonator held at $T = 10\,\mathrm{mK}$ and with an applied microwave drive power $P_{app} = -131.5\,\mathrm{dBm}$ ($\langle n\rangle \simeq 715$). The data was sampled at 100 Hz. The dashed line corresponds to a fit of the Lorentzian feature using a common set of fitting parameters for both traces.

The histograms discussed in the previous section are a useful tool for a quick comparison of some features across the resonators, however, for a more quantitative analysis and detailed comparison, we once again analyse the frequency fluctuations using the statistical tools presented chapter 5 and used throughout this chapter.

In Fig. 13.7, we show an example of the PSD and Allan deviation for the frequency fluctuations of the cavity, measured at a sampling rate of 100 Hz, $P_{app} = -131.5\,\mathrm{dBm}$ ($\langle n\rangle \simeq 715$) and at 10 mK. The data prominently features a single dominating Lorentzian (one dominant RTS fluctuator), which we can fit. Generally, the PSD and Allan variance exhibit multiple and partially overlapping Lorentzian-like features, sometimes at sufficient densities that they sum up to a $1/f$-like trend [260]. In the limit of few Lorentzians, or the $1/f$ limit, the data can be reliably fitted. However, between these limits, it becomes

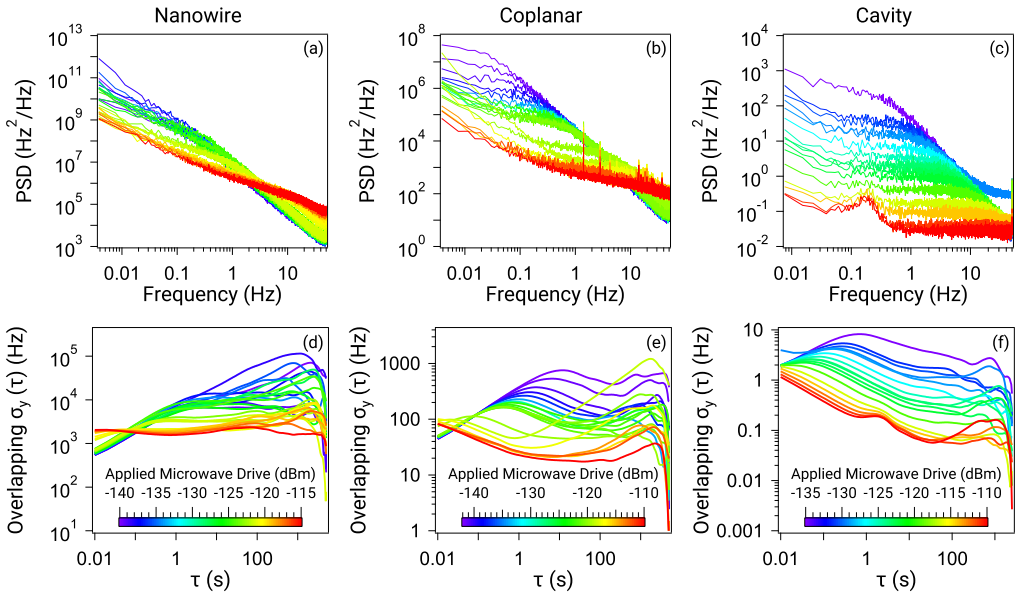

Figure 13.8: Noise analysis vs. applied power for the three resonators. Plots **(a–c)** show the Welch power spectral densities and plots **(d-f)** show the overlapping Allan deviations of the frequency fluctuations, for various applied powers. All the data was measured at $T = 10\,\mathrm{mK}$ and a sampling rate of 100 Hz. We observe that all three devices present similar noise profiles—featuring one dominant Lorentzian—albeit at widely different amplitudes: the nanowire is the noisiest and the cavity is the quietest. As the microwave drive is increased, we observe that the dominant Lorentzian feature in the PSD (Allan) is consistently moving toward higher frequencies (lower τ) for all devices.

non-trivial to determine the exact number of Lorentzians (RTS fluctuators). Therefore, for consistency, we focus on the dominant Lorentzian within our measurement window. In order to accurately determine the characteristic switching time τ_0 and amplitude A of the dominant Lorentzian in all of our data sets, we find it favourable to use the Allan variance rather than the PSD (although we use the same parameters in the fits shown in both panels of Fig. 13.7 and throughout).

We record fluctuations data for a range of drive powers available in our measurement setup, which translates into different ranges of $\langle n \rangle$ between the three resonators, depending on their characteristic impedances, coupling strengths, and internal quality factors; see Table 13.2 and Eq. 3.22. This data is shown in Fig. 13.8, and we observe that all three devices present similar noise profiles—featuring one dominant Lorentzian —albeit at widely different amplitudes: the nanowire is the noisiest and the cavity is the quietest.

The cavity resonator frequency is so stable that at high power, its noise falls below that of the frequency reference of our signal generator's phase-locked loop (PLL), which shows up as an additional peak in the PSD at around 200 mHz and correspondingly in the Allan deviation at around 5 s.

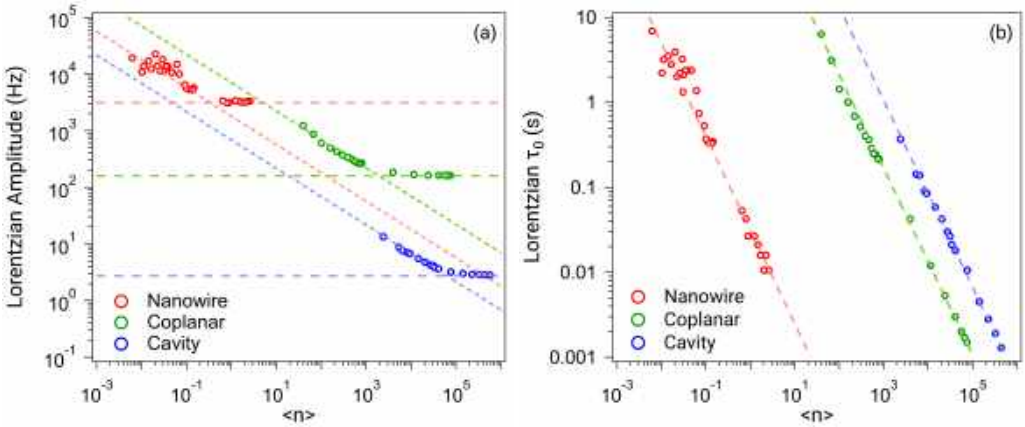

Figure 13.9: Drive-power dependence of the RTS amplitude A **(left)** and switching time constant τ_0 **(right)** determined from noise data from the three resonators (Fig. 13.8) fitted to a Lorentzian model. The horizontal dashed lines in (left) indicate the saturation $A \to A_0$, related to the minimum FWHM in Fig. 13.6 (d–f). The diagonal lines in (left) indicate $1/\sqrt{\langle n \rangle}$ scaling (not a fit). The dashed lines in (right) are fits of τ_0 to the power law $(\langle n \rangle / n_c)^{-\alpha}$ (Eq. 13.4), with $\alpha = 1.1$. The fitted parameters are presented in Table 13.3.

As the microwave drive is increased, we observe that the dominant Lorentzian feature in the PSD (Allan) consistently moves toward higher switching rates (lower τ) for all devices. We fit this dominant features of all the data sets in Fig. 13.8 and plot the resulting values of the Lorentzian amplitudes A and Lorentzian switching time constants τ_0 as a function of the average photon population in the resonator in Fig. 13.9. In the determination of τ_0 and A, we estimate the error bar to be about 4% (10%) for τ_0 (A) for the coplanar resonator and cavity, and for the nanowire at high powers. For the low-power data of the nanowire, we estimate about a factor of two error in both τ_0 and A. The collection of longer sets of data would reduce the error.

In Fig. 13.9 (left), we see that A is initially power dependent, decreasing with increasing power. However it saturates at high powers, starting at a photon number corresponding approximately to the coalescence of peaks in Fig. 13.6 (b–d) ($\langle n \rangle \sim 0.1$ for the nanowire and 10^4 for the coplanar). All three devices show this behaviour, although the amplitudes, saturation levels (see Table 13.3) and the cross-over point vary.

As shown in Fig. 13.9 (right), interestingly, the extracted τ_0 values of the three resonators follow a power law, which we determine empirically,

$$\tau_0(\langle n \rangle) = (1\,\mathrm{s}) \times (\langle n \rangle / n_c)^{-\alpha} \tag{13.4}$$

where α is found close to 1.1 in all three resonators, and n_c is a "critical" photon number, unique for each device; see the fit parameters in Table 13.3.

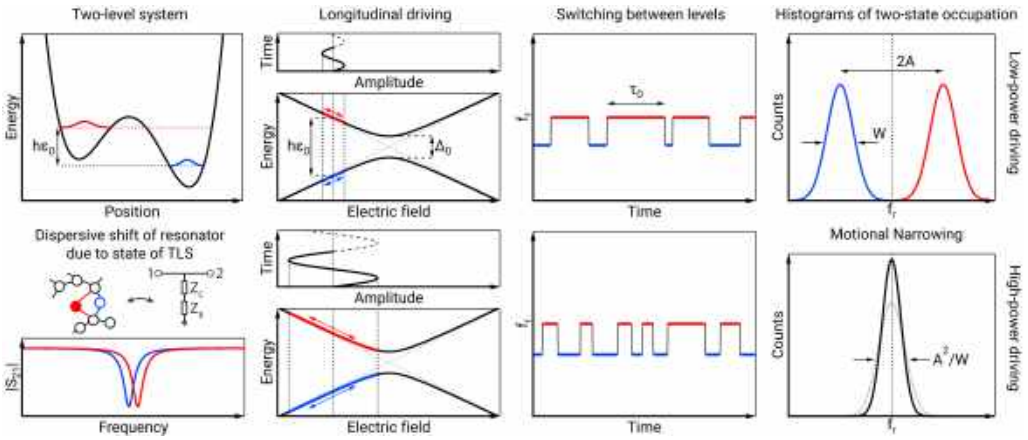

Figure 13.10: An illustration of the relevant RTS switching regimes (high and low power driving) resulting from small and large-amplitude driving of a TLS near (but not at) its degeneracy point. The resulting transitions between the two eigenstates of the TLS result in different dispersive shifts of the resonator, resulting in RTS fluctuations of the resonance frequency.

13.3.4 Discussion

The power dependence of the histogram width and the noise characteristics revealed by the Allan deviation can be understood in terms of motional narrowing by one or a few dominant RTS fluctuators. In this section, we show how the resonator field can drive two-level defects in the surrounding dielectric in a regime that results in RTS noise with the required power dependence to explain the observations. This effect of sympathetic driving of the bath of defects and the resulting motional narrowing likely influences the power dependence in many superconducting devices.

Motional narrowing

Together, the plots in Fig. 13.6 highlight the power-dependent transition from multi-peaked behaviour at low circulating power in the resonator to single-peaked behaviour at high power. Additionally, as the power increases, the widths of the histograms narrow. Such behaviour is indicative of motional narrowing (motional averaging) [278], where a multi-level system transitions into a single-level system that also exhibits increased spectral stability. Motional narrowing is a common phenomenon that has been found in a wide variety of systems: NMR spectra [278, 286], ESR spectra [279], gamma emissions [280], superconducting qubits [287], and two-level NV-centre defects [288, 289]. However, despite the similarity between an NV centre and a parasitic TLS, motional narrowing has not been considered in the framework of dielectric loss, charge noise, or other TLS phenomena that manifest within superconducting circuits.

The observation of quasi-stable resonant frequencies is consistent with the model of a bath of spectrally unstable, charged TLS that are dispersively coupled to the resonator [22,

23, 26, 290]. In previous studies of resonators, the coupling to many TLS manifested into a $1/f$ noise spectrum [26, 28, 259]. Within studies on superconducting qubits, the coupling to TLS has been strong enough to result in an RTS noise spectrum [24, 291] (see section 13.2 and Paper E). The RTS noise behaviour found here demonstrates a similarly strong coupling to single or few individual TLS.

Typically, in such a model of dispersively coupled (near-resonant) TLS, their dynamics are dominated by incoherent, low-frequency two-state fluctuators whose fluctuations dephase the TLS (widen its spectrum) or shift the TLS energy [22, 26, 292, 293]. This typically results in a $1/f$ noise spectrum which scales as $1/\sqrt{\langle n \rangle}$. Here we see single- or few-RTS dynamics rather than $1/f$ noise, where the RTS amplitude scales as $1/\sqrt{\langle n \rangle}$ (Fig. 13.9 (a)) up until some critical power, beyond which is power independent. However, a very clear nearly-$1/\langle n \rangle$ dependence of τ_0 (Fig. 13.9 (b)) over all powers suggests that the switching rate requires a different interpretation.

To understand the ramifications of the observed power dependence, we consider an RTS system with only two states at frequencies $\pm A$, with a characteristic switching rate between these states of W per unit time. For slow switching, $W \ll |A|$, the spectral response of the RTS signal consists of two peaks at frequencies $\pm A$ with a width (FWHM) given by W. In the opposite limit of strong driving, $W \gg |A|$, the resonance is a single peak centred at zero frequency with FWHM width A^2/W, which is narrower. Importantly, motional narrowing can extend beyond the simple two-state to one-state example that we have described [278]; in multiple-state examples [279, 280], multiple W and $\pm A$ exist, although the convergence towards a single narrow state still occurs in the strong driving limit [281, 282], which is the regime we focus on. The observation that $\tau_0 \propto 1/\langle n \rangle^{1.1}$ in the fast fluctuation limit therefore suggests that $W \propto \langle n \rangle^{1.1}$, and this observation is common across all three devices.

Landau–Zener transitions in the bath of TLS defects

In order to investigate the mechanism for modulation of the TLS defect by the resonator, and to explain the results presented above, we start from the assumption that the bath of fluctuators driving the RTS behaviour is described by the standard tunnelling model [290, 294], where each defect can be described by the TLS Hamiltonian

$$\hat{\mathcal{H}}_0 = (-h/2)(\varepsilon \hat{\sigma}_z + \Delta_0 \hat{\sigma}_x) \tag{13.5}$$

as illustrated in Fig. 13.10.

The tunnel coupling Δ_0 and bias ε vary from defect to defect and are a function of the local atomic environment. We assume that the electric field of the resonator couples to the defects via their charge dipole, i.e. longitudinally (along $\hat{\sigma}_z$) in the basis of uncoupled double wells. The bias is therefore comprised of a constant offset and a time dependent term,

$$\varepsilon(t) = \varepsilon_0 + \varepsilon_{\mathrm{rf}} \cos(2\pi f_r t), \tag{13.6}$$

where $\varepsilon_{\rm rf}$ has units of frequency but is proportional to the amplitude of the resonator electric field ($\propto\sqrt{\langle n\rangle}$), and hence to the rf voltage at the source.

For low-loss devices, there are relatively few defects with values of Δ_0 close to the resonator frequency [23, 129]; however, that is not the parameter regime we are considering. There are also TLS whose Δ_0 is relatively small, but whose equilibrium position (given by ε_0) is such that their eigenstates are nearly resonant with the resonator. For large resonator fields, the drive can sweep the fluctuator through the defect anti-crossing ($\varepsilon_{\rm rf} \approx \varepsilon_0$) or at least near it. We therefore need to consider the role of Landau-Zener (L-Z) tunnelling which can result in transitions between the ground and excited states of the TLS [295, 296].

We can rewrite the Hamiltonian (Eq. 13.5) above in a time-dependent rotating frame to obtain

$$\hat{\mathcal{H}}_{RF} = (-h/2)(\delta\hat{\sigma}_{\tilde{z}} + \Delta_0 J_1(\lambda)\hat{\sigma}_{\tilde{x}}), \tag{13.7}$$

where $\delta = \varepsilon_0 - f_r$ is the detuning between drive and frequency splitting at the bias point $\varepsilon = \varepsilon_0$, $J_1(\lambda)$ is the first-order (one photon) Bessel function of the first kind, representing a dressed gap, and $\lambda = \varepsilon_{\rm rf}/f_r$ is the ratio of driving amplitude to driving frequency.

The relevant regime of L-Z driving of TLS in the dielectric of the resonators is that the effective transition rate W between states is less than the dephasing rate (Γ_2) but greater than the relaxation rate (Γ_1), i.e. $\Gamma_1 < W < \Gamma_2$. In this regime, at resonance ($\delta = 0$) in the small-amplitude drive limit ($\varepsilon_{\rm rf} \ll f_r$), the one-photon transition rate between the eigenstates is given by [297]:

$$W(\lambda) = \frac{\pi^2}{2}\frac{\Delta_0^2\lambda^2}{\Gamma_2}. \tag{13.8}$$

Now, as there is little to no coherence between the two eigenstates, we can consider $W(\lambda)$ as the RTS switching rate, i.e., $\tau_0 = 1/W(\lambda)$, which means that $\tau_0 \propto 1/\varepsilon_{\rm rf}^2 \propto 1/\langle n\rangle$, where the proportionality constant (n_c in Eq. 13.4) is a product of three unknowns: the decoherence rate, the energy splitting, and the electric-field amplitude at the site of the TLS.

We note that our observed transition rate has a small additional contribution as the amplitude is increased (cf. the exponent $\alpha = 1.1$ in Eq. 13.4 found empirically for all three resonators). We may attribute this to the TLS having a sufficiently large response to the resonator field that higher photon number transitions are non-negligible.

The role of Landau–Zener driving of TLS in the dielectric of qubits and resonators has been previously studied [298–300]; however, in such experiments the mechanism is modulating the frequency splitting of near-resonant TLS as they traverse the resonator frequency, thereby driving non-adiabatic Landau–Zener transitions. The transitions we consider (away from the degeneracy point) influence the dephasing noise (i.e. the low-frequency, real part of the spectral function), similarly to Ref. [289], whereas Ref. [298] deals with the loss (i.e. the near-resonant, imaginary part leading to energy relaxation).

The role of the ensemble

While this picture explains the common response between devices and the power dependence of τ_0, it does not explain the low-power response of A_0 nor the 'more conventional' (but less universal) response of the FWHM. However, both can be explained in terms of the ensemble of RTS fluctuations stemming from multiple TLS. As the power is reduced, below the point of coalescence in the motional narrowing picture, the fit to a single RTS fluctuator no longer captures the key characteristics of the response. The contributions from both additional RTS sources and other noise processes start to dominate and this results in an additional power dependence to the noise amplitude. The diagonal lines in Fig. 13.9 (a) represent a $1/\sqrt{\langle n \rangle}$ scaling, which one would typically expect for $1/f$ noise, indicating that at lower powers, the ensemble response is more dominant. Similarly, the extracted FWHM in Fig. 13.6 (e–g) (Table 13.4) is a function of the entire spectrum, which includes both additional (non-TLS) processes and contributions due to the TLS-TLS interactions in the bath [21, 22, 244, 285]. As these contributions depend on the density and interaction strength between the TLS, they vary more between devices resulting in the differing power response.

13.3.5 Conclusion

We have studied the frequency noise of three commonly used superconducting resonators within the same measurement and anlysis infrastructure. We find that in all devices, the noise is described by an RTS process, which we attribute to spectrally unstable TLS. When studying the RTS behaviour with microwave drive power, we find that the switching times follow a common scaling across all types of resonators. We interpret the power dependence of the RTS switching times in terms of sympathetic driving of TLS defects by the resonator field. This driving induces Landau-Zener type resonant transitions, even for TLS whose equilibrium configuration is relatively detuned from the degeneracy point between the two states.

Fundamentally, this highlights the power of standardised testing with common methods. Here, the ability to directly compare different types of superconducting resonator has revealed a commonality of the dominant noise process. These findings expand the toolkit and material parameter range for examining parameter fluctuations, which has become the leading problem in superconducting quantum-computing efforts. Furthermore, the studies of the nanowire superinductor are particularly relevant to the rapidly growing area of high-impedance qubits [7, 9, 274].

Table 13.2: Device parameters for all three resonators.

Resonator	f_r (GHz)	Z_c (Ω)	Q_i	Q_c
Nanowire	5.3	6.8×10^3	2.5×10^4	8.0×10^4
Coplanar	4.3	50	5.4×10^5	1.8×10^5
Cavity	6.0	58	1.1×10^7	8.2×10^6

Table 13.3: Fit parameters for the dominant RTS fluctuators switching times τ_0 vs. drive power $\langle n \rangle$ (Eq. 13.4) and saturation values (A_0) of their amplitudes A for large $\langle n \rangle$, shown in Fig. 13.9. The FWHM values refer to the histograms in Fig. 13.6 (d–f) at high power.

Device	RTS τ_0	RTS A
Nanowire	$\alpha = 1.1$ $n_c = 4.3 \times 10^{-2}$	$A_0 = 2.8 \times 10^3$ Hz FWHM $= 1.2 \times 10^4$ Hz
Coplanar	$\alpha = 1.1$ $n_c = 2.0 \times 10^2$	$A_0 = 1.6 \times 10^2$ Hz FWHM $= 2.7 \times 10^2$ Hz
Cavity	$\alpha = 1.1$ $n_c = 1.1 \times 10^3$	$A_0 = 2.5$ Hz FWHM $= 9.4$ Hz

Table 13.4: Fitting parameters for Fig. 13.6 (e–g).

Device	F_0 (Hz)	F_1 (Hz)	β
Nanowire	1.3×10^4	5.5×10^3	0.58
Coplanar	4.2×10^2	6.4×10^4	0.82
Cavity	2.6	1.2×10^3	0.63

Chapter 14

Conclusion and Outlook

14.1 Conclusion

In this work, we have explored disordered superconductors and studied in detail the properties of NbN. Using this knowledge, we have deposited and patterned disordered NbN thin films and implemented the first nanowire superinductor.

We have thoroughly characterised these nanowire superinductors using both DC and RF measurements in order to understand their properties and the loss mechanism involved (Paper A). We find TLS to be the dominant cause of loss, which is in contrast to the high rates of dissipation found in other nanowire [14, 121] or strongly disordered thin-film devices [122]. We emphasize that demonstrating that nanowires' losses — at least in our implementation — are "conventional" is an important step forward, enabling high-coherence circuits, such as a nanowire fluxonium qubit [3, 7, 120, 301], improved phase-slip qubits [14, 121], or other circuits benefiting from high inductance.

Additionally, we have studied the effects of geometric scaling on the TLS participation ratio in superconducting resonators (Paper B). We obtain good agreement between our experimental results and electromagnetic simulations using the Maxwell–London equations. We show that reducing the width of the devices significantly increases the TLS participation ratio, which is unfavorable for nanoscale device dimensions. This emphasizes the need for careful materials engineering to reduce the density of TLS, in particular for nanowire devices. Furthermore, we report the intrinsic loss tangent of HSQ ($\delta^i_{HSQ} = 8 \times 10^{-3}$), a spin-on-glass resist commonly used for the fabrication of nanoscale devices, and show that it dominates the loss. This justifies the development of a process for the removal of HSQ, which would help significantly improve the performance of devices relying on the use of such resists.

Finally, we have studied low-frequency fluctuations in several superconducting quantum circuits and showed that their origin is consistent with individual TLS (Papers C-E). Analysing these fluctuations, we demonstrated that some measurement techniques common in the field of frequency metrology are well suited to revealing the loss dynamics in superconducting circuits. We identified signatures of individual fluctuators and showed that the coherence of current superconducting transmon qubits is limited by spectrally unstable TLS. Furthermore, by studying the frequency fluctuations in three different types of superconducting resonators, we found a reduced TLS instability with increasing resonator drive power and a common, seemingly universal power-dependent scaling of the switching rate and amplitude of the noise, suggesting a common mechanism.

14.2 Outlook

The nanowire superinductor is a powerful new tool in the mesoscopic circuits toolbox. Indeed, superinductors are central to several types of novel qubit architectures, such as the fluxonium qubit [6, 7] or topologically protected qubits [301, 302] and for exploring fundamental physics such as Bloch oscillations of charge for metrology applications [18, 303].

Furthermore, in the ever growing field of high impedance devices, high kinetic inductance disordered superconductors present significant advantages over the more traditionally used junctions chains: high critical current, magnetic-field tolerance [16], strong coupling to zero-point fluctuations of the electric field [304, 305], less stringent constraints on device geometry, and absence of parasitic modes. These advantages can be leveraged to improve the performance of existing types of circuits such as traveling-wave microwave parametric amplifiers [306–312], phase-slip qubits [14, 121], microwave kinetic-inductance photon detectors (MKIDs) [313, 314] or radio-frequency-readout of superconducting single-photon detectors (SSPDs) [314, 315].

Appendix A

Cleanroom Recipes

A.1 Wafer Cleaning

Silicon Wafer cleaning	
Acetone	With sonication (normal) at 100% power for 5 min
Methanol	With sonication (normal) at 100% power for 5 min
IPA	With sonication (normal) at 100% power for 5 min
QDR bath	Rinse in water and blow dry with N_2
SC1 bath	For 10 min
QDR bath	Rinse in water and blow dry with N_2
HF bath	Dip in 2% HF for 30 s
QDR bath	Rinse in water and blow dry with N_2

A.2 Thin-Film Deposition

NbN Sputtering	
Presputtering	Presputter for 5 min
Sputter	NbN deposition for 27 s at 200 W, 6.7 µbar 83.4 sccm of argon and 8.5 sccm of nitrogen

NbN/AlN/Au Sputtering	
Presputtering	Presputter for 5 min
Sputter	NbN deposition for 72 s at 200 W, 6.7 µbar 83.4 sccm of argon and 10 sccm of nitrogen
Presputtering	Presputter for 4 min
Sputter AlN	AlN deposition for 20 s at 100 W, 2.8 µbar 83.4 sccm of argon and 15 sccm of nitrogen
Presputtering	Presputter for 1 min
Sputter Au	Au deposition for 90 s at 50 W, 2.8 µbar 83.4 sccm of argon

Al Evaporation

Heating	Heat to 300 °C and hold for 10 min
Pump	Cool and pump to 6×10^{-8} mbar
Evaporate	Evaporate 150 nm of Al, 1 nm s^{-1}
Oxidation	Static oxidation, 10 mbar, 500 sccm, 10 min

A.3 Electron Beam Lithography

PMMA A6 Positive EBL Resist

Prebake	110 °C for 1 min
Spin PMMA A6	3000 rpm for 1 min, $t_{acc} = 1.5$ s
Bake on hotplate	160 °C for 5 min
Expose pattern	JBX-9300FS or EBPG5200, 100 kV, 800 µC cm^{-2}
Develop	MIBK:IPA 1:3, 5 min
IPA	Rinse in IPA and blow dry with N_2
Descumming	Ash in O_2 plasma at 50 W for 40 s

HSQ Negative EBL Resist

Prebake	60 °C for 1 min
Spin HSQ	5000 rpm for 1 min, $t_{acc} = 1.5$ s
Expose pattern	JBX-9300FS or EBPG5200, 100 kV, 8000 µC cm^{-2}
Develop	MF-319 for 60 s
QDR bath	Rinse in water and blow dry with N_2
Descumming/Hardening	Ash in O_2 plasma at 50 W for 40 s

A.4 Photolithography

S1805 Positive Photoresist

Dehydratation bake	110 °C for 1 min
Spin S1805 resist	3000 rpm for 1 min, $t_{acc} = 1.5$ s
Softbake on hotplate	110 °C for 1 min
Expose pattern	DWL2000 laser writer, focus 10, intensity 75 transmission 100%
Develop	MF-CD-26 for 60 s
QDR bath	Rinse in water and blow dry with N_2
Descumming	Ash in O_2 plasma at 50 W for 40 s

AZ1512HS Positive Photoresist

Dehydratation bake	110 °C for 1 min
Spin AZ1512HS resist	4000 rpm for 1 min, $t_{acc} = 1.5$ s
Softbake on hotplate	100 °C for 50 s
Expose pattern	DWL2000 laser writer, focus -5, intensity 80 transmission 100%
Develop	AZ Developper:H_2O 1:1 for 60 s
QDR bath	Rinse in water and blow dry with N_2
Descumming	Ash in O_2 plasma at 25 W for 20 s

LOR3B/S1805 Positive Photoresist Stack (Lift-off)

Dehydratation bake	110 °C for 1 min
Spin LOR3B resist	3000 rpm for 1 min, $t_{acc} = 1.5$ s
Hardbake on hotplate	170 °C for 5 min
Spin S1805 resist	3000 rpm for 1 min, $t_{acc} = 1.5$ s
Softbake on hotplate	110 °C for 1 min
Expose pattern	DWL2000 laser writer, focus 10, intensity 75 transmission 100%
Develop	MF319 for 60 s
QDR bath	Rinse in water and blow dry with N_2
Descumming	Ash in O_2 plasma at 50 W for 40 s

A.5 Etching

Reactive Ion Etching of NbN

RIE	RIE in Ar:Cl_2 50:4, 10 mTorr, 50 W for 4 min
Water	Immediately rinse in water and blow dry with N_2
Descumming	Ash in O_2 plasma at 50 W for 40 s
1165 Remover	85 °C for 5 min
IPA	For 5 min
QDR bath	Rinse in water and blow dry with N_2

Reactive Ion Etching of Silicon

RIE	RIE in NF_3, 20 mTorr, 100 W for 3 min
Descumming	Ash in O_2 plasma at 50 W for 30 s
1165 Remover	85 °C for 5 min
1165 Remover	85 °C for 5 min, sonication (sweep) at 40% power
Methanol	With sonication (sweep) at 40% power for 5 min
IPA	With sonication (sweep) at 40% power for 5 min
QDR bath	Rinse in water and blow dry with N_2

Wet Etching of Aluminium

Transene bath	Wet etch in Transene type A at 40 °C for 1 min5 s
QDR bath	Rinse in water and blow dry with N_2
1165 Remover	85 °C for 5 min
1165 Remover	85 °C for 5 min, sonication (sweep) at 40% power
Methanol	With sonication (sweep) at 40% power for 5 min
IPA	With sonication (sweep) at 40% power for 5 min
QDR bath	Rinse in water and blow dry with N_2

A.6 Process Flow: Nanowire Superinductors

1. Wafer Cleaning

- 1165 remover at 60 °C, IPA, QDR
- 30 s HF and QDR

2. NbN Deposition

- Room temperature sputtering of 20 nm of NbN at 10 sccm nitrogen flow

3. Microwave circuitry

- Dehydratation bake 110°C, Spin PMMA A6 at 3000 rpm, 60 s, bake at 160 °C, 5 min
- Expose in EBL at 800 µC cm^{-2}
- Develop in MIBK:IPA 1:3 for 5 min, rinse in IPA
- Ash 50 W for 40 s
- RIE in Ar:Cl_2 50:4, 10 mTorr, 50 W for 3 min
- Ash 50 W for 40 s
- 1165 remover at 60 °C for 2 min, rinse in IPA, QDR
- Ash 50 W for 40 s

4. Nanowires

- Dehydratation bake 110 °C, Spin HSQ at 5000 rpm, 60 s
- Expose in EBL at 8000 µC cm^{-2}
- Develop in MF-319 for 60 s
- Ash 50 W for 40 s
- Dehydratation bake 110 °C, Spin S1805 at 3000 rpm, 60 s, bake 110 °C, 60 s
- Expose in laser writer, focus 10, intensity 75, transmission 100%
- Develop in MC-CD-26 for 60 s
- Ash 50 W for 40 s
- RIE in Ar:Cl_2 50:4, 20 mTorr, 50 W for 3 min
- Ash 50 W for 40 s

- 1165 remover at 60°C for 2 min, rinse in IPA, QDR

A.7 Process Flow: NbN Resonators

1. Wafer Cleaning

- 1165 remover at 60 °C, IPA, QDR
- 30 s HF and QDR

2. NbN Deposition

- Room temperature sputtering of 20 nm of NbN at 10 sccm nitrogen flow

3. Microwave Resonators

- Dehydratation bake 110°C, Spin PMMA A6 at 3000 rpm, 60 s, bake at 160 °C, 5 min
- Expose in EBL at 800 µC cm^{-2}
- Develop in MIBK:IPA 1:1 for 1 min, rinse in IPA
- Ash 50 W for 40 s
- RIE in Ar:Cl_2 50:4, 10 mTorr, 50 W for 3 min
- Ash 50 W for 40 s
- 1165 remover at 60 °C for 2 min, rinse in IPA, QDR
- Ash 50 W for 40 s

4. Microwave Resonators (HSQ cover)

- Dehydratation bake 110 °C, Spin HSQ at 5000 rpm, 60 s
- Expose in EBL at 8000 µC cm^{-2}
- Develop in MF-319 for 60 s
- Ash 50 W for 40 s

A.8 Process Flow: Aluminium Resonators

1. Wafer Cleaning

- Acetone with sonication, 5 min
- Methanol with sonication, 5 min
- IPA with sonication, 5 min
- SC1 for 10 min, QDR, HF for 30 s, QDR

2. Al Deposition

- Heat to 300 °C, hold for 10 min
- Cooldown, pump overnight to $\sim 6 \times 10^{-8}$ mbar
- E-beam evaporation of 150 nm of Al
- Static oxidation, 10 mbar, 500 sccm, 10 min

3. Microwave Resonators

- Spin AZ1512HS at 4000 rpm, 60 s, bake at 100 °C, 50 s
- Expose in laser writer, focus -5, intensity 80, transmission 100%
- Develop in AZ developer:H_2O 1:1 for 30 s
- Ash 25 W for 20 s
- Wet etch in Transene type A, 40 °C, 1 min5 s, QDR

4. Si Etching

- RIE in NF_3, 20 mTorr, 100 W for 3 min
- 1165 remover at 60°C for 5 min and 5 min with sonication
- Methanol with sonication, 5 min
- IPA with sonication, 5 min

A.9 Process Flow: SIN Junctions

1. Wafer Cleaning

- 1165 remover at 60 °C, IPA, QDR
- 30 s HF and QDR

2. NbN/AlN/Au Trilayer Deposition

- Room temperature sputtering of 40 nm of NbN at 8.5 sccm nitrogen flow
- Room temperature sputtering of $\sim$ 2 nm of AlN
- Room temperature sputtering of 60 nm of Au
- E-beam evaporation of 10 nm of Ti

3. NbN/AlN/Au Trilayer Etching

- Dehydratation bake 110 °C, Spin S1805 at 3000 rpm, 60 s, bake 110 °C, 60 s
- Expose in laser writer, focus 10, intensity 75, transmission 100%
- Develop in MC-CD-26 for 60 s
- Ash 50 W for 40 s
- RIE in Ar:Cl_2 50:4, 20 mTorr, 50 W for 3 min
- Ash 50 W for 40 s
- 1165 remover at 60°C for 2 min, rinse in IPA, QDR
- Ash 50 W for 40 s

4. SiO_2 Deposition and Etching

- Room temperature sputtering of 120 nm of SiO_2
- Dehydratation bake 110 °C, Spin S1805 at 3000 rpm, 60 s, bake 110 °C, 60 s
- Expose in laser writer, focus 10, intensity 75, transmission 100%
- Develop in MC-CD-26 for 60 s
- Ash 50 W for 40 s
- RIE in NF_3, 20 mTorr, 100 W for 3 min
- Ash 50 W for 40 s

- 1165 remover at 60°C for 2 min, rinse in IPA, QDR
- Ash 50 W for 40 s

5. SiO_2/Au/AlN Etching

- Dehydratation bake 110 °C, Spin S1805 at 3000 rpm, 60 s, bake 110 °C, 60 s
- Expose in laser writer, focus 10, intensity 75, transmission 100%
- Develop in MC-CD-26 for 60 s
- Ash 50 W for 40 s
- RIE in NF_3, 20 mTorr, 100 W for 3 min
- RIE in Ar:Cl_2 50:4, 20 mTorr, 50 W for 3 min
- Ash 50 W for 40 s
- 1165 remover at 60°C for 2 min, rinse in IPA, QDR
- Ash 50 W for 40 s

6. Au Contacts Lift-off

- Dehydratation bake 110 °C
- Spin LOR3B at 3000 rpm, 60 s, bake 170 °C, 5 min
- Spin S1805 at 3000 rpm, 60 s, bake 110 °C, 60 s
- Expose in laser writer, focus 10, intensity 75, transmission 100%
- Develop in MF319 for 60 s
- Ash 50 W for 40 s
- E-beam evaporation of 10 nm of Ti
- E-beam evaporation of 100 nm of Au
- Lift-off in 1165 remover at 60°C for $\sim$ 1 h, rinse in IPA, QDR
- Ash 50 W for 40 s

Appendix B

Waveguide Impedance Calculation by Conformal Mapping

In this section, we present the equations used to simulate the characteristic impedance of a coplanar waveguide (CPW). In order to simulate the inductance and capacitance per unit length, the conformal mapping method is used [316]. The electric field lines between the center conductor and the ground planes of the CPW are mapped to the lines of the electric field from a parallel plate capacitor.

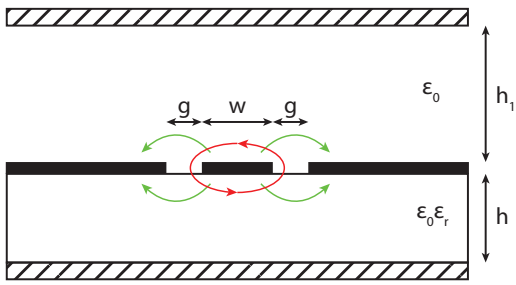

Figure B.1: Cross section of the coplanar waveguide geometry. The superconducting metal (thick black layer) is placed on top of a substrate with effective dielectric constant ε_r. The device is placed in vacuum and is surrounded by top and bottom enclosures. h denotes the thickness of the substrate and h_1 the distance to the top cover. The electric and magnetig field lines are shown respectively in green and red.

We first calculate C_{vac} and C_1, the capacitance contributions of the vacuum and of the substrate

$$C_{vac} = 2\varepsilon_0 \left[\frac{K(k_3)}{K(k_3')} + \frac{K(k_4)}{K(k_4')} \right] \tag{B.1}$$

$$C_1 = 2\varepsilon_0(\varepsilon_r - 1)\frac{K(k_3)}{K(k_3')} \tag{B.2}$$

where ε_0 and ε_r are the vacuum and relative permitivity respectively, and K the complete

elliptic integral of the first kind. k_3, k_3' k_4 and k_4' are defined by

$$k_3 = \frac{\tanh(\pi w/4h)}{\tanh(\pi(w+2g)/4h)} \qquad k_3' = \sqrt{1-k_3^2} \tag{B.3}$$

$$k_4 = \frac{\tanh(\pi w/4h_1)}{\tanh(\pi(w+2g)/4h_1)} \qquad k_4' = \sqrt{1-k_4^2} \tag{B.4}$$

This allows us to define an effective dielectric constant:

$$\varepsilon_{eff} = 1 + q_2(\varepsilon_r - 1) \tag{B.5}$$

where q_2 is a partial filling factors defined by

$$q_2 = \frac{K(k_3)}{K(k_3')}\left[\frac{K(k_3)}{K(k_3')} + \frac{K(k_4)}{K(k_4')}\right]^{-1} \tag{B.6}$$

This enables us to express the phase velocity and characteristic impedance in terms of ε_{eff}:

$$v_{ph} = \frac{c}{\sqrt{\varepsilon_{eff}}} \tag{B.7}$$

$$Z_0 = \frac{1}{cC_{vac}\sqrt{\varepsilon_{eff}}} = \frac{60\pi}{\sqrt{\varepsilon_{eff}}}\left[\frac{K(k_3)}{K(k_3')} + \frac{K(k_4)}{K(k_4')}\right]^{-1} \tag{B.8}$$

Finally, we can express the inductance and capacitance per unit length of the CPW:

$$L_{CPW} = \frac{\mu_0}{2}\left[\frac{K(k_3)}{K(k_3')} + \frac{K(k_4)}{K(k_4')}\right]^{-1} \tag{B.9}$$

$$C_{CPW} = 2\varepsilon_0\varepsilon_{eff}\left[\frac{K(k_3)}{K(k_3')} + \frac{K(k_4)}{K(k_4')}\right] \tag{B.10}$$

Appendix C

Additional NbN Transport Data

In chapter 10, we detail the measurements that were carried out to characterise the transport properties of the thin-films fabricated in this work and we illustrate these techniques with the complete characterisation of a select number of thin-films. Additionally, in chapter 11, we show the material parameters of the film used for the fabrication of our nanowire superinductors. During the optimisation of the NbN thin-film deposition recipe and in order to save some of the limited available measurement time in the cryostat, only the $R(T)$ characteristic was measured for most films. This is sufficient in most cases, as the $R(T)$ characteristic is enough to determine T_c, R_N and L_k (see section 10.2.1), which are the main relevant parameters for our applications. However, the complete characterisation of the material parameters (i.e. $R(T)$, Hall and $R(T, H)$ measurements) was done on more films than presented in chapter 10. In this appendix, we compile this additional data.

In table C.1, we present the complete set of measured material parameters for a 50 nm-thick NbN thin-film, deposited at room temperature on a silicon substrate, at a nitrogen mole fraction of 10.7 %.

In table C.2, we list all the material parameters of the films presented in Fig. 10.2. Here, all the films consist of a 10 nm-thick NbN and are deposited on a silicon substrate at room temperature and as a function of content of nitrogen present in the deposition chamber.

In table C.3, we present the results of a similar study, this time for 5 nm-thick NbN films on sapphire at room temperature. In both cases and as discussed in chapter 10, we note that the disorder in the film increases with the N_2 molar fraction x_{N_2}, with the notable exception of the films at $x_{N_2} = 5.65\,\%$. However, at such a low nitrogen content, these films most likely consist of a composite of NbN and Nb islands and the results of the measurements are hard to interpret quantitatively.

Table C.1: Material parameters for a 50 nm layer deposited at room temperature on silicon substrates and at the nitrogen mole fraction of 10.7 %. The experiments used to measure and calculate the values listed are detailed in chapter 10.

Parameter name	Symbol	Unit	Value
Critical temperature	T_c	K	10.2
Normal-state resistance	R_N	$\Omega/\square$	68.7
Hall coefficient	R_H	$\mathrm{m^3\,C^{-1}}$	6.20×10^{-11}
Upper critical field	$\mu_0 H_{c2}$	T	20.64
Superconducting gap	Δ_0	meV	1.83
Kinetic inductance	L_k	$\mathrm{pH}/\square$	7.88
Carrier density	n_n	$\mathrm{m^{-3}}$	1.01×10^{29}
Fermi wavevector	k_F	$\mathrm{m^{-1}}$	1.44×10^{10}
Fermi energy	ε_F	eV	7.89
Fermi velocity	v_F	$\mathrm{m\,s^{-1}}$	1.67×10^{6}
Density of states	$\rho_s(\varepsilon_F)$	$\mathrm{eV^{-1}\,m^{-3}}$	1.91×10^{28}
Electron mean free path	l	pm	171
Ioffe-Regel parameter	$k_F l$	-	2.46
London penetration depth	λ_{dirty}	nm	560
GL coherence length	ξ_{GL}	nm	3.99
BCS coherence length	ξ_0	nm	191
Electron diffusivity	D	$\mathrm{nm^2\,ps^{-1}}$	94.9
Critical current density	$j_c^{GL}(0)$	$\mathrm{A\,cm^{-2}}$	1.49×10^{7}

Table C.2: Material parameters for the NbN thin-films discussed in section 10.1. These films consists of a 10 nm layer deposited at room temperature on silicon substrates and at the nitrogen mole fraction listed in the table. The experiments used to measure and calculate the values listed are detailed in chapter 10.

Parameter name	Symbol	Unit	Value					
N_2 flow		sccm	5	6.5	8	9.5	11	12.5
N_2 mole fraction	x_{N_2}		5.65 %	7.25 %	8.75 %	10.2 %	11.7 %	13.0 %
Critical temperature	T_c	K	5.04	5.68	5.91	5.80	5.22	4.25
Normal-state resistance	R_N	$\Omega/\square$	611	415	696	844	1.04×10^3	1.93×10^3
Hall coefficient	R_H	$\mathrm{m^3\,C^{-1}}$	5.33×10^{-11}	6.17×10^{-11}	7.79×10^{-11}	1.08×10^{-10}	1.43×10^{-10}	2.05×10^{-10}
Upper critical field	$\mu_0 H_{c2}$	T	6.05	8.90	9.21	9.08	8.52	7.28
Superconducting gap	Δ_0	meV	9.03×10^{-1}	1.02	1.06	1.04	9.36×10^{-1}	7.61×10^{-1}
Kinetic inductance	L_k	$\mathrm{pH}/\square$	142	85.3	138	170	233	530
Carrier density	n_n	$\mathrm{m^{-3}}$	1.17×10^{29}	1.01×10^{29}	8.02×10^{28}	5.80×10^{28}	4.36×10^{28}	3.04×10^{28}
Fermi wavevector	k_F	$\mathrm{m^{-1}}$	1.51×10^{10}	1.44×10^{10}	1.33×10^{10}	1.20×10^{10}	1.09×10^{10}	9.66×10^{9}
Fermi energy	ε_F	eV	8.73	7.91	6.78	5.46	4.52	3.56
Fermi velocity	v_F	$\mathrm{m\,s^{-1}}$	1.75×10^6	1.67×10^6	1.54×10^6	1.39×10^6	1.26×10^6	1.12×10^6
Density of states	$\rho_s(\varepsilon_F)$	$\mathrm{eV^{-1}\,m^{-3}}$	2.01×10^{28}	1.92×10^{28}	1.77×10^{28}	1.59×10^{28}	1.45×10^{28}	1.28×10^{28}
Electron mean free path	l	pm	134	217	151	155	151	104
Ioffe-Regel parameter	$k_F l$	-	2.02	3.13	2.02	1.85	1.65	1.01
London penetration depth	λ_{dirty}	nm	809	497	632	702	822	1.24×10^3
GL coherence length	ξ_{GL}	nm	7.14	4.74	4.71	4.97	4.78	5.60
BCS coherence length	ξ_0	nm	406	343	306	279	282	308
Electron diffusivity	D	$\mathrm{nm^2\,ps^{-1}}$	78.1	121	77.9	71.5	63.6	38.8
Critical current density	$j_c^{GL}(0)$	$\mathrm{A\,cm^{-2}}$	4.94×10^6	7.00×10^6	5.52×10^6	4.61×10^6	3.38×10^6	1.72×10^6

Table C.3: Material parameters for 5 nm NbN thin-films deposited at room temperature on sapphire substrates and at the nitrogen mole fraction listed in the table. The experiments used to measure and calculate the values listed are detailed in chapter 10.

Parameter name	Symbol	Unit	Value					
N_2 flow		sccm	5	6.5	8	9.5	11	12.5
N_2 mole fraction	x_{N_2}		5.65 %	7.25 %	8.75 %	10.2 %	11.7 %	13.0 %
Critical temperature	T_c	K	5.65	10.1	10.6	10.4	6.33	7.58
Normal-state resistance	R_N	$\Omega/\square$	664	451	756	917	1.13×10^3	2.09×10^3
Hall coefficient	R_H	$\mathrm{m^3\,C^{-1}}$	4.33×10^{-11}	4.71×10^{-11}	6.59×10^{-11}	9.11×10^{-11}	1.09×10^{-10}	1.63×10^{-10}
Upper critical field	$\mu_0 H_{c2}$	T	6.46	14.6	14.8	13.3	14.4	10.5
Superconducting gap	Δ_0	meV	8.57×10^{-1}	1.54	1.60	1.57	1.41	1.15
Kinetic inductance	L_k	$\mathrm{pH/\square}$	162	61.2	98.7	122	167	380
Carrier density	n_n	$\mathrm{m^{-3}}$	1.44×10^{29}	1.33×10^{29}	9.48×10^{28}	6.85×10^{28}	5.71×10^{28}	3.84×10^{28}
Fermi wavevector	k_F	$\mathrm{m^{-1}}$	1.62×10^{10}	1.58×10^{10}	1.41×10^{10}	1.27×10^{10}	1.19×10^{10}	1.04×10^{10}
Fermi energy	ε_F	eV	10.0	9.48	7.58	6.11	5.40	4.15
Fermi velocity	v_F	$\mathrm{m\,s^{-1}}$	1.88×10^6	1.83×10^6	1.63×10^6	1.47×10^6	1.33×10^6	1.21×10^6
Density of states	$\rho_s(\varepsilon_F)$	$\mathrm{eV^{-1}\,m^{-3}}$	2.16×10^{28}	2.10×10^{28}	1.87×10^{28}	1.68×10^{28}	1.58×10^{28}	1.39×10^{28}
Electron mean free path	l	pm	139	217	162	166	151	107
Ioffe-Regel parameter	$k_F l$	-	2.26	3.42	2.28	2.10	1.80	1.11
London penetration depth	λ_{dirty}	nm	844	519	659	733	858	1.29×10^3
GL coherence length	ξ_{GL}	nm	7.14	4.74	4.71	4.97	4.78	5.60
BCS coherence length	ξ_0	nm	459	249	214	196	204	220
Electron diffusivity	D	$\mathrm{nm^2\,ps^{-1}}$	87.7	132	88.0	80.9	69.6	43.0
Critical current density	$j_c^{GL}(0)$	$\mathrm{A\,cm^{-2}}$	6.64×10^6	1.91×10^7	1.48×10^7	1.24×10^7	9.24×10^6	4.66×10^6

Appendix D

Superinductor Bifurcation Data

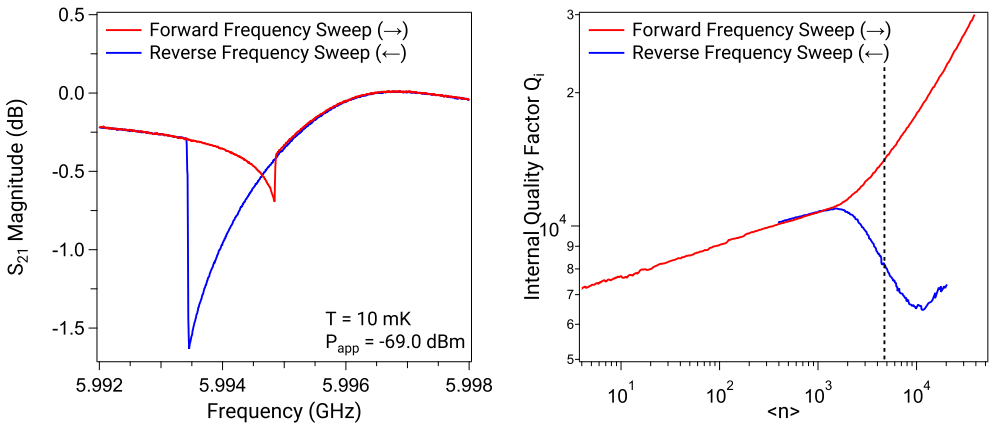

Figure D.1: **(left)** S_{21} magnitude response of the bifurcating nanowire superinductor resonator for a forward and reverse frequency sweep. **(right)** Q_i fitted using Eq. 3.23. The dashed line corresponds to the traces on the left panel.

In chapter 11 and in Paper A, we mention that the power dependence of the kinetic inductance in the resonator leads to a Duffing-like non-linearity [240] which translates into the bifurcation of the resonator at large applied microwave drive. Above the onset of bifurcation, the resonator response is no longer reciprocal and depends on the direction in which the generator frequency is swept: when the frequency is swept forward, the current circulating in the resonator increases as the detuning between the probing tone and the resonance frequency decreases. As the current in the resonator increases, the non-linear kinetic inductance causes the resonance frequency to shift downward, reducing the detuning further. Eventually, the probing tone crosses past the resonance dip of the resonator and the resonator jumps back to a non-energized state. Inversely, when the frequency is swept backwards, the probing tone "chases" the resonance dip of the resonator until the probing frequency sweeps past it and the resonator jumps back to a non-energized state. This behaviour is well illustrated in Fig. 3 of Ref. [240] and Fig. 15 of Ref. [317]. In Fig. D.1 (left), we show an example of the non-reciprocal response of a nanowire superinductor above the onset of bifurcation.

Because of this non-reciprocal response and because of the abrupt jump between a resonant and non-resonant state, the real and imaginary components of the resonator response no longer form a resonant circle (see section 3.5) which leads to an incorrect fit of the quality

factor when fitted with Eq. 3.23. In Fig. D.1 (right), we show the fitted values of Q_i for a nanowire superinductor below and above the onset of bifurcation, for both a forward and reverse frequency sweep. We observe that below the onset of bifurcation, where the resonator response is linear, the fitted Q_i are identical for the forward and reverse sweep direction. However, when the resonator bifurcates, the fit becomes unreliable and the fitted Q values differ greatly.

We have measured the non-linear response of a nanowire superinductor and to understand our experimental data, we base our analysis on the model derived by Swenson [240]. In this model and for $T \ll T_c$, the power dependence of the kinetic inductance is given by

$$L_k(I) = L_k(0)\left[1 + I^2/I_*^2 + \dots\right] \tag{D.1}$$

where I_* is a current close to the critical current and sets the scale of the non-linearity [317]. This non-linear kinetic inductance gives rise to a Duffing oscillator behaviour [318] and the energy stored in the oscillator is given by

$$E = \frac{2Q_l}{Q_c}\frac{1}{1+4Q_l^2x^2}\frac{P_{in}}{\omega_r} \tag{D.2}$$

where the detuning x must account for the downward frequency shift of the resonance frequency as a result of the non-linear kinetic inductance:

$$x = \frac{\omega-\omega_r}{\omega_r} + \frac{E}{E_*} \tag{D.3}$$

Here, E_* is the non-linear energy associated with I_* and is given by $E_* = 2L_kI_*^2/\alpha\kappa_*$, with the kinetic inductance fraction $\alpha \simeq 1$ in our devices, and $\kappa_* \simeq 0.95$ [319].

To find the S_{21} response of the resonator (see Eq. 3.23), we first solve Eqs. D.2 and D.3, the response is then given by

$$S_{21} = 1 - \frac{Q_l|Q_c|^{-1}e^{i\varphi}}{1+2iQ_lx} \tag{D.4}$$

We use Eq. D.4 to calculate the S_{21} response of our device and find that $E_* = 2.33\times10^{-15}\,\mathrm{J}$ best match our experimental data. In Fig. D.2, we show a side by side comparison of the experimental data and the calculated data for this value of E_*.

We note that using Eq. 49 in Ref. [317] and $E_* = 2L_kI_*^2/\alpha\kappa_*$, we get

$$\rho_s(\varepsilon_F) = \frac{1}{\Delta_0^2}\frac{\alpha\kappa_*E_*}{2Lwt} \tag{D.5}$$

where L, w and t are the length, width and thickness of the nanowire. Using the parameters of the thin-film used for the fabrication of this device ($R_N = 873\,\Omega/\square$, $T_c = 5.55\,\mathrm{K}$ and $L_k = 184\,\mathrm{pH}/^2$), our device parameters ($L = 592\,\mu\mathrm{m}$, $w = 100\,\mathrm{nm}$ and $t = 10\,\mathrm{nm}$) and $E_* = 2.33\times10^{-15}\,\mathrm{J}$ in Eq. D.5, we find $\rho_s(\varepsilon_F) = 1.17\times10^{28}\,\mathrm{eV}^{-1}\,\mathrm{m}^{-3}$, which is in reasonable agreement with the values listed in chapters 10 and 11 and appendix C.

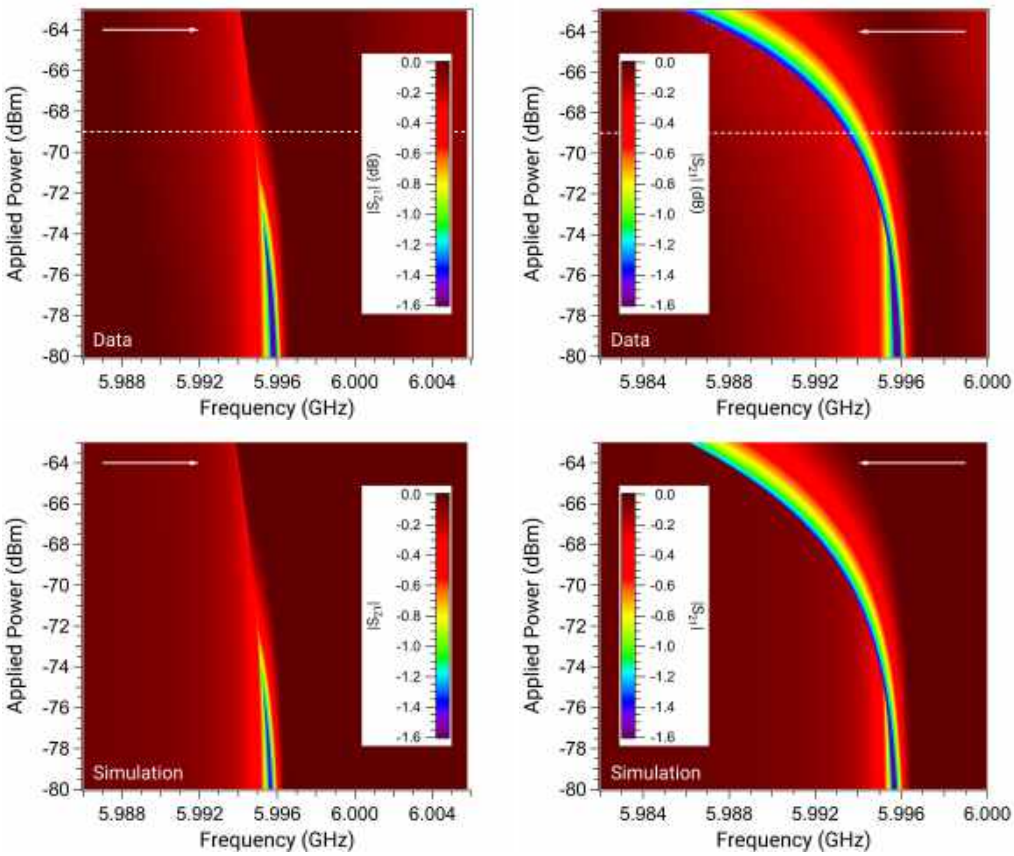

Figure D.2: **(top)** Measured S_{21} magnitude response at large applied powers for a nanowire superinductor. Above the onset of bifurcation, the microwave response of the device becomes non-linear and depends on the direction in which the probing tone is swept. **(bottom)** Simulated S_{21} magnitude response for the same device, using the model described in Ref. [240]. The direction of the frequency sweep is indicated by the white arrow at the top of each panel.

References

[1]X. Gu, A. F. Kockum, A. Miranowicz, Y.-x. Liu, and F. Nori, "Microwave photonics with superconducting quantum circuits", Phys. Rep. **718-719**, 1–102 (2017).

[2]W. D. Oliver and P. B. Welander, "Materials in superconducting quantum bits", MRS Bull. **38**, 816–825 (2013).

[3]I. M. Pop, K. Geerlings, G. Catelani, R. J. Schoelkopf, L. I. Glazman, and M. H. Devoret, "Coherent suppression of electromagnetic dissipation due to superconducting quasiparticles", Nature **508**, 369–372 (2014).

[4]F. Yan et al., "The flux qubit revisited to enhance coherence and reproducibility", Nat. Commun. **7**, 1–9 (2016).

[5]A. Dunsworth et al., "Characterization and reduction of capacitive loss induced by sub-micron Josephson junction fabrication in superconducting qubits", Appl. Phys. Lett. **111**, 022601 (2017).

[6]V. E. Manucharyan, J. Koch, L. I. Glazman, and M. H. Devoret, "Fluxonium: Single Cooper-Pair Circuit Free of Charge Offsets", Science **326**, 113–116 (2009).

[7]L. Grünhaupt et al., "Granular aluminium as a superconducting material for high-impedance quantum circuits", Nat. Mater., 1 (2019).

[8]M. Pita-Vidal et al., "A gate-tunable, field-compatible fluxonium", arXiv (2019).

[9]L. B. Nguyen, Y.-H. Lin, A. Somoroff, R. Mencia, N. Grabon, and V. E. Manucharyan, "High-Coherence Fluxonium Qubit", Phys. Rev. X **9**, 041041 (2019).

[10]N. A. Masluk, I. M. Pop, A. Kamal, Z. K. Minev, and M. H. Devoret, "Microwave Characterization of Josephson Junction Arrays: Implementing a Low Loss Superinductance", Phys. Rev. Lett. **109**, 137002 (2012).

[11]M. T. Bell, I. A. Sadovskyy, L. B. Ioffe, A. Yu. Kitaev, and M. E. Gershenson, "Quantum Superinductor with Tunable Nonlinearity", Phys. Rev. Lett. **109**, 137003 (2012).

[12]J. Koch, V. Manucharyan, M. H. Devoret, and L. I. Glazman, "Charging Effects in the Inductively Shunted Josephson Junction", Phys. Rev. Lett. **103**, 217004 (2009).

[13]A. Belkin, M. Brenner, T. Aref, J. Ku, and A. Bezryadin, "Little–Parks oscillations at low temperatures: Gigahertz resonator method", Appl. Phys. Lett. **98**, 242504 (2011).

[14]J. T. Peltonen et al., "Coherent flux tunneling through NbN nanowires", Phys. Rev. B **88**, 220506(R) (2013).

[15]J. Burnett, J. Sagar, O. W. Kennedy, P. A. Warburton, and J. C. Fenton, "Low-Loss Superconducting Nanowire Circuits Using a Neon Focused Ion Beam", Phys. Rev. Appl. **8**, 014039 (2017).

[16]N. Samkharadze, A. Bruno, P. Scarlino, G. Zheng, D. P. DiVincenzo, L. DiCarlo, and L. M. K. Vandersypen, "High-Kinetic-Inductance Superconducting Nanowire Resonators for Circuit QED in a Magnetic Field", Phys. Rev. Appl. **5**, 044004 (2016).

[17]J. Gao et al., "Experimental evidence for a surface distribution of two-level systems in superconducting lithographed microwave resonators", Appl. Phys. Lett. **92**, 152505 (2008).

[18]S. E. de Graaf, R. Shaikhaidarov, T. Lindström, A. Ya. Tzalenchuk, and O. V. Astafiev, "Charge control of blockade of Cooper pair tunneling in highly disordered TiN nanowires in an inductive environment", Phys. Rev. B **99**, 205115 (2019).

[19]P. Kamenov, W.-S. Lu, K. Kalashnikov, T. DiNapoli, M. T. Bell, and M. E. Gershenson, "Granular Aluminum Meandered Superinductors for Quantum Circuits", Phys. Rev. Appl. **13**, 054051 (2020).

[20]A. Glezer Moshe, E. Farber, and G. Deutscher, "Granular superconductors for high kinetic inductance and low loss quantum devices", Appl. Phys. Lett. **117**, 062601 (2020).

[21]L. Faoro and L. B. Ioffe, "Internal Loss of Superconducting Resonators Induced by Interacting Two-Level Systems", Phys. Rev. Lett. **109**, 157005 (2012).

[22]L. Faoro and L. B. Ioffe, "Interacting tunneling model for two-level systems in amorphous materials and its predictions for their dephasing and noise in superconducting microresonators", Phys. Rev. B **91**, 014201 (2015).

[23]P. V. Klimov et al., "Fluctuations of Energy-Relaxation Times in Superconducting Qubits", Phys. Rev. Lett. **121**, 090502 (2018).

[24]S. Schlör, J. Lisenfeld, C. Müller, A. Bilmes, A. Schneider, D. P. Pappas, A. V. Ustinov, and M. Weides, "Correlating Decoherence in Transmon Qubits: Low Frequency Noise by Single Fluctuators", Phys. Rev. Lett. **123**, 190502 (2019).

[25]J. D. Brehm, A. Bilmes, G. Weiss, A. V. Ustinov, and J. Lisenfeld, "Transmission-line resonators for the study of individual two-level tunneling systems", Appl. Phys. Lett. **111**, 112601 (2017).

[26]J. Burnett et al., "Evidence for interacting two-level systems from the 1/f noise of a superconducting resonator", Nat. Commun. **5**, 1–6 (2014).

[27]J. Burnett, L. Faoro, and T. Lindström, "Analysis of high quality superconducting resonators: consequences for TLS properties in amorphous oxides", Supercond. Sci. Technol. **29**, 044008 (2016).

[28]S. E. de Graaf, L. Faoro, J. Burnett, A. A. Adamyan, A. Ya. Tzalenchuk, S. E. Kubatkin, T. Lindström, and A. V. Danilov, "Suppression of low-frequency charge

noise in superconducting resonators by surface spin desorption", Nat. Commun. **9**, 1–6 (2018).

[29]K. H. Onnes, "The Superconductivity of Mercury", Comm. Phys. Lab. Univ. Leiden **251** (1911).

[30]W. Meissner and R. Ochsenfeld, "Ein neuer Effekt bei Eintritt der Supraleitfähigkeit", Naturwissenschaften **21**, 787–788 (1933).

[31]J. N. Rjabinin and L. W. Shubnikow, "Magnetic Properties and Critical Currents of Supra-conducting Alloys", Nature **135**, 581–582 (1935).

[32]C. J. Gorter and H. Casimir, "On supraconductivity I", Physica **1**, 306–320 (1934).

[33]F. London and H. London, "The electromagnetic equations of the superconductor", Proc. Royal Soc. Lond. A **149**, 71–88 (1935).

[34]V. L. Ginzburg and L. D. Landau, "On the Theory of superconductivity", Zh. Eksp. Teor. Fiz. **20**, 1064–1082 (1950).

[35]A. A. Abrikosov, "On the Magnetic Properties of Superconductors of the Second Group", J. Exp. Theor. Phys **5**, 1174 (1957).

[36]L. P. Gor'kov, "Microscopic Derivation of the Ginzburg-Landau Equations in the Theory of Superconductivity", J. Exp. Theor. Phys **9**, 1364 (1959).

[37]J. Bardeen, L. N. Cooper, and J. R. Schrieffer, "Microscopic Theory of Superconductivity", Phys. Rev. **106**, 162–164 (1957).

[38]J. Bardeen, L. N. Cooper, and J. R. Schrieffer, "Theory of Superconductivity", Phys. Rev. **108**, 1175–1204 (1957).

[39]D. C. Mattis and J. Bardeen, "Theory of the Anomalous Skin Effect in Normal and Superconducting Metals", Phys. Rev. **111**, 412–417 (1958).

[40]P. Drude, "Zur Elektronentheorie der Metalle", Ann. Phys. **306**, 566–613 (1900).

[41]P. Drude, "Zur Elektronentheorie der Metalle; II. Teil. Galvanomagnetische und thermomagnetische Effecte", Ann. Phys. **308**, 369–402 (1900).

[42]N. W. Ashcroft and N. D. Mermin, *Solid state physics* (Saunders College Publishing, 1976).

[43]R. Franz and G. Wiedemann, "Ueber die Wärme-Leitungsfähigkeit der Metalle", Ann. Phys. **165**, 497–531 (1853).

[44]A. Sommerfeld and N. H. Frank, "The Statistical theory of thermoelectric, galvano- and thermomagnetic phenomena in metals", Rev. Mod. Phys. **3**, 1–42 (1931).

[45]L. N. Cooper, "Bound Electron Pairs in a Degenerate Fermi Gas", Phys. Rev. **104**, 1189–1190 (1956).

[46]A. A. Abrikosov, "The magnetic properties of superconducting alloys", J. Phys. Chem. Solids **2**, 199–208 (1957).

[47]B. Mühlschlegel, "Die thermodynamischen Funktionen des Supraleiters", Z. Angew. Phys. **155**, 313–327 (1959).

[48]R. Romestain, B. Delaet, P. Renaud-Goud, I. Wang, C. Jorel, J.-C. Villegier, and J.-P. Poizat, "Fabrication of a superconducting niobium nitride hot electron bolometer for single-photon counting", New J. Phys. **6**, 129 (2004).

[49]D. J. Thouless, "Strong-Coupling Limit in the Theory of Superconductivity", Phys. Rev. **117**, 1256–1260 (1960).

[50]M. Tinkham, *Introduction to superconductivity* (Dover Books, 2004).

[51]T. P. Orlando, E. J. McNiff, S. Foner, and M. R. Beasley, "Critical fields, Pauli paramagnetic limiting, and material parameters of Nb_3Sn and V_3Si", Phys. Rev. B **19**, 4545–4561 (1979).

[52]M. Dressel, "Electrodynamics of Metallic Superconductors", Adv. Condens. Matter Phys. **2013** (2013) 10.1155/2013/104379.

[53]A. F. Ioffe and A. R. Regel, "Non-crystalline, amorphous, and liquid electronic semiconductors", Prog. Semicond. **4**, 237–291 (1960).

[54]P. W. Anderson, "Absence of Diffusion in Certain Random Lattices", Phys. Rev. **109**, 1492–1505 (1958).

[55]R. C. Dynes, J. P. Garno, and J. M. Rowell, "Two-Dimensional Electrical Conductivity in Quench-Condensed Metal Films", Phys. Rev. Lett. **40**, 479–482 (1978).

[56]J. Pearl, "Current Distribution in Superconducting Films Carrying Quantized Fluxoids", Appl. Phys. Lett. **5**, 65–66 (1964).

[57]E. Helfand and N. R. Werthamer, "Temperature and Purity Dependence of the Superconducting Critical Field, H_{c2}", Phys. Rev. Lett. **13**, 686–688 (1964).

[58]E. Helfand and N. R. Werthamer, "Temperature and Purity Dependence of the Superconducting Critical Field, H_{c2}. II", Phys. Rev. **147**, 288–294 (1966).

[59]N. R. Werthamer, E. Helfand, and P. C. Hohenberg, "Temperature and Purity Dependence of the Superconducting Critical Field, H_{c2}. III. Electron Spin and Spin-Orbit Effects", Phys. Rev. **147**, 295–302 (1966).

[60]S. Doyle, "Lumped Element Kinetic Inductance Detectors", PhD thesis (University of Cardiff, 2008).

[61]J. Gao, "The physics of superconducting microwave resonators", PhD thesis (2008).

[62]G. Bergmann, "Physical interpretation of weak localization: A time-of-flight experiment with conduction electrons", Phys. Rev. B **28**, 2914–2920 (1983).

[63]L. G. Aslamasov and A. I. Larkin, "The influence of fluctuation pairing of electrons on the conductivity of normal metal", Phys. Lett. A **26**, 238–239 (1968).

[64]V. L. Berezinsky, "Destruction of Long-range Order in One-dimensional and Two-dimensional Systems Possessing a Continuous Symmetry Group. II. Quantum Systems." J. Exp. Theor. Phys **34**, 610 (1972).

[65]J. M. Kosterlitz and D. J. Thouless, "Ordering, metastability and phase transitions in two-dimensional systems", J. Phys. C: Solid State Phys. **6**, 1181–1203 (1973).

[66]D. R. Nelson and J. M. Kosterlitz, "Universal Jump in the Superfluid Density of Two-Dimensional Superfluids", Phys. Rev. Lett. **39**, 1201–1205 (1977).

[67]M. R. Beasley, J. E. Mooij, and T. P. Orlando, "Possibility of Vortex-Antivortex Pair Dissociation in Two-Dimensional Superconductors", Phys. Rev. Lett. **42**, 1165–1168 (1979).

[68]A. F. Hebard and A. T. Fiory, "Critical-Exponent Measurements of a Two-Dimensional Superconductor", Phys. Rev. Lett. **50**, 1603–1606 (1983).

[69]J. E. Mooij, *Percolation, localization and superconductivity* (Plenum Press, 1984).

[70]S. Y. Hsieh and J. L. Levine, "Diffusion of Quasiparticles in Superconducting Aluminum Films", Phys. Rev. Lett. **20**, 1502–1504 (1968).

[71]P. W. Anderson, K. A. Muttalib, and T. V. Ramakrishnan, "Theory of the "universal"degradation of T_c in high-temperature superconductors", Phys. Rev. B **28**, 117–120 (1983).

[72]B. Hensel, M. Lippert, and H. Adrian, "Effects of electron diffusivity and coulomb interaction in superconducting amorphous films", Physica C **153-155**, 471–472 (1988).

[73]A. Semenov et al., "Optical and transport properties of ultrathin NbN films and nanostructures", Phys. Rev. B **80**, 054510 (2009).

[74]H. Bartolf, A. Engel, A. Schilling, K. Il'in, M. Siegel, H.-W. Hübers, and A. Semenov, "Current-assisted thermally activated flux liberation in ultrathin nanopatterned NbN superconducting meander structures", Phys. Rev. B **81**, 024502 (2010).

[75]A. Einstein, "Über die von der molekularkinetischen Theorie der Wärme geforderte Bewegung von in ruhenden Flüssigkeiten suspendierten Teilchen", Ann. Phys. **322**, 549–560 (1905).

[76]M. von Smoluchowski, "Zur kinetischen Theorie der Brownschen Molekularbewegung und der Suspensionen", Ann. Phys. **326**, 756–780 (1906).

[77]J. R. Waldram, *Superconductivity of Metals and Cuprates* (CRC Press, 1996).

[78]L. P. Gor'kov, "The Critical Supercooling Field in Superconductivity Theory", J. Exp. Theor. Phys **10**, 593 (1960).

[79]J. Bardeen, "Critical Fields and Currents in Superconductors", Rev. Mod. Phys. **34**, 667–681 (1962).

[80]M. Kupriyanov and V. Lukichev, "Temperature dependence of pair-breaking current in superconductors", Sov. J. Low Temp. Phys. **6**, 210 (1980).

[81]J. Romijn, T. M. Klapwijk, M. J. Renne, and J. E. Mooij, "Critical pair-breaking current in superconducting aluminum strips far below T_c", Phys. Rev. B **26**, 3648–3655 (1982).

[82]J. C. Fisher and I. Giaever, "Tunneling Through Thin Insulating Layers", J. Appl. Phys. **32**, 172–177 (1961).

[83]I. Giaever, "Energy Gap in Superconductors Measured by Electron Tunneling", Phys. Rev. Lett. **5**, 147–148 (1960).

[84]I. Giaever, "Electron Tunneling Between Two Superconductors", Phys. Rev. Lett. **5**, 464–466 (1960).

[85]R. C. Dynes, V. Narayanamurti, and J. P. Garno, "Direct Measurement of Quasiparticle-Lifetime Broadening in a Strong-Coupled Superconductor", Phys. Rev. Lett. **41**, 1509–1512 (1978).

[86]J. R. Waldram, A. B. Pippard, and J. Clarke, "Theory of the current-voltage characteristics of SNS junctions and other superconducting weak links", Philos. Trans. R. Soc. London, Ser. A **268** (1970) 10.1098/rsta.1970.0075.

[87]J. Clarke, A. B. Pippard, and J. R. Waldram, "A new theory of the current-voltage characteristics of weak links", Physica **55**, 405–412 (1971).

[88]B. D. Josephson, "Possible new effects in superconductive tunnelling", Physics Letters **1**, 251–253 (1962).

[89]B. D. Josephson, "The discovery of tunnelling supercurrents", Rev. Mod. Phys. **46**, 251–254 (1974).

[90]V. Ambegaokar and A. Baratoff, "Tunneling Between Superconductors", Phys. Rev. Lett. **10**, 486–489 (1963).

[91]V. Ambegaokar and A. Baratoff, "Tunneling Between Superconductors", Phys. Rev. Lett. **11**, 104 (1963).

[92]J. Koch et al., "Charge-insensitive qubit design derived from the Cooper pair box", Phys. Rev. A **76**, 042319 (2007).

[93]M. Büttiker, "Role of quantum coherence in series resistors", Phys. Rev. B **33**, 3020–3026 (1986).

[94]Y. Nakamura, Yu. A. Pashkin, and J. S. Tsai, "Coherent control of macroscopic quantum states in a single-Cooper-pair box", Nature **398**, 786–788 (1999).

[95]K. Bladh, T. Duty, D. Gunnarsson, and P. Delsing, "The single Cooper-pair box as a charge qubit", New J. Phys. **7**, 180 (2005).

[96]J. P. Turneaure and N. T. Viet, "Superconducting Nb TM_{010} Mode Electron-Beam Welded Cavities", Appl. Phys. Lett. **16**, 333–335 (1970).

[97]H. Padamsee, "The science and technology of superconducting cavities for accelerators", Supercond. Sci. Technol. **14**, R28–R51 (2001).

[98]S. Kuhr et al., "Ultrahigh finesse Fabry-Pérot superconducting resonator", Appl. Phys. Lett. **90**, 164101 (2007).

[99]M. Reagor, "Superconducting Cavities for Circuit Quantum Electrodynamics", PhD thesis (Yale University, 2016).

[100]M. Reagor et al., "Quantum memory with millisecond coherence in circuit QED", Phys. Rev. B **94**, 014506 (2016).

[101]M. Kudra, J. Biznárová, A. F. Roudsari, J. J. Burnett, D. Niepce, S. Gasparinetti, B. Wickman, and P. Delsing, "High Quality 3-Dimensional Aluminum Microwave Cavities", arXiv.org (2020).

[102]B. Bianco, A. Corana, L. Gogioso, S. Ridella, and M. Parodi, "Open-circuited coaxial lines as standards for microwave measurements", Electron. Lett. **16**, 373–374 (1980).

[103]D. M. Pozar, *Microwave engineering 3rd edition* (John Wiley & Sons, New York, 2005).

[104]A. Blais, R.-S. Huang, A. Wallraff, S. M. Girvin, and R. J. Schoelkopf, "Cavity quantum electrodynamics for superconducting electrical circuits: An architecture for quantum computation", Phys. Rev. A **69**, 062320 (2004).

[105]H. J. Visser, *Antenna theory and applications* (John Wiley & Sons, New York, 2012).

[106]C. P. Wen, "Coplanar Waveguide: A Surface Strip Transmission Line Suitable for Nonreciprocal Gyromagnetic Device Applications", IEEE Trans. Microwave Theory Tech. **17**, 1087–1090 (1969).

[107]D. Kajfez and P. Guillon, *Dielectric resonators* (SciTec, 1998).

[108]Y. Komatsu and Y. Murakami, "Coupling Coefficient Between Microstrip Line and Dielectric Resonator", IEEE Trans. Microwave Theory Tech. **31**, 34–40 (1983).

[109]R. Barends, "Photon-detecting superconducting resonators", PhD thesis (TU Delft, 2009).

[110]M. S. Khalil, M. J. A. Stoutimore, F. C. Wellstood, and K. D. Osborn, "An analysis method for asymmetric resonator transmission applied to superconducting devices", J. Appl. Phys. **111**, 054510 (2012).

[111]S. Probst, F. B. Song, P. A. Bushev, A. V. Ustinov, and M. Weides, "Efficient and robust analysis of complex scattering data under noise in microwave resonators", Rev. Sci. Instrum. **86**, 024706 (2015).

[112]B. A. Mazin, "Microwave kinetic inductance detectors", PhD thesis (California Institute of Technology, 2004).

[113]R. Barends et al., "Minimizing quasiparticle generation from stray infrared light in superconducting quantum circuits", Appl. Phys. Lett. **99**, 113507 (2011).

[114]A. D. Córcoles et al., "Protecting superconducting qubits from radiation", Appl. Phys. Lett. **99**, 181906 (2011).

[115]E. M. Levenson-Falk, F. Kos, R. Vijay, L. Glazman, and I. Siddiqi, "Single-Quasiparticle Trapping in Aluminum Nanobridge Josephson Junctions", Phys. Rev. Lett. **112**, 047002 (2014).

[116]I. Nsanzineza and B. L. T. Plourde, "Trapping a Single Vortex and Reducing Quasiparticles in a Superconducting Resonator", Phys. Rev. Lett. **113**, 117002 (2014).

[117]C. Wang et al., "Measurement and control of quasiparticle dynamics in a superconducting qubit", Nat. Commun. **5**, 1–7 (2014).

[118]C. Janvier et al., "Coherent manipulation of Andreev states in superconducting atomic contacts", Science **349**, 1199–1202 (2015).

[119]S. Gustavsson et al., "Suppressing relaxation in superconducting qubits by quasiparticle pumping", Science **354**, 1573–1577 (2016).

[120]L. Grünhaupt et al., "Loss Mechanisms and Quasiparticle Dynamics in Superconducting Microwave Resonators Made of Thin-Film Granular Aluminum", Phys. Rev. Lett. **121**, 117001 (2018).

[121]O. V. Astafiev, L. B. Ioffe, S. Kafanov, Yu. A. Pashkin, K. Yu. Arutyunov, D. Shahar, O. Cohen, and J. S. Tsai, "Coherent quantum phase slip", Nature **484**, 355–358 (2012).

[122]P. C. J. J. Coumou, M. R. Zuiddam, E. F. C. Driessen, P. J. de Visser, J. J. A. Baselmans, and T. M. Klapwijk, "Microwave Properties of Superconducting Atomic-Layer Deposited TiN Films", IEEE Trans. Appl. Supercond. **23**, 7500404 (2012).

[123]M. V. Feigel'man and L. B. Ioffe, "Microwave Properties of Superconductors Close to the Superconductor-Insulator Transition", Phys. Rev. Lett. **120**, 037004 (2018).

[124]A. D. O'Connell et al., "Microwave dielectric loss at single photon energies and millikelvin temperatures", Appl. Phys. Lett. **92**, 112903 (2008).

[125]P. Macha, S. H. W. van der Ploeg, G. Oelsner, E. Il'ichev, H.-G. Meyer, S. Wünsch, and M. Siegel, "Losses in coplanar waveguide resonators at millikelvin temperatures", Appl. Phys. Lett. **96**, 062503 (2010).

[126]D. P. Pappas, M. R. Vissers, D. S. Wisbey, J. S. Kline, and J. Gao, "Two Level System Loss in Superconducting Microwave Resonators", IEEE Trans. Appl. Supercond. **21**, 871–874 (2011).

[127]T. Lindström, J. E. Healey, M. S. Colclough, C. M. Muirhead, and A. Ya. Tzalenchuk, "Properties of superconducting planar resonators at millikelvin temperatures", Phys. Rev. B **80**, 132501 (2009).

[128]G. J. Grabovskij, T. Peichl, J. Lisenfeld, G. Weiss, and A. V. Ustinov, "Strain Tuning of Individual Atomic Tunneling Systems Detected by a Superconducting Qubit", Science **338**, 232–234 (2012).

[129]J. Lisenfeld, G. J. Grabovskij, C. Müller, J. H. Cole, G. Weiss, and A. V. Ustinov, "Observation of directly interacting coherent two-level systems in an amorphous material", Nat. Commun. **6**, 1–6 (2015).

[130]J. Wenner et al., "Surface loss simulations of superconducting coplanar waveguide resonators", Appl. Phys. Lett. **99**, 113513 (2011).

[131]C. Wang, C. Axline, Y. Y. Gao, T. Brecht, Y. Chu, L. Frunzio, M. H. Devoret, and R. J. Schoelkopf, "Surface participation and dielectric loss in superconducting qubits", Appl. Phys. Lett. **107**, 162601 (2015).

[132]O. Dial et al., "Bulk and surface loss in superconducting transmon qubits", Supercond. Sci. Technol. **29**, 044001 (2016).

[133]J. M. Gambetta, C. E. Murray, Y.-K.-K. Fung, D. T. McClure, O. Dial, W. Shanks, J. W. Sleight, and M. Steffen, "Investigating Surface Loss Effects in Superconducting Transmon Qubits", IEEE Trans. Appl. Supercond. **27**, 1–5 (2017).

[134]G. Calusine et al., "Analysis and mitigation of interface losses in trenched superconducting coplanar waveguide resonators", Appl. Phys. Lett. **112**, 062601 (2018).

[135]M. D. Abouzahra and L. Lewin, "Radiation from Microstrip Discontinuities", IEEE Trans. Microwave Theory Tech. **27**, 722–723 (1979).

[136]W. Schottky, "Über spontane Stromschwankungen in verschiedenen Elektrizitätsleitern", Ann. Phys. **362**, 541–567 (1918).

[137]W. Schottky, "Zur Berechnung und Beurteilung des Schroteffektes", Ann. Phys. **373**, 157–176 (1922).

[138]J. B. Johnson, "The Schottky Effect in Low Frequency Circuits", Phys. Rev. **26**, 71–85 (1925).

[139]J. B. Johnson, "Thermal Agitation of Electricity in Conductors", Phys. Rev. **32**, 97–109 (1928).

[140]H. Nyquist, "Thermal Agitation of Electric Charge in Conductors", Phys. Rev. **32**, 110–113 (1928).

[141]C. D. Tesche and J. Clarke, "dc SQUID: Noise and optimization", J. Low Temp. Phys. **29**, 301–331 (1977).

[142]D. J. Van Harlingen, R. H. Koch, and J. Clarke, "Superconducting quantum interference device with very low magnetic flux noise energy", Appl. Phys. Lett. **41**, 197–199 (1982).

[143]F. C. Wellstood, C. Urbina, and J. Clarke, "Low-frequency noise in dc superconducting quantum interference devices below 1 K", Appl. Phys. Lett. **50**, 772–774 (1987).

[144]K. I. Park, *Fundamentals of Probability and Stochastic Processes with Applications to Communications* (Springer, Cham, 2018).

[145]N. Wiener, "Generalized harmonic analysis", Acta Mathematica **55**, 117–258 (1930).

[146]A. Khintchine, "Korrelationstheorie der stationären stochastischen Prozesse", Math. Ann. **109**, 604–615 (1934).

[147]P. Welch, "The use of fast Fourier transform for the estimation of power spectra: A method based on time averaging over short, modified periodograms", IEEE Trans. Audio Electroacoust. **15**, 70–73 (1967).

[148]D. W. Allan, "Statistics of atomic frequency standards", Proc. IEEE **54**, 221–230 (1966).

[149]D. A. Howe, D. U. Allan, and J. A. Barnes, "Properties of Signal Sources and Measurement Methods", Thirty Fifth Annual Frequency Control Symposium, 669–716 (1981).

[150]W. Riley, *Handbook of Frequency Stability Analysis* (NIST, July 2008).

[151]J. J. Snyder, "An Ultra-High Resolution Frequency Meter", Thirty Fifth Annual Frequency Control Symposium, 464–469 (1981).

[152]E. Rubiola, *Phase Noise and Frequency Stability in Oscillators* (Cambridge University Press, Nov. 2008).

[153]J. Burnett, "High precision readout of superconducting resonators, for analysis of slow noise processes", PhD thesis (Royal Holloway, University of London, 2014).

[154]D. B. Leeson, "A simple model of feedback oscillator noise spectrum", Proc. IEEE **54**, 329–330 (1966).

[155]C. M. Van Vliet and P. H. Handel, "A new transform theorem for stochastic processes with special application to counting statistics", Physica A **113**, 261–276 (1982).

[156]S. Machlup, "Noise in Semiconductors: Spectrum of a Two-Parameter Random Signal", J. Appl. Phys. **25**, 341–343 (1954).

[157]Sh. Kogan, *Electronic Noise and Fluctuations in Solids* (Cambridge University Press, Aug. 1996).

[158]D. Wolf, *Noise in Physical Systems* (Springer, Berlin, Heidelberg, 1978).

[159]A. A. Balandin, *Noise and fluctuations control in electronic devices* (Amer. sci. publ. Stevenson Ranch (Ca), 2002).

[160]C. M. Wilson, L. Frunzio, and D. E. Prober, "Time-Resolved Measurements of Thermodynamic Fluctuations of the Particle Number in a Nondegenerate Fermi Gas", Phys. Rev. Lett. **87**, 067004 (2001).

[161]P. J. de Visser, J. J. A. Baselmans, P. Diener, S. J. C. Yates, A. Endo, and T. M. Klapwijk, "Generation-Recombination Noise: The Fundamental Sensitivity Limit for Kinetic Inductance Detectors", J. Low Temp. Phys. **167**, 335–340 (2012).

[162]C. Müller, J. Lisenfeld, A. Shnirman, and S. Poletto, "Interacting two-level defects as sources of fluctuating high-frequency noise in superconducting circuits", Phys. Rev. B **92**, 035442 (2015).

[163]F. Hurter and V. C. Driffield, "Photochemical Investigations and a New Method of Determination of the Sensitiveness of Photographic Plates", Journal of the Society of the Chemical Industry **9**, 455–469 (1890).

[164]D. H. Ziger and C. A. Mack, "Generalized approach toward modeling resist performance", AlChE J. **37**, 1863–1874 (1991).

[165]C. A. Mack, D. A. Legband, and S. Jug, "Data analysis for photolithography", Microelectron. Eng. **46**, 65–68 (1999).

[166]N. C. de Lucas, J. C. Netto-Ferreira, J. Andraos, and J. C. Scaiano, "Nucleophilicity toward Ketenes: Rate Constants for Addition of Amines to Aryl Ketenes in Acetonitrile Solution", J. Org. Chem. **66**, 5016–5021 (2001).

[167]Y. Chen, H. Yang, and Z. Cui, "Effects of developing conditions on the contrast and sensitivity of hydrogen silsesquioxane", Microelectron. Eng. **83**, 1119–1123 (2006).

[168]H. Yang, A. Jin, Q. Luo, C. Gu, and Z. Cui, "Comparative study of e-beam resist processes at different development temperature", Microelectron. Eng. **84**, 1109–1112 (2007).

[169]A. Tavakkoli, S. N. Piramanayagam, M. Ranjbar, R. Sbiaa, and T. C. Chong, "Path to achieve sub-10-nm half-pitch using electron beam lithography", Journal of Vacuum Science & Technology B, Nanotechnology and Microelectronics: Materials, Processing, Measurement, and Phenomena **29**, 011035 (2011).

[170]A. E. Grigorescu and C. W. Hagen, "Resists for sub-20-nm electron beam lithography with a focus on HSQ: state of the art", Nanotechnology **20**, 292001 (2009).

[171]H. Namatsu, T. Yamaguchi, M. Nagase, K. Yamazaki, and K. Kurihara, "Nanopatterning of a hydrogen silsesquioxane resist with reduced linewidth fluctuations", Microelectron. Eng. **41-42**, 331–334 (1998).

[172]M. A. Mohammad, S. K. Dew, S. Evoy, and M. Stepanova, "Fabrication of sub-10nm silicon carbon nitride resonators using a hydrogen silsesquioxane mask patterned by electron beam lithography", Microelectron. Eng. **88**, 2338–2341 (2011).

[173]ECHA, *NMP as a substrance of very high concern because of its CMR properties*, (2011) `https://echa.europa.eu/documents/10162/1c4e3474-34ee-4c15-aaef-dafd1cb47779`.

[174]C. Mack, *Fundamental Principles of Optical Lithography* (Nov. 2007).

[175]S. A. Campbell, *The Science and Engineering of Microelectronic Fabrication* (Oxford University Press, 1996).

[176]L. de Broglie, "Recherches sur la théorie des quanta", PhD thesis (Ann. Phys. (Paris), 1924).

[177]A. Potts, G. J. Parker, J. J. Baumberg, and P. A. J. de Groot, "CMOS compatible fabrication methods for submicron Josephson junction qubits", IEE Proceedings - Science, Measurement and Technology **148**, 225–228 (2001).

[178]S. Gladchenko, D. Olaya, E. Dupont-Ferrier, B. Douçot, L. B. Ioffe, and M. E. Gershenson, "Superconducting nanocircuits for topologically protected qubits", Nat. Phys. **5**, 48–53 (2008).

[179]X. Wu, J. L. Long, H. S. Ku, R. E. Lake, M. Bal, and D. P. Pappas, "Overlap junctions for high coherence superconducting qubits", Appl. Phys. Lett. **111**, 032602 (2017).

[180]J. Niemeyer and V. Kose, "Observation of large dc supercurrents at nonzero voltages in Josephson tunnel junctions", Appl. Phys. Lett. **29**, 380–382 (1976).

[181]G. J. Dolan, "Offset masks for lift-off photoprocessing", Appl. Phys. Lett. **31**, 337–339 (1977).

[182]J. M. Kreikebaum, K. P. O'Brien, and I. Siddiqi, "Improving wafer-scale Josephson junction resistance variation in superconducting quantum coherent circuits", arXiv (2019).

[183]A. Osman, "Reliability and reproducibility of Josephson junction fabrication - Steps toward an optimized process", MA thesis (Chalmers University of Technology, 2019).

[184]S. Franssila, *Introduction to Microfabrication* (Sept. 2010).

[185]R. V. Pound, "Electronic Frequency Stabilization of Microwave Oscillators", Rev. Sci. Instrum. **17**, 490–505 (1946).

[186]E. D. Black, "An introduction to Pound–Drever–Hall laser frequency stabilization", Am. J. Phys. **69**, 79 (2000).

[187]B. P. Abbott et al., "LIGO: the Laser Interferometer Gravitational-Wave Observatory", Rep. Prog. Phys. **72**, 076901 (2009).

[188]T. Lindström, J. Burnett, M. Oxborrow, and A. Ya. Tzalenchuk, "Pound-locking for characterization of superconducting microresonators", Rev. Sci. Instrum. **82**, 104706 (2011).

[189]S. E. d. Graaf, A. V. Danilov, A. Adamyan, T. Bauch, and S. E. Kubatkin, "Magnetic field resilient superconducting fractal resonators for coupling to free spins", J. Appl. Phys. **112**, 123905 (2012).

[190]S. E. de Graaf, A. A. Adamyan, T. Lindström, D. Erts, S. E. Kubatkin, A. Ya. Tzalenchuk, and A. V. Danilov, "Direct Identification of Dilute Surface Spins on Al_2O_3: Origin of Flux Noise in Quantum Circuits", Phys. Rev. Lett. **118**, 057703 (2017).

[191]J. Gambetta, W. A. Braff, A. Wallraff, S. M. Girvin, and R. J. Schoelkopf, "Protocols for optimal readout of qubits using a continuous quantum nondemolition measurement", Phys. Rev. A **76**, 012325 (2007).

[192]E. T. Jaynes and F. W. Cummings, "Comparison of quantum and semiclassical radiation theories with application to the beam maser", Proc. IEEE **51**, 89–109 (1963).

[193]C. Gerry and P. Knight, *Introductory Quantum Optics* (Cambridge University Press, Oct. 2004).

[194]J. M. Martinis, M. H. Devoret, and J. Clarke, "Experimental tests for the quantum behavior of a macroscopic degree of freedom: The phase difference across a Josephson junction", Phys. Rev. B **35**, 4682–4698 (1987).

[195]D. B. Davidson, *Computational Electromagnetics for RF and Microwave Engineering* (Cambridge University Press, 2010).

[196]Sonnet Software, Inc., *Sonnet EM Simulation Package*, (2020) `https://www.sonnetsoftware.com/`.

[197]Comsol, Inc., *Comsol Multiphysics*, (2020) `https://www.comsol.com/`.

[198]R. F. Harrington, *Field computation by moment methods* (Wiley-IEEE Press, 1993).

[199]J.-H. Yeh, J. LeFebvre, S. Premaratne, F. C. Wellstood, and B. S. Palmer, "Microwave attenuators for use with quantum devices below 100 mK", J. Appl. Phys. **121**, 224501 (2017).

[200]M. Scigliuzzo, L. E. Bruhat, A. Bengtsson, J. J. Burnett, A. F. Roudsari, and P. Delsing, "Phononic loss in superconducting resonators on piezoelectric substrates", New J. Phys. **22**, 053027 (2020).

[201]W. Woods et al., "Determining Interface Dielectric Losses in Superconducting Coplanar-Waveguide Resonators", Phys. Rev. Appl. **12**, 014012 (2019).

[202]V. Lahtinen and M. Möttönen, "Effects of device geometry and material properties on dielectric losses in superconducting coplanar-waveguide resonators", arXiv (2020).

[203]Y. Ivry, C.-S. Kim, A. E. Dane, D. De Fazio, A. N. McCaughan, K. A. Sunter, Q. Zhao, and K. K. Berggren, "Universal scaling of the critical temperature for thin films near the superconducting-to-insulating transition", Phys. Rev. B **90**, 214515 (2014).

[204]S. S. Mohan, M. del Mar Hershenson, S. P. Boyd, and T. H. Lee, "Simple accurate expressions for planar spiral inductances", IEEE J. Solid-State Circuits **34**, 1419–1424 (1999).

[205]D. F. Santavicca, J. K. Adams, L. E. Grant, A. N. McCaughan, and K. K. Berggren, "Microwave dynamics of high aspect ratio superconducting nanowires studied using self-resonance", J. Appl. Phys. **119**, 234302 (2016).

[206]B. Chiaro et al., "Dielectric surface loss in superconducting resonators with flux-trapping holes", Supercond. Sci. Technol. **29**, 104006 (2016).

[207]Y. Kumashiro, *Electric Refractory Materials* (CRC Press, 2000).

[208]S. Chaudhuri, M. R. Nevala, and I. J. Maasilta, "Niobium nitride-based normal metal-insulator-superconductor tunnel junction microthermometer", Appl. Phys. Lett. **102**, 132601 (2013).

[209]M. D. Henry et al., "Degradation of Superconducting Nb/NbN Films by Atmospheric Oxidation", IEEE Trans. Appl. Supercond. **27**, 1–5 (2017).

[210]A. Ermolieff, M. Girard, C. Raoul, C. Bertrand, and T. M. Duc, "An XPS comparative study on thermal oxide barrier formation on Nb and NbN thin films", Applications of Surface Science **21**, 65–79 (1985).

[211]T. Shiino, S. Shiba, N. Sakai, T. Yamakura, L. Jiang, Y. Uzawa, H. Maezawa, and S. Yamamoto, "Improvement of the critical temperature of superconducting NbTiN and NbN thin films using the AlN buffer layer", Supercond. Sci. Technol. **23**, 045004 (2010).

[212]R. E. Miller, W. H. Mallison, A. W. Kleinsasser, K. A. Delin, and E. M. Macedo, "Niobium trilayer Josephson tunnel junctions with ultrahigh critical current densities", Appl. Phys. Lett. **63**, 1423–1425 (1993).

[213]P. I. Bunyk, A. Oliva, V. K. Semenov, M. Bhushan, K. K. Likharev, J. E. Lukens, M. B. Ketchen, and W. H. Mallison, "High-speed single-flux-quantum circuit using planarized niobium-trilayer Josephson junction technology", Appl. Phys. Lett. **66**, 646–648 (1995).

[214]W. D. Sylwestrowicz, H. A. Elkholy, and G. W. Kammlott, "The effect of temperature and humidity on interdiffusion of gold and titanium in thin films", J. Mater. Sci. **14**, 873–881 (1979).

[215]N. G. Dhere and B. K. Patnaik, "Interdiffusion and phase formation in Ti/Au thin films", Thin Solid Films **85**, 316 (1981).

[216]M. Murakami, E. I. Alessandrini, and K. K. Kim, "Au/Ti resistors used for Nb/Pb-alloy Josephson junctions. I. Electrical stability", J. Appl. Phys. **56**, 2068–2075 (1984).

[217]K. Masahiro and S. Noboru, "Effects of temperature, thickness and atmosphere on mixing in Au-Ti bilayer thin films", J. Mater. Sci. **28**, 5088–5091 (1993).

[218]I. Shalish, S. M. Gasser, E. Kolawa, M.-A. Nicolet, and R. P. Ruiz, "Gold metallization for aluminum nitride", Thin Solid Films **289**, 166–169 (1996).

[219]M. S. Hossain, K. Yoshida, K. Kudo, K. Enpuku, and K. Yamafuji, "Enlargement of Kinetic Inductance of NbN Superconducting Thin Films for Device Applications", Jpn. J. Appl. Phys. **31**, 1033–1038 (1992).

[220]L. Kang et al., "Suppression of superconductivity in epitaxial NbN ultrathin films", J. Appl. Phys. **109**, 033908 (2011).

[221]B. G. Orr, H. M. Jaeger, and A. M. Goldman, "Local superconductivity in ultrathin Sn films", Phys. Rev. B **32**, 7586(R)–7589 (1985).

[222]D. B. Haviland, Y. Liu, and A. M. Goldman, "Onset of superconductivity in the two-dimensional limit", Phys. Rev. Lett. **62**, 2180–2183 (1989).

[223]L. N. Cooper, "Superconductivity in the Neighborhood of Metallic Contacts", Phys. Rev. Lett. **6**, 689–690 (1961).

[224]A. I. Gubin, K. S. Il'in, S. A. Vitusevich, M. Siegel, and N. Klein, "Dependence of magnetic penetration depth on the thickness of superconducting Nb thin films", Phys. Rev. B **72**, 064503 (2005).

[225]M. Yu, M. Strongin, and A. Paskin, "Consistent calculation of boundary effects in thin superconducting films", Phys. Rev. B **14**, 996–1001 (1976).

[226]Y. Guo et al., "Superconductivity Modulated by Quantum Size Effects", Science **306**, 1915–1917 (2004).

[227]S. Qin, J. Kim, Q. Niu, and C.-K. Shih, "Superconductivity at the Two-Dimensional Limit", Science **324**, 1314–1317 (2009).

[228]S. Krause et al., "Ambient Temperature Growth of Mono- and Polycrystalline NbN Nanofilms and Their Surface and Composition Analysis", IEEE Trans. Appl. Supercond. **26**, 1–5 (2016).

[229]E. H. Hall, "On a New Action of the Magnet on Electric Currents", American Journal of Mathematics **2**, 287–292 (1879).

[230]J. M. Graybeal, P. M. Mankiewich, R. C. Dynes, and M. R. Beasley, "Apparent Destruction of Superconductivity in the Disordered One-Dimensional Limit", Phys. Rev. Lett. **59**, 2697–2700 (1987).

[231]F. Sharifi, A. V. Herzog, and R. C. Dynes, "Crossover from two to one dimension in in situ grown wires of Pb", Phys. Rev. Lett. **71**, 428–431 (1993).

[232]M. Tinkham, J. U. Free, C. N. Lau, and N. Markovic, "Hysteretic $I - V$ curves of superconducting nanowires", Phys. Rev. B **68**, 134515 (2003).

[233]A. K. Elmurodov et al., "Phase-slip phenomena in NbN superconducting nanowires with leads", Phys. Rev. B **78**, 214519 (2008).

[234]P. Li, P. M. Wu, Y. Bomze, I. V. Borzenets, G. Finkelstein, and A. M. Chang, "Retrapping current, self-heating, and hysteretic current-voltage characteristics in ultranarrow superconducting aluminum nanowires", Phys. Rev. B **84**, 184508 (2011).

[235]G. L. Pollack, "Kapitza Resistance", Rev. Mod. Phys. **41**, 48–81 (1969).

[236]O. V. Lounasmaa, *Experimental principles and methods below 1K* (Academic Press, 1974).

[237]B. Strehl, T. Niinikoski, A. Rijllart, K. Winter, and M. Caria, "Observation of sub-nanosecond transients in a superconducting microstrip exposed to minimum ionizing radiation", Phys. Lett. B **242**, 285–292 (1990).

[238]S. P. Chockalingam, M. Chand, J. Jesudasan, V. Tripathi, and P. Raychaudhuri, "Superconducting properties and Hall effect of epitaxial NbN thin films", Phys. Rev. B **77**, 214503 (2008).

[239]M. Mondal et al., "Phase Fluctuations in a Strongly Disordered *s*-Wave NbN Superconductor Close to the Metal-Insulator Transition", Phys. Rev. Lett. **106**, 047001 (2011).

[240]L. J. Swenson, P. K. Day, B. H. Eom, H. G. Leduc, N. Llombart, C. M. McKenney, O. Noroozian, and J. Zmuidzinas, "Operation of a titanium nitride superconducting microresonator detector in the nonlinear regime", J. Appl. Phys. **113**, 104501 (2013).

[241]K. D. Osborn, J. A. Strong, A. J. Sirois, and R. W. Simmonds, "Frequency-Tunable Josephson Junction Resonator for Quantum Computing", IEEE Trans. Appl. Supercond. **17**, 166–168 (2007).

[242]P. Krantz et al., "Investigation of nonlinear effects in Josephson parametric oscillators used in circuit quantum electrodynamics", New J. Phys. **15**, 105002 (2013).

[243]S. Kafanov, H. Brenning, T. Duty, and P. Delsing, "Charge noise in single-electron transistors and charge qubits may be caused by metallic grains", Phys. Rev. B **78**, 125411 (2008).

[244]N. Kirsh, E. Svetitsky, A. L. Burin, M. Schechter, and N. Katz, "Revealing the nonlinear response of a tunneling two-level system ensemble using coupled modes", Phys. Rev. Mater. **1**, 012601(R) (2017).

[245]S.-W. Chung, J.-H. Shin, N.-H. Park, and J. W. Park, "Dielectric Properties of Hydrogen Silsesquioxane Films Degraded by Heat and Plasma Treatment", Jpn. J. Appl. Phys. **38**, 5214–5219 (1999).

[246]Y. Qianghua, Y. Guiqin, and N. Zhaoyuan, "Effect of Oxygen Plasma on Low Dielectric Constant HSQ (Hydrogensilsesquioxane) Films", Plasma Sci. Technol. **15**, 86–88 (2013).

[247]M. Morita, T. Ohmi, E. Hasegawa, M. Kawakami, and M. Ohwada, "Growth of native oxide on a silicon surface", J. Appl. Phys. **68**, 1272–1281 (1990).

[248]C. Kaiser, S. T. Skacel, S. Wünsch, R. Dolata, B. Mackrodt, A. Zorin, and M. Siegel, "Measurement of dielectric losses in amorphous thin films at gigahertz frequencies using superconducting resonators", Supercond. Sci. Technol. **23**, 075008 (2010).

[249]A. Romanenko and D. I. Schuster, "Understanding Quality Factor Degradation in Superconducting Niobium Cavities at Low Microwave Field Amplitudes", Phys. Rev. Lett. **119**, 264801 (2017).

[250]P. T. Liu et al., "The effects of plasma treatment for low dielectric constant hydrogen silsesquioxane (HSQ)", Thin Solid Films **332**, 345–350 (1998).

[251]F. Behroozi and M. P. Garfunkel, "Penetration depth in superconducting aluminum as a function of magnetic field and temperature", Physica **55**, 649–655 (1971).

[252]M. D. Maloney, F. de la Cruz, and M. Cardona, "Superconducting Parameters and Size Effects of Aluminum Films and Foils", Phys. Rev. B **5**, 3558–3572 (1972).

[253]B. W. Langley, S. M. Anlage, R. F. W. Pease, and M. R. Beasley, "Magnetic penetration depth measurements of superconducting thin films by a microstrip resonator technique", Rev. Sci. Instrum. **62**, 1801–1812 (1991).

[254]J. M. Sage, V. Bolkhovsky, W. D. Oliver, B. Turek, and P. B. Welander, "Study of loss in superconducting coplanar waveguide resonators", J. Appl. Phys. **109**, 063915 (2011).

[255]A. Megrant et al., "Planar superconducting resonators with internal quality factors above one million", Appl. Phys. Lett. **100**, 113510 (2012).

[256]M. Sandberg, M. R. Vissers, J. S. Kline, M. Weides, J. Gao, D. S. Wisbey, and D. P. Pappas, "Etch induced microwave losses in titanium nitride superconducting resonators", Appl. Phys. Lett. **100**, 262605 (2012).

[257]A. Bruno, G. de Lange, S. Asaad, K. L. van der Enden, N. K. Langford, and L. DiCarlo, "Reducing intrinsic loss in superconducting resonators by surface treatment and deep etching of silicon substrates", Appl. Phys. Lett. **106**, 182601 (2015).

[258]A. N. Ramanayaka, B. Sarabi, and K. D. Osborn, "Evidence for universal relationship between the measured 1/f permittivity noise and loss tangent created by tunneling atoms", arXiv (2015).

[259]C. Neill et al., "Fluctuations from edge defects in superconducting resonators", Appl. Phys. Lett. **103**, 072601 (2013).

[260]C. D. Nugroho, V. Orlyanchik, and D. J. Van Harlingen, "Low frequency resistance and critical current fluctuations in Al-based Josephson junctions", Appl. Phys. Lett. **102**, 142602 (2013).

[261]C. D. Nugroho, "Low frequency critical current noise and two level system defects in Josephson junctions", PhD thesis (University of Illinois at Urbana-Champaign, 2015).

[262]R. Barends et al., "Coherent Josephson Qubit Suitable for Scalable Quantum Integrated Circuits", Phys. Rev. Lett. **111**, 080502 (2013).

[263]M. V. Gustafsson, A. Pourkabirian, G. Johansson, J. Clarke, and P. Delsing, "Thermal properties of charge noise sources", Phys. Rev. B **88**, 245410 (2013).

[264]J. Bylander et al., "Noise spectroscopy through dynamical decoupling with a superconducting flux qubit", Nat. Phys. **7**, 565–570 (2011).

[265]A. A. Clerk and D. W. Utami, "Using a qubit to measure photon-number statistics of a driven thermal oscillator", Phys. Rev. A **75**, 042302 (2007).

[266]R. Barends et al., "Minimal resonator loss for circuit quantum electrodynamics", Appl. Phys. Lett. **97**, 023508 (2010).

[267]D. Ristè, C. C. Bultink, M. J. Tiggelman, R. N. Schouten, K. W. Lehnert, and L. DiCarlo, "Millisecond charge-parity fluctuations and induced decoherence in a superconducting transmon qubit", Nat. Commun. **4**, 1–6 (2013).

[268]K. B. Cooper, M. Steffen, R. McDermott, R. W. Simmonds, S. Oh, D. A. Hite, D. P. Pappas, and J. M. Martinis, "Observation of Quantum Oscillations between a Josephson Phase Qubit and a Microscopic Resonator Using Fast Readout", Phys. Rev. Lett. **93**, 180401 (2004).

[269]S. Gustavsson, F. Yan, J. Bylander, F. Yoshihara, Y. Nakamura, T. P. Orlando, and W. D. Oliver, "Dynamical Decoupling and Dephasing in Interacting Two-Level Systems", Phys. Rev. Lett. **109**, 010502 (2012).

[270]C. Müller, A. Shnirman, and Y. Makhlin, "Relaxation of Josephson qubits due to strong coupling to two-level systems", Phys. Rev. B **80**, 134517 (2009).

[271]D. J. Salvino, S. Rogge, B. Tigner, and D. D. Osheroff, "Low Temperature ac Dielectric Response of Glasses to High dc Electric Fields", Phys. Rev. Lett. **73**, 268–271 (1994).

[272]S. Ludwig, P. Nalbach, D. Rosenberg, and D. Osheroff, "Dynamics of the Destruction and Rebuilding of a Dipole Gap in Glasses", Phys. Rev. Lett. **90**, 105501 (2003).

[273]P. J. de Visser, J. J. A. Baselmans, P. Diener, S. J. C. Yates, A. Endo, and T. M. Klapwijk, "Number Fluctuations of Sparse Quasiparticles in a Superconductor", Phys. Rev. Lett. **106**, 167004 (2011).

[274]D. Niepce, J. Burnett, and J. Bylander, "High Kinetic Inductance NbN Nanowire Superinductors", Phys. Rev. Appl. **11**, 044014 (2019).

[275]D. Niepce, J. J. Burnett, M. G. Latorre, and J. Bylander, "Geometric scaling of two-level-system loss in superconducting resonators", Supercond. Sci. Technol. **33**, 025013 (2020).

[276]M. Reagor et al., "Reaching 10 ms single photon lifetimes for superconducting aluminum cavities", Appl. Phys. Lett. **102**, 192604 (2013).

[277]A. Romanenko, R. Pilipenko, S. Zorzetti, D. Frolov, M. Awida, S. Belomestnykh, S. Posen, and A. Grassellino, "Three-Dimensional Superconducting Resonators at $T < 20$ mK with Photon Lifetimes up to $\tau = 2$ s", Phys. Rev. Appl. **13**, 034032 (2020).

[278]A. Abragam, *Principles of nuclear magnetism* (Oxford University Press, 1961), p. 447.

[279]P. P. Borbat, A. J. Costa-Filho, K. A. Earle, J. K. Moscicki, and J. H. Freed, "Electron Spin Resonance in Studies of Membranes and Proteins", Science **291**, 266–269 (2001).

[280]G. J. Perlow, "Influence of Radio-Frequency Magnetic Fields on the Mössbauer Effect in Magnetic Co^{57} Sources", Phys. Rev. **172**, 319–324 (1968).

[281]A. Berthelot, I. Favero, G. Cassabois, C. Voisin, C. Delalande, P. Roussignol, R. Ferreira, and J. M. Gérard, "Unconventional motional narrowing in the optical spectrum of a semiconductor quantum dot", Nat. Phys. **2**, 759–764 (2006).

[282]C. G., "Spectral diffusion dephasing and motional narrowing in single semiconductor quantum dots", in *Optical generation and control of quantum coherence in semiconductor nanostructures*, edited by G. Slavcheva and P. Roussignol, NanoScience and Technology (Springer, Berlin, Heidelberg, 2010), pp. 25–35.

[283]D. S. Wisbey, J. Gao, M. R. Vissers, F. C. S. da Silva, J. S. Kline, L. Vale, and D. P. Pappas, "Effect of metal/substrate interfaces on radio-frequency loss in superconducting coplanar waveguides", J. Appl. Phys. **108**, 093918 (2010).

[284]H. Paik and K. D. Osborn, "Reducing quantum-regime dielectric loss of silicon nitride for superconducting quantum circuits", Appl. Phys. Lett. **96**, 072505 (2010).

[285]A. L. Burin and A. O. Maksymov, "Theory of nonlinear microwave absorption by interacting two-level systems", Phys. Rev. B **97**, 214208 (2018).

[286]T. Kohmoto, Y. Fukuda, M. Kunitomo, K. Ishikawa, M. Tanigawa, K. Ebina, and M. Kaburagi, "Hole burning in well-defined noise fields: Motional narrowing", Phys. Rev. B **49**, 15352–15355 (1994).

[287]J. Li et al., "Motional averaging in a superconducting qubit", Nat. Commun. **4**, 1–6 (2013).

[288]L. Jiang, M. V. G. Dutt, E. Togan, L. Childress, P. Cappellaro, J. M. Taylor, and M. D. Lukin, "Coherence of an Optically Illuminated Single Nuclear Spin Qubit", Phys. Rev. Lett. **100**, 073001 (2008).

[289]D. Bluvstein, Z. Zhang, C. A. McLellan, N. R. Williams, and A. C. B. Jayich, "Extending the quantum coherence of a near-surface qubit by coherently driving the paramagnetic surface environment", Phys. Rev. Lett. **123**, 146804 (2019).

[290]C. Müller, J. H. Cole, and J. Lisenfeld, "Towards understanding two-level-systems in amorphous solids: insights from quantum circuits", Rep. Prog. Phys. **82**, 124501 (2019).

[291]J. J. Burnett, A. Bengtsson, M. Scigliuzzo, D. Niepce, M. Kudra, P. Delsing, and J. Bylander, "Decoherence benchmarking of superconducting qubits", npj Quantum Inf. **5**, 54 (2019).

[292]C. Müller, A. Shnirman, and Y. Makhlin, "Relaxation of josephson qubits due to strong coupling to two-level systems", Phys. Rev. B **80**, 134517 (2009).

[293]C. Müller, J. Lisenfeld, A. Shnirman, and S. Poletto, "Interacting two-level defects as sources of fluctuating high-frequency noise in superconducting circuits", Phys. Rev. B **92**, 035442 (2015).

[294]W. A. Phillips, "Two-level states in glasses", Rep. Prog. Phys. **50**, 1657–1708 (1987).

[295]W. D. Oliver and S. O. Valenzuela, "Large-amplitude driving of a superconducting artificial atom", Quantum Information Processing **8**, 261–281 (2009).

[296]W. D. Oliver, Y. Yu, J. C. Lee, K. K. Berggren, L. S. Levitov, and T. P. Orlando, "Mach-Zehnder Interferometry in a Strongly Driven Superconducting Qubit", Science **310**, 1653–1657 (2005).

[297]D. M. Berns, W. D. Oliver, S. O. Valenzuela, A. V. Shytov, K. K. Berggren, L. S. Levitov, and T. P. Orlando, "Coherent quasiclassical dynamics of a persistent current qubit", Phys. Rev. Lett. **97**, 150502 (2006).

[298]S. Matityahu, H. Schmidt, A. Bilmes, A. Shnirman, G. Weiss, A. V. Ustinov, M. Schechter, and J. Lisenfeld, "Dynamical decoupling of quantum two-level systems by coherent multiple landau–zener transitions", npj Quantum Information **5**, 114 (2019).

[299]A. L. Burin, M. S. Khalil, and K. D. Osborn, "Universal dielectric loss in glass from simultaneous bias and microwave fields", Phys. Rev. Lett. **110**, 157002 (2013).

[300]M. S. Khalil, S. Gladchenko, M. J. A. Stoutimore, F. C. Wellstood, A. L. Burin, and K. D. Osborn, "Landau-zener population control and dipole measurement of a two-level-system bath", Phys. Rev. B **90**, 100201 (2014).

[301]A. J. Kerman, "Metastable Superconducting Qubit", Phys. Rev. Lett. **104**, 027002 (2010).

[302]P. Brooks, A. Kitaev, and J. Preskill, "Protected gates for superconducting qubits", Phys. Rev. A **87**, 052306 (2013).

[303]W. Guichard and F. W. J. Hekking, "Phase-charge duality in Josephson junction circuits: Role of inertia and effect of microwave irradiation", Phys. Rev. B **81**, 064508 (2010).

[304]A. Stockklauser et al., "Strong Coupling Cavity QED with Gate-Defined Double Quantum Dots Enabled by a High Impedance Resonator", Phys. Rev. X **7**, 011030 (2017).

[305]N. Samkharadze et al., "Strong spin-photon coupling in silicon", Science **359**, 1123–1127 (2018).

[306]B. Ho Eom, P. K. Day, H. G. LeDuc, and J. Zmuidzinas, "A wideband, low-noise superconducting amplifier with high dynamic range", Nat. Phys. **8**, 623 (2012).

[307]C. Bockstiegel et al., "Development of a Broadband NbTiN Traveling Wave Parametric Amplifier for MKID Readout", J. Low Temp. Phys. **176**, 476–482 (2014).

[308]K. O'Brien, C. Macklin, I. Siddiqi, and X. Zhang, "Resonant Phase Matching of Josephson Junction Traveling Wave Parametric Amplifiers", Phys. Rev. Lett. **113**, 157001 (2014).

[309]T. C. White et al., "Traveling wave parametric amplifier with Josephson junctions using minimal resonator phase matching", Appl. Phys. Lett. **106**, 242601 (2015).

[310]C. Macklin, K. O'Brien, D. Hover, M. E. Schwartz, V. Bolkhovsky, X. Zhang, W. D. Oliver, and I. Siddiqi, "A near–quantum-limited Josephson traveling-wave parametric amplifier", Science **350**, 307–310 (2015).

[311]M. R. Vissers, R. P. Erickson, H.-S. Ku, L. Vale, X. Wu, G. C. Hilton, and D. P. Pappas, "Low-noise kinetic inductance traveling-wave amplifier using three-wave mixing", Appl. Phys. Lett. **108**, 012601 (2016).

[312]A. A. Adamyan, S. E. de Graaf, S. E. Kubatkin, and A. V. Danilov, "Superconducting microwave parametric amplifier based on a quasi-fractal slow propagation line", J. Appl. Phys. **119**, 083901 (2016).

[313]R. M. J. Janssen, A. Endo, J. J. A. Baselmans, P. J. de Visser, R. Barends, and T. M. Klapwijk, "Power Handling and Responsivity of Submicron Wide Superconducting Coplanar Waveguide Resonators", J. Low Temp. Phys. **167**, 354–359 (2012).

[314]E. Schroeder, P. Mauskopf, H. Mani, S. Bryan, K. K. Berggren, and D. Zhu, "Operation of a Superconducting Nanowire in Two Detection Modes: KID and SPD", J. Low Temp. Phys. **194**, 386–393 (2019).

[315]A. K. Sinclair, E. Schroeder, D. Zhu, M. Colangelo, J. Glasby, P. D. Mauskopf, H. Mani, and K. K. Berggren, "Demonstration of Microwave Multiplexed Readout of DC-Biased Superconducting Nanowire Detectors", IEEE Trans. Appl. Supercond. **29**, 1–4 (2019).

[316]R. N. Simons, *Coplanar Waveguide Circuits, Components, and Systems* (Mar. 2001).

[317]J. Zmuidzinas, "Superconducting Microresonators: Physics and Applications", Annu. Rev. Condens. Matter Phys. **3**, 169–214 (2012).

[318]G. Duffing, *Erzwungene schwingungen bei veränderlicher eigenfrequenz und ihre technische bedeutung* (F. Vieweg & sohn, 1918).

[319]A. Anthore, H. Pothier, and D. Esteve, "Density of States in a Superconductor Carrying a Supercurrent", Phys. Rev. Lett. **90**, 127001 (2003).

Paper A

High Kinetic Inductance NbN Nanowire Superinductors

High Kinetic Inductance NbN Nanowire Superinductors

David Niepce,* Jonathan Burnett, and Jonas Bylander
Microtechnology and Nanoscience, Chalmers University of Technology, Gothenburg SE-41296, Sweden

(Received 6 February 2018; revised manuscript received 22 December 2018; published 4 April 2019)

We demonstrate that a high kinetic inductance disordered-superconductor nanowire can realize a circuit element – known as a superinductor – with a characteristic impedance greater than the quantum resistance ($R_Q = h/4e^2 \simeq 6.5\,\mathrm{k\Omega}$) and a quality factor of 25 000 at single-photon excitation. By examining loss rates, we demonstrate that the microwave dissipation can be fully understood in the framework of two-level-system dielectric loss. Superinductors can suppress the quantum fluctuations of charge in a circuit, which has applications, for example, in devices for quantum computing, photon detection, and other sensors based on mesoscopic circuits.

DOI: 10.1103/PhysRevApplied.11.044014

I. INTRODUCTION

Disorder within superconductors can reveal nontrivial electrodynamics [1–3], dual Josephson effects [4], and superconducting-insulating phase transitions [5]. In general, disorder increases the normal-state resistance of the superconductor, which also enhances the kinetic inductance due to the inertia of the charge carriers (the Cooper pairs).

High kinetic inductance can be used to design circuits with characteristic impedances exceeding the quantum resistance ($R_Q = h/4e^2 \simeq 6.5\,\mathrm{k\Omega}$). A quantum circuit element with zero dc resistance, low microwave losses, and a characteristic impedance above R_Q is known as a superinductor [6,7]. The fluxonium qubit, based on superinductors, is immune to charge fluctuations [8] and has demonstrated extraordinary relaxation times [9]; it also has a much greater anharmonicity than the predominantly used superconducting qubits, thereby facilitating the high-fidelity quantum gate operations required for quantum computing. However, these examples of superinductors have been based on the kinetic inductance of Josephson junction arrays (JJA), and not on disordered materials, which places constraints on the possible device parameters and geometries.

An attractive alternative to JJAs is offered by the high kinetic inductance of nanowires made of strongly disordered superconducting thin films [10]. Such a superinductor should possess tremendous magnetic field tolerance, suitable for hybrid qubits, which operate at high magnetic fields [11,12]. It also exhibits an increased coupling between photons and charge, due to the enhanced zero-point fluctuations of the electric field afforded by the high impedance [12,13]. High-impedance resonators have enabled strong coupling between microwave photons and the charge in semiconductor quantum dots [14,15] and could enable strong coupling to spins [16]; superinductors should increase these effects even more. High-impedance circuits can also be used in photon detectors [17] or in mesoscopic-transport experiments, e.g., for metrology applications [18]. Additionally, nanowire-based superinductors have a wide parameter space to suppress self-resonant modes [6], which are an obstacle for demonstrating some topologically protected qubit designs [10,19].

A superconducting nanowire-based approach was previously overlooked, because a variety of circuits fabricated with strongly disordered superconductors were found to exhibit significant internal dissipation [20–23], with quality factors of 500 to 1000. There is clear experimental evidence of the existence of a disorder-related loss [24] and recent theoretical work attributes these losses to the presence of low-lying subgap states in the proximity of the superconducting-insulating transition [25].

However, it has recently been shown that it is possible to fabricate superconducting nanowires embedded within resonators that do not exhibit high dissipation [26]. In addition, 100-nm-wide resonators made from weakly disordered superconductors have also shown high-quality factors at the relatively high temperature of 280 mK and approximately 1000-photon population [13]. This motivates the need to fabricate a sufficiently disordered superconductor to obtain high inductance, but not so disordered as to induce dissipation, where the requirements can be balanced by using moderately thin films. Therefore, to maximize the characteristic impedance, it becomes crucial to minimize the stray capacitance, which can be achieved with a nanowire geometry. However, the nanowire geometry is itself more susceptible to parasitic two-level systems (TLS) compared to wider conductors. This is due to an

*david.niepce@chalmers.se

enhanced participation ratio [17] of the TLS host volume, within dielectrics, to the total volume threaded by the electric field.

In this paper, we demonstrate a nanowire-based superinductor with a characteristic impedance of 6.795 kΩ. We developed a process, based on dry etching of a hydrogen silsesquioxane (HSQ) mask defined by high-resolution electron-beam lithography, to pattern a 20-nm-thick film of niobium nitride (NbN) into a 40-nm wide and approximately 680-μm-long nanowire. This is sufficiently narrow to ensure a large inductance and sufficiently wide to exponentially suppress unwanted phase slips of the superconducting order parameter [21]. The thickness is chosen so as to yield a strongly but not excessively disordered film to balance the requirements of high kinetic inductance and low losses. We study both the microwave transmission and dc transport properties of several nanowires to characterize their impedance and microwave losses: they exhibit a quality factor at single-photon excitation of 2.5×10^4, which is comparable to JJA-based superinductors [6]. We find that the dominant loss mechanism is parasitic TLS, which is exacerbated by the unfavorable TLS participation ratio [17] that arises from the small dimensions required to obtain a high impedance.

II. METHODS

The measured sample contains five nanowires that are inductively coupled to a common microwave transmission line. It also contains separate dc transport test structures. Figures 1(a) and 1(b) show micrographs of a typical device. The fabrication process is detailed in Appendix A and materials and design considerations in Appendix D.

We study the microwave properties of these resonators by measuring the forward transmission (S_{21}) response. In a similar way to the devices measured in Ref. [13], the coupling to the fundamental mode in our resonators is extremely weak. Therefore, in the following, we focus our study on the next resonant mode. Figure 1(c) shows a typical S_{21} magnitude response measured at 10 mK and with an average photon population $\langle n \rangle = 1$. We determine the resonator parameters by fitting the data with an open-source traceable fit routine [27], from which we find a resonant frequency $f_r = 4.835$ GHz and an internal quality factor $Q_i = 2.5 \times 10^4$. Detailed experimental methods are included in Appendices B–C.

III. RESULTS AND DISCUSSION

To understand this resonance, we first study the transport properties of our NbN nanowires. We estimate the kinetic inductance contribution $L_k^{\square}(0)$ using [28]

$$L_k^{\square}(0) = \frac{\hbar R_N^{\square}}{\pi \Delta_0}, \tag{1}$$

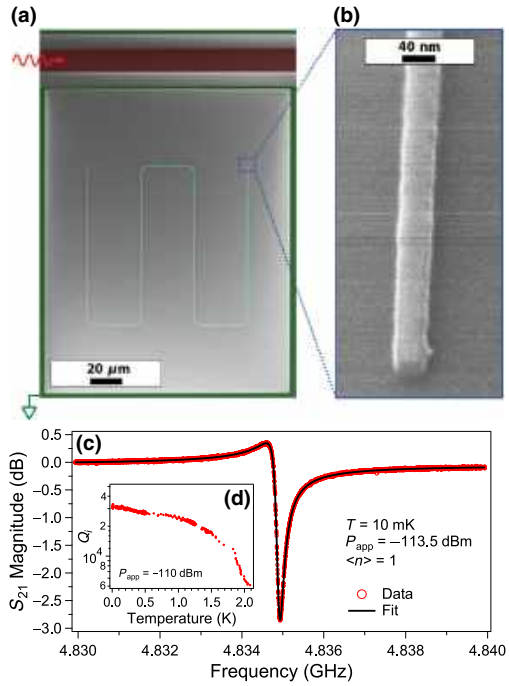

FIG. 1. (a) False-color scanning electron microscope micrograph of a nanowire resonator coupled to a microwave feed line; the NbN feed line is shown in red, the NbN ground planes are shown in green, the exposed Si substrate where NbN has been etched away is in gray and the 40 nm × 680 μm nanowire is highlighted in cyan. (b) A helium focused ion beam image of the nanowire highlighting a very good line edge roughness and a low concentration of shape defects. (c) S_{21} magnitude response of the device, in the single-photon regime. The black line is a fit to determine the resonance parameters. (d) A plot of the internal quality factor Q_i of a nanowire superinductor resonator as a function of temperature.

where $R_N^{\square}$ is the normal-state sheet resistance, $\hbar$ the reduced Planck constant, and Δ_0 the superconducting gap at zero temperature. NbN is experimentally found to be a strongly coupled superconductor with $\Delta_0 = 2.08 k_B T_c$ [2], where T_c is the critical temperature and k_B is the Boltzmann constant. By measuring the $R(T)$ characteristic we find $R_N^{\square} = 503\ \Omega/\square$ and $T_c = 7.20$ K. Using Eq. (1), this yields $L_k^{\square}(0) = 82$ pH/□. For a 40-nm-wide nanowire, this corresponds to an inductance per unit length of 2.05 mH m^{-1}. From an empirical formula [29], the magnetic inductance, due to the geometry of the nanowire, is estimated to be only $L_m \simeq 1\ \mu$H m^{-1}. Therefore, we assume that the nanowire inductance arises entirely from the kinetic inductance, so that $L_{\mathrm{NW}} = L_k$. Further materials and geometrical

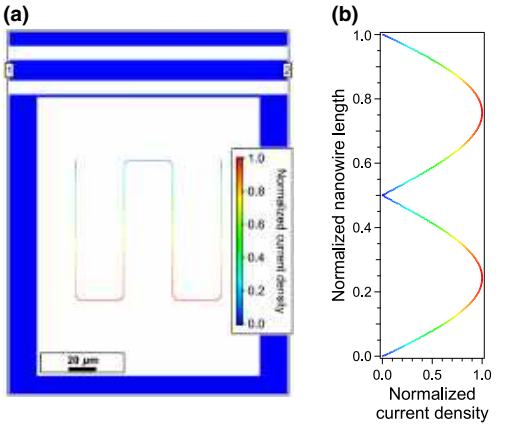

FIG. 2. (a) Microwave simulation of the current density in the device for the second resonant mode. (b) Normalized current density along the nanowire extracted from the simulation. The obtained mode structure is consistent with the second mode of a distributed $\lambda/2$ resonator. See also Appendix D 2 c and Figs. 10–11.

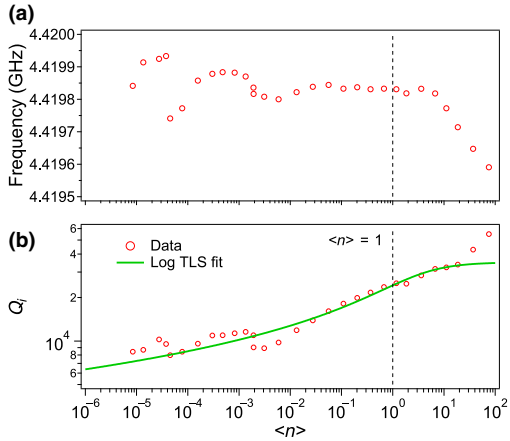

FIG. 3. (a) Resonant frequency of a typical nanowire resonator as a function of microwave drive. (b) Internal quality factor (Q_i) of a typical nanowire superinductor resonator as a function of the microwave drive. The solid line is a fit to Eq. (3). The vertical dashed lines highlight the single microwave photon regime.

considerations for nanowires are explained in detail in Appendix D.

We simulate our devices using Sonnet *em* microwave simulator. The simulation results, shown in Figs. 2(a) and 2(b), confirm that our device behaves as a distributed $\lambda/2$ resonator with a well-defined wave impedance (see also Appendix D 2 c). From the simulation we also estimate the capacitance per unit length to be $C_{\mathrm{NW}} = 44.4\ \mathrm{pF\,m^{-1}}$. Combining these properties leads to estimated resonant frequencies within 1% of the measured f_r for all of our resonators. Using these parameters, we calculate the characteristic impedance of our nanowires to be $Z_c = \sqrt{L_{\mathrm{NW}}/C_{\mathrm{NW}}} = 6.795\ \mathrm{k\Omega} \pm 35\ \Omega$. Therefore, $Z_c \geq R_Q$, indicating that they are indeed superinductors.

Having demonstrated superinductors, we now examine their behavior as a function of applied microwave drive and varying temperature. We first determine the range of temperatures at which we can operate our device. Figure 1(d) shows a measurement of the internal quality factor Q_i against temperature. We show that from 10 mK to 1.4 K, it only marginally decreases from 3×10^4 to 2×10^4. This offers a far greater range of operation than aluminum JJA-based superinductors, which show significant dissipation above 100 mK [6].

We now investigate the low-temperature loss mechanisms as a function of microwave power. When probed with an applied power P_{in}, the average energy stored in a resonator of characteristic impedance Z_c is given by $\langle E_{\mathrm{int}}\rangle = \langle n\rangle/hf_r = Z_0 Q_l^2 P_{\mathrm{in}}/\pi^2 Z_c Q_c f_r$, where $\langle n\rangle$ is the average number of photons in the resonator, h is Planck's constant, $Z_0 = 50\ \Omega$, and Q_c and Q_l are the coupling and loaded quality factors, respectively. Due to the large characteristic impedance of our resonator, we are able to measure in the low photon regime with a high applied power. Consequently, this enables us to measure, with good signal-to-noise ratio (without using a quantum-limited parametric amplifier), photon populations 2 to 3 orders of magnitude lower than in conventional resonators.

In Fig. 3(a), starting at $\langle n\rangle = 1$, as we increase the power, the resonant frequency does not change until $\langle n\rangle \simeq 10$. Upon a further increase of the power, the frequency decreases until the resonator bifurcates. This is explained by the power dependence of the kinetic inductance, which behaves as a Duffing-like nonlinearity [30]. We note that this nonlinearity occurs at similar microwave drive powers as for junction-embedded resonators [31]. Starting again at $\langle n\rangle = 1$, as we now decrease the power, we see the frequency remains approximately constant. As $\langle n\rangle$ is decreased below $\langle n\rangle \simeq 10^{-3}$, the resonator exhibits frequency jitter consistent with TLS-induced changes of the permittivity $\epsilon(f)$ [32]. This frequency noise results in spectral broadening of the resonance curve.

We now examine the internal quality factor as a function of applied microwave power. In Fig. 3(b), within the power range between $\langle n\rangle \simeq 10^{-5}$ and $\langle n\rangle \simeq 10^{-3}$, we find that Q_i is approximately constant, with changes in the fitted value caused by frequency-jitter-induced spectral broadening. As we increase the power from $\langle n\rangle \simeq 10^{-3}$, Q_i increases, which is consistent with depolarization of TLS. For $\langle n\rangle \geq 40$, Q_i is overestimated due to the Duffing nonlinearity.

In order to fit the data, it is usual to sum inverse quality factors to produce a loss model that can distinguish different loss channels. Of these quality factors, we first consider the dielectric loss of a capacitor, which is described by $1/Q_{\rm cap} = \epsilon''/\epsilon'$. Conventionally, we label this in terms of TLS susceptibility [$\chi(f) = \epsilon(f) - 1$], which can be split into a real (dispersive) term $\chi'(f)$, and an imaginary (dissipative) term $\chi''(f)$ [33,34]. Typically, data such as that in Fig. 3(b) is fitted to a loss model based on $\chi''(f)$ [26,35], where the resulting quality factor is justified either by simulation [36] or by measurement of a tanh-like temperature dependence [26]. However, unless the statistics of Q_i are sufficient to reliably extract the mean [37], this approach can suffer from errors in determining the TLS quality factor. This spread in Q_i arises from spectral instability of TLS [32,38,39], which leads to a time-varying number of near-resonant TLS. Crucially, $\chi''(f)$ is strongly peaked [33] (Lorentzian-like) and therefore is particularly sensitive to fluctuations of a narrow spectrum of TLS.

Instead, it is preferable to determine the TLS losses by using $\chi'(f)$, which can be accurately inferred from a measurement of the shift of the resonant frequency as a function of temperature, $\Delta f\,(T)$. The real part χ' decays slowly in frequency [33], in contrast to χ'', and therefore is robust against spectral instabilities. Consequently, $\chi''(f)$ can be determined from $\chi'(f)$ by the Kramers-Kronig relation to reliably determine the TLS-related quality factor, whose inverse is then called the *intrinsic* loss tangent, $F\delta^i_{\rm TLS}$ [17].

To measure $\Delta f\,(T)$ we lock onto the resonant frequency using a Pound frequency-locked loop (PFLL) [32,40], and continuously track frequency changes of the resonator as we vary the temperature (See Appendix C for details of the experimental setup). TLS can become thermally excited and the multiple TLS states correspond to different permittivity (susceptibility, i.e., capacitance): as we vary the temperature, the permittivity changes and therefore the frequency changes. Figure 4(a) shows the changes in resonant frequency against the natural energy scale of the TLS (hf_r/k_BT) for temperatures ranging from 10 mK to 1 K. This frequency shift is described by [17]

$$\Delta f\,(T) = F\delta^i_{\rm TLS}\left\{\ln\left(\frac{T}{T_0}\right) - [g(T,f_r) - g(T_0,f_r)]\right\}, \quad (2)$$

where $\Delta f\,(T) = [f_r(T) - f_r(T_0)]/f_r(T_0)$, T_0 is a reference temperature, the participation ratio F is the ratio of electric field threading TLS to the total electric field, $g(T,f) = {\rm Re}\left[\Psi\left(\frac{1}{2} + hf\,/2\pi ik_BT\right)\right]$, and Ψ is the complex digamma function.

We use Eq. (2) to fit the measured data in Fig. 4. Importantly, this expression only fits the TLS contribution but does not fit the temperature-dependent kinetic-inductance contribution, which occurs below $hf_r/k_BT = 0.1$. Table I contains the resulting values for the intrinsic loss tangent

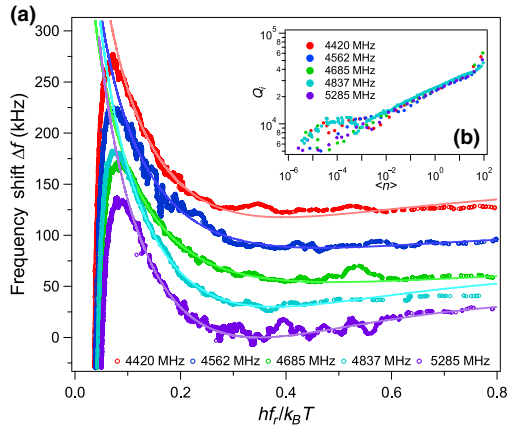

FIG. 4. (a) Frequency shift Δf as a function of the normalized frequency f_r of all measured nanowire superinductor resonators. The data is experimentally obtained with the PFLL by tracking the changes in resonant frequency against temperature between 10 mK and 1 K. The solid lines show fits to the theory described by Eq. (2). For clarity, the curves have been offset by 30 kHz. (b) Q_i vs microwave drive power for the same nanowire superinductor resonators (cf. Fig. 3).

$F\delta^i_{\rm TLS}$, which, in turn, can be used to fit the data in Fig. 3 using a model that takes TLS interactions into account [32,41]:

$$\frac{1}{Q_i} = F\delta^i_{\rm TLS}P_\gamma \ln\left(\frac{cn_c}{\langle n\rangle} + \delta'_0\right)\tanh\left(\frac{hf_r}{2k_BT}\right). \quad (3)$$

Here c is a large constant, δ'_0 is the log-scaled next dominant loss rate and P_γ is the TLS switching rate ratio, defined by $P_\gamma = 1/\ln(\gamma_{\rm max}/\gamma_{\rm min})$ where $\gamma_{\rm max}$ and $\gamma_{\rm min}$ are the maximum and minimum rate of TLS switching, respectively. These rates have been measured in the TLS-related charge-noise spectrum of single-electron transistors. They were found to extend from $\gamma_{\rm min} \simeq 100$ Hz to $\gamma_{\rm max} \simeq 25$ kHz [42], corresponding to $P_\gamma = 0.18$. Our fitted values of P_γ are summarized in Table I: we find values between 0.153 and 0.218, in good agreement with this estimate and other results [40,43,44]. Table I also details the next dominant (i.e., non-TLS) loss term, δ'_0; this number represents an upper bound (of the loss, or equivalently, lower bound of the Q'_0) due to the onset of bifurcation. Examination of any temperature dependence of δ'_0 could be used to pin down whether the residual loss arises due to quasiparticles or other mechanisms.

We have demonstrated that dissipation in our nanowires is not an intrinsic property of disorder within the film [24,25] but is instead caused by TLS. This is not surprising as TLS are the predominant source of dissipation

TABLE I. Nanowire superinductance resonator parameters. $F\delta^i_{\mathrm{TLS}}$ is obtained from fits to Eq. (2), P_γ and δ'_0 from fits to Eq. (3).

NW $f_r(Mhz)$	$F\delta^i_{\mathrm{TLS}}$ ($\times 10^{-5}$)	P_γ	δ'_0
4420	4.37	0.195	≤ 28.3
4562	3.84	0.183	≤ 47.5
4685	3.53	0.218	≤ 41.8
4837	4.40	0.153	≤ 48.4
5285	4.12	0.213	≤ 28.1

and decoherence in a wide variety of quantum devices. An important consideration is the role of the TLS participation ratio. The ratio of E field threading TLS to the total E field is known to scale as approximately $1/\bar{w}$ [17], where $\bar{w}$ is the center conductor width of a resonator. Consequently, the 40-nm width used here to produce a superinductor leads to an unfavorable participation ratio and therefore a much lower Q_i than is found for wider, micrometer-sized resonator geometries. Additionally, the nanowire lithography relies on the use of a spin-on glass resist (HSQ), which resembles amorphous silicon oxide. Silicon oxide is a well-known host of TLS [45] and because some HSQ remains unetched atop our nanowires, we suspect that this is the dominant source of TLS in our devices. Therefore, improvements to the fabrication, specifically the nontrivial removal of the HSQ mask should result in significant improvements in device performance.

IV. CONCLUSION

In conclusion, we demonstrate a nanowire superinductance with a characteristic impedance of 6.795 kΩ and a quality factor at single-photon excitation of $Q_i = 2.5 \times 10^4$. This quality factor is comparable to both JJA-based superinductors [6] and the temperature-scaled TLS loss [$\tanh(hf_r/2k_BT)$] in similar nanowire resonators [13]. We have analyzed the loss mechanisms in our devices and find TLS to be the dominant cause of loss, which is in contrast to the high rates of dissipation found in other nanowire [4,21] or strongly disordered thin film devices [24]. We emphasize that demonstrating that nanowires losses are "conventional" is a important step forward for all nanowire-based quantum circuits. Therefore, this enables long-lived nanowire-based superconducting circuits, such as a nanowire fluxonium qubits [10], improved phase-slip qubits [4,21], or other circuits benefiting from high-inductance, high-impedance devices.

ACKNOWLEDGMENTS

The authors thank O.W. Kennedy for He FIB imaging of our devices. We acknowledge useful discussions with S.E. Kubatkin, A.V. Danilov, and P. Delsing as well as support from the Chalmers Nanofabrication Laboratory staff. This research has been supported by funding from the Swedish Research Council and Chalmers Area of Advance Nanotechnology.

APPENDIX A: SAMPLE FABRICATION

Samples are fabricated on high-resistivity ($\rho \geq 10$ kΩ cm) (100) intrinsic silicon substrates. Before processing, the substrate is dipped for 30 s in hydrofluoric acid (HF) to remove any surface oxide. Within 5 min, the wafer is loaded into a UHV sputtering chamber where a 20-nm-thick NbN thin film is deposited by reactive dc magnetron sputtering from a 99.99% pure Nb target in a 6:1 Ar:N_2 atmosphere. A 500-nm-thick layer of PMMA A6 resist is spin coated and then exposed with electron-beam lithography (EBL) to define the microwave circuitry. After development, the pattern is transferred to the film by reactive ion etching (RIE) in a 50:4 Ar:Cl_2 plasma at 50 W and 10 mTorr. The nanowires are patterned in a subsequent EBL exposure using a 50-nm layer of hydrogen silsesquioxane (HSQ), an ultra-high-resolution negative resist suitable for ≤ 10 nm features [46].

A common problem with HSQ is the formation of small agglomerates that are not completely dissolved during development. These small particles tend to accumulate on the edges of developed structures and act as micromasks when the pattern is etched. From FIB micrographs of our devices (see Fig. 5), we estimate a lithographic defect rate of less than three defects per 10 μm and that each defect contributes to the geometry of the device as approximately one square. For a 680-μm long and 40-nm nanowire, this translates to a maximum uncertainty in the total number of squares of $n_\square = 17\,000 \pm 200$ squares, which is consistent with the 1% error reported in the main text.

APPENDIX B: TRANSPORT CHARACTERIZATION

As described in the main text, we estimate the kinetic inductance contribution $L_k^\square(0)$ in our devices using [28]

$$L_k^\square(0) = \frac{\hbar R_N^\square}{\pi \Delta_0}. \tag{B1}$$

For that purpose, we measure the $R(T)$ characteristic of our nanowires as shown in Fig. 6. We observe that from room temperature, as the temperature decreases, the resistance increases until a plateau is reached at about 15 K. This behavior is typical of weak localization in strongly disordered materials [47]. As the temperature further decreases from 15 K, the resistance starts to decrease and we observe a 2-K-wide superconducting transition.

The width of this superconducting transition can be fully described by two different mechanisms. Above T_c, thermodynamic fluctuations give rise to short-lived Cooper pairs,

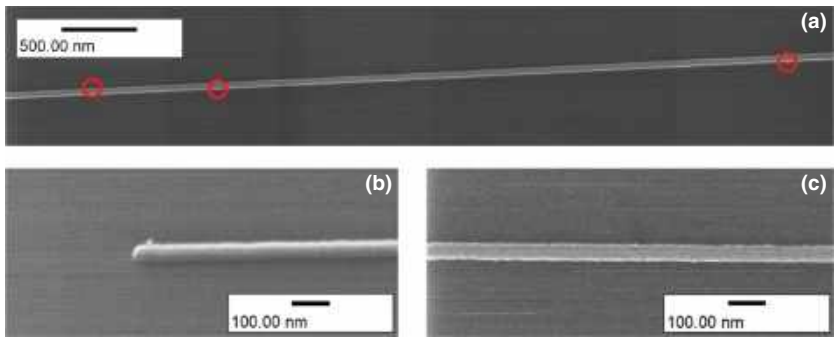

FIG. 5. Helium FIB micrographs of a nanowire superinductor, courtesy of O.W. Kennedy, University College London. (a) Low-magnification image of a long section (5.5 μm) of the nanowire. Lithographic defects are circled in red. (b) High-magnification image of the end of the nanowire. Here we can see that the defect is approximately 10-nm wide. (c) High-magnification image of a section of nanowire without defects. Here we see that the edge roughness is approximately ± 1 nm.

which increase the conductivity. These conductivity fluctuations have been described in the 2D case by Aslamasov and Larkin [28] and are given by

$$\sigma_{2D}(T) = \frac{e^2}{16\hbar d}\left(\frac{T_c}{T - T_c}\right), \tag{B2}$$

where T is the temperature, e is the electron charge, and d is the film thickness. The total conductivity above T_c is now expressed as $\sigma(T) = \sigma_n + \sigma_{2D}(T)$.

Below T_c, the resistance does not immediately vanish. This can be explained by a Berezinskii-Kosterlitz-Thouless (BKT) transition [48] where thermal fluctuations excite pairs of vortices. These vortex-antivortex pairs (VAP) are bound states, formed by vortices with supercurrents circulating in opposite directions. Above the ordering temperature T_{BKT}, VAPs start to dissociate and their movement cause the observed finite resistance. This resistivity is described by [48]

$$\rho(T) = a\exp\left(-2\sqrt{b\frac{T_c - T}{T - T_{BKT}}}\right), \tag{B3}$$

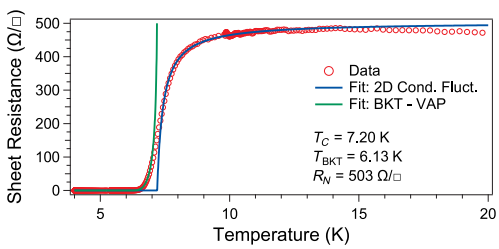

FIG. 6. $R(T)$ characteristic of an NbN nanowire. The blue and green lines are fits to Eqs. (B2) and (B3), respectively.

with $T_{BKT} < T < T_c$, and where a, b are material-dependent parameters.

By fitting the $R(T)$ to Eqs. (B2)–(B3), $R_N^{\square}$ and T_c can be obtained and $L_k^{\square}(0)$ is then calculated using Eq. (1).

APPENDIX C: MEASUREMENT SETUP

The sample is wire bonded in a connectorized copper sample box that is mounted onto the mixing chamber stage of a Bluefors LD250 dilution refrigerator [Fig. 7(a)]. The inbound microwave signal is attenuated at each temperature stage by a total of 60 dB before reaching the device under test. Accounting for cable losses and sample-box insertion loss, the total attenuation of the signal reaching the sample is 70 dB. To avoid any parasitic reflections and noise leakage from amplifiers, the transmitted signal is fed through two microwave circulators (Raditek RADI-4.0-8.0-Cryo-4-77K-1WR) and a 4–8-GHz band-pass filter. Finally, the signal is amplified by a LNF LNC4_8A HEMT cryogenic amplifier (45-dB gain) installed on the 2.8-K stage. Additional amplification is done at room temperature (Pasternack PE-1522 gain-block amplifiers).

This microwave setup is connected to a vector network analyzer (Keysight PNA-X N5249A or R&S ZNB20) for initial characterization and quality-factor measurements of the nanowire resonators at various excitation powers [Fig. 7(a)]. However, as highlighted in the main text, at low drive powers, VNA measurements require significant amounts of averaging to increase the SNR. At low microwave energies, frequency jitter leads to spectral broadening.

To reliably determine the TLS loss contribution, we instead measure the resonant frequency of the resonator against temperature [17,49]. For that purpose, the microwave setup is included in a frequency-locked loop

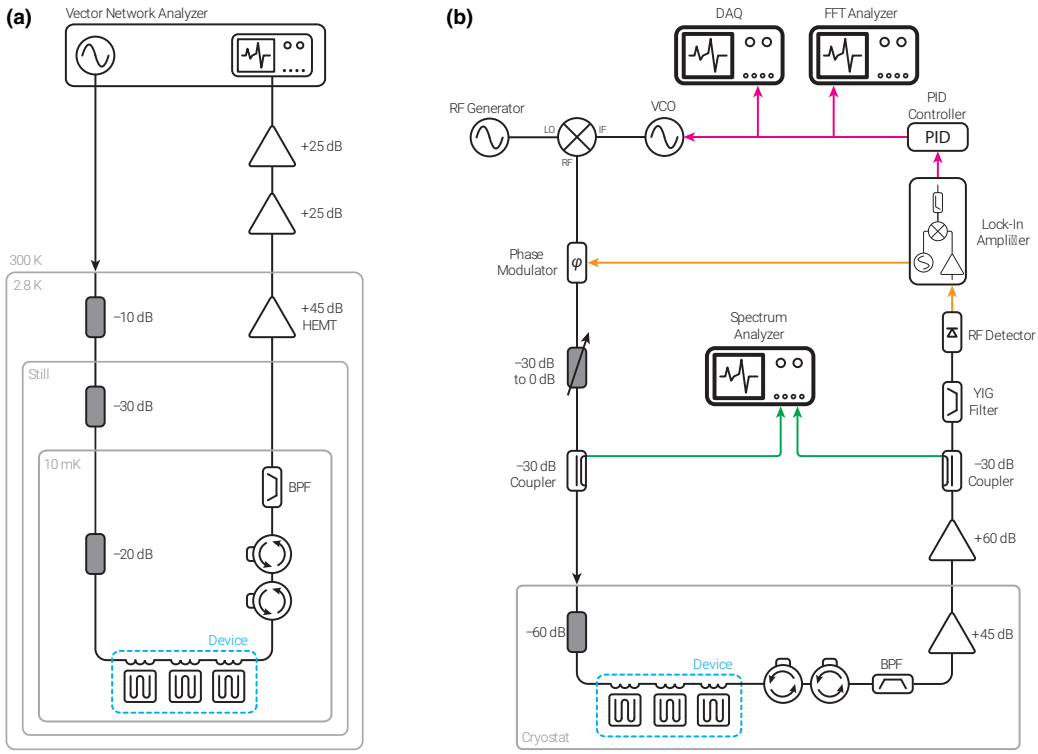

FIG. 7. (a) Cryogenic microwave setup. (b) Schematic of the Pound frequency-locked loop (PFLL).

using the so-called Pound locking technique [Fig. 7(b)]. Originally developed for microwave oscillators [50], this technique is commonly used in optics for frequency stabilization of lasers [51] and has been recently used for noise [49,52] and ESR [40,53] measurements with superconducting microwave resonators. In this method, a carrier signal is generated by mixing the output of a microwave source (Keysight E8257D) and a VCO (Keysight 33622A) operating at 50 MHz. This carrier is phase-modulated (Analog Devices HMC538) before being passed through the resonator under test. The phase modulation frequency is set so that the sidebands are not interacting with the resonator and therefore only the central tone undergoes a phase shift while the sidebands pass unaltered. After amplification, the signal is filtered (MicroLambda MLBFP-64008) to remove the unwanted mixer image and rectified using an rf detector diode (Pasternack PE8016). The diode output is demodulated with a lock-in amplifier (Zurich Instruments HF2LI). The principle of operation is close to that of the PLL; however, the phase modulation allows for a common-mode rejection of any phase fluctuations. An additional benefit is that the readout is done at a higher frequency (2 MHz vs dc), which reduces any parasitic electronic noise.

The feedback loop consist of an analog PID controller (SRS SIM960) locked on the zero crossing of the error signal. This gives an output directly proportional to any shift in resonant frequency of the resonator. This output signal is then used to drive the frequency modulation of the VCO, varying its frequency accordingly and enabling the loop to be locked on the resonator.

In this work, we only sample the PID output slowly ($\leq$ 100 Hz) to track frequency changes (Keithley 2000), but noise in the resonator can also be studied using a frequency counter (Keysight 53132A), a fast-sampling DAQ (NI PXI-6259 DAQ) or an FFT analyzer (Keysight 35670A). This will be the focus of future work.

APPENDIX D: PRACTICAL CONSIDERATIONS FOR NANOWIRE SUPERINDUCTORS

As described in the main text, a superinductor is a low-loss circuit element with characteristic impedance Z_c larger than the superconducting resistance quantum R_Q. This is a

natural definition as charge and flux are electromagnetic dual quantities, whose competing quantum fluctuations become equal in strength at $Z = R_Q$, at which point the magnitudes of the respective zero-point quantum fluctuations (rms) are half a Cooper pair and half a flux quantum, respectively [54].

These prerequisites pose several constraints on the successful design of a superinductor: in the context of disordered superconductors, this implies that the thin film should have a high kinetic inductance while the fabricated structure should have a capacitance as low as possible. In this appendix, we detail the implications of these constraints on several aspects of the design of a nanowire superinductor.

1. Materials

In the main text and in Appendix B, we highlight that the kinetic inductance contribution for a disordered superconductor is derived using the Mattis-Bardeen framework (Eq. 1). This formula reveals that in order to achieve a highly inductive film, we need a superconductor that exhibits a high normal-state resistance R_N and a small superconducting gap (i.e., a small critical temperature T_c).

However, there are several caveats in this simple interpretation. First of all, while a small gap is favorable for a high inductance, a working temperature too close to T_c leads to the presence of quasiparticles. In turn, these quasiparticles lead to significant losses and breach the low-loss criterion for a superinductor. This therefore imposes a practical limit on the critical temperature of the superconductor to realize such a device: for a practically obtainable temperature of 10 mK, the minimum practical critical temperature is around 1 K.

Additionally, while it is tempting to arbitrarily increase R_N (i.e., the level of disorder) to achieve a high kinetic inductance, films exhibit disorder-related losses as they get close to the superconductor-insulator transition [20–24]. A recent theory attributes these losses to the presence of low-lying subgap states in the proximity of the superconducting-insulating transition [25]. Experimentally, disorder-induced subgap states [2] and spatial inhomogeneity of the gap [3] were demonstrated for NbN thicknesses below about 6 nm. Consequently, we need to fabricate a sufficiently disordered (thin) superconductor to obtain high inductance, but not so disordered as to induce dissipation.

In this work, our choice of superconductor is niobium nitride. NbN has a high bulk critical temperature (16 K), however, the critical temperature is suppressed as the thickness of the film is reduced [55], which leads to a favorable scaling of the superconducting gap in Eq. (1). After a careful optimization of the NbN thin-film fabrication, a target thickness of 20 nm, corresponding to a critical temperature $T_c = 7.20$ K, and a normal-state resistance

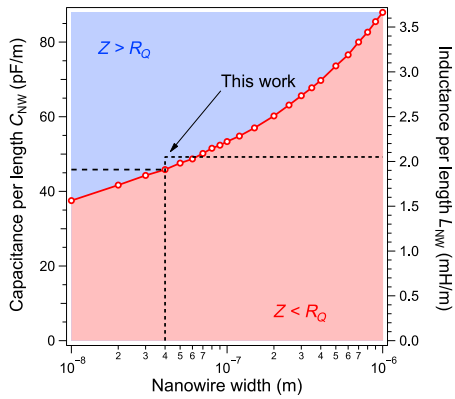

FIG. 8. Simulated capacitance per unit length, $C_{NW}(\bar{w})$ (red circles), for nanowire widths $\bar{w}$ ranging from 1 μm down to 10 nm. The right axis corresponds to the minimum inductance per unit length, $L_{NW}(\bar{w})$, required to obtain a characteristic impedance $Z_c = [L_{NW}(\bar{w})/C_{NW}(\bar{w})]^{1/2} > R_Q$. The superinductance regime – the area highlighted in blue – should be understood as the range in which $L_{NW}(\bar{w})$ is sufficiently high, for a fixed $\bar{w}$, that it will yield $Z > R_Q$.

$R_N = 503\ \Omega/\square$ represent a good compromise between disorder and kinetic inductance, with a corresponding sheet kinetic inductance $L_k = 82$ pH/$\square$.

2. Geometry

a. Nanowire geometry

In the previous section, we establish that because of losses we cannot arbitrarily increase the inductance to maximize the impedance. Therefore, to realize a superinductor, it becomes crucial to minimize the stray capacitance, which can be achieved with a nanowire geometry. We simulate the capacitance per length for several nanowires with widths varying from 1 μm down to 10 nm. The results are shown in Fig. 8. This figure also shows the corresponding minimum inductance per length required for a superinductance.

b. TLS filling factor (participation ratio)

In the main text, we highlight the role of the TLS filling factor in the losses and mention that reducing the physical dimensions of a resonator leads to an unfavorable scaling. To support this claim, we simulate the TLS filling factor using an electrostatic simulation in COMSOL for nanowires of various width. In our model, we assume a TLS host volume V_{TLS} consisting of a 10-nm-thick layer of silicon oxide and a 30-nm-thick layer of HSQ (modeled as silicon oxide). The filling factor is obtained by calculating the ratio of the electric energy stored in the TLS host volume

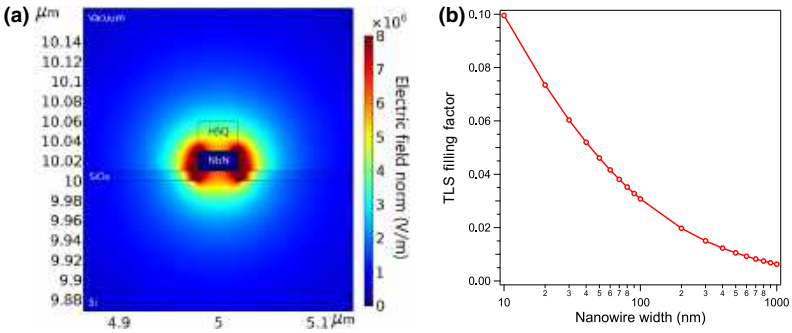

FIG. 9. (a) Magnitude of the electric field for a 40-nm-wide nanowire. (b) TLS filling factor for nanowire widths ranging from 1 μm down to 10 nm.

to the total electric energy [56]:

$$F = \frac{\int_{V_{\mathrm{TLS}}} \varepsilon_{\mathrm{TLS}} \vec{E}^2 d\vec{r}}{\int_V \varepsilon \vec{E}^2 d\vec{r}}. \tag{D1}$$

The results of the simulation are shown in Fig. 9. We note the significant increase of the filling factor as the width is reduced.

c. Parasitic capacitance of meanders

In this section, we analyze the geometry-dependent parasitic capacitance due to meandering of the nanowire. For that purpose, we simulate the frequency response and current density using Sonnet *em* microwave simulator. In order to reduce meshing and simulation times, we simulate 100-nm-wide wires in a simple step-impedance resonator geometry. We start by simulating a straight wire as a reference and then proceed to a meandered geometry with a fixed meander length $b = 20\,\mu$m while gradually decreasing the distance between meanders from $a = 30\,\mu$m (typical distance in our devices) to 100 nm (see Fig. 10).

Figures 10 and 11 show the normalized current density along the nanowires at the fundamental resonant frequency of the simulated structure. To be clear, for meandered geometries, the current density is not measured as a line cut along the x axis, but instead the geometry is unwound and the current density is extracted at every point along the nanowire. We observe that for the straight wire and for meanders with $a > 5\,\mu$m, the current density is consistent with the expected $\lambda/2$ mode structure of such a resonator and the characteristic impedance is well defined to $Z_c = \sqrt{L_{\mathrm{NW}}/C_{\mathrm{NW}}}$ as described in the main text.

However, below $a = 5\,\mu$m, we observe that, as the distance between the meanders is reduced, the resonant frequency significantly diverges from the straight nanowire reference value and the current density is severely distorted [57]. This is explained by the increasing influence of parasitic capacitance between each meander. This parasitic capacitance is equivalent to shunting the nanowire with an extra capacitance and lowering its characteristic

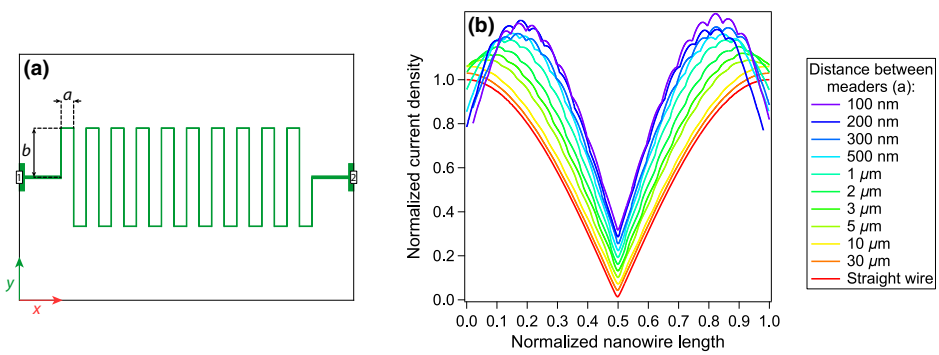

FIG. 10. (a) Schematic representation of a typical meandered nanowire resonator structure simulated in this section. a and b are the distance between meanders and the meander length, respectively. 1 and 2 are the excitation and measurement ports and the black outline represents the grounded edge of the simulation box. (b) Normalized current densities at the fundamental resonance frequencies for all the simulated structures. For clarity, the curves have been offset by 0.03.

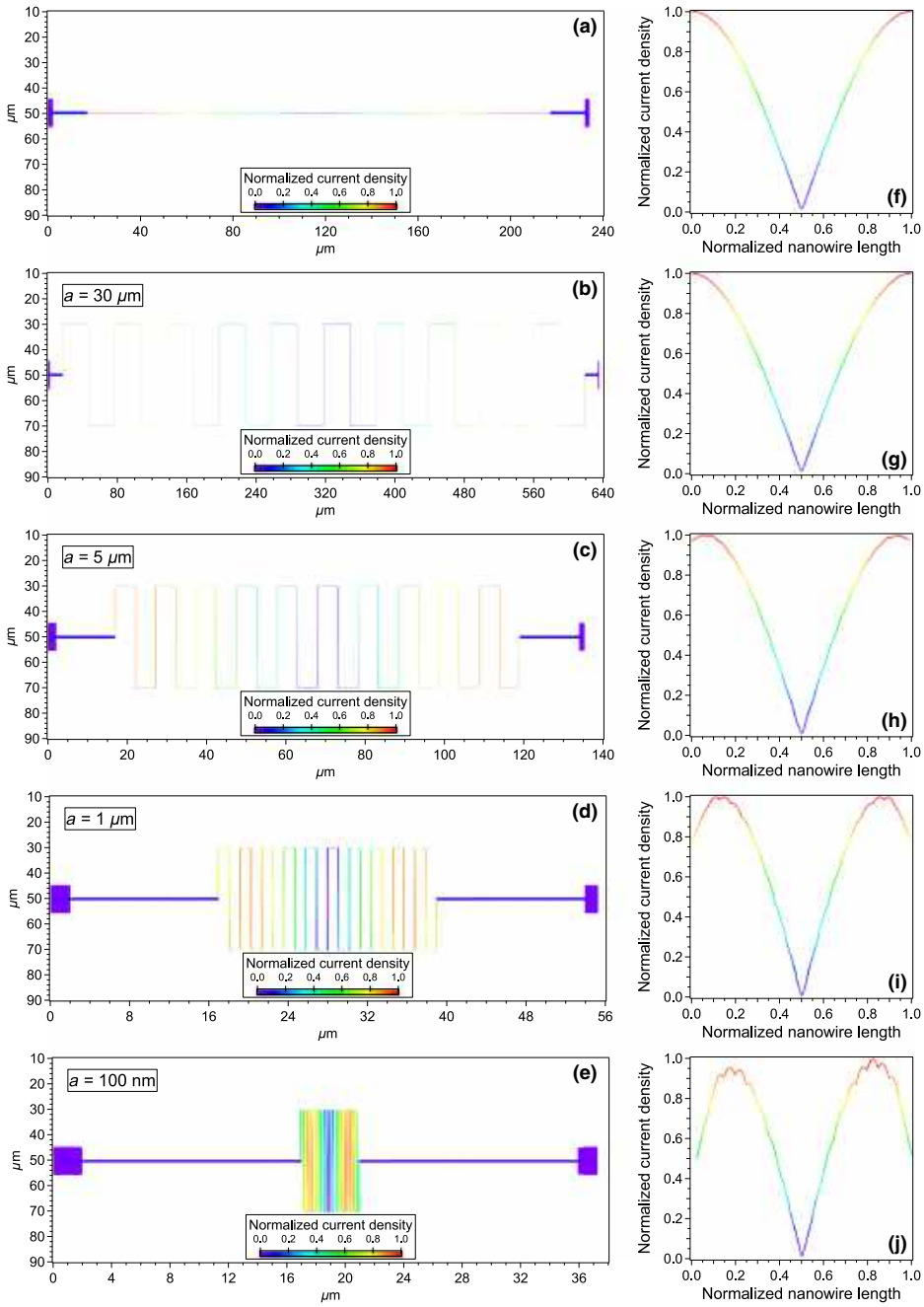

FIG. 11. (a)–(e) Current density distribution in nanowires at several inter-meander distances. (f-j) Corresponding normalized current density along the nanowire.

TABLE II. Nanowire superinductance film and device parameters.

Parameter	Symbol	Value
Normal-state sheet resistance	$R_N^{\square}$	503 Ω□
Sheet kinetic inductance	$L_k^{\square}$	82 $pH/\square$
Nanowire length	l	680 μm
Nanowire width	$\bar{w}$	40 nm

impedance. Moreover, the structure then cannot be treated as a $\lambda/2$ resonator anymore and therefore has no well-defined wave impedance.

d. Exponentially suppressed phase-slip rate

In the main text, we make the argument that the device dimensions are chosen to exponentially suppress phase slips. We estimate the phase-slip rate $\Gamma_S = E_S/h = E_0/h\exp(-\kappa\bar{w})$ for our device within the phenomenological model for strongly disordered superconductors. Our analysis is similar to that of Peltonen *et al.* [21]. In this model, E_S is the phase-slip energy and we have $E_0 = \rho\sqrt{l/\bar{w}}$, where l and $\bar{w}$ are the nanowire length and average width, respectively, $\rho = (\hbar/2e)^2/L_k^{\square}$ represents the superfluid stiffness, $\kappa = \eta\sqrt{\nu_p\rho}$, $\eta \simeq 1$, and $\nu_p = 1/(2e^2R_N^{\square}D)$ is the Cooper-pair density of states with $D \simeq 0.45\,\mathrm{cm}^2\,\mathrm{s}$. For our device parameters (summarized in Table II), we find $\Gamma_S \simeq 7\times10^{-5}$ Hz. This corresponds to an average of one phase-slip event every 4 h, which is entirely negligible.

APPENDIX E: CONVENTIONAL AND INTERACTING (LOG) TLS MODELS

Traditionally, the loss of superconducting microwave devices is parameterized by a model, which splits the loss into a power-dependent term, associated with TLS, and a power-independent term (δ_0), associated with resistive losses (quasiparticles) or parasitic microwave modes. An example of this model is described by [26]

$$\frac{1}{Q_i} = \delta_{\mathrm{tot}}^i = F\delta_{\mathrm{TLS}}^0\frac{\tanh\left(hf_r/2k_BT\right)}{\left(1+\langle n\rangle/n_c\right)^{\beta}} + \delta_0. \qquad \text{(E1)}$$

Here, the first term contains the power dependence and relates to the TLS. Specifically, the imaginary part of the TLS susceptibility is accounted for here and resembles a Lorentzian function [33] so that the loss arises from TLS that are spectrally close to the resonator. In this model, n_c is the number of photons equivalent to the saturation field of one TLS, F is the filling factor, which is the ratio of electric field threading the TLS to the total electric field. Collectively, $F\delta_{\mathrm{TLS}}^0$ gives the TLS loss, where, assuming TLS of predominantly similar dipole moments, δ_{TLS}^0 describes a density of TLS.

Recent results have demonstrated that TLS are not spectrally stable [32,41,58,59], which results in a time-varying number of near-resonant TLS that is revealed as a time-varying quality factor [37]. In the context of the TLS loss model, this spectral instability of the TLS means that the TLS spends less time resonant with the resonator. Consequently, the TLS is not always present as a loss channel to the resonator, which motivates a weaker power dependence of the TLS loss term. In the above, β describes the strength of TLS saturation with power and the original TLS model predicts $\beta = 0.5$ [43]. However, due to the spectral instability of TLS, recent results [26,32,40,44] commonly find a weaker scaling. Therefore, we allow β to be a fit parameter initialized to $\beta = 0.5$ and we find that $\beta \simeq 0.2$ best describes our data (see Table III). Rather than allowing β to be a fit parameter, Faoro and Ioffe [41] showed that the spectral instability of TLS results in the microwave-power dependence of the dielectric loss becoming logarithmic. This is the model we use in the main text to fit our data, and it is given by

$$\frac{1}{Q_i} = F\delta_{\mathrm{TLS}}^i P_\gamma \ln\left(\frac{cn_c}{\langle n\rangle} + \delta_0'\right)\tanh\left(\frac{hf_r}{2k_BT}\right). \qquad \text{(E2)}$$

Here, F is once again the filling factor and δ_{TLS}^i is the intrinsic TLS loss tangent. Additionally, P_γ is the TLS switching rate ratio, defined by $P_\gamma = 1/\ln(\gamma_{\max}/\gamma_{\min})$ where $\gamma_{\max}$ and $\gamma_{\min}$ are the maximum and minimum rate of TLS switching, respectively, c is a large constant, n_c is the number of photons generating the electric field saturating a TLS, and δ_0' is the log-scaled next dominant loss rate. The temperature-dependent hyperbolic tangent scaling highlights the thermal saturation of TLS. As shown in the main text, this model describes our data well and the obtained fitted values are in good agreement with other results [40,43,44].

The intrinsic loss tangent δ_{TLS}^i used above is obtained, by means of the Kramers-Kronig relation via the real component of the TLS susceptibility, by measuring the $f_r(T)$ using the PFLL. Measuring the real component is preferable for a variety of reasons: fundamentally, it scales more slowly vs frequency [33], making it more robust to the spectral instability of TLS. Another factor is simply that measuring frequency is significantly more accurate than measuring quality factors. Additionally, we note that $F\delta_{\mathrm{TLS}}^0$

TABLE III. Nanowire superinductance resonator parameters of five devices. $F\delta_{\mathrm{TLS}}^0$ and β are obtained from fits to Eq. (E1), $F\delta_{\mathrm{TLS}}^i$ from fits to Eq. (2) of the main text, and finally P_γ from fits to Eq. (3).

NW f_r (MHz)	β	$F\delta_{\mathrm{TLS}}^0$ ($\times10^{-5}$)	$F\delta_{\mathrm{TLS}}^i$ ($\times10^{-5}$)	P_γ
4420	0.198	8.81	4.37	0.195
4562	0.196	7.51	3.84	0.183
4685	0.187	10.7	3.53	0.218
4837	0.180	8.24	4.40	0.153
5285	0.184	10.8	4.12	0.213

and $F\delta^{i}_{\mathrm{TLS}}$ differ by a factor 2 to 3, which is significantly larger than the approximately 15% difference typically observed [26]. However, this is not unexpected, as the low value of β indicated that we are outside of the range of validity of Eq. (E1) [26,40].

[1] E. F. C. Driessen, P. C. J. J. Coumou, R. R. Tromp, P. J. de Visser, and T. M. Klapwijk, Strongly Disordered TiN and NbTiN *s*-Wave Superconductors Probed by Microwave Electrodynamics, Phys. Rev. Lett. **109**, 107003 (2012).

[2] Mintu Mondal, Anand Kamlapure, Madhavi Chand, Garima Saraswat, Sanjeev Kumar, John Jesudasan, L. Benfatto, Vikram Tripathi, and Pratap Raychaudhuri, Phase Fluctuations in a Strongly Disordered *s*-Wave NbN Superconductor Close to the Metal-Insulator Transition, Phys. Rev. Lett. **106**, 047001 (2011).

[3] Y. Noat, V. Cherkez, C. Brun, T. Cren, C. Carbillet, F. Debontridder, K. Ilin, M. Siegel, A. Semenov, H.-W. Huübers, and D. Roditchev, Unconventional superconductivity in ultrathin superconducting NbN films studied by scanning tunneling spectroscopy, Phys. Rev. B **88**, 014503 (2013).

[4] O. V. Astafiev, L. B. Ioffe, S. Kafanov, Yu A. Pashkin, K. Yu Arutyunov, D. Shahar, O. Cohen, and J. S. Tsai, Coherent quantum phase slip, Nature **484**, 355 (2012).

[5] D. B. Haviland, Y. Liu, and A. M. Goldman, Onset of Superconductivity in the Two-Dimensional Limit, Phys. Rev. Lett. **62**, 2180 (1989).

[6] Nicholas A. Masluk, Ioan M. Pop, Archana Kamal, Zlatko K. Minev, and Michel H. Devoret, Microwave Characterization of Josephson Junction Arrays: Implementing a Low Loss Superinductance, Phys. Rev. Lett. **109**, 137002 (2012).

[7] M. T. Bell, I. A. Sadovskyy, L. B. Ioffe, A. Yu Kitaev, and M. E. Gershenson, Quantum Superinductor with Tunable Nonlinearity, Phys. Rev. Lett. **109**, 137003 (2012).

[8] Vladimir E. Manucharyan, Jens Koch, Leonid I. Glazman, and Michel H. Devoret, Fluxonium: Single Cooper-pair circuit free of charge offsets, Science **326**, 113 (2009).

[9] Ioan M. Pop, Kurtis Geerlings, Gianluigi Catelani, Robert J. Schoelkopf, Leonid I. Glazman, and Michel H. Devoret, Coherent suppression of electromagnetic dissipation due to superconducting quasiparticles, Nature **508**, 369 (2014).

[10] Andrew J. Kerman, Metastable Superconducting Qubit, Phys. Rev. Lett. **104**, 027002 (2010).

[11] F. Luthi, T. Stavenga, O. W. Enzing, A. Bruno, C. Dickel, N. K. Langford, M. A. Rol, T. S. Jespersen, J. Nygård, P. Krogstrup, and L. DiCarlo, Evolution of Nanowire Transmon Qubits and their Coherence in a Magnetic Field, Phys. Rev. Lett. **120**, 100502 (2018).

[12] N. Samkharadze, G. Zheng, N. Kalhor, D. Brousse, A. Sammak, U. C. Mendes, A. Blais, G. Scappucci, and L. M. K. Vandersypen, Strong spin-photon coupling in silicon, Science **359**, 1123 (2018).

[13] N. Samkharadze, A. Bruno, P. Scarlino, G. Zheng, D. P. DiVincenzo, L. DiCarlo, and L. M. K. Vandersypen, High-Kinetic-Inductance Superconducting Nanowire Resonators for Circuit QED in a Magnetic Field, Phys. Rev. Appl. **5**, 044004 (2016).

[14] A. Stockklauser, P. Scarlino, J. V. Koski, S. Gasparinetti, C. K. Andersen, C. Reichl, W. Wegscheider, T. Ihn, K. Ensslin, and A. Wallraff, Strong Coupling Cavity QED with Gate-Defined Double Quantum Dots Enabled by a High Impedance Resonator, Phys. Rev. X **7**, 011030 (2017).

[15] A. J. Landig, J. V. Koski, P. Scarlino, U. C. Mendes, A. Blais, C. Reichl, W. Wegscheider, A. Wallraff, K. Ensslin, and T. Ihn, Coherent spin-photon coupling using a resonant exchange qubit, Nature **560**, 179 (2018).

[16] J. J. Viennot, M. C. Dartiailh, A. Cottet, and T. Kontos, Coherent coupling of a single spin to microwave cavity photons, Science **349**, 408 (2015).

[17] Jiansong Gao, Miguel Daal, Anastasios Vayonakis, Shwetank Kumar, Jonas Zmuidzinas, Bernard Sadoulet, Benjamin A. Mazin, Peter K. Day, and Henry G. Leduc, Experimental evidence for a surface distribution of two-level systems in superconducting lithographed microwave resonators, Appl. Phys. Lett. **92**, 152505 (2008).

[18] W. Guichard and F. W. J. Hekking, Phase-charge duality in Josephson junction circuits: Role of inertia and effect of microwave irradiation, Phys. Rev. B **81**, 064508 (2010).

[19] Peter Brooks, Alexei Kitaev, and John Preskill, Protected gates for superconducting qubits, Phys. Rev. A **87**, 052306 (2013).

[20] Andrey Belkin, Matthew Brenner, Thomas Aref, Jaseung Ku, and Alexey Bezryadin, Little–Parks oscillations at low temperatures: Gigahertz resonator method, Appl. Phys. Lett. **98**, 242504 (2011).

[21] J. T. Peltonen, O. V. Astafiev, Yu P. Korneeva, B. M. Voronov, A. A. Korneev, I. M. Charaev, A. V. Semenov, G. N. Golt'sman, L. B. Ioffe, T. M. Klapwijk, and J. S. Tsai, Coherent flux tunneling through NbN nanowires, Phys. Rev. B **88**, 220506 (2013).

[22] J. T. Peltonen, Z. H. Peng, Yu P. Korneeva, B. M. Voronov, A. A. Korneev, A. V. Semenov, G. N. Gol'tsman, J. S. Tsai, and O. V. Astafiev, Coherent dynamics and decoherence in a superconducting weak link, Phys. Rev. B **94**, 180508 (2016).

[23] J. T. Peltonen, P. C. J. J. Coumou, Z. H. Peng, T. M. Klapwijk, J. S. Tsai, and O. V. Astafiev, Hybrid rf squid qubit based on high kinetic inductance, Sci. Rep. **8**, 10033 (2018).

[24] P. C. J. J. Coumou, M. R. Zuiddam, E. F. C. Driessen, P. J. de Visser, J. J. A. Baselmans, and T. M. Klapwijk, Microwave properties of superconducting atomic-layer deposited tin films, IEEE T. Appl. Supercon. **23**, 7500404 (2013).

[25] M. V. Feigel'man and L. B. Ioffe, Microwave Properties of Superconductors Close to the Superconductor-Insulator Transition, Phys. Rev. Lett. **120**, 037004 (2018).

[26] J. Burnett, J. Sagar, O. W. Kennedy, P. A. Warburton, and J. C. Fenton, Low-Loss Superconducting Nanowire Circuits using a Neon Focused Ion Beam, Phys. Rev. Appl. **8**, 014039 (2017).

[27] S. Probst, F. B. Song, P. A. Bushev, A. V. Ustinov, and M. Weides, Efficient and robust analysis of complex scattering data under noise in microwave resonators, Rev. Sci.Instrum. **86**, 024706 (2015).

[28] M. Tinkham, *Introduction to Superconductivity* (Dover Books, Mineola, NY, 2004).

[29] S. S. Mohan, M. del Mar Hershenson, S. P. Boyd, and T. H. Lee, Simple accurate expressions for planar spiral inductances, IEEE J. Solid-St. Circ. **34**, 1419 (1999).
[30] L. J. Swenson, P. K. Day, B. H. Eom, H. G. Leduc, N. Llombart, C. M. McKenney, O. Noroozian, and J. Zmuidzinas, Operation of a titanium nitride superconducting microresonator detector in the nonlinear regime, J. Appl. Phys. **113**, 104501 (2013).
[31] K. D. Osborn, J. A. Strong, A. J. Sirois, and R. W. Simmonds, Frequency-tunable Josephson junction resonator for quantum computing, IEEE T. Appl. Supercond. **17**, 166 (2007).
[32] J. Burnett, L. Faoro, I. Wisby, V. L. Gurtovoi, A. V. Chernykh, G. M. Mikhailov, V. A. Tulin, R. Shaikhaidarov, V. Antonov, P. J. Meeson, A. Ya Tzalenchuk, and T. Lindström, Evidence for interacting two-level systems from the 1/f noise of a superconducting resonator, Nat. Commun. **5**, 4119 (2014).
[33] D. P. Pappas, M. R. Vissers, D. S. Wisbey, J. S. Kline, and J. Gao, Two level system loss in superconducting microwave resonators, IEEE T. Appl. Supercond. **21**, 871 (2011).
[34] Christian Enss and Siegfried Hunklinger, *Low-Temperature Physics* (Springer-Verlag, Berlin, Heidelberg, 2005).
[35] P. Macha, S. H. W. van der Ploeg, G. Oelsner, E. Ilichev, H.-G. Meyer, S. Wünsch, and M. Siegel, Losses in coplanar waveguide resonators at millikelvin temperatures, Appl. Phys. Lett. **96**, 062503 (2010).
[36] G. Calusine, A. Melville, W. Woods, R. Das, C. Stull, V. Bolkhovsky, D. Braje, D. Hover, D. K. Kim, X. Miloshi, D. Rosenberg, A. Sevi, J. L. Yoder, E. Dauler, and W. D. Oliver, Analysis and mitigation of interface losses in trenched superconducting coplanar waveguide resonators, Appl. Phys. Lett. **112**, 062601 (2018).
[37] C. T. Earnest, J. H. Beéjanin, T. G. McConkey, E. A. Peters, A. Korinek, H. Yuan, and M. Mariantoni, Substrate surface engineering for high-quality silicon/aluminum superconducting resonators, Supercond. Sci. Technol. **31**, 125013 (2018).
[38] Jürgen Lisenfeld, Grigorij J. Grabovskij, Clemens Müller, Jared H. Cole, Georg Weiss, and Alexey V. Ustinov, Observation of directly interacting coherent two-level systems in an amorphous material, Nat. Commun. **6**, 6182 (2015).
[39] Lara Faoro and Lev B. Ioffe, Internal Loss of Superconducting Resonators Induced by Interacting Two-Level Systems, Phys. Rev. Lett. **109**, 157005 (2012).
[40] S. E. de Graaf, L. Faoro, J. Burnett, A. A. Adamyan, A. Ya Tzalenchuk, S. E. Kubatkin, T. Lindstrooöm, and A. V. Danilov, Suppression of low-frequency charge noise in superconducting resonators by surface spin desorption, Nat. Commun. **9**, 1143 (2018).
[41] Lara Faoro and Lev B. Ioffe, Interacting tunneling model for two-level systems in amorphous materials and its predictions for their dephasing and noise in superconducting microresonators, Phys. Rev. B **91**, 014201 (2015).
[42] S. Kafanov, H. Brenning, T. Duty, and P. Delsing, Charge noise in single-electron transistors and charge qubits may be caused by metallic grains, Phys. Rev. B **78**, 125411 (2008).
[43] J. Burnett, L. Faoro, and T. Lindström, Analysis of high quality superconducting resonators: Consequences for TLS properties in amorphous oxides, Supercond. Sci. Tech. **29**, 044008 (2016).
[44] Naftali Kirsh, Elisha Svetitsky, Alexander L. Burin, Moshe Schechter, and Nadav Katz, Revealing the nonlinear response of a tunneling two-level system ensemble using coupled modes, Phys. Rev. Mat. **1**, 012601 (2017).
[45] R. Barends, H. L. Hortensius, T. Zijlstra, J. J. A. Baselmans, S. J. C. Yates, J. R. Gao, and T. M. Klapwijk, Contribution of dielectrics to frequency and noise of NbTiN superconducting resonators, Appl. Phys. Lett. **92**, 223502 (2008).
[46] Y. Chen, H. Yang, and Z. Cui, Effects of developing conditions on the contrast and sensitivity of hydrogen silsesquioxane, Microelect. Eng. **83**, 1119 (2006).
[47] Gerd Bergmann, Physical interpretation of weak localization: A time-of-flight experiment with conduction electrons, Phys. Rev. B **28**, 2914 (1983).
[48] J. E. Mooij, *Percolation, Localization and Superconductivity* (Plenum Press, New York, NY, 1984).
[49] T. Lindström, J. E. Healey, M. S. Colclough, C. M. Muirhead, and A. Ya Tzalenchuk, Properties of superconducting planar resonators at millikelvin temperatures, Phys. Rev. B **80**, 132501 (2009).
[50] R. V. Pound, Electronic frequency stabilization of microwave oscillators, Rev. Sci. Instrum. **17**, 490 (1946).
[51] Eric D. Black, An introduction to Pound–Drever–Hall laser frequency stabilization, Am. J. Phys. **69**, 79 (2001).
[52] T. Lindström, J. Burnett, M. Oxborrow, and A. Ya Tzalenchuk, Pound-locking for characterization of superconducting microresonators, Rev. Sci. Instrum. **82**, 104706 (2011).
[53] S. E. de Graaf, A. V. Danilov, A. Adamyan, T. Bauch, and S. E. Kubatkin, Magnetic field resilient superconducting fractal resonators for coupling to free spins, J. Appl. Phys. **112**, 123905 (2012).
[54] M. H. Devoret, Steven Girvin, and Robert Schoelkopf, Circuit-QED: How strong can the coupling between a Josephson junction atom and a transmission line resonator be? Ann. Phys. **16**, 767 (2007).
[55] Yachin Ivry, Chung-Soo Kim, Andrew E. Dane, Domenico De Fazio, Adam N. McCaughan, Kristen A. Sunter, Qingyuan Zhao, and Karl K. Berggren, Universal scaling of the critical temperature for thin films near the superconducting-to-insulating transition, Phys. Rev. B **90**, 214515 (2014).
[56] J. Gao, Ph.D. thesis, School California Institute of Technology, 2008.
[57] Daniel F. Santavicca, Jesse K. Adams, Lierd E. Grant, Adam N. McCaughan, and Karl K. Berggren, Microwave dynamics of high aspect ratio superconducting nanowires studied using self-resonance, J. Appl. Phys. **119**, 234302 (2016).
[58] Clemens Müller, Jürgen Lisenfeld, Alexander Shnirman, and Stefano Poletto, Interacting two-level defects as sources of fluctuating high-frequency noise in superconducting circuits, Phys. Rev. B **92**, 035442 (2015).
[59] P. V. Klimov *et al.*, Fluctuations of Energy-Relaxation Times in Superconducting Qubits, Phys. Rev. Lett. **121**, 090502 (2018).

Paper B

Geometric Scaling of Two-Level-System Loss in Superconducting Resonators

OPEN ACCESS
IOP Publishing
Superconductor Science and Technology
Supercond. Sci. Technol. 33 (2020) 025013 (8pp)
https://doi.org/10.1088/1361-6668/ab6179

Geometric scaling of two-level-system loss in superconducting resonators

David Niepce[1], Jonathan J Burnett[2], Martí Gutierrez Latorre[1] and Jonas Bylander[1]

[1] Chalmers University of Technology, Microtechnology and Nanoscience, SE-41296, Gothenburg, Sweden
[2] National Physical Laboratory, Hampton Road, Teddington, Middlesex, TW11 0LW, United Kingdom

E-mail: david.niepce@chalmers.se

Received 7 August 2019, revised 18 November 2019
Accepted for publication 13 December 2019
Published 8 January 2020

Abstract

We perform an experimental and numerical study of dielectric loss in superconducting microwave resonators at low temperature. Dielectric loss, due to two-level systems, is a limiting factor in several applications, e.g. superconducting qubits, Josephson parametric amplifiers, microwave kinetic-inductance detectors, and superconducting single-photon detectors. Our devices are made of disordered NbN, which, due to magnetic-field penetration, necessitates 3D finite-element simulation of the Maxwell–London equations at microwave frequencies to accurately model the current density and electric field distribution. From the field distribution, we compute the geometric filling factors of the lossy regions in our resonator structures and fit the experimental data to determine the intrinsic loss tangents of its interfaces and dielectrics. We put emphasis on the loss caused by a spin-on-glass resist such as hydrogen silsesquioxane (HSQ), used for ultrahigh lithographic resolution relevant to the fabrication of nanowires. We find that, when used, HSQ is the dominant source of loss, with a loss tangent of $\delta^{i}_{\mathrm{HSQ}} = 8 \times 10^{-3}$.

Keywords: disordered superconductor, two level systems, filling factor, participation ratio, microwave resonators, hydrogen silsesquioxane, 3D FEM simulation

(Some figures may appear in colour only in the online journal)

1. Introduction

Several modern circuits rely on superconducting devices with high microwave characteristic impedance and low dissipation. High impedance is usually implemented using the kinetic inductance of a chain of Josephson junctions [1–3] or with sub-micron-width wires made of a disordered superconductor such as NbN [4], NbTiN [5], or granular Al [6–8]. Despite being less studied, nanowires have some advantages over junction chains—high critical current, magnetic-field tolerance [5], strong coupling to zero-point fluctuations of the electric field [9, 10], less stringent constraints on device geometry, and absence of parasitic modes.

Applications of high-impedance devices include qubit architectures such as the fluxonium [3, 8], which depends on a superinductor (a low-loss inductor with reactive characteristic wave impedance exceeding the resistance quantum, $Z_c > R_Q \sim 6.5\ \mathrm{k\Omega}$ [1, 2, 4]) and travelling-wave microwave parametric amplifiers [11–17], relying on the kinetic inductance nonlinearity. Superconducting disordered nanowires are also interesting for newer types of microwave kinetic-inductance photon detectors [18, 19] and radio-frequency-readout of superconducting single-photon detectors [19, 20].

Dielectric loss and noise associated with two-level systems (TLS) residing in surfaces and interfaces are longstanding problems in superconducting circuits [21]. Specifically, TLS limit the quantum coherence times and lead to parameter fluctuations of superconducting qubits [22–25]. The participation ratios of the losses of the constituent dielectrics can be estimated through electro-magnetic simulation. Traditionally, the air-facing surfaces are found to be relatively insignificant,

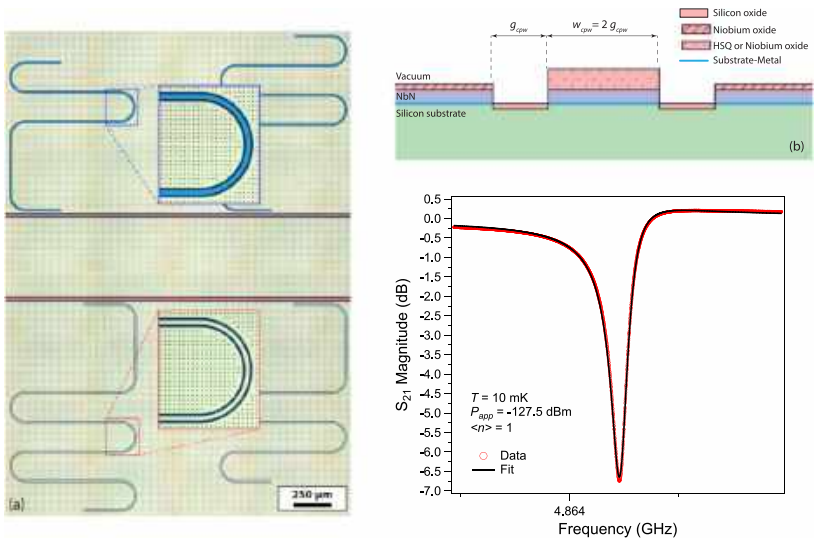

Figure 1. (a) False-coloured optical micrograph of the four resonators used in this work. The resonators are coupled to microwave feed lines (red overlay); the exposed Si substrate, where the NbN has been etched away, is in black. Additionally, HSQ covers the central conductor of the top resonators (cyan overlay). (b) Schematic of the cross-section of the resonators. (c) S_{21} magnitude response of a typical resonator in the single-photon regime (red points). The black line is a fit to determine the resonance parameters.

instead, the majority of the loss originates from the substrate-metal and substrate-air interfaces [26–30]. Moreover, for nanowires, the small dimensions exacerbate the TLS contribution to the loss, since the electric field becomes concentrated near the conductor edges. This concentration leads to an increase in the geometric filling factor (F) of the lossy dielectric layers compared to that of the loss-less vacuum. Therefore, it has been demonstrated that TLS remain the dominant loss mechanism even in disordered superconductors with high kinetic inductance, as long as the films are made moderately thin and not excessively disordered [4].

Across nanowire technologies it becomes necessary to use a spin-on-glass resist to define the sub-micron dimensions. The most prevalent spin-on-glass resist is hydrogen silsesquioxane, HSQ. While HSQ offers unmatched resolution ($\leqslant$10 nm [31]), its structure after development resembles porous amorphous silicon oxide [32, 33], which is a well-known host of TLS [34]. HSQ is hard to remove after e-beam exposure, and it is therefore often left on top of the finished devices [4].

Therefore, when attempting to understand and improve nanowire device performance, we have a rich landscape of small dimensions, disordered superconductors, and spin-on-glass dielectrics, all three of which are quite different from the more commonly used (and consequently well understood) wide ($>10\ \mu$m) Al or Nb features fabricated with conventional, removable resists.

In this paper, we explore the geometrical scaling, toward nanowire dimensions, of dielectric losses in microwave resonators. We make nominally identical devices with and without spin-on-glass top dielectric and clearly find that in all cases the HSQ makes microwave losses worse. Then, to quantify the loss contributions, we simulate the filling factors and find that due to the ratio of the device dimensions to the London penetration depth, disordered superconductors of small dimensions are not amenable to electrostatic simulations that are traditionally used. To accurately capture the physics, we instead perform 3D finite-element simulations of the current density and electric and magnetic fields at microwave frequencies, from which we extract the various filling factors. This reveals that, while the metal-air (MA) interface indeed has a small filling factor, the loss of the HSQ top dielectric is large enough to represent the largest combined loss, in agreement with measurements.

Combining measurements of the loss and numerical simulation of the filling factors of the different interfaces, we determine the value of the loss tangent of HSQ: $\delta^{i}_{\mathrm{HSQ}} = 8 \times 10^{-3}$, i.e. four times that of SiO_x [27, 29, 35], which would have been the assumption due to the similarities between spin-on-glass resists and silicon oxide.

2. Experimental methods, results

In order to study the geometric scaling of dielectric losses, we fabricated NbN coplanar waveguide resonators, with and without HSQ dielectric on top of the centre conductor. These devices span a range of widths of the centre conductor and of the gap between centre conductor and ground planes. The gap width ranges from $g_{cpw} = 500$ nm to 5 μm, with the ratio of the gap to the centre conductor kept fixed. Figure 1(a) shows a micrograph of a typical device, and figure 1(b) shows a sketch of the cross section of the resonators.

The samples are fabricated on a high-resistivity ($\rho \leqslant 10\,\mathrm{k}\Omega\,\mathrm{cm}$) (100) intrinsic silicon substrate. The substrate is dipped for 30 s in a 2% hydrofluoric acid (HF) bath to remove the silicon surface oxide. Within 5 min, the wafer is loaded into a UHV sputtering chamber, where a NbN thin-film of thickness 15 nm is deposited by reactive DC magnetron sputtering from a 99.99% pure Nb target in a 6:1 Ar:N_2 atmosphere at 12.7 μbar. Next, a 500 nm thick layer of PMMA A6 resist is spin-coated and then exposed by electron-beam lithography (EBL) to define the microwave circuitry and resonators. The pattern is developed for 60 s in MIBK: IPA (1:1) and transferred to the film by reactive ion etching in a 50:4 Ar:Cl_2 plasma at 50 W and 10 mTorr. In a subsequent EBL step, a 30 nm layer of HSQ is first spun and then exposed on the centre conductor of half of the microwave resonators such that, after development in a 2.45% TMAH solution, each sample has two copies of each design: one covered with HSQ and one without HSQ.

The samples are wire bonded in a connectorised copper sample box that is mounted onto the mixing chamber of a Bluefors LD250 dilution refrigerator. The inbound microwave signal is attenuated at each temperature stage by a total of 60 dB before reaching the device under test. Accounting for cable losses and sample-box insertion loss, the total attenuation of the signal reaching the sample is 70 dB. To avoid any parasitic reflections and noise leakage from amplifiers, the transmitted signal is fed through two microwave circulators (Raditek RADI-4.0-8.0-Cryo-4-77K-1WR) and a 4–8 GHz band pass filter. Finally, the signal is amplified by a LNF LNC4_8A HEMT cryogenic amplifier (45 dB gain) installed on the 2.8 K stage. Additional amplification is performed at room temperature (Pasternack PE-1522 gain-block amplifiers). This measurement environment has been shown to support measurements of resonators with quality factors of several millions [36] and therefore provides an ideal test bench for characterising loss in superconducting microwave resonators.

We study the microwave properties of each of these resonators by measuring the forward transmission (S_{21}) response using a Keysight N5249A vector network analyser. When probed with an applied power P_{app}, the average energy stored in a resonator of characteristic impedance Z_c and resonant frequency f_r is given by $\langle E_{int}\rangle = hf_r\langle n\rangle = Z_0 Q_l^2 P_{app}/\pi^2 Z_c Q_c f_r$, where $\langle n\rangle$ is the average number of photons in the resonator, h is Planck's constant, $Z_0 = 50\ \Omega$, and Q_c and Q_l are the coupling and loaded quality factors, respectively. Figure 1(c) shows a typical S_{21} magnitude response measured at 10 mK and has average photon population $\langle n\rangle = 1$. The resonator parameters are extracted by fitting the data with an open-source traceable fit routine [37].

In order to reliably determine the TLS loss contribution, we measure the resonant frequency of each resonator against temperature between 10 mK and 1 K [38, 39] using a Pound frequency-locked loop (P-FLL). We measured resonator pairs on the same chip, of the same length and gap widths, with/without HSQ on top of the centre conductor. The data is shown in figure 2, while the cryogenic microwave setup with the VNA and P-FLL schematics are explained in detail in [4]. This method only probes TLS effects and has the benefit of being sensitive to a wide frequency distribution of TLS. Consequently, the intrinsic loss tangent is robust against spectrally unstable TLS that produce time variations in the quality factor [40]. This allows us to independently determine the intrinsic loss tangent (times the filling factor) $F_{\mathrm{TLS}}\delta^i_{\mathrm{TLS}}$. The fitted values are presented in table 1.

3. Modelling of TLS loss

Figure 2 shows that in our devices, the losses are dominated by TLS, even for thin-film nanowires with widths down to 40 nm. In order to accurately account for the individual contributions of all TLS-containing regions of the circuit, we split the dielectric loss into a linear combination of loss tangents each associated with a corresponding filling factor [26–29, 41]

$$\frac{1}{Q_{\mathrm{TLS}}} = F_{\mathrm{TLS}}\delta^i_{\mathrm{TLS}} = \sum_k F_k \delta^i_k, \tag{1}$$

where δ^i_k is the intrinsic loss tangent of region k. Additionally, the filling factor of a given TLS host region k, of volume V_k and relative permittivity ε_k, is given by

$$F_k = \frac{U_k}{U_{total}} = \frac{\int_{V_k}\varepsilon_k \vec{E}^2(\vec{r})d\vec{r}}{\int_V \varepsilon \vec{E}^2(\vec{r})d\vec{r}}, \tag{2}$$

where U_k and U_{total} are the electric energy stored in region k and the total electric energy, respectively, $\vec{E}$ is the electric field, and ε is the effective permittivity of the entire volume V.

Several previous works have studied the loss participation of the different interfaces. O'Connell *et al* [35] perform low-temperature, low-power microwave measurements, report the intrinsic loss tangent of dielectrics, and interpret their results using a TLS defect model.

Wenner *et al* [26] numerically calculate the participation ratios of TLS losses in CPW and microstrip resonators, and find that the losses, at a level of $\delta \sim 5 \times 10^{-6}$, predominantly arise due to the substrate-metal (SM) and substrate-air (SA) interfaces, with only a 1% contribution from the MA interface.

Wang *et al* [27] conduct an experimental and numerical study of losses in Al transmon qubits and attribute the dominant loss to surface dielectrics, consistent with the TLS loss model. In a literature study of transmons made with the standard lift-off process, they find a seemingly universal value $\tan\delta \sim 2.6 \times 10^{-3}$. We note that the spread between data points pertaining to different devices is within the range of temporal variation, due to spectrally unstable TLS, recently reported in both qubit T_1 [25] and resonator Q [40].

Dial *et al* [28] experimentally study 3D transmon qubits, with results consistent with the SM and SA interfaces being the dominant contributors to loss.

Calusine *et al* [29, 30] trench the substrate of TiN resonators, achieving a mean low-power quality factor of

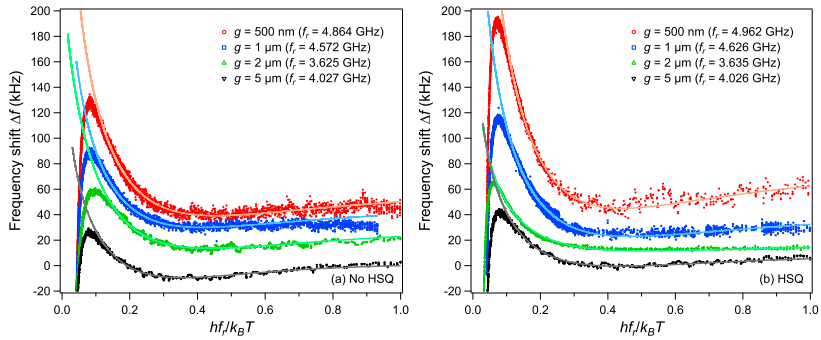

Figure 2. Frequency shift Δf as a function of the normalised frequency f_r of the measured resonators without HSQ (a) and with HSQ covering the central conductor (b). The data is obtained by applying $P_{app} = -110$ dBm and tracking the changes in resonant frequency against temperature between 10 mK and 1 K using the P-FLL. It is plotted against the natural energy scale of the TLS (hf_r/k_BT). The downturn in frequency occurring below $hf_r/k_BT = 0.1$ corresponds to the temperature-dependent kinetic inductance contribution and is not TLS-related. For clarity, the curves have been offset by 15 kHz. The solid lines are fits to $\Delta f(T) = F_{\mathrm{TLS}}\delta^i_{\mathrm{TLS}}(\ln(T/T_0) + [g(T, f_r) - g(T_0, f_r)])$ [38, 39], where $\Delta f(T) = [f_r(T) - f_r(T_0)]/f_r(T_0)$, T_0 is a reference temperature, $g(T, f) = \mathrm{Re}\left(\Psi\left(\frac{1}{2} + hf/2\pi ik_BT\right)\right)$, and Ψ is the complex digamma function.

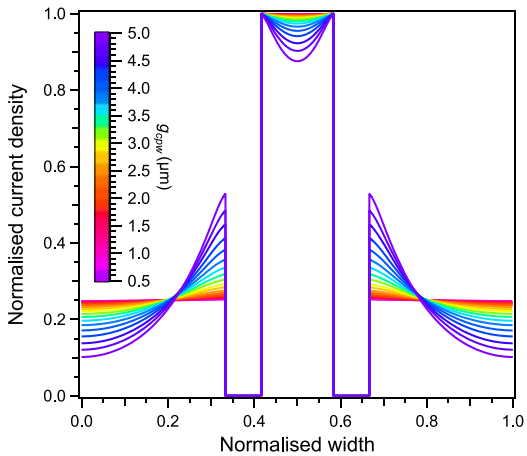

Figure 3. Simulated normalised current density inside the superconductors, extracted along a line half-way inside it (half the thickness), for all simulated values g_{cpw} in the 500 nm to 5 μm range.

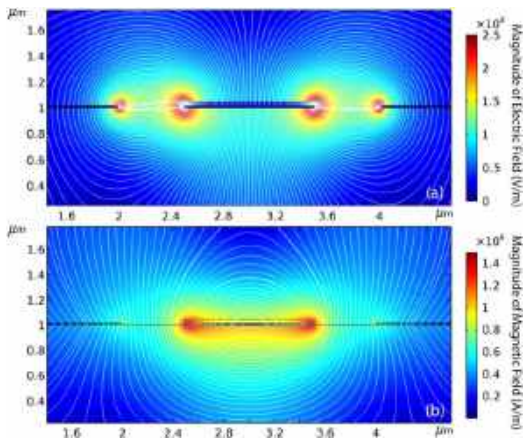

Figure 4. Magnitude and field lines of the simulated electric (a) and magnetic fields (b) for a cross section of the resonators with HSQ covering the central conductor. The permittivity in equation (5), with $\omega/2\pi = 5$ GHz, is given as an input to the Comsol Multiphysics simulation tool.

Table 1. Resonator parameters. $F_{\mathrm{TLS}}\delta^i_{\mathrm{TLS}}$ is obtained from fits of the data in figure 2.

g_{cpw} (μm)	Z_c (Ω)	f_r (no HSQ) (MHz)	f_r (with HSQ) (MHz)	$F_{\mathrm{TLS}}\delta^i_{\mathrm{TLS}}$ (no HSQ) ($\times 10^{-5}$)	$F_{\mathrm{TLS}}\delta^i_{\mathrm{TLS}}$ (with HSQ) ($\times 10^{-5}$)
5	207	4027	4026	1.36	1.66
2	312	3625	3635	1.60	1.87
1	441	4572	4626	1.98	2.50
0.5	632	4864	4962	2.74	3.92

3×10^6, and demonstrate agreement with a finite-element electrostatic simulation of dielectric loss.

4. Filling factor simulations

In order to analyse dielectric and interfacial losses in our devices, and in particular to identify those from the HSQ top dielectric, we perform electro-magnetic simulations (with and without the HSQ layer) in Comsol Multiphysics for a wide

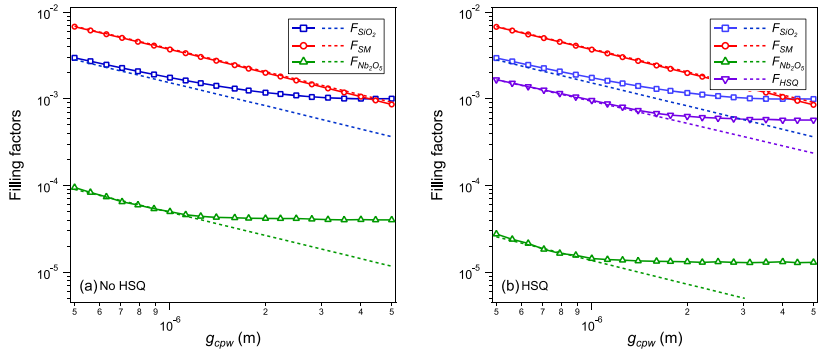

Figure 5. Simulated filling factors F as a function of the co-planar waveguide gap g_{cpw} for resonators without HSQ (a) and with HSQ covering the central conductor (b). The dashed lines represent the incorrect F obtained with electrostatic simulations.

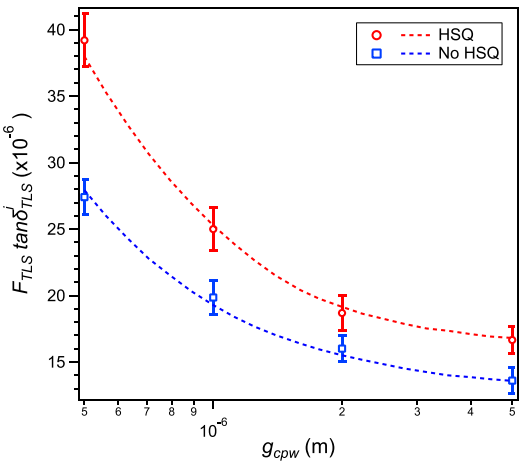

Figure 6. Total TLS loss $F_{\mathrm{TLS}}\delta^i_{\mathrm{TLS}}$ versus gap width g_{cpw} of the co-planar waveguide for all four measured resonators. The $F_{\mathrm{TLS}}\delta^i_{\mathrm{TLS}}$ values are determined from fits of the $\Delta f\,(T)$ data in figure 2—see table 1. The error bars represent two standard deviations of uncertainty (95% confidence interval). The dashed lines are fits to equation (1) using the simulated filling factors F_{TLS} shown in figure 5.

Table 2. Fitted loss tangents of the different lossy regions. The values are obtained from fits to equation (1) using the simulated filling factors.

Region	Symbol	Value
HSQ	δ^i_{HSQ}	8.0×10^{-3}
Substrate-metal interface	δ^i_{SM}	1.3×10^{-3}
Niobium oxide	$\delta^i_{\mathrm{Nb_2O_5}}$	4.7×10^{-2}
Silicon oxide	$\delta^i_{\mathrm{SiO_2}}$	2.1×10^{-3}

range of resonator geometries. A sketch of the cross-section of the simulated structures is shown in figure 1(b). The simulation parameters for the constituent materials are as follows: the SA interface is modelled as a 5 nm thick layer of SiO_2 [42] with relative permittivity $\varepsilon_r(\mathrm{SiO_2}) = 4.2$. The MA interface consists of a 5 nm thick layer of Nb_2O_5 [43] with relative permittivity $\varepsilon_r(\mathrm{Nb_2O_5}) = 33$ [44, 45]. The SM interface is modelled by a 2 nm thick layer inside the substrate ($\varepsilon_r(\mathrm{SM}) = \varepsilon_r(\mathrm{Si}) = 11.7$) [29]. Finally, the HSQ region has a thickness of 30 nm and relative permittivity $\varepsilon_r(\mathrm{HSQ}) = 3$ [33]. Because Nb_2O_5 requires several days to achieve any meaningful thickness [43], it is assumed that no Nb_2O_5 is present underneath the HSQ. Therefore, on the samples without HSQ, Nb_2O_5 resides on both the central conductor and ground planes, whereas on the samples with HSQ, Nb_2O_5 is present only on the ground planes.

The superconductor part of the structure requires extra care to simulate accurately: strongly disordered superconductors, like NbN, have an extremely small electron mean free path l (on the order of 0.5 nm and smaller [46]) and are therefore in the local dirty limit [47]. In this limit, several quantities become dependent on the mean free path and need to be adjusted from their BCS values [48, 49]. Most importantly for this study, the magnetic penetration depth in disordered superconductors and at zero temperature becomes

$$\lambda_{dirty}(0) = \lambda_L(0)\sqrt{\frac{\xi_0}{l}} = \sqrt{\frac{\hbar}{\pi\mu_0\Delta_0\sigma_n}}, \tag{3}$$

where $\lambda_L(0)$ is the London penetration depth at $T = 0$ K, ξ_0 is the BCS coherence length, $\hbar$ is the reduced Planck constant, μ_0 is the vacuum permeability, Δ_0 is the superconducting gap at zero temperature, and σ_n is the normal-state conductivity. Additionally, the temperature dependence of the penetration depth is given by

$$\frac{\lambda_{dirty}(T)}{\lambda_{dirty}(0)} = \left[\frac{\Delta(T)}{\Delta_0}\tanh\left(\frac{\Delta(T)}{2k_BT}\right)\right]^{-1/3}. \tag{4}$$

By measuring the resistance versus temperature of our NbN thin films, we find $T_c = 7.20$ K and $\sigma_n = 1.32 \times 10^5$ S m^{-1} (measured at the onset of the superconducting transition). Using $\Delta_0 = 2.08 k_B T_c$ [50], we obtain $\lambda_{dirty} = 987$ nm $\simeq 1$ μm, which is comparable to the lateral dimension of our resonators.

Consequently, it is not sufficient to approximate the current density in our NbN devices as a surface density, since magnetic fields significantly penetrate the superconductor.

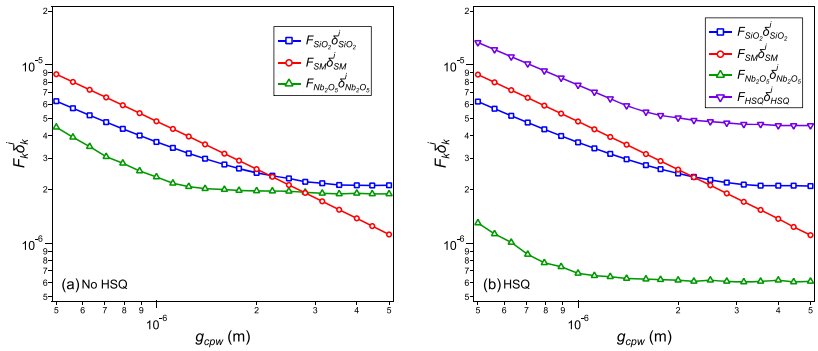

Figure 7. Contribution of each individual lossy region for resonators without HSQ (a) and with HSQ (b) covering the central conductor.

This is in contrast to resonators made of a conventional superconductor such as aluminium ($\lambda_L(0) \simeq 30$ nm [51]) or niobium (100 nm [52]). In a similar way, it is insufficient to assume a uniform current distribution in the superconductor when the resonator dimensions are larger than $\lambda_L(T)$.

Therefore, a static solution of Maxwell's equations is insufficient here, in particular for the wider geometries. Instead we need to solve the Maxwell–London equations, at the relevant frequency of the alternating current, in order to accurately simulate the densities of the current and electromagnetic fields. We achieve this in a 3D finite-element simulator by considering the superconductor as an environment with a complex permittivity [53, 54]

$$\varepsilon_r(\omega, T) = \varepsilon_0 - \frac{1}{\omega^2 \mu_0 \lambda_{dirty}(T)^2} - j\frac{\sigma_1(\omega, T)}{\omega}, \qquad (5)$$

where $\sigma_1(\omega, T)$ is the real part of the Mattis–Bardeen conductivity.

The meshing of the simulated structure has to be carefully optimised due the vast difference of length scales within the resonator structure (widths, thicknesses, and also the wavelength). The simulation mesh is manually defined using Comsol's swept mesh functionality and consists of rectangular elements. Rectangular elements are preferred over the more standard tetrahedral elements to avoid poor meshing quality inherent to high-aspect ratio tetrahedrons. The edge length of each element is varied from 3 nm to 100 nm, with smaller elements close to the regions of interest (superconducting thin-film and dielectric layers). Due to memory constraints, however, the edge length alongside the wave propagation direction is kept constant to 100 nm and only a short section of co-planar waveguide is simulated ($l_{cpw} = 4\ \mu$m). A relative tolerance of 1×10^{-5} was found as a good compromise between the accuracy of the converged solution and the duration of the simulation.

Figures 3 and 4 show the simulated current density and electric and magnetic fields, respectively, for a cross section of a resonator with $g_{cpw} = 500$ nm. From the electric fields, we calculate the filling factor of each region using equation (2) and present the result in figure 5. Additionally, figure 5 shows filling factors calculated by means of electrostatic simulation to highlight the significant deviation from the Maxwell–London simulation results for $w_{cpw} > \lambda_L$.

Using these simulated filling factors, we can fit equation (1) to the experimental results in table 1—see figure 6—and in this way determine the intrinsic loss tangent of each lossy region. These results are summarised in table 2.

5. Discussion

Our results are consistent with values found by other groups in similar types of devices [27, 29, 35, 44]. However, we emphasise that the fabrication of our devices was not focused on minimising the influence of TLS.

We find the intrinsic loss tangent for HSQ to be $\delta^i_{\mathrm{HSQ}} = 8.0 \times 10^{-3}$. Paired with the relatively large filling factor of the HSQ region, this makes HSQ the dominant contribution to the loss for all dimensions, as highlighted in figure 7; and for a given dimension, $F_{\mathrm{TLS}}\delta^i_{\mathrm{TLS}}$ is systematically higher for the sample covered with HSQ, as shown in figure 6. These results confirms that the porous amorphous silicon oxide structure of developed HSQ [32, 33] is a major source of dielectric loss, and therefore, a process that allows for the removal of the HSQ mask would lead to significant improvements in device performance.

6. Conclusion

In conclusion, we fabricated and measured co-planar waveguide resonators with dimensions ranging from $g_{cpw} = 5\ \mu$m down to 500 nm in order to study the geometric dependence of TLS loss. Using 3D finite-element electro-magnetic simulations we calculated the relative contributions of the different sources of TLS loss. Such simulations provide a valuable tool to predict the performance of superconducting resonators and other superconducting quantum devices.

Additionally, by comparing resonators with the central conductor covered by HSQ and resonators without HSQ, we were able to extract the intrinsic loss tangent of this dielectric: $\delta^i_{\mathrm{HSQ}} = 8.0 \times 10^{-3}$.

Acknowledgments

We acknowledge support in the device fabrication from the Chalmers Nanofabrication Laboratory staff. The authors are grateful to Philippe Tassin for granting access to his nodes in the Chalmers C3SE computational cluster where our simulations were performed. This research has been supported by funding from the Swedish Research Council and Chalmers Area of Advance Nanotechnology. In addition, JJB acknowledges financial support from the Industrial Strategy Challenge Fund Metrology Fellowship as part of the UK government's Department for Business, Energy and Industrial Strategy.

ORCID iDs

David Niepce https://orcid.org/0000-0002-3864-0658
Martí Gutierrez Latorre https://orcid.org/0000-0001-6041-3139

References

[1] Masluk N A, Pop I M, Kamal A, Minev Z K and Devoret M H 2012 Microwave characterization of josephson junction arrays: implementing a low loss superinductance *Phys. Rev. Lett.* **109** 137002
[2] Bell M T, Sadovskyy I A, Ioffe L B, Kitaev A Y and Gershenson M E 2012 Quantum superinductor with tunable nonlinearity *Phys. Rev. Lett.* **109** 137003
[3] Vladimir E, Manucharyan Jens, Koch Leonid I, Glazman and Devoret Michel H 2009 Fluxonium: single cooper-pair circuit free of charge offsets *Science* **326** 113–6
[4] Niepce D, Burnett J and Bylander J 2019 High kinetic inductance NbN nanowire superinductors *Phys. Rev. Appl.* **11** 044014
[5] Samkharadze N, Bruno A, Scarlino P, Zheng G, DiVincenzo D P, DiCarlo L and Vandersypen L M K 2016 High-kinetic-inductance superconducting nanowire resonators for circuit QED in a magnetic field *Phys. Rev. Appl.* **5** 044004
[6] Rotzinger H, Skacel S T, Pfirrmann M, Voss J N, Münzberg J, Probst S, Bushev P, Weides M P, Ustinov A V and Mooij J E 2016 Aluminium-oxide wires for superconducting high kinetic inductance circuits *Supercond. Sci. Technol.* **30** 025002
[7] Zhang W, Kalashnikov K, Lu W-S, Kamenov P, DiNapoli T and Gershenson M E 2019 Microresonators fabricated from high-kinetic-inductance aluminum films *Phys. Rev. Appl.* **11** 011003
[8] Grünhaupt L *et al* 2019 Granular aluminium as a superconducting material for high-impedance quantum circuits *Nat. Mater.* **18** 816–9
[9] Stockklauser A, Scarlino P, Koski J V, Gasparinetti S, Andersen C K, Reichl C, Wegscheider W, Ihn T, Ensslin K and Wallraff A 2017 Strong coupling cavity QED with gate-defined double quantum dots enabled by a high impedance resonator *Phys. Rev.* X **7** 011030
[10] Samkharadze N, Zheng G, Kalhor N, Brousse D, Sammak A, Mendes U C, Blais A, Scappucci G and Vandersypen L M K 2018 Strong spin-photon coupling in silicon *Science* **359** 1123–7
[11] Eom B H, Day P K, LeDuc H G and Zmuidzinas J 2012 A wideband, low-noise superconducting amplifier with high dynamic range *Nat. Phys.* **8** 623
[12] Bockstiegel C, Gao J, Vissers M R, Sandberg M, Chaudhuri S, Sanders A, Vale L R, Irwin K D and Pappas D P 2014 Development of a broadband NbTiN traveling wave parametric amplifier for MKID readout *J. Low Temp. Phys.* **176** 476–82
[13] O'Brien K, Macklin C, Siddiqi I and Zhang X 2014 Resonant phase matching of josephson junction traveling wave parametric amplifiers *Phys. Rev. Lett.* **113** 157001
[14] White T C *et al* 2015 Traveling wave parametric amplifier with Josephson junctions using minimal resonator phase matching *Appl. Phys. Lett.* **106** 242601
[15] Macklin C, O'Brien K, Hover D, Schwartz M E, Bolkhovsky V, Zhang X, Oliver W D and Siddiqi I 2015 A near-quantum-limited Josephson traveling-wave parametric amplifier *Science* **350** 307–10
[16] Vissers M R, Erickson R P, Ku H-S, Vale L, Wu X, Hilton G C and Pappas D P 2016 Low-noise kinetic inductance traveling-wave amplifier using three-wave mixing *Appl. Phys. Lett.* **108** 012601
[17] Adamyan A A, de Graaf S E, Kubatkin S E and Danilov A V 2016 Superconducting microwave parametric amplifier based on a quasi-fractal slow propagation line *J. Appl. Phys.* **119** 083901
[18] Janssen R M J, Endo A, Baselmans J J A, de Visser P J, Barends R and Klapwijk T M 2012 Power handling and responsivity of submicron wide superconducting coplanar waveguide resonators *J. Low Temp. Phys.* **167** 354–9
[19] Schroeder E, Mauskopf P, Mani H, Bryan S, Berggren K K and Zhu D 2019 Operation of a superconducting nanowire in two detection modes: KID and SPD *J. Low Temp. Phys.* **194** 386–93
[20] Sinclair A K, Schroeder E, Zhu D, Colangelo M, Glasby J, Mauskopf P D, Mani H and Berggren K K 2019 Demonstration of microwave multiplexed readout of DC-Biased superconducting nanowire detectors *IEEE Trans. Appl. Supercond.* **29** 1–4
[21] Müller Clemens, Cole Jared H and Lisenfeld Jürgen 2019 Towards understanding two-level-systems in amorphous solids: insights from quantum circuits *Reports on Progress in Physics* **82** 124501
[22] Müller C, Lisenfeld J, Shnirman A and Poletto S 2015 Interacting two-level defects as sources of fluctuating high-frequency noise in superconducting circuits *Phys. Rev.* B **92** 035442
[23] Klimov P V *et al* 2018 Fluctuations of energy-relaxation times in superconducting qubits *Phys. Rev. Lett.* **121** 090502
[24] Schlör S, Lisenfeld J, Müller C, Bilmes A, Schneider A, Pappas D P, Ustinov A V and Weides M 2019 Correlating decoherence in transmon qubits: low frequency noise by single fluctuators *Phys. Rev. Lett.* **123** 190502
[25] Burnett J J, Bengtsson A, Scigliuzzo M, Niepce D, Kudra M, Delsing P and Bylander J 2019 Decoherence benchmarking of superconducting qubits *NPJ Quantum Inf.* **5** 54
[26] Wenner J *et al* 2011 Surface loss simulations of superconducting coplanar waveguide resonators *Appl. Phys. Lett.* **99** 113513
[27] Wang C, Axline C, Gao Y Y, Brecht T, Chu Y, Frunzio L, Devoret M H and Schoelkopf R J 2015 Surface participation and dielectric loss in superconducting qubits *Appl. Phys. Lett.* **107** 162601
[28] Dial O, McClure D T, Poletto S, Keefe G A, Rothwell M B, Gambetta J M, Abraham D W, Chow J M and Steffen M 2016 Bulk and surface loss in superconducting transmon qubits *Supercond. Sci. Technol.* **29** 044001

[29] Calusine G *et al* 2018 Analysis and mitigation of interface losses in trenched superconducting coplanar waveguide resonators *Appl. Phys. Lett.* **112** 062601
[30] Woods W, Calusine G, Melville A, Sevi A, Golden E, Kim D K, Rosenberg D, Yoder J L and Oliver W D 2019 Determining interface dielectric losses in superconducting coplanar-waveguide resonators *Phys. Rev. Appl.* **12** 014012
[31] Chen Y, Yang H and Cui Z 2006 Effects of developing conditions on the contrast and sensitivity of hydrogen silsesquioxane *Microelectron. Eng.* **83** 1119–23
[32] Namatsu H, Yamaguchi T, Nagase M, Yamazaki K and Kurihara K 1998 Nano-patterning of a hydrogen silsesquioxane resist with reduced linewidth fluctuations *Microelectron. Eng.* **41–42** 331–4
[33] Liu P T *et al* 1998 The effects of plasma treatment for low dielectric constant hydrogen silsesquioxane (HSQ) *Thin Solid Films* **332** 345–50
[34] Barends R, Hortensius H L, Zijlstra T, Baselmans J J A, Yates S J C, Gao J R and Klapwijk T M 2008 Contribution of dielectrics to frequency and noise of NbTiN superconducting resonators *Appl. Phys. Lett.* **92** 223502
[35] O'Connell A D *et al* 2008 Microwave dielectric loss at single photon energies and millikelvin temperatures *Appl. Phys. Lett.* **92** 112903
[36] Burnett J, Bengtsson A, Niepce D and Bylander J 2018 Noise and loss of superconducting aluminium resonators at single photon energies *J. Phys.: Conf. Ser.* **969** 012131
[37] Probst S, Song F B, Bushev P A, Ustinov A V and Weides M 2015 Efficient and robust analysis of complex scattering data under noise in microwave resonators *Rev. Sci. Instrum.* **86** 024706
[38] Gao J, Daal M, Vayonakis A, Kumar S, Zmuidzinas J, Sadoulet B, Mazin B A, Day P K and Leduc H G 2008 Experimental evidence for a surface distribution of two-level systems in superconducting lithographed microwave resonators *Appl. Phys. Lett.* **92** 152505
[39] Lindström T, Healey J E, Colclough M S, Muirhead C M and Tzalenchuk A Y 2009 Properties of superconducting planar resonators at millikelvin temperatures *Phys. Rev.* B **80** 132501
[40] Earnest C T, Béjanin J H, McConkey T G, Peters E A, Korinek A, Yuan H and Mariantoni M 2018 Substrate surface engineering for high-quality silicon/aluminum superconducting resonators *Supercond. Sci. Technol.* **31** 125013
[41] Gambetta J M, Murray C E, Fung Y-K-K, McClure D T, Dial O, Shanks W, Sleight J W and Steffen M 2017 Investigating surface loss effects in superconducting transmon qubits *IEEE Trans. Appl. Supercond.* **27** 1–5
[42] Morita M, Ohmi T, Hasegawa E, Kawakami M and Ohwada M 1990 Growth of native oxide on a silicon surface *J. Appl. Phys.* **68** 1272–81
[43] Henry M D, Wolfley S, Young T, Monson T, Pearce C J, Lewis R, Clark B, Brunke L and Missert N 2017 Degradation of superconducting Nb/NbN films by atmospheric oxidation *IEEE Trans. Appl. Supercond.* **27** 1–5
[44] Kaiser C, Skacel S T, Wünsch S, Dolata R, Mackrodt B, Zorin A and Siegel M 2010 Measurement of dielectric losses in amorphous thin films at gigahertz frequencies using superconducting resonators *Supercond. Sci. Technol.* **23** 075008
[45] Romanenko A and Schuster D I 2017 Understanding quality factor degradation in superconducting niobium cavities at low microwave field amplitudes *Phys. Rev. Lett.* **119** 264801
[46] Chockalingam S P, Chand M, Jesudasan J, Tripathi V and Raychaudhuri P 2008 Superconducting properties and Hall effect of epitaxial NbN thin films *Phys. Rev.* B **77** 214503
[47] Dressel M 2013 Electrodynamics of metallic superconductors *Adv. Condens. Matter Phys.* **2013** 104379
[48] Gor'kov L P 1959 Microscopic derivation of the Ginzburg–Landau equations in the theory of superconductivity *J. Exp. Theor. Phys.* **9** 1364
[49] Tinkham M 2004 *Introduction to Superconductivity* (New York: Dover)
[50] Mondal M, Kamlapure A, Chand M, Saraswat G, Kumar S, Jesudasan J, Benfatto L, Tripathi V and Raychaudhuri P 2011 Phase fluctuations in a strongly disordered s-Wave NbN superconductor close to the metal-insulator transition *Phys. Rev. Lett.* **106** 047001
[51] Maloney M D, de la Cruz F and Cardona M 1972 Superconducting parameters and size effects of aluminum films and foils *Phys. Rev.* B **5** 3558–72
[52] Langley B W, Anlage S M, Pease R F W and Beasley M R 1991 Magnetic penetration depth measurements of superconducting thin films by a microstrip resonator technique *Rev. Sci. Instrum.* **62** 1801–12
[53] Vendik O G, Vendik I B and Kaparkov D I 1998 Empirical model of the microwave properties of high-temperature superconductors *IEEE Trans. Microwave Theory Tech.* **46** 469–78
[54] Javadzadeh S M H, Farzaneh F and Fardmanesh M 2013 Nonlinear circuit model for discontinuity of step in width in superconducting microstrip structures and its impact on nonlinear effects *IEEE Trans. Appl. Supercond.* **23** 1301208

Paper C

Stability of Superconducting Resonators: Motional Narrowing and the Role of Landau-Zener Driving of Two-level Defects

Stability of superconducting resonators: motional narrowing and the role of Landau-Zener driving of two-level defects

David Niepce,[1] Jonathan J. Burnett,[2] Marina Kudra,[1] Jared H. Cole,[3] and Jonas Bylander[1,*]

[1] *Chalmers University of Technology, Microtechnology and Nanoscience, SE-41296, Gothenburg, Sweden*
[2] *National Physical Laboratory, Hampton Road, Teddington, Middlesex, TW11 0LW, United Kingdom*
[3] *Chemical and Quantum Physics, School of Science, RMIT University, Melbourne VIC 3001, Australia*

(Dated: August 17, 2020)

Frequency instability of superconducting resonators and qubits leads to dephasing and time-varying energy-loss and hinders quantum-processor tune-up. Its main source is dielectric noise originating in surface oxides. Thorough noise studies are needed in order to develop a comprehensive understanding and mitigation strategy of these fluctuations. Here we use a frequency-locked loop to track the resonant-frequency jitter of three different resonator types—one niobium-nitride superinductor, one aluminium coplanar waveguide, and one aluminium cavity—and we observe strikingly similar random-telegraph-signal fluctuations. At low microwave drive power, the resonators exhibit multiple, unstable frequency positions, which for increasing power coalesce into one frequency due to motional narrowing caused by sympathetic driving of individual two-level-system defects by the resonator. In all three devices we probe a dominant fluctuator, finding that its amplitude saturates with increasing drive power, but its characteristic switching rate follows the power-law dependence of quasiclassical Landau-Zener transitions.

I. INTRODUCTION

Superconducting microwave resonators [1], in a variety of geometries, are essential tools in circuits for quantum computing [2], microwave quantum optics [3], low-noise amplifiers [4], radiation detectors [1], and particle accelerators [5, 6]. While the reduction of energy loss of resonators and qubits has received significant attention [1, 2, 7], leading to long-lived qubits [8, 9] and high-quality resonators [10], far fewer studies report on parameter fluctuations [9, 11–13]. Such fluctuations present a challenge to the bring-up and calibration stability of current quantum processors [14]. Thorough noise studies are needed in order to understand and mitigate these fluctuations. Here, we examine the low-frequency jitter of three different types of superconducting resonator with the same experimental setup and observe strikingly similar random telegraph signal (RTS) fluctuations. At low excitation power, the RTS lead to multiple quasi-stable frequency positions that coalesce at high powers, which we interpret as motional narrowing caused by direct (sympathetic) driving of individual two-level system (TLS) defects by the resonator field, causing Landau–Zener transitions between the TLS states.

While the community agrees on the many underlying decoherence mechanisms which contribute to decoherence, it remains divided on the relative importance of each mechanism. For example, the dissipation within Al resonators has been separately found to be limited by free-space-photon generated quasiparticles [15] and two-level defects [16]. Similarly, dissipation in granular aluminium oxide resonators has been separately found to be limited by non-equilibrium quasiparticles [17] and also by two-level defects [18]. Untangling these effects is complicated by experimental details that often differ: different signal filtering, use of infra-red absorber, magnetic shielding, and circuit-board enclosure vs. cavity enclosure. These differences make reports difficult to directly compare, resulting in conflicting interpretations of the underlying mechanism. This clearly demonstrates the need for experiments with common experimental details and for the standardization of measurement techniques.

Here we specifically use an identical measurement and analysis infrastructure to compare three very distinct types of superconducting resonators: an NbN (T_c = 7.2 K) 20 nm thick nanowire superinductor [19], an Al (T_c = 1.05 K) 150 nm thick coplanar resonator, and finally an Al (T_c = 1.18 K) mm-scale 3D cavity resonator [20]. The device characteristics are summarised in Table I and in Methods. All three devices have similar resonant frequencies f_r but vastly different superconducting properties, electric-field distributions, kinetic-inductance fractions, and internal quality factors Q_i. By performing the same detailed analysis of the frequency 'jitter' of these devices as a function of drive power we are able to directly compare the noise characteristics of all three devices.

A key observation is that the frequency response of these devices fluctuates as an RTS, i.e. the frequency switches instantaneously between two or more discrete levels—see Fig. 1(a). As the devices differ greatly in terms of design and dimensions, we attribute these fluctuations to two-level system (TLS) defects, omnipresent in the dielectrics of superconductor surfaces and interfaces. Dielectric *loss*, due to near-resonant TLS, is a limiting factor for resonator internal quality factors, qubit relaxation times (T_1), MKID detection efficiencies [1], and accelerator cavity efficacies [5, 6]. Simultaneously, dielec-

* jonas.bylander@chalmers.se

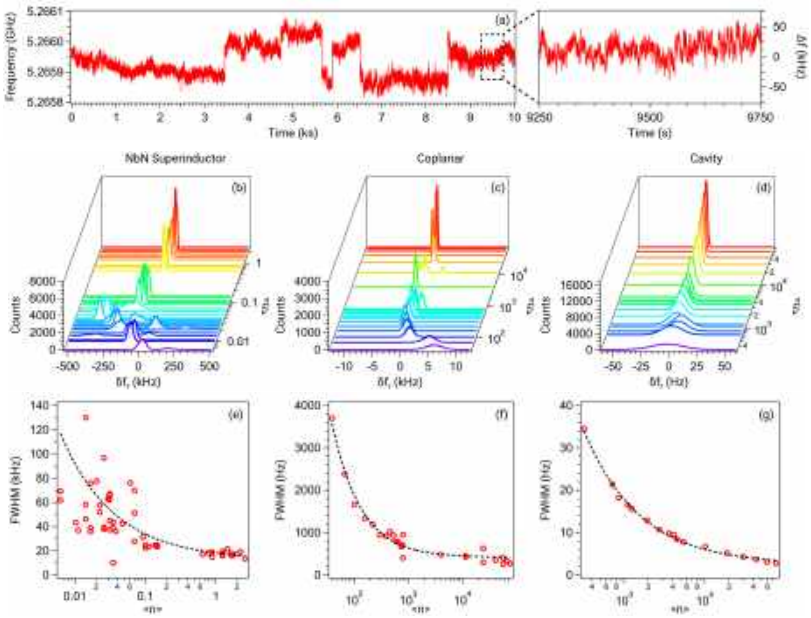

FIG. 1. **(a)** Raw frequency jitter of the nanowire resonator sampled at 100 Hz, at an applied power corresponding to an average number of $\langle n \rangle \simeq 3 \times 10^{-2}$ photons in the resonator. **(b–d)** Histograms of the frequency fluctuations for the three resonators vs. applied power. The data is normalised to the mean frequency of the highest applied power. **(e–g)** Peak widths (FWHM) of the data in (b–d). (Note that FWHM refers to the width of one peak in the histogram and not to the distance between resolvable peaks that correspond to quasi-stable configurations.)

tric *noise*, due to low-frequency TLS, leads to spectral instability, i.e. fluctuations of T_1 (typically by 20%) and of qubit frequencies (typically by a few kilohertz) with concomitant dephasing. The observed noise response reported here is entirely consistent with recent reports on fluctuations of single-TLS or few-TLS defects within superconducting qubits [9, 11–13]; however, in this setup, we are able to go further and identify the characteristics of a dominant TLS and even differentiate between device-specific response revealing TLS behaviour which is surprisingly consistent across devices. Analysis of the temporal fluctuations by spectral density and, particularly, by Allan-deviation techniques offers a window into the dynamics. As a result, we attribute the observed power dependence to sympathetic driving of the TLS bath by the resonator field. Then, by analysing the fluctuations, we find that the RTS switching rate of all resonators follows a common power-law dependence that is consistent with the quasiclassical expression for the Landau-Zener transition rate.

II. RESULTS

A. Temporal frequency fluctuations

We use a Pound frequency-locked loop to measure the fluctuations of f_r of the resonators for 2 h 45 min (see Methods). Figure 1(a) shows an example of such a data set. We observe that the frequency fluctuates between discrete points, as is characteristic of an RTS. In fact, these fluctuations occur at all observable timescales as can be seen in the insert over a much shorter time period.

To qualitatively compare between the different devices, we calculate the histogram of frequency fluctuations measured on each of the resonators against circulating power in units of the average photon occupation number $\langle n \rangle$ (Fig. 1 (b–d)) and extract the histogram full width at half maximum (FWHM) (Fig. 1 (e–g)). We observe that the fluctuation amplitude (histogram width) is the highest for the nanowire resonator (b,e), lower in the coplanar resonator (c,f), and lowest in the cavity (d,g). We attribute this to fluctuations of the real part of the dielectric susceptibility, which acts as an effective capacitance noise on the resonator and therefore leads to frequency fluctuations. Indeed, the nanowire has the highest sen-

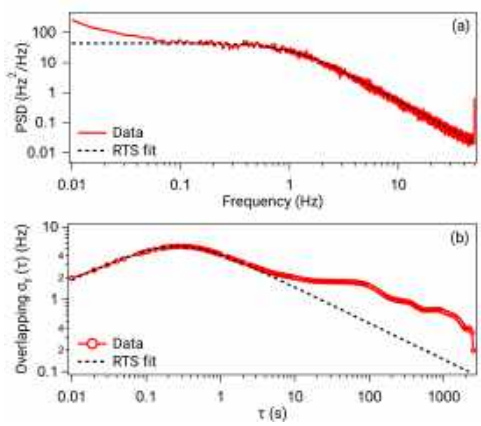

FIG. 2. Fitting of the noise to an RTS fluctuator model. The plots show an example of a Welch power spectral density $S_y(f)$ **(a)** and overlapping Allan deviation $\sigma_y(\tau)$ **(b)** for the measured frequency-fluctuation data from the cavity resonator held at $T = 10\,\mathrm{mK}$ and with an applied microwave drive power $P = -131.5\,\mathrm{dBm}$ ($\langle n\rangle \simeq 715$). The data was sampled at 100 Hz. The dashed line corresponds to a fit of the RTS fluctuator feature using a common set of fitting parameters for both traces (eqs. 7–8). The data below 0.1 Hz (above 10 s) represents the tail of one or several secondary RTS fluctuators (see discussion in the main text).

sitivity to electric fields, due to its very high impedance and high electric-field filling factor [19, 21]. In the coplanar resonator, the electric field is not as strongly coupled. Lastly, the cavity has the smallest filling factor and will therefore exhibit the least amount of frequency fluctuations. We note that while the losses of superconducting cavities have been studied at sub-kelvin temperatures [5, 6, 20, 22], we have found no reports of frequency noise of superconducting cavities at these temperatures.

Qualitatively, Fig. 1(b–d) demonstrate all the hallmarks of motional narrowing due to one or more RTS fluctuators [23–27]. At low power, we see multiple frequency positions, which can be attributed to several slowly varying RTS signals. If we were to continue measuring for even longer time periods, we would ultimately expect a Gaussian distribution of frequency shifts [27]. As the power is increased, these peaks coalesce into a single distribution whose width narrows as the power increases. To obtain an estimate for the power dependence of this narrowing, we fit the FWHM, shown via the dashed lines in Fig. 1(e–g), to the functional form $F_0 + F_1/\langle n\rangle^{\beta}$, and we find a β value of 0.58, 0.82, and 0.63 for the nanowire, resonator, and cavity, respectively (see Table S1 and discussion in supplement).

TABLE I. Characteristics of the three resonators

Resonator	f_r (GHz)	$Z_c\,(\Omega)$	Q_i	Q_c
Nanowire [19]	5.3	6.8×10^3	2.5×10^4	8.0×10^4
Coplanar [28]	4.3	50	5.4×10^5	1.8×10^5
Cavity [20]	6.0	58	1.1×10^7	8.2×10^6

B. Spectral and Allan analysis of fluctuations: universal dependence of individual RTS fluctuators on the applied drive power

To gain further insight into the fluctuations, we examine the spectral properties (Fig. 2(a)) and Allan deviation (Fig. 2(b)) of the frequency fluctuations. While the frequency spurs in the time-series data in Fig. 1(a) are indicative of RTS noise, the spectral and Allan responses allow us to quantitatively fit the data and identify the unique characteristics of an RTS response [29], in contrast to other types of noise (e.g. 'white' or '$1/f$'). The data in Fig. 2 prominently features a single dominating RTS fluctuator (see Methods, eqs. (7–8) for the functional form), which we can fit to extract its amplitude A, corresponding to a frequency step size between the states of the telegraph noise process, and characteristic time τ_0.

We analyse the fluctuation data for a range of drive powers, shown in Supplementary Fig. S1, and we observe that all three devices present similar noise profiles—featuring one dominant RTS fluctuator—albeit at widely different amplitudes: the nanowire is the noisiest and the cavity is the quietest. Generally, there exists other less-prominent RTS features, sometimes at sufficient densities that they sum up to a $1/f$-like trend [30]. In the limit of few RTS fluctuators, or alternatively in the $1/f$ limit, the data can be reliably fitted. However, between these limits, it becomes non-trivial to determine the exact number of RTS fluctuators that describe the fluctuations. For consistency, we therefore focus on determining the characteristic switching time τ_0 and amplitude A of the dominant RTS fluctuator within our measurement window and plot the resulting values of A and τ_0 vs. $\langle n\rangle$ in Fig. 3(a) and (b), respectively.

When examining the raw frequency jitter (Fig. 1(a)), an initial assumption would be that the noise present is a mixture of RTS (on ∼100-second timescale) and 'white' frequency noise (i.e. $S_y \propto f^0$ and $\sigma_y \propto \tau^{-0.5}$). However, from the PSD and Allan deviation methods, it is clear that no white frequency noise is present (in the supplemental this is shown for all microwave drives). Therefore, the noise present is a combination of an RTS at timescales of ∼100 seconds and other RTS at much smaller timescales ∼1 ms to 1 s (see Fig. 3(b)). As such, the multi-peak behaviour of Fig. 1(b–d) occurs due to the longer-timescale RTS, whereas the width in Fig. 1(e–g) is determined by the smaller-timescale RTS. Within our measurement window, the shorter timescale RTS dominates the signal, from which we extract the parameters A and τ_0.

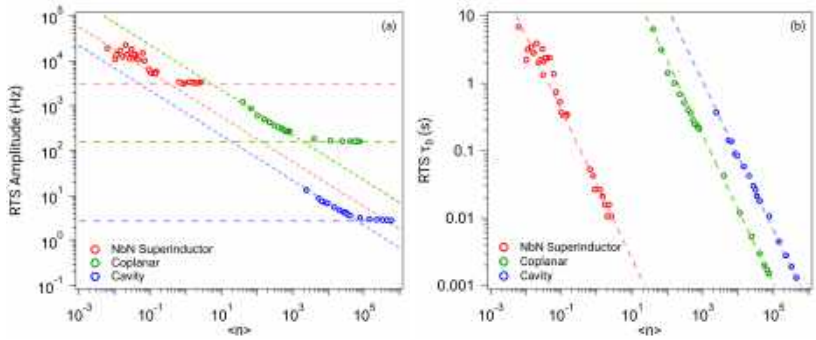

FIG. 3. Drive-power dependence of the RTS amplitude A **(a)** and switching time constant τ_0 **(b)** determined from noise data from the three resonators (Fig. S1) fitted to the RTS model (Eq. 8). The horizontal dashed lines in (a) indicate the saturation $A \to A_0$, related to the minimum FWHM in Fig. 1(e–g); the diagonal lines in (a) indicate $1/\sqrt{\langle n \rangle}$ scaling (not a fit). The dashed lines in (b) are fits of τ_0 to the power law $(\langle n \rangle / n_c)^{-\alpha}$ (Eq. 1), with $\alpha = 1.1$. The fitted parameters are presented in Table II.

In Fig. 3(a), we see that A is initially power dependent, decreasing with increasing power. However, it saturates at high powers, starting at a photon number corresponding approximately to the coalescence of peaks in Fig. 1(b–d) ($\langle n \rangle \sim 0.1$ for the nanowire and 10^4 for the cavity; here we emphasise that the conversion from photon occupation to electric field is very different for each resonator). All three devices show this behaviour, although the amplitudes, saturation levels A_0 (see Table II), and the cross-over points vary.

Furthermore, as shown in Fig. 3(b), we find that the extracted τ_0 values of the three resonators follow an empirical power law

$$\tau_0(\langle n \rangle) = (1\,\mathrm{s}) \times (\langle n \rangle / n_c)^{-\alpha} \qquad (1)$$

where α is found close to 1.1 in all three resonators, and n_c is a "critical" photon number, unique for each device; see the fit parameters in Table II.

TABLE II. Fit parameters for the dominant RTS fluctuators' switching times τ_0 vs. drive power $\langle n \rangle$ (Eq. 1) and saturation values (A_0) of their amplitudes A for large $\langle n \rangle$, shown in Fig. 3. The FWHM values refer to the histograms in Fig. 1(e–g) at high power.

Device	RTS τ_0	RTS A
Nanowire	$\alpha = 1.1$	$A_0 = 2.8 \times 10^3$ Hz
	$n_c = 4.3 \times 10^{-2}$	FWHM $= 1.2 \times 10^4$ Hz
Coplanar	$\alpha = 1.1$	$A_0 = 1.6 \times 10^2$ Hz
	$n_c = 2.0 \times 10^2$	FWHM $= 2.7 \times 10^2$ Hz
Cavity	$\alpha = 1.1$	$A_0 = 2.5$ Hz
	$n_c = 1.1 \times 10^3$	FWHM $= 9.4$ Hz

III. DISCUSSION

The power dependence of the histogram width and the noise characteristics revealed by the Allan deviation can be understood in terms of motional narrowing by one or a few dominant RTS fluctuators. We now show how the resonator field can 'sympathetically' drive two-level defects in the surrounding dielectric in a regime that results in RTS noise with the required power dependence to explain the observations. This effect of sympathetic driving of the bath of defects and the resulting motional narrowing likely influences the power dependence in many superconducting devices.

A. Motional narrowing

Together, the plots in Fig. 1 highlight the power-dependent transition from multi-peaked behaviour at low circulating power in the resonator to single-peaked behaviour at high power. Additionally, as the power increases, the widths of the histograms narrow. Such behaviour is indicative of motional narrowing (motional averaging) [23], where a multi-level system transitions into a single-level system that also exhibits increased spectral stability. Motional narrowing is a common phenomenon that has been found in a wide variety of systems: NMR spectra [23, 31], ESR spectra [24], gamma emissions [25], superconducting qubits [32], and two-level NV-centre defects [33, 34]. However, despite the similarity between an NV centre and a parasitic TLS, motional narrowing has not been considered in the framework of dielectric loss, charge noise, or other TLS phenomena that manifest within superconducting circuits.

The observation of quasi-stable resonant frequencies is consistent with the model of a bath of spectrally unsta-

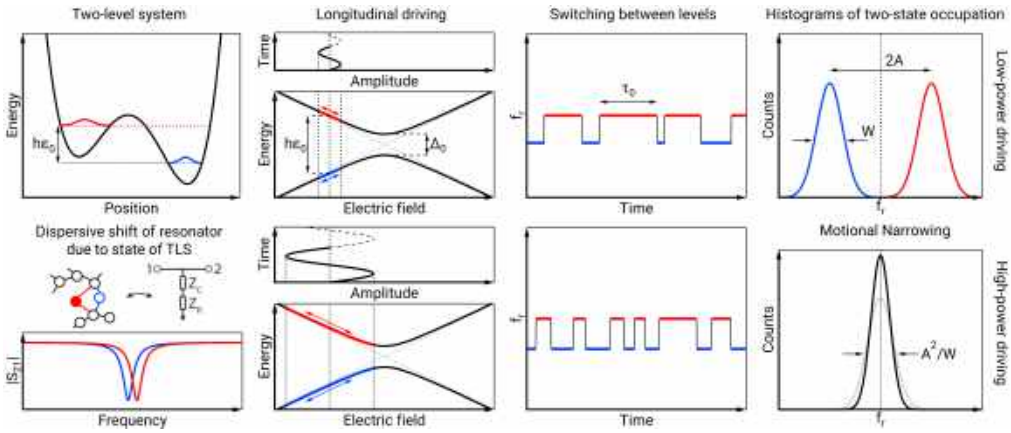

FIG. 4. An illustration of the relevant RTS switching regimes (high and low power driving) resulting from small and large-amplitude driving of a TLS about a bias point ε_0 near (but not at) its degeneracy point $\varepsilon = 0$. The resulting transitions between the two eigenstates of the TLS result in different dispersive shifts of the resonator, resulting in RTS fluctuations of the resonance frequency.

ble, charged TLS that are dispersively coupled to the resonator [7, 12, 35, 36]. In previous studies of resonators, the coupling to many TLS manifested as a $1/f$ noise spectrum [35, 37, 38]. Within studies on superconducting qubits, the coupling to TLS has been strong enough to result in an RTS noise spectrum [9, 13]. The RTS noise behaviour found here demonstrates a similarly strong coupling to single or few individual TLS.

Typically, in such a model of dispersively coupled (near-resonant) TLS, their dynamics are dominated by incoherent, low-frequency two-state fluctuators whose fluctuations dephase the TLS (widen its spectrum) or shift the TLS energy [11, 35, 36, 39]. This results in a $1/f$ noise spectrum which scales as approximately $1/\sqrt{\langle n\rangle}$. Here we see single- or few-RTS dynamics rather than $1/f$ noise, where the RTS amplitude scales as $1/\sqrt{\langle n\rangle}$ (Fig. 3(a)) up until some critical power, beyond which is becomes power independent. However, a very clear nearly $1/\langle n\rangle$ dependence of τ_0 (Fig. 3(b)) over all powers suggests that the switching rate requires a different interpretation.

To understand the ramifications of the observed power dependence, we consider an RTS system with only two states, at frequencies $\pm A$, with a characteristic switching rate between these states of W per unit time. For slow switching, $W \ll |A|$, the spectral response of the RTS signal consists of two peaks at frequencies $\pm A$ with a width (FWHM) given by W. In the opposite limit of strong driving, $W \gg |A|$, the resonance is a single peak centred at zero frequency with FWHM width A^2/W, which is narrower. Importantly, motional narrowing can extend beyond the simple two-state to one-state example that we have described [23]; in multiple-state examples [24, 25], multiple W and $\pm A$ exist, although the convergence towards a single narrow state still occurs in the strong driving limit [26, 27], which is the regime we focus on. The observation that $\tau_0 \propto 1/\langle n\rangle^{1.1}$ in the fast fluctuation limit therefore suggests that $W \propto \langle n\rangle^{1.1}$, and this observation is common across all three devices.

B. Landau–Zener transitions in the bath of TLS defects

In order to investigate the mechanism for modulation of the TLS defect by the resonator, and to explain the results presented above, we start from the assumption that the bath of fluctuators driving the RTS behaviour is described by the standard tunnelling model [7, 40], where each defect can be described by the TLS Hamiltonian

$$\hat{\mathcal{H}}_0 = (-h/2)(\varepsilon\hat{\sigma}_z + \Delta_0\hat{\sigma}_x) \tag{2}$$

as illustrated in Fig. 4. The tunnel coupling Δ_0 and bias ε vary from defect to defect and are a function of the local atomic environment. We assume that the electric field of the resonator couples to the defects via their charge dipole, i.e. longitudinally (along $\hat{\sigma}_z$) in the basis of uncoupled double wells. The bias is therefore comprised of a constant offset and a time dependent term,

$$\varepsilon(t) = \varepsilon_0 + \varepsilon_{\rm rf}\cos(2\pi f_r t), \tag{3}$$

where $\varepsilon_{\rm rf}$ has units of frequency but is proportional to the amplitude of the resonator electric field ($\propto\sqrt{\langle n\rangle}$), and hence to the radio-frequecy (rf) voltage at the source.

For low-loss devices, there are relatively few defects with values of Δ_0 close to the resonator frequency [12, 41]; however, that is not the parameter regime we are

considering. There are also TLS whose Δ_0 is relatively small, but whose equilibrium position (given by ε_0) is such that their eigenstates are nearly resonant with the resonator (see Fig. 4). For large resonator fields, the drive can sweep the fluctuator through the TLS anticrossing ($\varepsilon_{\rm rf} \approx \varepsilon_0$) or at least near it. We therefore need to consider the role of Landau-Zener (L-Z) tunnelling which can result in transitions between the ground and excited states of the TLS [42, 43].

We can rewrite the Hamiltonian (2) above in a time-dependent rotating frame to obtain

$$\hat{\mathcal{H}}_{RF} = (-h/2)(\delta\hat{\sigma}_{\tilde{z}} + \Delta_0 J_1(\lambda)\hat{\sigma}_{\tilde{x}}), \tag{4}$$

where $\delta = \varepsilon_0 - f_r$ is the detuning between drive and frequency splitting at the bias point $\varepsilon = \varepsilon_0$, $J_1(\lambda)$ is the first-order (one photon) Bessel function of the first kind, representing a dressed gap, and $\lambda = \varepsilon_{\rm rf}/f_r$ is the ratio of driving amplitude to driving frequency [42].

The relevant regime of L-Z driving of TLS in the dielectric of the resonators is that the effective transition rate W between states is less than the dephasing rate (Γ_2) but greater than the relaxation rate (Γ_1), i.e. $\Gamma_1 < W < \Gamma_2$. In this regime, at resonance ($\delta = 0$) in the small-amplitude drive limit ($\varepsilon_{\rm rf} \ll f_r$), the one-photon transition rate between the eigenstates is given by [44]

$$W(\lambda) = \frac{\pi^2}{2}\frac{\Delta_0^2\lambda^2}{\Gamma_2}. \tag{5}$$

Now, as there is little to no coherence between the two eigenstates, we can consider $W(\lambda)$ as the RTS switching rate, i.e., $\tau_0 = 1/W(\lambda)$, which means that $\tau_0 \propto 1/\varepsilon_{\rm rf}^2 \propto 1/\langle n\rangle$, where the proportionality constant (n_c in Eq. 1) is a product of three unknowns: the decoherence rate, the energy splitting, and the electric-field amplitude at the site of the TLS.

We note that our observed transition rate has a small additional contribution as the amplitude is increased (cf. the exponent $\alpha = 1.1$ in Eq. (1) found empirically for all three resonators). We may attribute this to the TLS having a sufficiently large response to the resonator field that higher photon number transitions are non-negligible.

The role of Landau–Zener driving of TLS in the dielectric of qubits and resonators has been previously studied [45–47]; however, in such experiments the mechanism is modulating the frequency splitting of near-resonant TLS as they traverse the resonator frequency, thereby driving non-adiabatic Landau–Zener transitions. The transitions we consider (away from the degeneracy point) influence the dephasing noise (i.e. the low-frequency, real part of the spectral function), similarly to Ref. [34], whereas Ref. [45] deals with the loss (i.e. the near-resonant, imaginary part leading to energy relaxation).

C. The role of the ensemble

While this picture explains the common response between devices and the power dependence of τ_0, it does not explain the low-power response of A_0 nor the 'more conventional' (but less universal) response of the FWHM. However, both can be explained in terms of the ensemble of RTS fluctuations stemming from multiple TLS. As the power is reduced, below the point of coalescence in the motional narrowing picture, the fit to a single RTS fluctuator no longer captures the key characteristics of the response. The contributions from both additional RTS sources and other noise processes start to dominate and this results in an additional power dependence to the noise amplitude. The diagonal lines in Fig. 3(a) represent a $1/\sqrt{\langle n\rangle}$ scaling, which one would typically expect for $1/f$ noise, indicating that at lower powers, the ensemble response is more dominant. Similarly, the extracted FWHM in Fig. 1(e–g) is a function of the entire spectrum, which includes both additional (non-TLS) processes and contributions due to the TLS-TLS interactions in the bath [36, 48–50]. As these contributions depend on the density and interaction strength between the TLS, they vary more between devices resulting in the differing power response; cf. Table S1 in Supplement.

IV. CONCLUSION

We have studied the frequency noise of three commonly used superconducting resonators within the same measurement and analysis infrastructure. We find that in all devices, the noise is described by an RTS process, which we attribute to spectrally unstable TLS. When studying the RTS behaviour with microwave drive power, we find that the switching times follow a common scaling across all types of resonators. We interpret the power dependence of the RTS switching times in terms of sympathetic driving of TLS defects by the resonator field. This driving induces Landau-Zener-type resonant transitions, even for TLS whose equilibrium configuration is relatively detuned from the degeneracy point between the two states.

Fundamentally, this highlights the power of standardised testing with common methods. Here, the ability to directly compare different types of superconducting resonator has revealed a commonality of the dominant noise process. These findings expand the toolkit and material parameter range for examining parameter fluctuations, which has become the leading problem in superconducting quantum-computing efforts. Furthermore, the studies of the nanowire superinductor are particularly relevant to the rapidly growing area of high-impedance qubits [19, 51–53].

V. METHODS

A. Device characteristics

The examined resonators have similar resonant frequencies, but otherwise have very different superconducting properties and microwave electric-field distributions. The superinductor consists of a disordered NbN nanowire with high kinetic inductance, and consequently high characteristic impedance Z_c, on a Si substrate. The coplanar waveguide resonator was made of Al on Si. The stub-geometry 3D cavity was machined out of 4N-grade Al. The device characteristics of the three resonators are summarised in Table I, and their designs and fabrication techniques are thoroughly described in the given references.

The internal quality factors, Q_i, of the nanowire and the coplanar waveguide were determined at an average photon occupation number of $\langle n\rangle = 1$, whereas that of the cavity was determined at $\langle n\rangle = 132$ (the lowest measured); in all cases, this photon occupation corresponds to when Q_i has saturated to a low level, consistent with the depolarization of two-level defects. We determine $\langle n\rangle$, knowing the applied drive power P and the Q_i at that power, $Q_i(P)$, using the relation

$$hf_r\langle n\rangle = Z_0 Q_l^2 P/\pi^2 Z_c Q_c f_r. \tag{6}$$

Here, h is Planck's constant, f_r is the resonant frequency, $Z_0 = 50\,\Omega$ is the impedance of the feedline, and Q_c and Q_l are the coupling and loaded quality factors, respectively, with $Q_l^{-1} = Q_c^{-1} + Q_i^{-1}(P)$.

B. Measurement techniques

The nanowire and coplanar resonators each exhibit a resonance dip due to coupling to a microwave transmission line. The use of a circulator at the cavity input leads to the cavity also exhibiting a resonance dip. The Pound frequency-locked loop (P-FLL) is locked to this resonance dip. We measure the resonant-frequency fluctuations by sampling the frequency of the P-FLL voltage-controlled oscillator using a frequency counter (Keysight 53230A) at a sampling rate of either 100 Hz or 4 kHz. Each noise trace consists of 1×10^6 samples. In addition, once per noise trace, the absolute frequency and microwave power of the signal going into the cryostat are measured with a spectrum analyzer (Agilent E4440A). During a measurement, the cryostat temperature is held constant and noise traces are recorded at various inbound microwave powers. A detailed description of these measurement techniques is found in Refs. [19, 54].

C. Spectral and Allan analysis of fluctuations

The same raw frequency fluctuations data is used to produce the spectrum of frequency fluctuations $S_y(f)$, using the Welch power spectral density (PSD) estimate with 50% overlap and a Hamming window, and the overlapping Allan deviation $\sigma_y(\tau)$. A detailed description of this data analysis technique is given in Refs. [9, 55].

The spectral response of a single RTS fluctuator is given by

$$S_y(f) = \frac{4A^2\tau_0}{1 + (2\pi f\tau_0)^2} \tag{7}$$

where A and τ_0 denote the RTS amplitude and characteristic time, respectively. The corresponding Allan deviation is given by Ref. [29]:

$$\sigma_y(\tau) = \frac{A\tau_0}{\tau}\left(4e^{-\tau/\tau_0} - e^{-2\tau/\tau_0} + 2\frac{\tau}{\tau_0} - 3\right)^{1/2} \tag{8}$$

A key strength of the Allan analysis is that it often allows the identification of τ_0 against the noise background, although we use the same parameters when fitting $S_y(f)$ and $\sigma_y(\tau)$.

D. Estimate of errors

In the determination of τ_0 and A (circles in Fig. 3), we estimate the two standard deviations error to be about 4% (10%) for τ_0 (for A) for the coplanar and cavity resonators, and for the nanowire resonator at high powers. For the low-power data of the nanowire resonator, we estimate about a factor of two error in both τ_0 and A. The collection of longer sets of data would reduce the error.

ACKNOWLEDGEMENTS

We gratefully acknowledge useful discussions with A. Danilov, P. Delsing, and S. Kubatkin. This research has been supported by funding from the Swedish Research Council, Chalmers Area of Advance Nanotechnology, and the Wallenberg Center for Quantum Technology (WACQT). JHC is supported by the Australian Research Council Centre of Excellence program through Grant number CE170100026 and the Australian National Computational Infrastructure facility. JJB acknowledges financial support from the Industrial Strategy Challenge Fund Metrology Fellowship as part of the UK governments Department for Business, Energy and Industrial Strategy.

[1] J. Zmuidzinas, Annu. Rev. Condens. Matter Phys. **3**, 169 (2012).

[2] C. McRae, H. Wang, J. Gao, M. Vissers, A. Dunsworth, D. Pappas, and J. Mutus, arXiv:2006.04718 (2020).

[3] X. Gu, A. F. Kockum, A. Miranowicz, Y. xi Liu, and F. Nori, Physics Reports **718-719**, 1 (2017).

[4] J. Aumentado, IEEE Microwave Magazine **21**, 45 (2020).

[5] A. Romanenko and D. I. Schuster, Phys. Rev. Lett. **119**, 264801 (2017).

[6] A. Romanenko, R. Pilipenko, S. Zorzetti, D. Frolov, M. Awida, S. Belomestnykh, S. Posen, and A. Grassellino, Phys. Rev. Appl. **13**, 034032 (2020).

[7] C. Müller, J. H. Cole, and J. Lisenfeld, Rep. Prog. Phys. **82**, 124501 (2019).

[8] F. Yan, S. Gustavsson, A. Kamal, J. Birenbaum, A. P. Sears, D. Hover, T. J. Gudmundsen, D. Rosenberg, G. Samach, S. Weber, *et al.*, Nature communications **7**, 1 (2016).

[9] J. J. Burnett, A. Bengtsson, M. Scigliuzzo, D. Niepce, M. Kudra, P. Delsing, and J. Bylander, npj Quantum Inf. **5**, 54 (2019).

[10] A. Bruno, G. de Lange, S. Asaad, K. L. van der Enden, N. K. Langford, and L. DiCarlo, Appl. Phys. Lett. **106**, 182601 (2015).

[11] C. Müller, J. Lisenfeld, A. Shnirman, and S. Poletto, Phys. Rev. B **92**, 035442 (2015).

[12] P. V. Klimov, J. Kelly, Z. Chen, M. Neeley, A. Megrant, B. Burkett, R. Barends, K. Arya, B. Chiaro, Y. Chen, A. Dunsworth, A. Fowler, B. Foxen, C. Gidney, M. Giustina, R. Graff, T. Huang, E. Jeffrey, E. Lucero, J. Y. Mutus, O. Naaman, C. Neill, C. Quintana, P. Roushan, D. Sank, A. Vainsencher, J. Wenner, T. C. White, S. Boixo, R. Babbush, V. N. Smelyanskiy, H. Neven, and J. M. Martinis, Phys. Rev. Lett. **121**, 090502 (2018).

[13] S. Schlör, J. Lisenfeld, C. Müller, A. Bilmes, A. Schneider, D. P. Pappas, A. V. Ustinov, and M. Weides, Phys. Rev. Lett. **123**, 190502 (2019).

[14] P. V. Klimov, J. Kelly, J. M. Martinis, and H. Neven, arXiv:2006.04594 (2020).

[15] R. Barends, J. Wenner, M. Lenander, Y. Chen, R. C. Bialczak, J. Kelly, E. Lucero, P. O'Malley, M. Mariantoni, D. Sank, H. Wang, T. C. White, Y. Yin, J. Zhao, A. N. Cleland, J. M. Martinis, and J. J. A. Baselmans, Appl. Phys. Lett. **99**, 113507 (2011).

[16] C. M. Quintana, A. Megrant, Z. Chen, A. Dunsworth, B. Chiaro, R. Barends, B. Campbell, Y. Chen, I.-C. Hoi, E. Jeffrey, J. Kelly, J. Y. Mutus, P. J. J. O'Malley, C. Neill, P. Roushan, D. Sank, A. Vainsencher, J. Wenner, T. C. White, A. N. Cleland, and J. M. Martinis, Appl. Phys. Lett. **105**, 062601 (2014).

[17] L. Grünhaupt, N. Maleeva, S. T. Skacel, M. Calvo, F. Levy-Bertrand, A. V. Ustinov, H. Rotzinger, A. Monfardini, G. Catelani, and I. M. Pop, Phys. Rev. Lett. **121**, 117001 (2018).

[18] W. Zhang, K. Kalashnikov, W.-S. Lu, P. Kamenov, T. DiNapoli, and M. E. Gershenson, Phys. Rev. Appl. **11**, 011003 (2019).

[19] D. Niepce, J. Burnett, and J. Bylander, Phys. Rev. Appl. **11**, 044014 (2019).

[20] M. Kudra, J. Biznárová, A. F. Roudsari, J. J. Burnett, D. Niepce, S. Gasparinetti, B. Wickman, and P. Delsing, arXiv.org (2020), 2006.02213.

[21] D. Niepce, J. J. Burnett, M. G. Latorre, and J. Bylander, Supercond. Sci. Technol. **33**, 025013 (2020).

[22] M. Reagor, H. Paik, G. Catelani, L. Sun, C. Axline, E. Holland, I. M. Pop, N. A. Masluk, T. Brecht, L. Frunzio, M. H. Devoret, L. Glazman, and R. J. Schoelkopf, Appl. Phys. Lett. **102**, 192604 (2013).

[23] A. Abragam, *Principles of Nuclear Magnetism* (Oxford University Press, 1961) p. 447.

[24] P. P. Borbat, A. J. Costa-Filho, K. A. Earle, J. K. Moscicki, and J. H. Freed, Science **291**, 266 (2001).

[25] G. J. Perlow, Phys. Rev. **172**, 319 (1968).

[26] A. Berthelot, I. Favero, G. Cassabois, C. Voisin, C. Delalande, P. Roussignol, R. Ferreira, and J. M. Gérard, Nat. Phys. **2**, 759 (2006).

[27] C. G., "Spectral diffusion dephasing and motional narrowing in single semiconductor quantum dots," in *Optical Generation and Control of Quantum Coherence in Semiconductor Nanostructures*, NanoScience and Technology, Vol. 0, edited by G. Slavcheva and P. Roussignol (Springer, Berlin, Heidelberg, 2010) pp. 25–35.

[28] J. Burnett, A. Bengtsson, D. Niepce, and J. Bylander, J. Phys. Conf. Ser. **969**, 012131 (2018).

[29] C. M. Van Vliet and P. H. Handel, Physica A **113**, 261 (1982).

[30] C. D. Nugroho, V. Orlyanchik, and D. J. Van Harlingen, Appl. Phys. Lett. **102**, 142602 (2013).

[31] T. Kohmoto, Y. Fukuda, M. Kunitomo, K. Ishikawa, M. Tanigawa, K. Ebina, and M. Kaburagi, Phys. Rev. B **49**, 15352 (1994).

[32] J. Li, M. P. Silveri, K. S. Kumar, J.-M. Pirkkalainen, A. Vepsäläinen, W. C. Chien, J. Tuorila, M. A. Sillanpää, P. J. Hakonen, E. V. Thuneberg, and G. S. Paraoanu, Nat. Commun. **4**, 1 (2013).

[33] L. Jiang, M. V. G. Dutt, E. Togan, L. Childress, P. Cappellaro, J. M. Taylor, and M. D. Lukin, Phys. Rev. Lett. **100**, 073001 (2008).

[34] D. Bluvstein, Z. Zhang, C. A. McLellan, N. R. Williams, and A. C. B. Jayich, Phys. Rev. Lett. **123**, 146804 (2019).

[35] J. Burnett, L. Faoro, I. Wisby, V. L. Gurtovoi, A. V. Chernykh, G. M. Mikhailov, V. A. Tulin, R. Shaikhaidarov, V. Antonov, P. J. Meeson, A. Ya. Tzalenchuk, and T. Lindström, Nat. Commun. **5**, 4119 (2014).

[36] L. Faoro and L. B. Ioffe, Phys. Rev. B **91**, 014201 (2015).

[37] C. Neill, A. Megrant, R. Barends, Y. Chen, B. Chiaro, J. Kelly, J. Y. Mutus, P. J. J. O'Malley, D. Sank, J. Wenner, T. C. White, Y. Yin, A. N. Cleland, and J. M. Martinis, Appl. Phys. Lett. **103**, 072601 (2013).

[38] S. E. de Graaf, L. Faoro, J. Burnett, A. A. Adamyan, A. Ya. Tzalenchuk, S. E. Kubatkin, T. Lindström, and A. V. Danilov, Nat. Commun. **9**, 1143 (2018).

[39] C. Müller, A. Shnirman, and Y. Makhlin, Phys. Rev. B **80**, 134517 (2009).

[40] W. A. Phillips, Rep. Prog. Phys. **50**, 1657 (1987).

[41] J. Lisenfeld, G. J. Grabovskij, C. Müller, J. H. Cole, G. Weiss, and A. V. Ustinov, Nat. Commun. **6**, 1 (2015).

[42] W. D. Oliver and S. O. Valenzuela, Quantum Information Processing **8**, 261 (2009).

[43] W. D. Oliver, Y. Yu, J. C. Lee, K. K. Berggren, L. S. Levitov, and T. P. Orlando, Science **310**, 1653 (2005).
[44] D. M. Berns, W. D. Oliver, S. O. Valenzuela, A. V. Shytov, K. K. Berggren, L. S. Levitov, and T. P. Orlando, Phys. Rev. Lett. **97**, 150502 (2006).
[45] S. Matityahu, H. Schmidt, A. Bilmes, A. Shnirman, G. Weiss, A. V. Ustinov, M. Schechter, and J. Lisenfeld, npj Quantum Information **5**, 114 (2019).
[46] A. L. Burin, M. S. Khalil, and K. D. Osborn, Phys. Rev. Lett. **110**, 157002 (2013).
[47] M. S. Khalil, S. Gladchenko, M. J. A. Stoutimore, F. C. Wellstood, A. L. Burin, and K. D. Osborn, Phys. Rev. B **90**, 100201 (2014).
[48] L. Faoro and L. B. Ioffe, Phys. Rev. Lett. **109**, 157005 (2012).
[49] N. Kirsh, E. Svetitsky, A. L. Burin, M. Schechter, and N. Katz, Phys. Rev. Materials **1**, 012601 (2017).
[50] A. L. Burin and A. O. Maksymov, Phys. Rev. B **97**, 214208 (2018).
[51] L. Grünhaupt, M. Spiecker, D. Gusenkova, N. Maleeva, S. T. Skacel, I. Takmakov, F. Valenti, P. Winkel, H. Rotzinger, W. Wernsdorfer, A. V. Ustinov, and I. M. Pop, Nat. Mater. , 1 (2019).
[52] L. B. Nguyen, Y.-H. Lin, A. Somoroff, R. Mencia, N. Grabon, and V. E. Manucharyan, Physical Review X **9**, 041041 (2019).
[53] T. Hazard, A. Gyenis, A. Di Paolo, A. Asfaw, S. A. Lyon, A. Blais, and A. A. Houck, Physical review letters **122**, 010504 (2019).
[54] T. Lindström, J. Burnett, M. Oxborrow, and A. Ya. Tzalenchuk, Rev. Sci. Instrum. **82**, 104706 (2011).
[55] E. Rubiola, *Phase Noise and Frequency Stability in Oscillators* (Cambridge University Press, 2008).

Supplemental Material

SI. SPECTRAL AND ALLAN ANALYSIS OF THE FLUCTUATIONS DATA VS. POWER FOR ALL THREE RESONATORS

For completeness, here we include the calculated PSD and Allan deviations for all measured powers of each device. In Fig. S1, the top row shows the calculated PSD, and the bottom row shows the calculated overlapping Allan deviation. The functional form of the RTS feature was shown in Fig. 2 in the main text. Here, the RTS switching time is clearly shown to move towards higher times as the microwave amplitude is decreased.

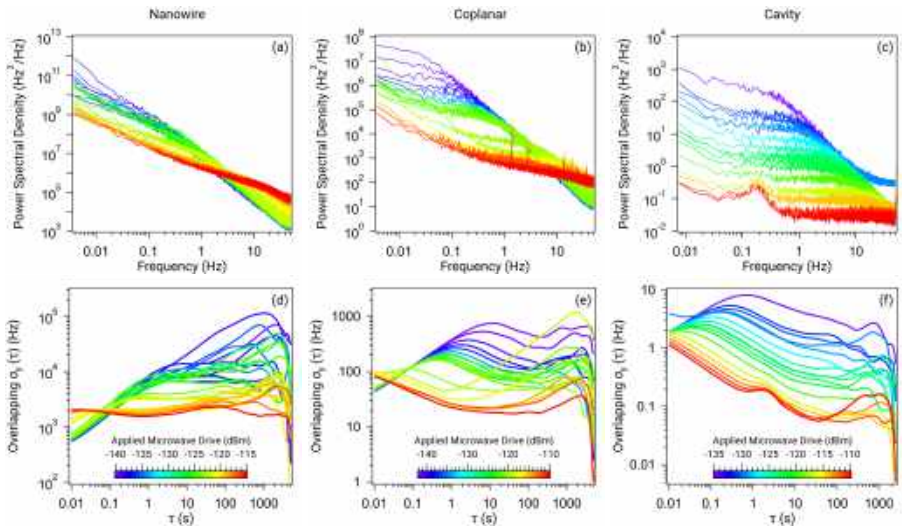

FIG. S1. Noise analysis vs.applied power for the three resonators. Plots **(a–c)** show the Welch power spectral densities, and plots **(d–f)** show the overlapping Allan deviations of the frequency fluctuations, for various applied powers. All the data was measured at $T = 10\,\mathrm{mK}$ and a sampling rate of 100 Hz. We observe that all three devices present similar noise profiles—featuring one dominant Lorentzian—albeit at widely different amplitudes: the nanowire is the noisiest and the cavity is the quietest. As the microwave drive is increased, we observe that the dominant Lorentzian feature in the PSD (Allan) is consistently moving toward higher frequencies (lower τ) for all devices. The cavity resonator frequency is so stable that at high power, its noise falls below that of the reference of our frequency-locked loop, which shows up as an additional peak in the PSD at around 0.2 Hz.

SII. POWER DEPENDENCE OF THE RESONATOR RESPONSE WIDTH

A key method for understanding the influence of decoherence mechanisms in superconducting devices is to map the power dependence of their response. The standard tunnelling model predicts that the Q factor of a resonator scales as $\sqrt{1+\langle n\rangle/n_c}$, for some critical photon number n_c; however, variations from this scaling are often seen in experiments. Therefore, several authors have fitted the power dependence of Q to $\sqrt{1+(\langle n\rangle/n_c)^{\beta}}$, where $\beta = 1$ corresponds to the STM prediction, but typically $\beta < 1$ is observed [S1–S6, S20]. Deviations from the STM-predicted scaling have been interpreted as evidence for TLS-TLS interactions [S4, S8–S11], in which case such variations between devices would be considered unsurprising. However, in this experiment, it is the frequency jitter that is measured, not the Q factor, and so it is unclear if one would expect a similar response, although the $1/f$ noise has been found to scale with the loss tangent (i.e. with $1/\sqrt{1+\langle n\rangle/n_c}$) [S4, S9]. To compare to previous work on Q factors, we use a similar power-law expression to fit to the FWHM of the histograms in Fig. 1(e-g), namely $F_0 + F_1/\langle n\rangle^{\beta}$. The resulting fit values are given in Table S1, showing typical values $0.5 < \beta < 1$, but which vary from device to device. Such variation between devices is considered 'normal' in the literature and serves to highlight how surprisingly similar the scaling of the single-RTS switching rate (Fig. 3(b)), revealed by the Allan analysis, is across all three devices measured.

TABLE S1. Fitting parameters for Fig. 1(e–g).

Device	F_0 (Hz)	F_1 (Hz)	β
Nanowire	1.3×10^4	5.5×10^3	0.58
Coplanar	4.2×10^2	6.4×10^4	0.82
Cavity	2.6	1.2×10^3	0.63

[S1] P. Macha, S. H. W. van der Ploeg, G. Oelsner, E. Il'ichev, H.-G. Meyer, S. Wünsch, and M. Siegel, Appl. Phys. Lett. **96**, 062503 (2010).

[S2] D. S. Wisbey, J. Gao, M. R. Vissers, F. C. S. da Silva, J. S. Kline, L. Vale, and D. P. Pappas, J. Appl. Phys. **108**, 093918 (2010).

[S3] H. Paik and K. D. Osborn, Appl. Phys. Lett. **96**, 072505 (2010).

[S4] J. Burnett, L. Faoro, I. Wisby, V. L. Gurtovoi, A. V. Chernykh, G. M. Mikhailov, V. A. Tulin, R. Shaikhaidarov, V. Antonov, P. J. Meeson, A. Ya. Tzalenchuk, and T. Lindström, Nat. Commun. **5**, 4119 (2014).

[S5] J. Burnett, J. Sagar, O. W. Kennedy, P. A. Warburton, and J. C. Fenton, Phys. Rev. Appl. **8**, 014039 (2017).

[S6] A. Romanenko and D. I. Schuster, Phys. Rev. Lett. **119**, 264801 (2017).

[S7] M. Kudra, J. Biznárová, A. F. Roudsari, J. J. Burnett, D. Niepce, S. Gasparinetti, B. Wickman, and P. Delsing, arXiv.org (2020), 2006.02213.

[S8] L. Faoro and L. B. Ioffe, Phys. Rev. Lett. **109**, 157005 (2012).

[S9] L. Faoro and L. B. Ioffe, Phys. Rev. B **91**, 014201 (2015).

[S10] N. Kirsh, E. Svetitsky, A. L. Burin, M. Schechter, and N. Katz, Phys. Rev. Materials **1**, 012601 (2017).

[S11] A. L. Burin and A. O. Maksymov, Phys. Rev. B **97**, 214208 (2018).

Paper D

Noise and Loss of Superconducting Aluminium Resonators at Single Photon Energies

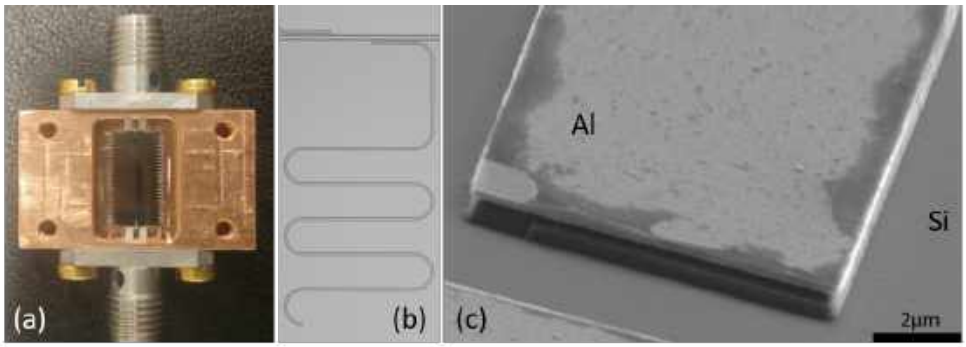

Figure 1. (a) An optical photograph of a copper sample enclosure, with sample in the centre. **(b)** An optical photograph of a $\lambda/4$ resonator, capacitively coupled to a microwave transmission line. The Si substrate is shown by the darker gray tone, while the Al superconductor is shown by the lighter gray tone. The ground plane contains holes for flux trapping. **(c)** A scanning electron micrograph of the open end of the central conductor of the resonator. The image is taken at an angle to demonstrate the trenching of the Si substrate.

In principle, these would be most directly found by performing noise measurements at single photon energies. However, to date noise studies have proved non trivial to perform for fewer than 10 photons in the resonator [16–18, 22].

Here, we study the loss and noise of a superconducting aluminium $\lambda/4$ resonator. We demonstrate a level of loss which is comparable to the literature. We then study the noise of this resonator at single photon energies. This opens up the possibility of directly measuring noise in superconducting qubits as well as further examining the nature of interacting TLS which are the limiting factor for many quantum circuits.

2. Sample details

Fabrication of the device begins with a solvent clean of a high resistivity silicon wafer. Following this, the wafer is submerged in a 2% hydrofluoric acid bath to remove the native surface oxide and passivate the surface with hydrogen. Within 3 minutes, the wafer is placed under vacuum inside the load lock of a Plassys MEB deposition system. The wafer is then heated to 300^{o}C while the vacuum chamber pumps. Once the wafer has cooled to room temperature and a base pressure of 1.1x10^{-7} mbar is reached, 150 nm of Al is deposited at a rate of 0.5 nm/s. Next, the vacuum chamber is filled to 10 mbar of 99.99% pure molecular oxygen for 10 minutes, after this the chamber vented to atmosphere. A 1.2 μm thick layer of AZ1512HS photoresist is then patterned by direct-write laser lithography to realise the microwave circuitry. The photoresist is developed in AZ developer diluted with H_2O 1:1, which minimises the parasitic etching of aluminium. This pattern is transferred into the Al film by a wet etch in a mixture of phosphoric, nitric, and acetic acids. Then, a reactive ion etch using an inductively coupled NF_3 plasma was used to isotropically etch the Si substrate, forming a 1 μm deep trench with a 400 nm undercut below the Al features. After dicing, the resulting chip is cleaned using hot solvents, then wirebonded within a light-tight connectorised copper sample enclosure (shown in Fig. 1a). This sample enclosure is then placed on a gold-plated copper cold finger at the 9.5 mK stage of a dilution refrigerator. A photograph of a typical microwave resonator, and a SEM image of an etched area, are shown in Fig. 1 b and c, respectively. The black residues close to the aluminium edge are indicative of burnt resist from the RIE process. This is supported by samples that only had

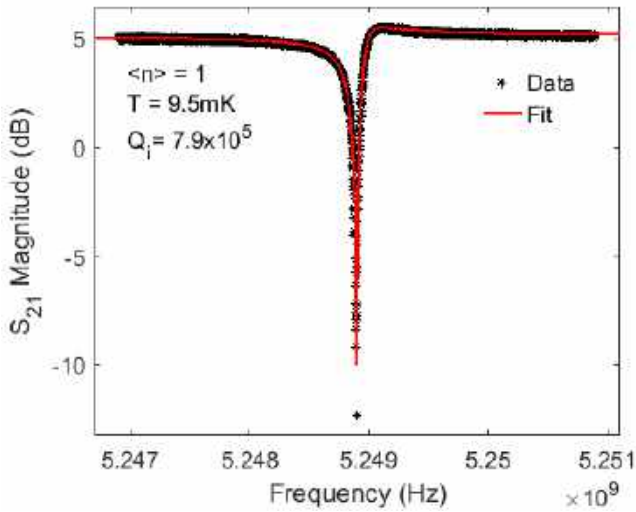

Figure 2. Plot of the S_{21} magnitude response of the superconducting resonator. In red is a fit to the data which extracts the resonator parameters. The measurement was performed at 9.5 mK, with P_{app} = -146 dBm, which corresponds to $\langle n \rangle = 1$.

a wet etch not showing these residues.

3. Dielectric loss measurements

The S_{21} transmission response of the superconducting resonator is measured at 9.5 mK while the microwave power is varied. A traceable fit routine [23] is used to extract the resonant frequency (ω_0), internal quality factor (Q_{i}) and coupling quality factor (Q_{c}). Figure 2 shows the fitted S_{21} magnitude response of the resonator at 9.5 mK. For an applied microwave power (P_{app}) of -146 dBm, this reveals $\omega_0/2\pi$ = 5.24889 GHz, $Q_{\mathrm{c}} = 33{\times}10^3$ and $Q_{\mathrm{i}} = 7.9{\times}10^5$. As P_{app} is changed, Q_{i} is found to vary due to depolarisation of TLS [2–5, 16–18]. The average number of photons within the resonator ($\langle n \rangle$) varies with P_{app} as [5]

$$\langle n \rangle = \frac{\langle E_{\mathrm{int}} \rangle}{\hbar\omega_0} = \frac{2}{\hbar\omega_0^2}\frac{Z_0}{Z_{\mathrm{r}}}\frac{Q_{\mathrm{l}}^2}{Q_{\mathrm{c}}}P_{\mathrm{app}} \tag{1}$$

where Z_0 is the characteristic impedance ($Z_0 = 50\Omega$), Z_r is the resonator impedance (Z_r is chosen to be close to 50Ω), $\langle E_{\mathrm{int}} \rangle$ is the average energy stored within the resonator and Q_{l} is the loaded quality factor ($1/Q_{\mathrm{l}} = 1/Q_{\mathrm{c}} + 1/Q_{\mathrm{i}}$). Figure 3 shows the effect of TLS depolarisation in a measurement of Q_{i} as a function of $\langle n \rangle$. This TLS depolarisation can be fit to a TLS-based loss model [17]

$$\frac{1}{Q_{\mathrm{i}}} = F\delta_{\mathrm{TLS}}^0 \frac{\tanh\left(\frac{\hbar\omega_0}{2k_BT}\right)}{\left(1+\left(\frac{\langle n \rangle}{n_c}\right)\right)^{\beta}} + \delta_{\mathrm{other}} \tag{2}$$

where F is the filling factor describing the ratio of E-field in the TLS host volume to the total volume. $\delta_{\mathrm{TLS}}^0 = 1/Q_{\mathrm{TLS}}$ is the TLS loss tangent, n_c is the critical number of photons within

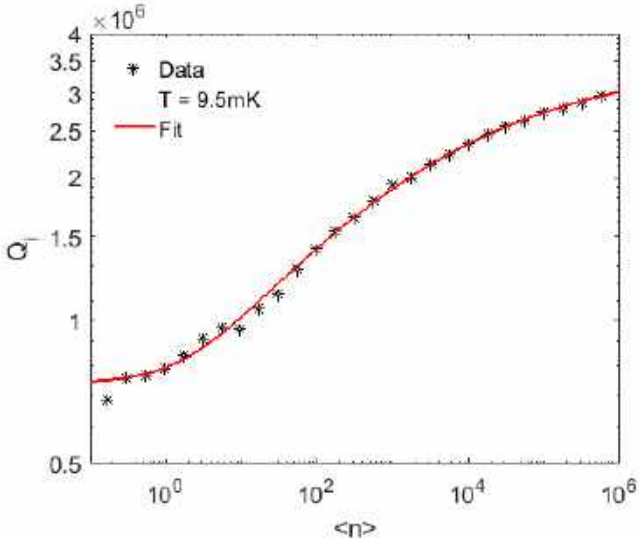

Figure 3. Plot of Q_i as a function of $\langle n \rangle$ for the resonator at 9.5 mK. In red is a fit to TLS losses described by Eq. (2).

the resonator to generate the E-field required to saturate one TLS. δ_other is the contribution from non-TLS loss mechanisms, which are generally associated with loss at high microwave drives. A fit to Eq. (2) is shown in Fig. 3. This shows $\delta_\mathrm{other} \approx 1/(3.5{\times}10^6)$, while indicating that $F\delta^0_\mathrm{TLS} \approx 1/(8.7{\times}10^5)$. Both of these loss rates are comparable with those found for the best Al resonators [3]. Further improvements to δ_other are possible by improving the infrared filtering [24] or the magnetic screening [6]. While further improvements to δ^0_TLS are also possible with either increased trenching of the substrate [4,5] or by cleaning of resist residues [25] which are found in Fig. 1c.

4. Noise measurements

The loss induced by the TLS corresponds to the resonant absorption of microwave photons. Recent experiments have examined the role of these resonant TLS in contributing noise to the resonator [16, 22]. The dependence of TLS-induced noise has been measured as a function of P_app and temperature. Within these studies, the temperature dependence has been thoroughly examined in the range of 50–700 mK. However, the span of P_app that was examined corresponds to $\langle n \rangle = 7$–10^4. Consequently, the TLS noise in the limit of single-photon excitation has not been examined. Not only is this limit most relevant to dephasing in superconducting qubits, but it is also relevant to revealing properties of TLS in general.

A Pound setup is used to form a frequency locked loop which can continuously monitor $\omega_0(t)$. The Pound setup we use is identical to one previously used in the study of low frequency noise in superconducting resonators [16,26,27]. Here, the Pound setup is operated with a low bandwidth of 300 Hz. This improves the signal-to-noise, enabling the Pound setup to monitor a resonator at single photon energies. However, the low bandwidth means that this setup is only suitable for studying 'slow' fluctuations. Figure 4a shows a 500 s window of a measurement of the frequency jitter of the resonator, measured at $\langle n \rangle = 1$ and 9.5 mK. This frequency jitter can be better understood by examining the spectrum of frequency fluctuations (S_y). This is obtained using

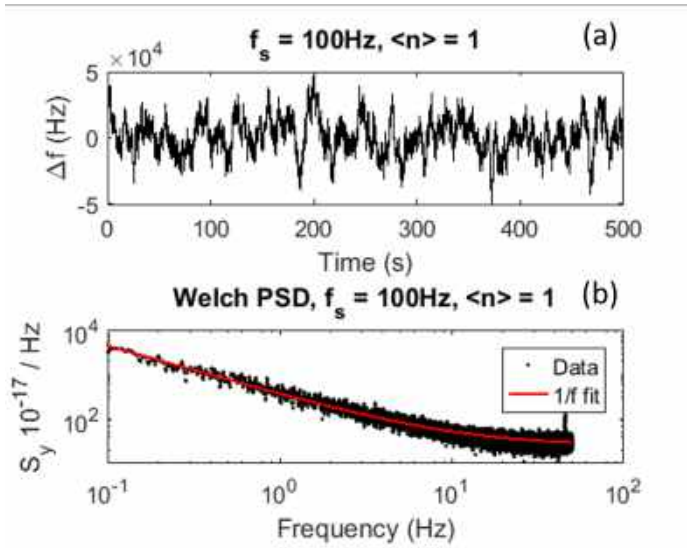

Figure 4. (a) A plot of the raw frequency jitter of the resonator measured at $\langle n \rangle = 1$ and at a temperature of 9.5 mK. **(b)** A plot of the spectrum of fractional frequency fluctuations (S_Y). In red is a fit to a $1/f$ noise model shown in Eq. (3).

the Welch spectral density estimate with a 50% overlap and a Hanning window. The resulting plot of S_y is shown in Fig. 4b; this data is fit to a general noise model

$$S_y(f) = \frac{h_{-1}}{f^{\alpha}} + h_0 \tag{3}$$

where h_0 is a white frequency noise level, h_{-1} is a flicker frequency noise level and α is an exponent describing the strength of low frequency noise components. When $\alpha = 1$, the first term represents a true flicker noise process. From this fit we find that the white noise level is described by $h_0 = 2.5{\times}10^{-16}$, while the flicker noise level is described by $\alpha = 1.05$ and $h_{-1} = 3.5{\times}10^{-15}$. This level of noise is larger than that previously observed [16–18]. However, since we measure at both lower microwave powers and at lower temperatures, this is expected from the strong power and temperature dependence of dielectric noise [20].

5. Summary

In summary, we measured frequency noise of a high-Q superconducting resonator at single photon energies. This is an important step towards studies of the interacting nature of TLS, which are currently limiting the performance of many superconducting circuits. In showing that noise can be measured at single photon energies, the technique could be extended to the circuit-QED architecture. Here, a superconducting qubit in the dispersive regime shifts the resonator frequency with $\chi = -g^2/\Delta$, where g is the qubit–resonator coupling and Δ is the frequency detuning between the qubit and the resonator. The frequency shift implies that any noise of the qubit frequency will get mapped to a frequency noise of the resonator. For normal values of g and Δ the effective noise of the resonator will be between 0.01 and 0.001 times than that of the qubit. This gives a straightforward method to measure flux noise of qubits by measuring

the frequency noise of the resonator, without needing to use advanced pulse sequences [28, 29]. It is important to point out that such measurement should be performed at sub single photon levels in the resonator, to avoid additional noise due to the AC-stark effect [30]. To have a stable locking of the Pound loop at such low energies, a parametric amplifier between the sample and the semiconductor amplifier, would be needed. We believe that this technique could lead to more efficient investigations of the origins of flux noise in superconducting circuits [31–33].

Acknowledgments
We acknowledge fruitful discussions with Andrey Danilov and the mechanical work from Lars Jönsson. Financial support came from the Knut and Alice Wallenberg foundation, and the Swedish research council.

[1] A. Dunsworth *et al.*, arXiv preprint arXiv:1706.00879 (2017).
[2] J. M. Sage, V. Bolkhovsky, W. D. Oliver, B. Turek, and P. B. Welander, Journal of Applied Physics **109**, 063915 (2011).
[3] A. Megrant *et al.*, Applied Physics Letters **100**, 113510 (2012).
[4] M. Sandberg *et al.*, Applied Physics Letters **100**, 262605 (2012).
[5] A. Bruno *et al.*, Applied Physics Letters **106**, 182601 (2015).
[6] B. Chiaro *et al.*, Superconductor Science and Technology **29**, 104006 (2016).
[7] J. Wenner *et al.*, Superconductor Science and Technology **24**, 065001 (2011).
[8] I. Nsanzineza and B. L. T. Plourde, Phys. Rev. Lett. **113**, 117002 (2014).
[9] C. Müller, J. H. Cole, and J. Lisenfeld, arXiv preprint arXiv:1705.01108 (2017).
[10] A. Romanenko and D. I. Schuster, arXiv preprint arXiv:1705.05982 (2017).
[11] J. Lisenfeld *et al.*, Nature Communications **6**, 6182 (2015).
[12] W. Arnold and S. Hunklinger, Solid State Communications **17**, 883 (1975).
[13] D. J. Salvino, S. Rogge, B. Tigner, and D. D. Osheroff, Phys. Rev. Lett. **73**, 268 (1994).
[14] H. M. Carruzzo, E. R. Grannan, and C. C. Yu, Phys. Rev. B **50**, 6685 (1994).
[15] A. L. Burin, Journal of Low Temperature Physics **100**, 309 (1995).
[16] J. Burnett *et al.*, Nature Communications **5**, 4119 (2014).
[17] J. Burnett, L. Faoro, and T. Lindström, Superconductor Science and Technology **29**, 044008 (2016).
[18] A. Ramanayaka, B. Sarabi, and K. Osborn, arXiv preprint arXiv:1507.06043 (2015).
[19] L. Faoro and L. B. Ioffe, Physical Review Letters **109**, 157005 (2012).
[20] L. Faoro and L. B. Ioffe, Physical Review B **91**, 014201 (2015).
[21] C. Müller, J. Lisenfeld, A. Shnirman, and S. Poletto, Phys. Rev. B **92**, 035442 (2015).
[22] C. Neill *et al.*, Applied Physics Letters **103**, 072601 (2013).
[23] S. Probst, F. Song, P. Bushev, A. Ustinov, and M. Weides, Review of Scientific Instruments **86**, 024706 (2015).
[24] R. Barends *et al.*, Applied Physics Letters **99**, 113507 (2011).
[25] C. Quintana *et al.*, Applied Physics Letters **105**, 062601 (2014).
[26] T. Lindström, J. Burnett, M. Oxborrow, and A. Y. Tzalenchuk, Review of Scientific Instruments **82**, 104706 (2011).
[27] J. Burnett *et al.*, Physical Review B **87**, 140501 (2013).
[28] J. Bylander *et al.*, Nature Physics **7**, 565 (2011).
[29] F. Yan *et al.*, Phys. Rev. B **85**, 174521 (2012).
[30] D. I. Schuster *et al.*, Nature **445**, 515 (2007).
[31] P. Kumar *et al.*, Physical Review Applied **6**, 041001 (2016).
[32] S. de Graaf *et al.*, Physical Review Letters **118**, 057703 (2017).
[33] C. Quintana *et al.*, Physical Review Letters **118**, 057702 (2017).

Paper E

Decoherence Benchmarking of Superconducting Qubits

npj | Quantum Information

www.nature.com/npjqi

Corrected: Publisher Correction

ARTICLE OPEN

Decoherence benchmarking of superconducting qubits

Jonathan J. Burnett[1,2], Andreas Bengtsson[1], Marco Scigliuzzo[1], David Niepce[1], Marina Kudra[1], Per Delsing[1] and Jonas Bylander[1]

We benchmark the decoherence of superconducting transmon qubits to examine the temporal stability of energy relaxation, dephasing, and qubit transition frequency. By collecting statistics during measurements spanning multiple days, we find the mean parameters $\overline{T_1} = 49$ µs and $\overline{T_2^*} = 95$ µs; however, both of these quantities fluctuate, explaining the need for frequent re-calibration in qubit setups. Our main finding is that fluctuations in qubit relaxation are local to the qubit and are caused by instabilities of near-resonant two-level-systems (TLS). Through statistical analysis, we determine sub-millihertz switching rates of these TLS and observe the coherent coupling between an individual TLS and a transmon qubit. Finally, we find evidence that the qubit's frequency stability produces a 0.8 ms limit on the pure dephasing which we also observe. These findings raise the need for performing qubit metrology to examine the reproducibility of qubit parameters, where these fluctuations could affect qubit gate fidelity.

npj Quantum Information (2019)5:54 ; https://doi.org/10.1038/s41534-019-0168-5

INTRODUCTION

Universal, fault-tolerant quantum computers—a Holy Grail of quantum information processing—are currently being pursued by academia and industry alike. To achieve fault tolerance in a quantum information processor, a scheme for quantum error correction[1] is needed due to the limited coherence lifetimes of its constituent qubits and the consequently imperfect quantum-gate fidelities. Such schemes, e.g., the surface code,[2] rely on gate fidelities exceeding a certain break-even threshold. Adequately high fidelity was recently demonstrated with superconducting qubits;[3] however, this break-even represents a best-case scenario without any temporal or device-to-device variation in the coherence times or gate fidelities. Therefore, a fault-tolerant quantum computer importantly requires not only improvements of the best-case single-[4] and two-qubit[3] gate fidelities: it actually requires the *typical* performance—in the presence of fluctuations—to exceed the error correction threshold. In the more immediate term, so-called Noisy Intermediate-Scale Quantum (NISQ)[5] circuits will be operated without quantum error correction. In NISQ systems, gate fidelities and the fluctuations thereof directly limit the circuit depth, i.e., the number of consecutive gates in an algorithm that can be successfully implemented.

In experiments with superconducting qubits, it is usual to perform qubit metrology[6] to benchmark the gate fidelity and quantify its error, although these benchmarks are not typically repeated in time to determine any temporal dependence. Since gate fidelities are at least partially limited by qubit T_1 energy relaxation,[4] one would expect a fluctuation in gate fidelity resulting from a fluctuation in the underlying decoherence parameters. However, benchmarking of decoherence, to quantify the mean lifetime together with its stability or variation, is also uncommon. Consequently, it is unclear whether reports on improvements in coherence times—cf. the review by Oliver and Welander[7] and that by Gu and Frisk Kockum et al.[8]—are reports of *typical* or of *exceptional* performance. Quantifying this difference is crucial for future work aimed at improving qubit coherence times.

In this paper, we benchmark the stability of decoherence properties of superconducting qubits: T_1, T_2^* (free-induction decay), T_ϕ (pure dephasing), and f_{01} (qubit frequency). This study is distinct from numerous studies that report on singular measurements of qubit lifetimes for different background conditions, such as temperature[9] or magnetic flux.[10,11] Some studies[11–17] examine repeated measurements of qubit lifetimes under static conditions. However, when discussing these examples, it is important to quantify both the number of counts and the total duration of the measurement. Here, the number of counts relates to the statistical confidence, while the total duration relates to the timescale of fluctuations to which the study is sensitive. Therefore, to confidently report on fluctuations relevant to the calibration period of a quantum processor (for example a few times a day for the IBM Q Experience[18]), we only discuss reports featuring both a large number of counts ($N > 1000$) and a total duration exceeding 5 h.

The first study to satisfy these requirements for relaxation measurements was that of Müller et al.,[14] which revealed that unstable near-resonant two-level-systems (TLS) can induce fluctuations in qubit T_1. They proposed a model in which the TLS produces a strongly peaked Lorentzian noise profile at the TLS frequency (which is near the qubit frequency). Under the separate model of interacting TLS,[19,20] the frequency of this near-resonant TLS varies in time. Consequently, the qubit probes the different parts of the TLS-based Lorentzian noise profile, leading to variations in the qubit's T_1. Although the mechanism was clearly demonstrated, this work[14] was unable to determine properties of the TLS such as switching rates or dwell times of specific TLS frequency positions. Follow-up work by Klimov et al.[17] used a tuneable qubit to map the trajectories of individual TLS. These findings[17] supported the interacting-TLS model and Müller's

[1]Microtechnology and Nanoscience, Chalmers University of Technology, SE-412 96 Göteborg, Sweden; [2]Present address: National Physical Laboratory, Hampton road, Teddington TW11 0LW, UK
Correspondence: Jonas Bylander (bylander@chalmers.se)
These authors contributed equally: Jonathan J. Burnett, Andreas Bengtsson

Received: 2 February 2019 Accepted: 3 June 2019
Published online: 26 June 2019

Published in partnership with The University of New South Wales

npj nature partner journals

findings, and were able to clearly determine TLS switching rates, as well as reveal additional diffusive motion of the TLS.

We demonstrate that sufficient statistical analysis can reveal the TLS-based Lorentzian noise spectrum and allow for extraction of switching rates. Importantly, this method does not require a tuneable qubit or advanced reset protocols[21] and is therefore general to any qubit or setup. Furthermore, the lack of tuning results in a more frequency-stable qubit and consequently less dephasing. This enables us to go beyond the studies of Müller et al. and Klimov et al. by studying the qubit's frequency instabilities due to other noise sources, which reveals a $1/f$ frequency noise that is remarkably similar to interacting-TLS-induced $1/f$ capacitance noise found in superconducting resonators.[20,22] This frequency instability produces a limit on pure dephasing which we observe through sequential inter-leaved measurements of qubit relaxation, dephasing, and frequency.

RESULTS

Our circuit is made of aluminium on silicon and consists of a single-junction Xmon-type transmon qubit[23] capacitively coupled to a microwave readout resonator (see the Methods section IV A for more details). The shunt capacitor and the absence of magnetic-flux tunability (absence of a SQUID) effectively decouple the qubit frequency from electrical charge and magnetic flux, reducing the sensitivity to these typical $1/f$ noise sources.[24,25] Although these qubits lack frequency tunability, they remain suitable for multi-qubit architectures using all-microwave-based two-qubit-gates.[26–29] The circuit is intentionally kept simple so that the decoherence is dominated by intrinsic mechanisms and not external ones in the experimental setup. Therefore, there are no individual qubit drive lines, nor any qubit-to-qubit couplings. In addition, both the spectral linewidth of the resonator and the resonator-qubit coupling are kept small, such that photon emission into the resonator (Purcell effect) and dephasing induced by residual thermal population of the resonator are minimised.[30] A detailed experimental setup together with all device parameters are found in the Methods and Table 1.

This study involves two qubits on separate chips which we name A and B. The main differences are their Josephson and charging energies and that the capacitor of qubit B was trenched to reduce the participation of dielectric loss.[31]

First we assess the stability of the energy-relaxation time T_1 by consecutive measurements. The transmon is driven from its ground to first-excited state by a calibrated π pulse. The qubit state is then read out with a variable delay. The population of the excited state, as a function of the readout delay, is fit to a single-exponential decay to determine T_1. Figure 1 shows a 65-h measurement of two separate qubits (in separate sample enclosures) that are measured simultaneously. The first observation is that the periods of low-T_1 values are not synchronised between the two qubits, indicating that the dominant mechanism for T_1 fluctuations is local to each qubit. (The lack of correlation is quantified in Supplementary Fig. 6). In Fig. 1b, we histogram the T_1 data: this demonstrates that T_1 can vary by more than a factor 2 for both qubits, similarly to previous studies.[14,17]

Table 1. Summary of device parameters

Parameters	Qubit A	Qubit B
f_R	6.035 GHz	5.540 GHz
f_{01}	4.437 GHz	3.759 GHz
$f_{12}-f_{01}$	−0.226 GHz	−0.278 GHz
E_J/h	13.42 GHz	8.57 GHz
E_c/h	0.201 GHz	0.235 GHz
E_J/E_c	66.67	36.54
ϵ/h	−524 Hz	−109 kHz

Note: f_R is the frequency of the readout resonator and f_{01} that of the qubit's 01 transition. $f_{12}-f_{01}$ is the frequency difference between the qubit's 12 transition and 01 transition. E_J is the qubit's Josephson energy, E_c its charging energy, h is Planck's constant, and ϵ its charge dispersion

To make a fair comparison of the mean T_1 for two qubits with different frequencies, we can rescale to quality factors ($Q = 2\pi f_{01} T_1$). We see that qubit B ($Q = 1.67 \times 10^6$) has a higher quality factor compared with qubit A ($Q = 1.29 \times 10^6$). However, while the quality of qubit B is higher, qubit B has a lower ratio of Josephson to charging energy (see Table 1), resulting in a larger sensitivity to charge noise and parity effects.[32] Consequently, qubit B exhibits switching between two different transition frequencies, which was not suitable for later dephasing and frequency instability studies. Therefore, most of the paper focuses on qubit A.

We continue by measuring T_1 consecutively for approximately 128 h, and plot the decays in a colour map (Fig. 2a). Here, the colour map makes some features of the data simpler to visualise. Firstly, the fluctuations are comprised of a switching between different T_1 values, where the switching is instantaneous, but the dwell time at a particular value is typically between 2 h and 12.5 h. This behaviour (also seen in Fig. 1a) resembles telegraphic noise with switching rates ranging from 20 to 140 μHz. Later, we quantify these rates and their reproducibility.

The white box of Fig. 2a and inset Fig. 2b show this switching behaviour occurring within a single iteration. The decay can be fit to two different values of T_1, one before the switch and one afterwards. This type of decay profile is found in approximately 3% of the iterations. In all presented T_1 values (histograms or sequential plots), the lower T_1 value is used. This is motivated by quantum algorithms being limited by the shortest-lived qubit.

The black box and inset Fig. 2c highlight a decay-profile that is no longer purely exponential, but instead exhibits revivals. Similar revivals have been observed in both phase[33] and flux[34] qubits, and were attributed to coherently coupled TLS residing in one of the qubit junctions. From the oscillations we extract a qubit-to-TLS

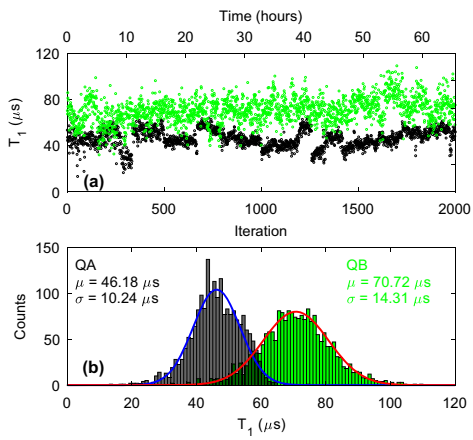

Fig. 1 Synchronous measurement of T_1 in two separate qubits. **a** Multiple T_1 measurements performed simultaneously on qubits A (black) and B (green). The data consists of 2000 consecutive T_1 measurements that lasted a total duration of 2.36×10^5 s (approximately 65 h). **b** Histograms of the T_1 values in **a**. The histograms have been fit (solid line) to Gaussian distributions with the parameters shown. This data was taken during cooldown 6

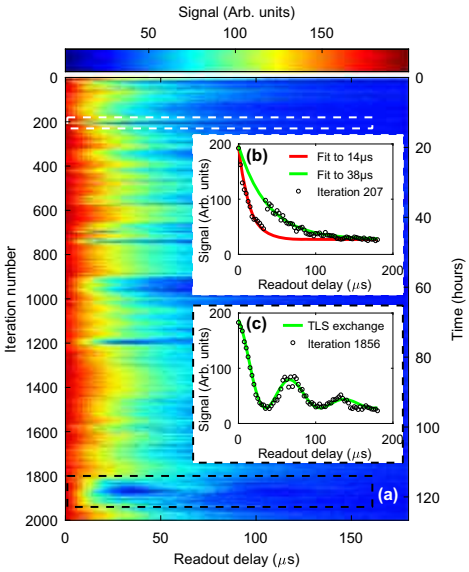

Fig. 2 Raw data of T_1 decay-profile. **a** Consecutive T_1 measurements, spanning 4.6×10^5 s (approximately 128 h), of qubit A. **b** A data set showing a change in T_1 within a single iteration. These jumps are found to occur in approximately 3% of all measurements. **c** A data set showing a decaying sinusoidal (rather than a purely exponential) decay profile. The appearance of revivals is due to the resonant exchange with a TLS. These profiles are found to occur in approximately 5% of all iterations. This data was taken during cooldown 5

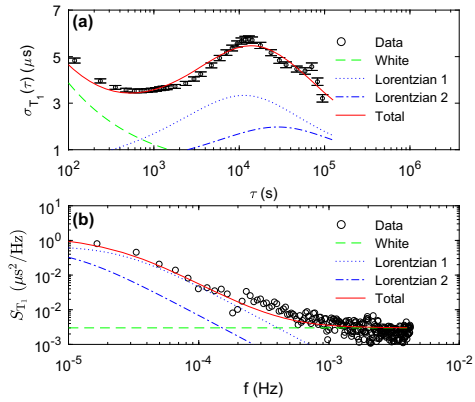

Fig. 3 Time and frequency domain analysis of T_1 fluctuation. Statistical analysis of 2001 sequential T_1 measurements of qubit A spanning a total measurement duration of 2.36×10^5 s. **a** Overlapping Allan deviation of T_1 fluctuations. **b** Welch-method spectral density of T_1 fluctuations. In both plots there are fits to the total noise (red line) which is formed of white noise (green lines) and two different Lorentzians (blue lines). The amplitudes and time constants of all noise processes are the same for both types of analysis. The error-bars of the Allan deviation correspond to 1 standard deviation. This data was taken during cooldown 2

coupling of $g_{TLS} = 4.8$ kHz. Assuming a TLS dipole moment of 1 eÅ,[35] the coupling corresponds to an electric field line of 39 μm (see the Supplementary section C for more details). This length is larger than the Josephson junction; therefore, we conclude that this particular TLS is located on one of the surfaces of the shunting capacitor (not within the junction). Since the invention of transmons and improvement in capacitor dielectrics, individual TLS have only been found to incoherently couple to a transmon,[23] and the authors are not familiar with any examples of a coherent coupling between a TLS and a transmon.

Approximately 5% of decay profiles show a clear revival structure, with a further 3% showing hints of it. Of these, some revival shapes (such as the one shown in the black box) remained stable and persisted for approximately 10 h, whereas others lasted for only 2–3 traces (around 10 min). Since the qubit here is fixed in frequency, these appearances/disappearances of the coherent TLS arise due to the TLS shifting in frequency[14,17,19,20] relative to the static qubit. The observation of coherent oscillations in the decay, and in particular that oscillation periods remained stable for hours (for the same duration as the T_1 fluctuations), constitutes clear evidence for TLS being the origin of the T_1 fluctuations, in agreement with both the Müller[14] and Klimov[17] results.

To gain further insight into these fluctuations we perform statistical analysis commonly used in the field of frequency metrology. In parallel, we examine both the overlapping Allan deviation (Fig. 3a) and the spectral properties (Fig. 3b) of the T_1 fluctuations. Allan deviation is a standard tool for identifying different noise sources in e.g. clocks and oscillators.[36] Here, we introduce the Allan deviation as a tool to identify the cause of fluctuations in qubits. The most striking feature in Fig. 3a is the peak and subsequent decay around $\tau = 10^4$ s. Importantly, no power-law noise process can produce such a peak; instead, it is an unambiguous sign of a Lorentzian noise process. Such Lorentzian-like switching was observed in the T_1-vs.-time measurement in Fig. 1a. In Fig. 3, we model the noise with two Lorentzians with a white noise floor, and apply the modelled noise to both the spectrum and the Allan deviation. Therefore, the noise parameters are the same for both plots: the Methods section has more details on the scaling of Lorentzian noise between the Allan and spectral analysis methods. From Fig. 3, we obtain Lorentzian switching rates of 80.6 and 158.7 μHz.

Within Fig. 4 and Table 2, we show the reproducibility of these features across thermal cycles. Collectively, we find switching rates ranging from 71.4 μHz to 1.9 mHz—slower than those obtained by measurements of charge noise[37] but similar to bulk-TLS dynamics[38,39] and in agreement with rates determined from measurements tracking the time evolution of individual TLS.[17] These measurements demonstrate not only that superconducting

Table 2. Summary of the noise parameters for modelling T_1 fluctuations

Data	h_0 (μs²/Hz)	$1/\tau_0^{Lor1}$ (μHz)	A^{Lor1} (μs)	$1/\tau_0^{Lor2}$ (μHz)	A^{Lor2} (μs)
QA_C2	3.0×10^{-3}	158.7	5.4	80.6	3.2
QA_C3	2.6×10^{-3}	200.0	2.4	100.0	4.5
QA_C5	2.0×10^{-3}	142.9	5.2	83.3	2.6
QA_C6	1.2×10^{-3}	333.3	4.5	71.4	1.8
QB_C1	1.3×10^{-2}	1851.8	2.5	–	–
QB_C5	1.4×10^{-2}	1000.0	3.2	90.9	6.6
QB_C6	5.7×10^{-3}	1111.1	4.2	76.9	2.2

Note: The data is labelled as Q (qubit) A or B and C# (# denotes cooldown number). The superscripts *Lor*1/2 correspond to the Lorentzian being parameterised

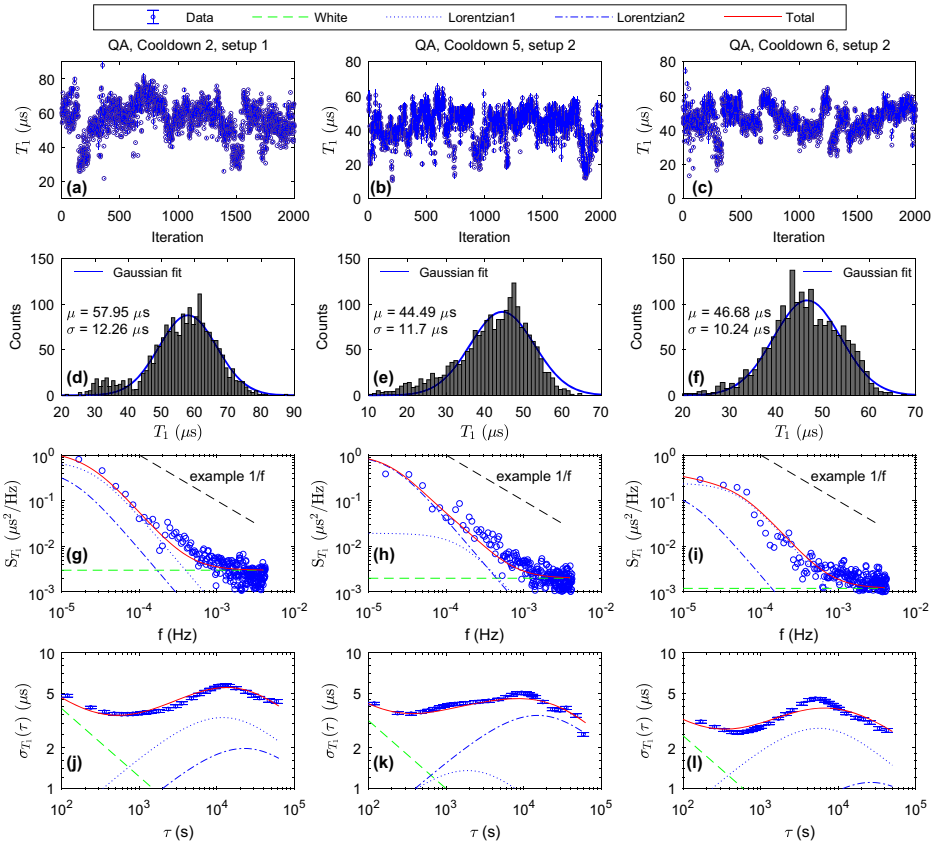

Fig. 4 Reproducibility of T_1 fluctuations in qubit A across separate cooldowns. **a**–**c** Time evolution of T_1 vs. iteration. **d**–**f** Statistics of T_1 plotted as a histogram, with a Gaussian fit. **g**–**i** Welch spectral density estimate of the T_1 fluctuations. **j**–**l** Overlapping Allan deviation of T_1 fluctuations. Across **g**–**i** and **j**–**l** the noise model is the same, where the parameters can be found within Table 2. For illustrative purposes, we include a 1/*f* noise guideline within **g**–**i**. The error-bars of the time evolution of T_1 vs. iteration correspond to 1 standard deviation. Similar data for qubit B can be found within Supplementary Fig. 2

qubits are useful probes of TLS, but unambiguously demonstrate the role of a TLS-based Lorentzian noise profile as a limiting factor to the temporal stability of qubit coherence.

In addition to studying T_1 fluctuations, we also explore fluctuations in qubit frequency and dephasing. To this end, we measure the qubit frequency and the characteristic decay time T_2^* by means of a de-tuned Ramsey fringe. We interleave the Ramsey sequence, point-by-point, with the previously discussed T_1 relaxation sequence. For clarity, if we consider the energy-relaxation measurements in Fig. 2, the main plot (a) represents the complete measurement set, which is formed from 2000 iterations. Each iteration (e.g., either inset) consists of data points which are themselves the averaged results of 1000 repeated measurements. In the interleaved sequence, we measure the data point in the T_1 sequence and then the data point in the Ramsey sequence for each delay time (i.e., the time between the π pulse and readout, in the T_1 measurement, and in-between the $\pi/2$ pulses, in the Ramsey T_2^* measurement). This sequence is then looped through all values of the delay time to map out the T_1 and Ramsey decay profiles (i.e., the iteration). While averaging each point in the inner loop gives a longer iteration time, and increases the noise window to which the Ramsey fringe is sensitive,[40] it allows for all qubit parameters to be known in each iteration. From the so-obtained T_1 and T_2^* we calculate the pure-dephasing time T_ϕ from $1/T_2^* = 1/2T_1 + 1/T_\phi$. These values are shown in Fig. 5b, and the histogram of T_2^* values is shown in Fig. 5c.

In Fig. 5a we have extracted, from the Ramsey fringes, the frequency motion of the qubit relative to its mean frequency ($f_{01} - \overline{f_{01}}$). In general, the observed frequency shifts are on the order of 1 to 3 kHz, with infrequent shifts of up to 20 kHz. A histogram of the qubit frequency (Fig. 5d) reveals a main peak with a full-width at half-maximum of approximately 2 kHz. These frequency shifts are significantly smaller than the approximately 500 kHz frequency instability found in flux-tuneable qubits.[17] From the perspective of gate fidelity, a 1-kHz frequency shift should have negligible effect, meaning that our qubits are well suited for quantum information processing since no re-calibration of the qubit frequency is needed. However, a fluctuating qubit frequency necessarily leads to qubit dephasing so it is important to quantify this fluctuation and therefore aid in efforts to find, and mitigate, the noise source.

To provide more information on possible mechanisms for the frequency instability, we examine both the overlapping Allan deviation (Fig. 5e) and the spectrum of frequency fluctuations

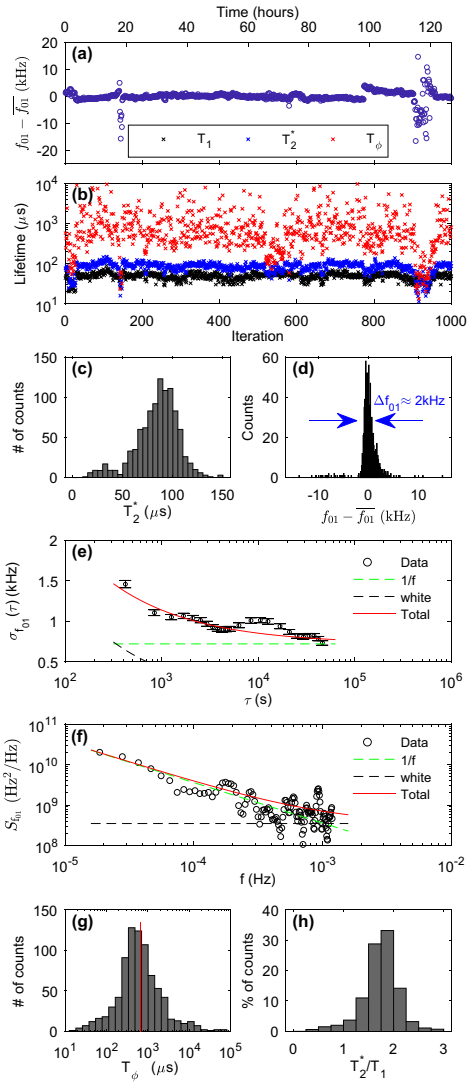

Fig. 5 An interleaved series of 1000 T_1 relaxation and T_2^* Ramsey measurements of qubit A. **a** Qubit frequency (f_{01}) shift relative to its mean ($\overline{f_{01}}$) determined from the Ramsey experiments. **b** Extracted T_1 (black), T_2^* (blue), and T_ϕ (red). **c** Histogram of T_2^* from the data in **b**. **d** Histogram of the data in **a**. The frequency fluctuations from **a** are analysed by overlapping Allan deviation (**e**) and by Welch-method spectrum (**f**). The solid and dashed lines represent the modelled noise, where the noise amplitudes are the same for both types of analysis. **g** Histogram of T_ϕ from the data in **b**. The solid line indicates the T_ϕ limit calculated by integrating the frequency noise from **e**. **h** Histogram of T_2^*/T_1 from the data in **b**. We find $1.4<T_2^*/T_1<2.2$ in 81.7% of the counts. This data was taken during cooldown 3

(Fig. 5f). In red, the frequency noise is modelled to $A/f + B$, where the exponent of f is 1. Similarly to the previous T_1 analysis, the noise model is scaled so that the red line has the same amplitude in both Fig. 5e, f. In this model, the 1/f noise amplitude is $A = 3.6 \times 10^5$ Hz^2.

DISCUSSION

For both qubits, across all cooldowns, we found fluctuations in T_1 that could be described by Lorentzian noise with switching rates in the range from 75 μHz to 1 mHz. For all superconducting qubits, three relaxation channels are usually discussed: TLS, quasiparticles, and parasitic microwave modes. Of these, parasitic microwave modes should not cause fluctuation since they are defined by the physical geometry. For quasiparticles in aluminium, we can compare our observed slow fluctuations with quasiparticle mechanisms found in the qubit literature: the quasiparticle recombination rate is 1 kHz;[41] the timescale of quasiparticle number fluctuations leads to rates in the range from 0.1 kHz to 10 kHz; and finally, quasiparticle tunnelling (parity switching events) in transmons have rates in the range 0.1 kHz to 30 kHz.[32] Therefore, fluctuations in the properties of the superconductor occur over rates which differ by over six orders of magnitude compared to those found in our experiment. Instead, we highlight that, at low temperatures, bulk-TLS dynamics[38,39] and TLS-charge noise[34,37] vary over long timescales equivalent to rates in the range from 10 mHz to 100 Hz.

The observed coherent qubit–TLS coupling (Fig. 2c) is an unambiguous sign of the existence of near-resonant TLS. Its fluctuation follows similar time constants as the T_1 fluctuations, which constitutes clear evidence of spectral instability, as expected from the interacting-TLS model.[19,20] We therefore attribute the origin of the T_1 decay to near-resonant TLS, and the Lorentzian fluctuations in the qubit's T_1 (shown in Figs. 3 and 4g–l) arise due to spectral instabilities of the TLS as described by Müller et al.[14] The extracted switching rates then represent the rate at which the near-resonant TLS is changing frequency. Similarly, the quality factor of superconducting resonators has also been found to vary[42] due to spectrally unstable TLS.

In general, we find that two separate Lorentzians are required to describe the fluctuation. This does not necessarily imply the existence of two near-resonant TLS—instead it is a limitation of the analysis, as we cannot resolve the difference between, say, two near-resonant TLS, each with two preferential frequencies, vs. one near-resonant TLS that has four preferential frequencies. Such a difference could be inferred by measuring the local density of near-resonant TLS,[17] although such a measurement has demonstrated that both scenarios above are possible.[17] In addition, when repeating the measurements across multiple cooldowns, we consistently find a near-resonant TLS that follows similar switching statistics. Between each cooldown, the TLS configuration is expected to completely change. Essentially, this means that the detuning and coupling of the observed near-resonant TLS should vary for each cooldown. However, despite any expected reconfiguration, at least one spectrally unstable near-resonant TLS is always found to exist.

When examining the frequency stability of qubit A, we found a frequency noise of approximately 2 kHz, which was well described by a 1/f amplitude of 3.6×10^5 Hz^2 (Fig. 5d–f). Typically, dephasing is thought to arise due to excess photons within the cavity,[9,43] flux noise,[25] charge noise,[34,37] quasiparticles tunnelling through the Josephson junctions,[32] or the presence of excess quasiparticles.[44] For qubit A, the charge dispersion is calculated to 524 Hz, much smaller than most of the observed frequency shifts. This rules out charge noise and tunnelling quasiparticles as the main source of the observed frequency fluctuations. Quasiparticle fluctuations have been extensively studied,[41] where the magnitude of frequency shifts scales with the kinetic inductance. Therefore, while they can be of order 100 kHz in disordered superconductors,[45] they are much smaller in elemental superconductors. In fact, recent experiments[41] showed that the quasiparticles in aluminium produced an un-measurably small frequency shift; instead, the quasiparticles' influence was revealed only by examining correlated amplitude and frequency noise. Therefore, not only do quasiparticles produce immeasurably small frequency

shifts, but, as noted earlier, they act over much shorter timescales (i.e., rates are equivalent to kHz[32,41] rather than the sub-mHz timescales observed here).

Instead we highlight two further TLS-based mechanisms. Firstly, TLS within the Josephson junction can cause critical-current noise,[46] which can produce a frequency noise by modulating the Josephson energy. Alternatively, superconducting resonators demonstrate that TLS can produce frequency instabilities[20,22] (capacitance noise). Both of these mechanisms exhibit a $1/f$ noise, where the noise amplitude is close to that which we find here. One could distinguish between these two effects by examining the temperature dependence of the qubit's frequency noise. Here, critical current noise[46] scales $\propto T$ while capacitance noise[20,22] scales $\propto 1/T^{1.3}$.

Irrespective of the origin of the frequency instability, the noise spectrum in Fig. 5f can be integrated to estimate the pure dephasing of the qubit.[47] From this calculation, the expected T_ϕ is 0.8 ms. In Fig. 5g we histogram the T_ϕ to reveal a peak around 0.7 ms, with diminishing counts above 1 ms, in good agreement with the estimate from the integrated frequency noise.

In Fig. 5b, c, T_2^* is almost always longer than T_1, implying that $T_\phi > 2T_1$. In Fig. 5h this is quantified, as the histogram of the ratio of T_2^*/T_1 reveals that the qubit dephasing is almost always near $2T_1$. Therefore, the qubit's T_2^* is mainly limited by T_1. To the authors' knowledge all other demonstrations of T_1-limited T_2 required dynamical decoupling by either a Hahn-echo (spin-echo)[9,25] or CPMG[11] sequence. However, neither of those works provide any statistics on whether the qubits were *always* T_1-limited. The histogram in Fig. 5h also reveals counts where the ratio is above 2: these correspond to the instances where the T_1 has fluctuated within an iteration, similar to that shown in Fig. 2b.

In summary, we have measured the stability of qubit lifetimes across more cooldowns and for measurement spans longer than previous studies. Collectively, this demonstrates that qubit fluctuations, due to spectrally unstable TLS, are consistently observed, even when T_1 is high (approaching 100 µs). The spectral motion of TLS is particularly problematic for gates requiring frequency movement (e.g., CPHASE[3]). Here, leakage to TLS during gate operations, and the optimum idling frequencies become time-varying on a per-qubit basis. In addition, since gate fidelities contain a non-negligible error contribution from T_1,[48] the optimal gate duration will be affected by T_1 varying in time. Therefore, these fluctuations demonstrate why it is necessary to re-calibrate qubits every few hours. Fundamentally, this also demonstrates that future reports on qubit coherence times require not only statistics for reproducibility, but also that the measurement duration should exceed several hours in order to adequately report the *typical* rather than *exceptional* coherence time.

Note added—Recently, a preprint on comparable observations was published by Schlör et al.,[49] who independently demonstrated that single fluctuators (TLS) are responsible for frequency and dephasing fluctuations in superconducting qubits. In addition, another recent preprint by Hong et al.,[50] specifically measures fluctuations in gate fidelity and independently identifies T_1 fluctuation of the underlying qubits as the probable cause.

METHODS

Experimental details

The qubits are fabricated out of electron-beam evaporated aluminium on a high-resistivity intrinsic silicon substrate. Everything except the Josephson junction is defined using direct-write laser lithography and etched using wet chemistry. The Josephson junction is defined in a bi-layer resist stack using electron-beam lithography, and later deposited using a two-angle evaporation technique that does not create any extra junctions or floating islands.[51] An additional lithography step is included to ensure a superconducting contact between the junction and the rest of the circuit; after the lithography, but prior to deposition of aluminium, an argon ion

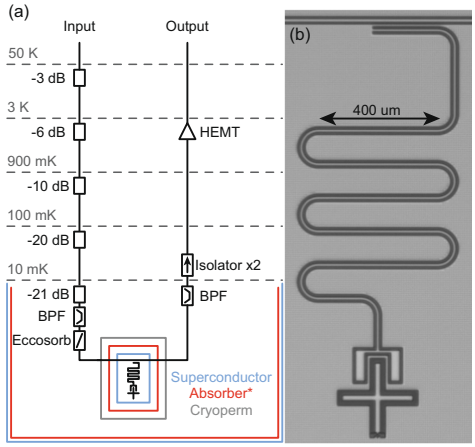

Fig. 6 An overview of the experiment. **a** Simplified schematic of the experimental setup. The main features are the various shielding layers. The absorber coating (red and with an asterisk) was added for setup 2. **b** Optical image of the qubit sample. It shows a common microwave transmission line, a $\lambda/4$ resonator and a transmon qubit with a coplanar capacitor (Xmon-geometry). The arrow represents a 400 micron scale bar

mill is used to remove native aluminium oxide. This avoids milling underneath the junction, which has been shown to increase the density of TLS.[10] Finally, the wafer is diced into individual chips and cleaned thoroughly using both wet and dry chemistry. Moreover, qubit B underwent a trenching step where approximately 1 µm of the silicon dielectric was removed from both the qubit and the resonator using an fluorine based reactive-ion etch.[52]

A simplified schematic of the experimental setup is shown in Fig. 6a. The samples sit within a superconducting enclosure, which itself is inside of an absorber-lined radiation shield and a cryoperm layer. This is located within a further absorber-lined radiation shield and a further superconducting layer which encloses the entire mixing chamber. Everything inside the cryoperm layer (screws, sample enclosures, and cables) is non-magnetic. The setup, including absorber recipe, is similar to a typical qubit box-in-a-box setup.[44] For the different cooldowns, two setups (labelled 1 and 2) were used. Setup 2 was as described above, whereas setup 1 lacked the absorber coating marked with a red asterisk in Fig. 6a.

Data handling

The qubit decoherence data is processed in the following way. First, the digitiser signal is rotated to one quadrature. Next, the signal is normalised to the maximum visibility of the qubit $|0\rangle$ and $|1\rangle$ states. Then, for qubit relaxation data, a fit to a single exponential is performed. Within Fig. 4a–c, T_1 data is presented with error-bars. These error-bars correspond to 1 standard deviation, determined from confidence intervals of the exponential fit. For the Ramsey measurements, the initial processing is as described above. However, the Ramsey frequency (f_{Ram}) is initially determined by FFT of the data. The resulting frequency from the FFT is used as an initial frequency guess to a model of the form:

$$\langle P_e(t)\rangle = \exp(-t/T_2^*)\cos(2\pi f_{\mathrm{Ram}} + \phi_0) \quad (1)$$

where ϕ_0 is a phase offset that is generally zero. Across all of the data-sets examined for qubit A, the FFT reveals only one oscillation frequency, whereas for qubit B, two frequencies are observed due to a larger charge dispersion. Consequently, Eq. (1) does not fit well for qubit B, and we omit qubit B from the dephasing and frequency results.

For the qubit relaxation, we did attempt fits to a double exponential model.[11,53] Within this model, an additional relaxation channel due to quasiparticles near the junction can lead to a skewing of the decay-profile. Here, we found the confidence interval for numerous parameters was unphysically large, indicating that the model over-parameterised our data. Therefore, we continued to use the single-exponential model. However,

this is not surprising as the double-exponential is typically used for flux-qubits and fluxoniums, rather than the single-junction transmon-type qubit studied here.

Sample handling

Here, we clarify the sample handling across the entire experiment. For each qubit sample, after completing fabrication, they were covered in protective resist until the morning of their first cooldown (cooldown 1 for qubit B and cooldown 2 for qubit A). After removal of the resist, the samples were wire-bonded within a sample enclosure. Once sealed, the samples remained within their enclosures and were kept attached to the fridge for the entire experimental run. Therefore, when the fridge was warm, the samples were kept at the ambient conditions of the lab. Qubit B was not measured between cooldown 2 and cooldown 5, although it was still cooled down. However, qubit B was examined again in cooldowns 5 and 6 to gather statistics on the reproducibility of parameter fluctuations.

Spectral and Allan analysis

Within the main text, information on TLS switching rates is inferred by examining the reproducibility of coherence parameters. Primarily, this is obtained by examining the Allan statistics and spectral properties of T_1 fluctuations. Here, the same data set is used to produce a plot of a Welch-method FFT ($S_{T_1}(f)$) and an overlapping Allan deviation ($\sigma_{T_1}(\tau)$). For the Welch analysis, the quantity analysed is $T_1 - \overline{T_1}$ (or for frequency it is $f_{01} - \overline{f_{01}}$). Therefore, the analysed quantity is not presented in fractional units. Consequently, the units of spectral analysis are μs^2/Hz for T_1 fluctuations (Hz^2/Hz for frequency analysis). Equivalently, the Allan statistics are presented in units of μs for T_1 fluctuation (Hz for frequency fluctuation).

The Allan deviation offers a few advantages compared with the spectrum. The method is directly traceable in that the Allan methods use simple mathematical functions that do not require any careful handling of window functions or overlap. When examining low-frequency processes, this eases a considerable burden in FFT-analysis which is to distinguish real features from remnants of window functions. This traceability is core to the usage within the frequency metrology community. The Allan method also provides clear error bars (defined as equal to 1 standard deviation), which translate to an efficient use of the data with optimum averaging of all data that shares a common separation, that is, all data pairs for any separation (τ in the Allan plot) are averaged over. Moreover, the Allan method can distinguish linear drift from any other divergent noise processes. Within an FFT, a linear drift appears as a general $1/f^{\alpha}$ slope where α is not unique compared with other noise sources. Within the Allan, a linear drift appears as τ^{α} where α is distinct and unique compared with other divergent noise types.

From here, beginning with the Allan deviation, we consider the standard power-law model[36] of noise processes,

$$\begin{aligned}\sigma_{T_1}(\tau) = &\left(\tfrac{h_0}{2}\right)^{\frac{1}{2}}\tau^{-\frac{1}{2}} \\ &+(2\ln(2)h_{-1})^{\frac{1}{2}} \\ &+\left(\tfrac{(2\pi)^2}{6}h_{-2}\right)^{\frac{1}{2}}\tau^{\frac{1}{2}}\end{aligned} \tag{2}$$

which can also be represented as spectral noise

$$S_{T_1}(f) = \frac{h_{-2}}{f^2} + \frac{h_{-1}}{f} + h_0 \tag{3}$$

where, in frequency metrology notation, h_{-2} is the amplitude of a random walk noise process, h_{-1} is the amplitude of a $1/f$ noise process and h_0 is the amplitude of white noise.

In general terms, the power-law noise processes create a well-like shape in the Allan analysis, where, with the terms listed above, the walls have slopes of $\propto \tau^{-\frac{1}{2}}$ and $\propto \tau^{\frac{1}{2}}$. If more terms are included in the power-law noise model, the available slope gradients increase, but the well-like shape remains. When applied to the T_1 fluctuations (Fig. 3), this model is not able to describe the most striking feature: the hill-like peak with subsequent second decreasing slope. Within Allan analysis, the rise and fall of a single peak can only be represented by a Lorentzian noise process. Therefore, starting from

$$S(f) = \frac{4A^2\tau_0}{1 + (2\pi f\tau_0)^2} \tag{4}$$

where A represents the Lorentzian noise amplitude and τ_0 is the characteristic timescale, Lorentzian noise can be represented in Allan deviation by ref. [54].

$$\sigma(\tau) = \frac{A\tau_0}{\tau}\left(4e^{(-\tau/\tau_0)} - e^{(-2\tau/\tau_0)} - 3 + 2\tau/\tau_0\right)^{1/2} \tag{5}$$

From here, we model the T_1 fluctuations by two separate Lorentzians and white noise. When plotted, the noise from these sources is identical (i.e., the same h_0, A, and τ_0) for both the Welch-FFT and Allan deviation. For the rest of the data sets, we tabulate the Lorentzian parameters and white noise level in Table 2.

DATA AVAILABILITY

The data that supports the findings of this study is available from the corresponding authors upon reasonable request.

CODE AVAILABILITY

The code that supports the findings of this study is available from the corresponding authors upon reasonable request.

ACKNOWLEDGEMENTS

We wish to express our gratitude to Philip Krantz and Tobias Lindström for insightful discussions. We acknowledge financial support from the Knut and Alice Wallenberg Foundation, the Swedish Research Council, and the EU Flagship on Quantum Technology H2020-FETFLAG-2018-03 project 820363 OpenSuperQ. In addition, J.J.B acknowledges financial support from the Industrial Strategy Challenge Fund Metrology Fellowship as part of the UK government's Department for Business, Energy and Industrial Strategy.

AUTHOR CONTRIBUTIONS

J.J.B. and A.B. are considered co-first authors. J.J.B., A.B., and J.B. planned the experiment, A.B. designed the samples, A.B. fabricated the samples with input from J.J.B. The experiments were mainly performed by J.J.B. and A.B. with help from M.S., D.N., and M.K. Analysis was performed by J.J.B. and A.B. with input from P.D. and J.B. The manuscript was written by J.J.B., A.B., and J.B. with input from all authors. J.B. and P.D. provided support for the work.

ADDITIONAL INFORMATION

Supplementary information accompanies the paper on the *npj Quantum Information* website (https://doi.org/10.1038/s41534-019-0168-5).

Competing interests: The authors declare no competing interests.

Publisher's note: Springer Nature remains neutral with regard to jurisdictional claims in published maps and institutional affiliations.

REFERENCES

1. Preskill, J. Reliable quantum computers. *Proc. R. Soc. London Ser A* **454**, 385–410 (1998).
2. Fowler, A. G., Mariantoni, M., Martinis, J. M. & Cleland, A. N. Surface codes: towards practical large-scale quantum computation. *Phys. Rev. A* **86**, 032324 (2012).
3. Barends, R. et al. Superconducting quantum circuits at the surface code threshold for fault tolerance. *Nature* **508**, 500–503 (2014).
4. Rol, M. A. et al. Restless tuneup of high-fidelity qubit gates. *Phys. Rev. Appl.* **7**, 041001 (2017).
5. Preskill, J. Quantum computing in the NISQ era and beyond. *Quantum* **2**, 79 (2018).
6. Martinis, J. M. Qubit metrology for building a fault-tolerant quantum computer. *NPJ Quantum Inf.* **1**, 15005 (2015).
7. Oliver, W. D. & Welander, P. B. Materials in superconducting quantum bits. *MRS Bull.* **38**, 816–825 (2013).
8. Gu, X., Kockum, A. F., Miranowicz, A., Liu, Y.-x & Nori, F. Microwave photonics with superconducting quantum circuits. *Phys. Rep.* **718**, 1–102 (2017).
9. Wang, Z. et al. Cavity attenuators for superconducting qubits. *Phys. Rev. Appl.* **11**, 014031 (2019).
10. Dunsworth, A. et al. A method for building low loss multi-layer wiring for superconducting microwave devices. *Appl. Phys. Lett.* **112**, 063502 (2018).

11. Yan, F. et al. The flux qubit revisited to enhance coherence and reproducibility. *Nat. Commun.* **7**, 12964 (2016).
12. Dial, O. et al. Bulk and surface loss in superconducting transmon qubits. *Supercond. Sci. Technol.* **29**, 044001 (2016).
13. Rosenberg, D. et al. 3D integrated superconducting qubits. *NPJ Quantum Inf.* **3**, 42 (2017).
14. Müller, C., Lisenfeld, J., Shnirman, A. & Poletto, S. Interacting two-level defects as sources of fluctuating high-frequency noise in superconducting circuits. *Phys. Rev. B* **92**, 035442 (2015).
15. Gustavsson, S. et al. Suppressing relaxation in superconducting qubits by quasiparticle pumping. *Science* **354**, 1573–1577 (2016).
16. Chang, J. B. et al. Improved superconducting qubit coherence using titanium nitride. *Appl. Phys. Lett.* **103**, 012602 (2013).
17. Klimov, P. V. et al. Fluctuations of energy-relaxation times in superconducting qubits. *Phys. Rev. Lett.* **121**, 090502 (2018).
18. IBM Q. IBM Q Experience website. https://www.research.ibm.com/ibm-q/. Accessed July 2018.
19. Faoro, L. & Ioffe, L. B. Interacting tunneling model for two-level systems in amorphous materials and its predictions for their dephasing and noise in superconducting microresonators. *Phys. Rev. B* **91**, 014201 (2015).
20. Burnett, J. et al. Evidence for interacting two-level systems from the 1/f noise of a superconducting resonator. *Nat. Commun.* **5**, 4119 (2014).
21. Geerlings, K. et al. Demonstrating a driven reset protocol for a superconducting qubit. *Phys. Rev. Lett.* **110**, 120501 (2013).
22. de Graaf, S. E. et al. Suppression of low-frequency charge noise in superconducting resonators by surface spin desorption. *Nat. Commun.* **9**, 1143 (2018).
23. Barends, R. et al. Coherent Josephson qubit suitable for scalable quantum integrated circuits. *Phys. Rev. Lett.* **111**, 080502 (2013).
24. Gustafsson, M. V., Pourkabirian, A., Johansson, G., Clarke, J. & Delsing, P. Thermal properties of charge noise sources. *Phys. Rev. B* **88**, 245410 (2013).
25. Bylander, J. et al. Noise spectroscopy through dynamical decoupling with a superconducting flux qubit. *Nat. Phys.* **7**, 565–570 (2011).
26. McKay, D. C. et al. Universal gate for fixed-frequency qubits via a tunable bus. *Phys. Rev. Appl.* **6**, 064007 (2016).
27. Chow, J. M. et al. Simple all-microwave entangling gate for fixed-frequency superconducting qubits. *Phys. Rev. Lett.* **107**, 080502 (2011).
28. Economou, S. E. & Barnes, E. Analytical approach to swift nonleaky entangling gates in superconducting qubits. *Phys. Rev. B* **91**, 161405(R) (2015).
29. Paik, H. et al. Experimental demonstration of a resonator-induced phase gate in a multiqubit circuit-QED system. *Phys. Rev. Lett.* **117**, 250502 (2016).
30. Clerk, A. A. & Utami, D. W. Using a qubit to measure photon-number statistics of a driven thermal oscillator. *Phys. Rev. A* **75**, 042302 (2007).
31. Barends, R. et al. Minimal resonator loss for circuit quantum electrodynamics. *Appl. Phys. Lett.* **97**, 023508 (2010).
32. Riste, D. et al. Millisecond charge-parity fluctuations and induced decoherence in a superconducting transmon qubit. *Nat. Commun.* **4**, 1913 (2013).
33. Cooper, K. et al. Observation of quantum oscillations between a Josephson phase qubit and a microscopic resonator using fast readout. *Phys. Rev. Lett.* **93**, 180401 (2004).
34. Gustavsson, S. et al. Dynamical decoupling and dephasing in interacting two-level systems. *Phys. Rev. Lett.* **109**, 010502 (2012).
35. Martinis, J. et al. Decoherence in Josephson qubits from dielectric loss. *Phys. Rev. Lett.* **95**, 210503 (2005).
36. Rubiola, E. Phase noise and frequency stability in oscillators. In *The Cambridge RF and Microwave Engineering Series* (Cambridge University Press, 2009). https://www.cambridge.org/core/books/phase-noise-and-frequency-stability-inoscillators/445C12C4ECBFCD7765116E61561EC0FE https://doi.org/10.1017/CBO9780511812798.
37. Kafanov, S., Brenning, H., Duty, T. & Delsing, P. Charge noise in single-electron transistors and charge qubits may be caused by metallic grains. *Phys. Rev. B* **78**, 125411 (2008).
38. Salvino, D. J., Rogge, S., Tigner, B. & Osheroff, D. D. Low temperature ac dielectric response of glasses to high dc electric fields. *Phys. Rev. Lett.* **73**, 268–271 (1994).
39. Ludwig, S., Nalbach, P., Rosenberg, D. & Osheroff, D. Dynamics of the destruction and rebuilding of a dipole gap in glasses. *Phys. Rev. Lett.* **90**, 105501 (2003).
40. Martinis, J., Nam, S., Aumentado, J., Lang, K. & Urbina, C. Decoherence of a superconducting qubit due to bias noise. *Phys. Rev. B* **67**, 094510 (2003).
41. de Visser, P. J. et al. Number fluctuations of sparse quasiparticles in a superconductor. *Phys. Rev. Lett.* **106**, 167004 (2011).
42. Earnest, C. T. et al. Substrate surface engineering for high-quality silicon/aluminum superconducting resonators. *Supercond. Sci. Technol.* **31**, 125013 (2018).
43. Rigetti, C. et al. Superconducting qubit in a waveguide cavity with a coherence time approaching 0.1 ms. *Phys. Rev. B* **86**, 100506(R) (2012).
44. Barends, R. et al. Minimizing quasiparticle generation from stray infrared light in superconducting quantum circuits. *Appl. Phys. Lett.* **99**, 113507 (2011).
45. Grünhaupt, L. et al. Loss mechanisms and quasiparticle dynamics in superconducting microwave resonators made of thin-film granular aluminum. *Phys. Rev. Lett.* **121**, 117001 (2018).
46. Nugroho, C. D., Orlyanchik, V. & Van Harlingen, D. J. Low frequency resistance and critical current fluctuations in al-based josephson junctions. *Appl. Phys. Lett.* **102**, 142602 (2013).
47. Koch, J. et al. Charge-insensitive qubit design derived from the Cooper pair box. *Phys. Rev. A* **76**, 042319 (2007).
48. O'Malley, P. J. J. et al. Qubit metrology of ultralow phase noise using randomized benchmarking. *Phys. Rev. Appl.* **3**, 044009 (2015).
49. Schlör, S. et al. Correlating decoherence in transmon qubits: low frequency noise by single fluctuators. Preprint at arXiv:1901.05352 (2019).
50. Hong, S. et al. Demonstration of a parametrically-activated entangling gate protected from flux noise. Preprint at arXiv:1901.08035 (2019).
51. Gladchenko, S. et al. Superconducting nanocircuits for topologically protected qubits. *Nat. Phys.* **5**, 48–53 (2009).
52. Burnett, J., Bengtsson, A., Niepce, D. & Bylander, J. Noise and loss of superconducting aluminium resonators at single photon energies. *J. Phys. Conf. Ser.* **969**, 012131 (2018).
53. Pop, I. M. et al. Coherent suppression of electromagnetic dissipation due to superconducting quasiparticles. *Nature* **508**, 369–372 (2014).
54. Van Vliet, C. M. & Handel, P. H. A new transform theorem for stochastic processes with special application to counting statistics. *Phys. A* **113**, 261–276 (1982).

Supplementary information for Decoherence benchmarking of superconducting qubits

Jonathan J. Burnett[†],[*] Andreas Bengtsson,[†] Marco Scigliuzzo,
David Niepce, Marina Kudra, Per Delsing, and Jonas Bylander[‡]
Microtechnology and Nanoscience, Chalmers University of Technology, SE-412 96, Göteborg, Sweden
(Dated: June 3, 2019)

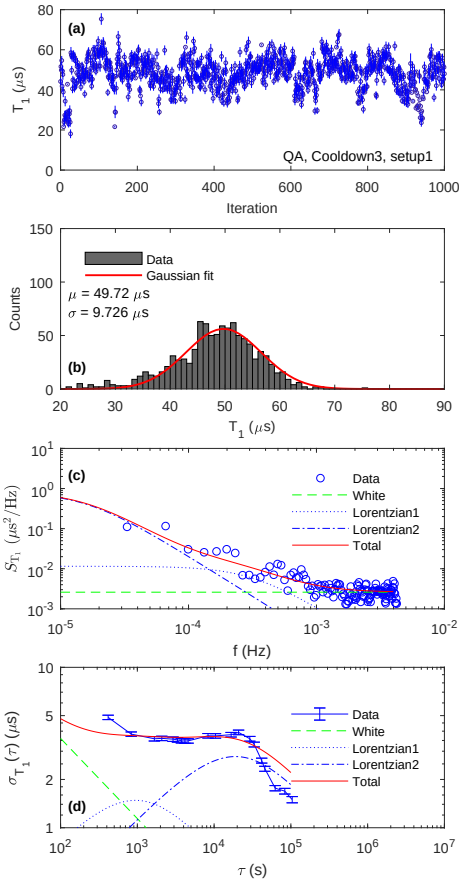

Supplementary Figure 1. **1000 sequential T_1 measurements of Qubit A within cooldown 3.** (**a**) T_1 vs. iteration. (**b**) T_1 histogram. (**c**) Welch spectral density estimate of the T_1 fluctuations. (**e**) Overlapping Allan deviation of T_1 fluctuations.

A. Reproducibility of data

In the main text, the reproducibility of data for qubit A was shown by summaries of T_1 values vs. measurement iteration; a histogram of T_1 values with a fit determining the mean and standard deviation; and a Welch FFT and overlapping Allan deviation of the T_1 series. That summary only featured the datasets with the highest number of counts. Therefore, the remaining data set is included here (see Fig. 1). Additionally we include the data sets for qubit B (se Fig. 2)

By examining the reproducibility of T_1 fluctuations across thermal cycles, the study grew to span multiple months. Between these thermal cycles, the samples were kept at ambient conditions within the laboratory room. Therefore, with the many thermal cycles, the samples may spend a non-negligible amount of time outside of the controlled vacuum and cryogenic conditions of the cryostat. Therefore, we start to raise the possibility of becoming sensitive to the device aging. Aging of Josephson junctions is well-known and often reported as causing a drift in the Josephson energy.

Here, we are interested in whether the qubit lifetimes degrade over time. Anecdotally, there is an awareness that devices age, where, for example, increased surface oxidation can increase dielectric losses. However, the authors are not aware of any studies which demonstrate robust statistics on any aging process. In Fig. 3, we show several measurements of T_1 statistics across several cooldowns. These demonstrate that the observed fluctuations are *typical* for all cooldowns. Additionally, we find that the standard deviation of the T_1 fluctuation is around 20% of the mean, for mean T_1 ranging from 40 µs to 82 µs.

Table I quantifies the number of days that the samples were cold (temperature below 3 K) or at ambient condi-

	QA			QB		
Cooldown	$\overline{T_1}$ (µs)	days$_c^{tot}$	days$_w^{tot}$	$\overline{T_1}$ (µs)	days$_c^{tot}$	days$_w^{tot}$
1	-	-	-	74.56	0	1
2	57.95	0	1	-	39	5
3	49.72	49	5	-	88	9
4	-	80	10	-	119	14
5	44.49	133	15	81.63	192	19
6	46.68	197	23	71.22	236	27

Supplementary Table I. Statistics on qubit T_1 over time. We tabulate the mean T_1 (denoted $\overline{T_1}$), the cumulative total days cold (days$_c^{tot}$), and the cumulative total days warm (days$_w^{tot}$).

[*] Present address: National Physical Laboratory, Hampton road, Teddington, UK, TW11 0LW
[†] These two authors contributed equally
[‡] bylander@chalmers.se

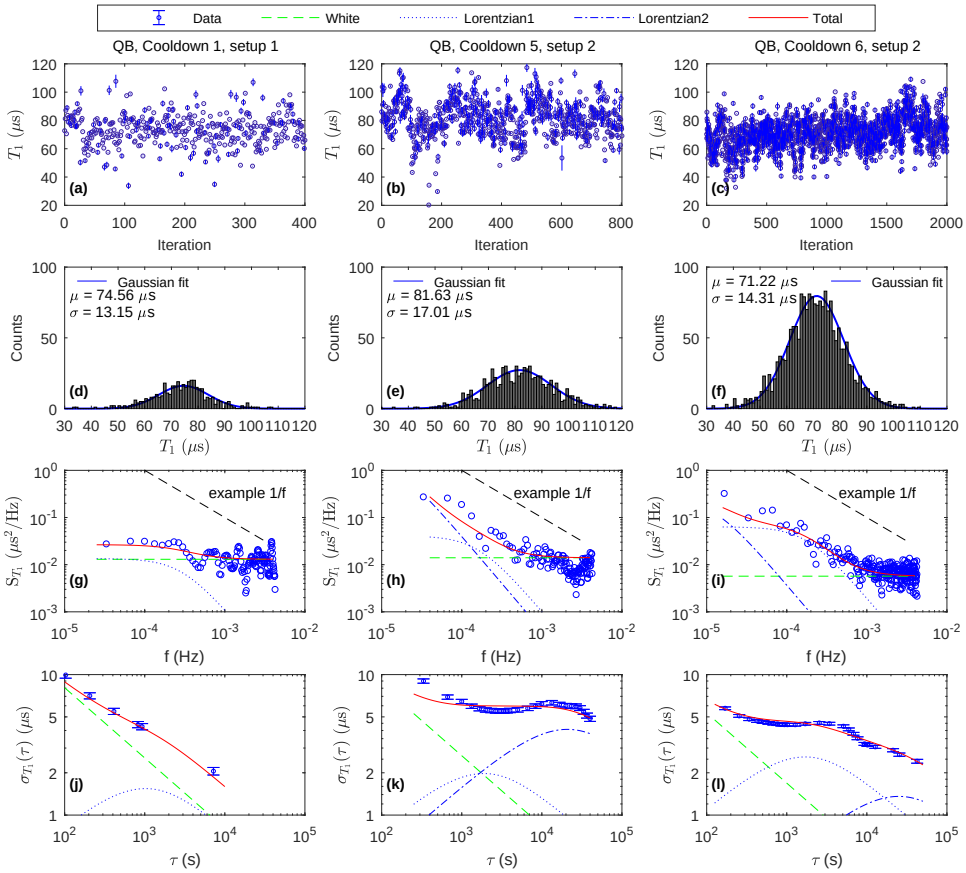

Supplementary Figure 2. **Reproducibility of T_1 fluctuations in qubit B across separate cooldowns.** (**a-c**) Time evolution of T_1 vs. iteration. (**d-f**) Statistics of T_1 plotted as a histogram, with a Gaussian fit. (**g-h**) Welch spectral density estimate of the T_1 fluctuations. (**j-l**) Overlapping Allan deviation of T_1 fluctuations. Across (**g-i**) and (**j-l**) the noise model is the same, where the parameters can be found within Table II of the main text. For illustrative purposes, we include a $1/f$ noise guideline within (**g-i**).

tions. We observe that qubit A experiences degradation within the first 15 days at ambient conditions. Here, the mean T_1 drops from $\approx 60\,\mu$s to around $\approx 45\,\mu$s, where no further degradation is observed. Here, we are limited to too few samples to make definitive statements on qubit aging. None-the-less, the observation of degradation across the cooldowns is a hint that aging could occur. Importantly, we demonstrate that in order to actually resolve the small degradation in performance, large statistics (larger than typically reported) are essential.

B. Fits to alternative noise models

In the main text, we have modeled the T_1 fluctuations by two different Lorentzians. Primarily, this was motivated by the peak within the Allan deviation that could not be understood by other noise processes (e.g. $1/f$ noise). However, there are some sets of data where the Lorentzian peak is not that prominent (e.g. Cooldown 5 for either qubit).

In Fig. 4, we examine three sets of data and show alternative noise models to describe them. These alternative models consist of,

- **Fig. 4a–b:** single Lorentzian + white noise
- **Fig. 4c–d:** single Lorentzian + $1/f$ + white noise
- **Fig. 4e–f:** $1/f$ + white noise

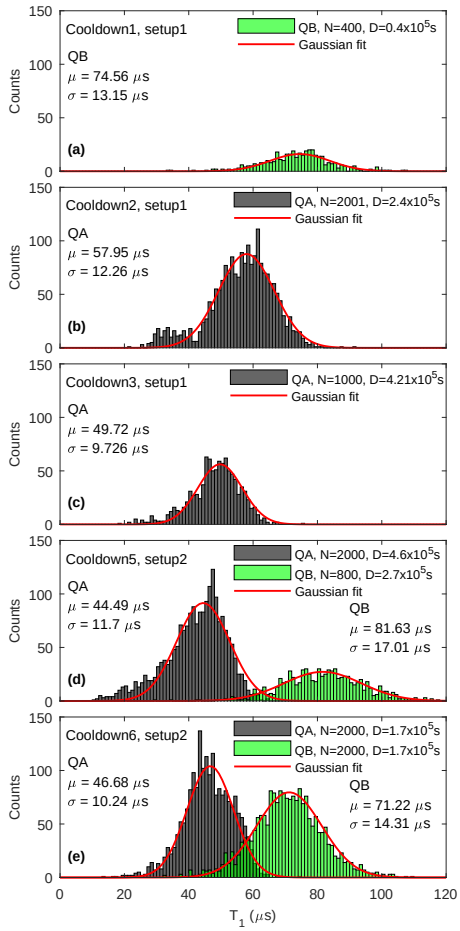

Supplementary Figure 3. **Statistics on T_1 across cooldowns.** Histograms from N measurements spanning a measurement duration (D) for qubit A (in black) and qubit B (in green) across several separate cooldowns. Setup 2 represents the full schematic demonstrated in the main text, while setup 1 does not include the absorber coating

Beginning with a dataset that shows a strong Lorentzian characteristic (Fig. 4a–b). We examine whether the noise can be described just by a single Lorentzian. The model parameters are $h_0 = 1.2 \times 10^{-3}\,\mu\text{s}^2/\text{Hz}$, $A^{Lor1} = 6\,\mu\text{s}$ and $1/\tau_0^{Lor1} = 250\,\mu\text{Hz}$. In this example, the Allan deviation (Fig. 4b) is very well described. However, the agreement with the FFT (Fig. 4a) is worse, with a consistent over-estimation of the Lorentzian noise and under-estimation of the white noise. In the main text, we favoured the two-Lorentzian model as it produces a better agreement across both the FFT and Allan deviation analysis methods.

Next, in Fig. 4c–d, we consider a dataset where the Lorentzian peak is less prominent. Consequently, it is possible to model the T_1 fluctuation as the sum of a single Lorentzian ($1/\tau_0 = 250\,\mu\text{Hz}$ and amplitude of $4.3\,\mu\text{s}$), $1/f$ (amplitude of $1 \times 10^{-12}\,\mu\text{Hz}^2$), and white noise. In this example, the noise spectrum is well modelled, while the Allan deviation shows discrepancies at the lowest and highest times.

Finally, in Fig. 4e–f, we examine a dataset with the least prominent Lorentzian characteristic. Here, it is possible to model the T_1 fluctuation as the sum of just $1/f$ (amplitude of $5.2 \times 10^{-12}\,\mu\text{Hz}^2$) and white noise. In this example, again the noise spectrum is well modelled, while the Allan deviation shows clear structure that is not captured by the $1/f$ noise alone.

The transition between multiple Lorentzians and $1/f$ has been studied before[1], in which work it was highlighted that whether there are sufficient Lorentzians to superimpose to a pure $1/f$ depends on the density of TLS. Here, we emphasize that the two-Lorentzian model within the main text better captures all details of the data. Therefore, we fitted to two-Lorentzians, because that model was able to describe the data across all cooldowns.

The use of alternative noise models can also be extended to the qubit's frequency noise. In Fig. 5 we fit the qubit's frequency fluctuations to a single Lorentzian. The model parameters are $h_0 = 1.0 \times 10^9\ \text{Hz}^2/\text{Hz}$, $A^{Lor1} = 1.2\,\text{kHz}$ and $1/\tau_0^{Lor1} = 133\,\mu\text{Hz}$. Here, the Allan deviation (Fig. 5b) is very well described by the single Lorentzian. Equally the FFT is well described by the Lorentzian; however, in the FFT (Fig. 5a), the white noise is significantly over-estimated. In the main text, we favoured the $1/f$ model in order to enable comparison with other $1/f$ models. Physically, this was motivated by the broadband nature of the TLS dispersive coupling.

C. Qubit-TLS coupling

Within the main text, there are data sets which show revival features in time within measurements of the qubit relaxation (see main text Fig. 2c). These features arise due to the coherent coupling between the qubit and a single TLS, described by the Hamiltonian[2],

$$\frac{\hat{H}}{h} = -\frac{f_{01}}{2}\sigma_z - \frac{f_{\text{TLS}}}{2}\tau_z + \frac{g_{\text{TLS}}}{2}\sigma_x\tau_x, \tag{1}$$

where h is Planck's constant, and σ_i and τ_i correspond to the Pauli matrices for the qubit and the TLS, respectively. Due to this coupling, the qubit excited state can hybridize and form two, almost degenerate, states. The coupling strength g_{TLS} can be extracted from measuring the energy relaxation decay of the qubit and fitting it to

$$\begin{aligned}\langle\sigma_z(t)\rangle = \langle\sigma_z\rangle_\infty &+ a_{\downarrow,1}e^{-\Gamma_{\downarrow,1}t} \\ &+ a_{\downarrow,2}e^{-\Gamma_{\downarrow,2}t} \\ &+ a_{osc}\cos(2\pi f_{osc}t)e^{-\Gamma_{osc}t}\end{aligned} \tag{2}$$

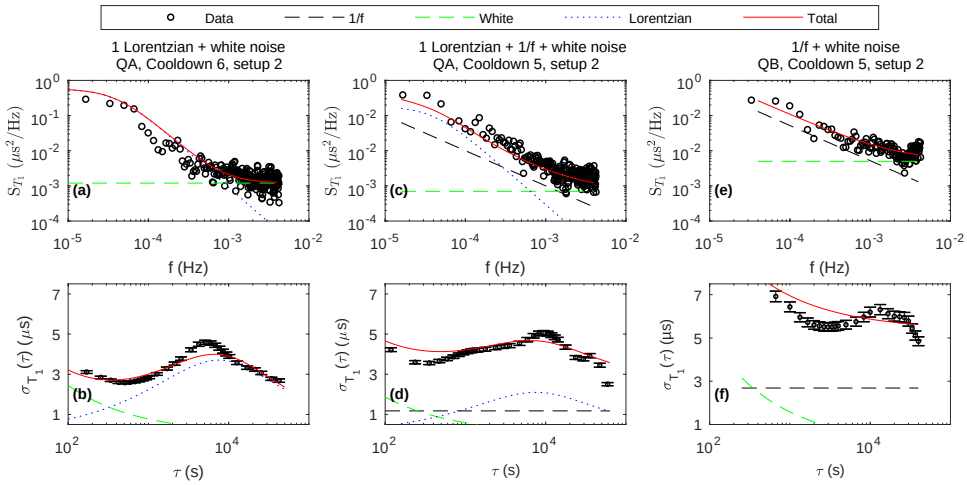

Supplementary Figure 4. T_1 fluctuation fits to alternative noise models. **(a)**, **(c)**, and **(e)** show the FFT of T_1 fluctuations, while **(b)**, **(d)**, and **(f)** show the overlapping Allan deviation analysis of T_1 fluctuations. **(a)** and **(b)** show a dataset with a clearly pronounced Lorentzian characteristic (QA Cooldown 6), fit to a noise model consisting of a single Lorentzian and white noise. **(c)** and **(d)** show a dataset with a less pronounced Lorentzian characteristic (QA Cooldown 5), fit to a noise model consisting of a single Lorentzian, $1/f$, and white noise. **(e)** and **(f)** show a dataset with a less pronounced Lorentzian characteristic (QB Cooldown 5), fit to a noise model consisting of $1/f$ and white noise.

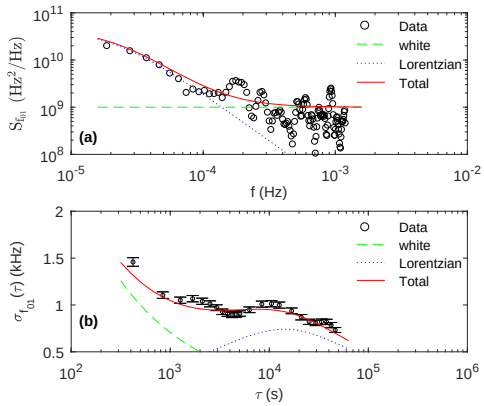

Supplementary Figure 5. **Frequency fluctuation data from qubit A, cooldown 3** (cf. Fig. 1). **(a)** Overlapping Allan deviation of frequency fluctuations. **(b)** Welch-method spectral density of frequency fluctuations. In both plots, the frequency fluctuation is fit to the sum of white noise and a single Lorentzian, where the amplitudes are the same for both types of analysis.

where $\langle\sigma_z\rangle$ is the expectation value of the Pauli matrix for the qubit, $\langle\sigma_z\rangle_\infty$ is the zero-temperature equilibrium value, $a_{\downarrow,k}$ and $\Gamma_{\downarrow,k}$ are the amplitude and decay rate from the two excited states k ($k = 1, 2$) to the ground state, and a_{osc}, f_{osc}, and Γ_{osc} describe the amplitude, frequency, and decay rate of an oscillation in $\langle\sigma_z\rangle$. These parameters can be rewritten in terms of coupling, g_{TLS}, and detuning, $\delta f = f_{01} - f_{\mathrm{TLS}}$

$$f_{osc} = \sqrt{g_{\mathrm{TLS}}^2 + \delta f^2} \tag{3}$$

$$a_{osc} = \frac{g_{\mathrm{TLS}}^2}{g_{\mathrm{TLS}}^2 + \delta f^2} \tag{4}$$

From this model we find a coupling rate of 4.8 kHz for the data in the main text. By assuming an electric dipole coupling between the qubit and the TLS, we can calculate a lower bound on the length of the electric field line, x, using[3]

$$x = \frac{2d}{hg_{\mathrm{TLS}}}\sqrt{E_c h f_{01}} \approx 39\,\mu\mathrm{m}, \tag{5}$$

where $d = 1$ Å is the assumed TLS dipole length.

Additionally, from Eq. (4) and the data in main text Fig. 2c, we find a TLS coherence time of approximately 100 µs. Such a lifetime is considerable larger than those found within the tunnel barrier of phase qubits[4]. However, it is strongly dependent on the coupling strength to the qubit. In absence of coupling[5], the phonon-limited relaxation time of a TLS is approximately 1 ms.

The main text also shows TLS switching rates as low as 75 µHz. These low switching rates are important in the general context of understanding TLS dynamics. Generally, measurements of charge noise[6]

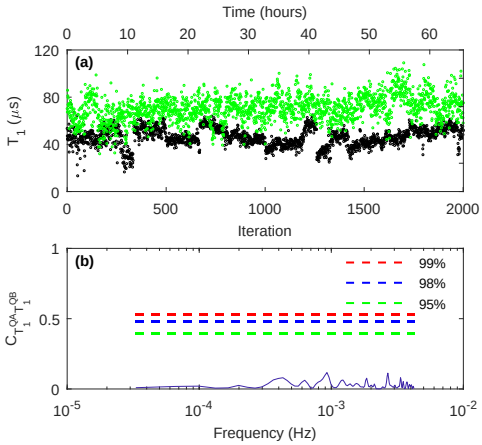

Supplementary Figure 6. **Magnitude-squared coherence analysis of T_1 fluctuations in both qubits. (a)** Multiple T_1 measurements performed simultaneously on qubits A (black) and B (green). The data consists of 2000 consecutive T_1 measurements that lasted a total duration of 2.36×10^5 s (approximately 65 hours). **(b)** Magnitude-squared coherence of the data in (a); the dashed lines represent the significance levels obtained from statistical bootstrapping.

are used to determine the switching rates of TLS. Those measurements found a minimum switching rate of γ_{min} = 100 Hz and a maximum switching rate of γ_{max} = 25 kHz. Combining these leads to a TLS switching ratio ($P_\gamma = 1/\ln(\gamma_{max}/\gamma_{min})$) of 0.18, a value in agreement with some experiments[7, 8], although other studies have found lower values[9]. A lower value of P_γ can be obtained if γ_{min} is smaller. From T_1 data we find switching rates ranging from 75 μHz to 2 mHz. Therefore, even the fastest rate is slower than those found in charge noise studies. This demonstrates that superconducting qubits are excellent probes of the TLS and highlights the need for further study of TLS dynamics.

D. Local vs. non-local origins

Within the main text, a simultaneous measurement of both qubits is performed to examine whether the observed fluctuations in T_1 are local to each qubit. To assess this, we calculate the magnitude-squared-coherence of the two data sets (shown in Fig. 6). This examines how much the T_1 of qubit A corresponds to the T_1 of qubit B. The value of the magnitude-squared coherence is normalized to between 0 and 1, where 1 relates to completely correlated (at that frequency). In Fig. 6 there are also dashed lines representing the threshold levels for significant correlation. These thresholds are calculated by statistical bootstrapping (repeatedly examining the magnitude-squared coherence of randomly resampled sets of one of the data set vs. the other original data set). The data in Fig. 6 is clearly far below these thresholds, as would be expected for uncorrelated noise that is local to each qubit.

[1] Nugroho, C. D., Orlyanchik, V. & Van Harlingen, D. J. Low frequency resistance and critical current fluctuations in al-based josephson junctions. *Applied Physics Letters* **102**, 142602 (2013). https://doi.org/10.1063/1.4801521.

[2] Müller, C., Shnirman, A. & Makhlin, Y. Relaxation of Josephson qubits due to strong coupling to two-level systems. *Physical Review B* **80** (2009).

[3] Martinis, J. *et al.* Decoherence in Josephson qubits from dielectric loss. *Physical Review Letters* **95** (2005).

[4] Shalibo, Y. *et al.* Lifetime and Coherence of Two-Level Defects in a Josephson Junction. *Physical Review Letters* **105** (2010).

[5] Faoro, L. & Ioffe, L. B. Interacting tunneling model for two-level systems in amorphous materials and its predictions for their dephasing and noise in superconducting microresonators. *Physical Review B* **91** (2015).

[6] Kafanov, S., Brenning, H., Duty, T. & Delsing, P. Charge noise in single-electron transistors and charge qubits may be caused by metallic grains. *Physical Review B* **78** (2008).

[7] Niepce, D., Burnett, J. & Bylander, J. High Kinetic Inductance NbN Nanowire Superinductors. *Physical Review Applied* **11** (2019).

[8] Burnett, J., Faoro, L. & Lindstrom, T. Analysis of high quality superconducting resonators: consequences for TLS properties in amorphous oxides. *Superconductor Science & Technology* **29** (2016).

[9] de Graaf, S. E. *et al.* Suppression of low-frequency charge noise in superconducting resonators by surface spin desorption. *Nature Communications* **9** (2018).